Spring 2021

Discovery and Investigation of Ammonia Decomposition Catalysts

Katherine McCullough

Recommended Citation

McCullough, K.(2021). *Discovery and Investigation of Ammonia Decomposition Catalysts.* (Doctoral dissertation). Retrieved from https://scholarcommons.sc.edu/etd/6345

Discovery and Investigation of Ammonia Decomposition Catalysts

by

Katherine McCullough

Bachelor of Science
University of South Carolina, 2016

Submitted in Partial Fulfillment of the Requirements

For the Degree of Doctor of Philosophy in

Chemical Engineering

College of Engineering and Computing

University of South Carolina

2021

Accepted by:

Jochen Lauterbach, Major Professor

Andreas Heyden, Committee Member

John Regalbuto, Committee Member

Hans-Conrad zur Loye, Committee Member

Melissa Moss, Committee Member

Tracey L. Weldon, Interim Vice Provost and Dean of the Graduate School

ABSTRACT

Liquid ammonia can be used as a hydrogen transportation and generation source for use in PEM fuel cells. Current Ru catalysts for ammonia decomposition contain high loadings of Ru and require reaction temperatures at or above 550°C to attain equilibrium conversion. For on-site hydrogen generation, it is of interest to combine hydrogen generation from ammonia decomposition directly with PEM fuel cells. For this occur, operating temperatures need to be considerably lowered and effluent concentrations of ammonia need to be minimized to avoid poisoning of the membrane. Therefore, it is of interest to develop a low-cost catalyst that exhibits high activity at temperatures at or below 450°C.

Prior work from our group discovered the use of supported hollandite (KRu_4O_8) exhibited excellent low temperature ammonia decomposition activity. This work further investigates under what conditions and synthesis parameters the hollandite structure can form, and further delves into the working state of the catalyst before exposure to ammonia. Here we show that the hollandite is a sacrificial structure that forms metallic Ru in various particle sizes depending on the H_2 reduction temperature through *in-situ* XRD analysis. Additionally, we compare these mixed metal Ru oxide catalysts with K promoted Ru catalysts synthesized via strong electrostatic adsorption (SEA). Next, we report the synthesis and high throughput catalytic screening of K promoted Ru based catalysts that have one of 31 additional metals incorporated, at three different Ru and secondary metal weight loadings.

Next, we report the synthesis and high throughput catalytic screening of K promoted Ru based catalysts that have one of 31 additional metals incorporated, at three different Ru and secondary metal weight loadings. The Ru weight loading varied from 3 wt% to 1 wt%. In total, over 100 catalysts (including duplicates) were synthesized via incipient wetness impregnation method and screened for ammonia decomposition activity using a 16-channel parallel plug flow reactor. Fourier transform infrared (FTIR) imaging was used to analyze all 16 effluent streams in parallel in under two minutes. At 300°C, catalysts containing Mg, Ca, Sr, Sc, Y, Zr, Hf, Ta, Rh and Ir with 3wt% Ru were found to have excellent ammonia decomposition activity compared a K promoted 4wt% Ru catalyst that was previously optimized by our group. Catalysts containing 1 wt% Ru and 3 wt% Sc, Y, Zr or Hf were found to outperform the K promoted 4wt% Ru catalyst at the same reaction conditions. Many of these catalyst combinations reported here have not been reported for ammonia decomposition previously. Further insight into Sr and Fe containing catalysts were further investigated for their turnover frequency (TOF), apparent activation energy, H_2 uptake, and through CO adsorption to understand mechanistically the difference between the two different kinds of catalysts.

Additional insight into the working of the catalysts were investigated through XRD phase identification and profile fitting to determine how the different Ru species present, crystallite size and secondary metal influenced the ammonia decomposition activity. A machine learning algorithm was developed to extract the activity descriptors and elemental characteristics that are responsible for ammonia decomposition activity at different operating temperatures. We demonstrate the application of a random forest machine learning algorithm to high-throughput experimental data to increase understanding of

catalyst behaviour through knowledge extraction and to guide catalyst discovery through predictions. The knowledge extracted from this material agnostic machine learning algorithm can be used to design a second iteration of catalysts, where features that contributed to the greatest change in activity were accentuated. Additionally, this information can be further applied to the design of ammonia synthesis catalysts at ambient pressures.

TABLE OF CONTENTS

LIST OF TABLES

LIST OF FIGURES

CHAPTER 1

INTRODUCTION

1.1 Hydrogen Energy and Storage

The rising concern of greenhouse gas emissions generated from non-renewable energy sources has promoted a wealth of research on sustainable, carbon free energy. Carbon dioxide emissions from natural gas, coal and oil are considered to be the largest threat to the environment, and yet world consumption of these energy sources continue to increase yearly (*1*). To date, oil consumption around the world has increased by 10% and natural gas consumption by 16% since 2010 (*1*, *2*). Continued research efforts to make clean energy technologies more efficient, abundant, and cost effective has resulted in a steady increase in the use of renewable energies. Primarily, renewable and sustainable energy sources include nuclear (*3*, *4*), solar, hydro and wind (*5*–*8*) and hydrogen energy (*9*–*12*). Ultimately, the challenges facing sustainable energy comes down to reliability, and an efficient means of storage and conversion for these energy technologies. Of these sustainable energy sources, hydrogen energy has gained traction and increased funding over the past decades since the proposal of the “hydrogen economy” during the oil crisis in 1972 (*13*–*15*). This term refers to the integration of hydrogen as one of the main components in energy systems, primarily for heating and hydrogen vehicles, as well as long term storage and transportation options (*16*). Globally, hydrogen has the capability to provide 3% of energy consumption by 2050 and has a significantly higher energy density than other conventional fuel sources (*10*, *17*).

Advances in proton exchange membrane fuel cells (PEMFCs) have also accelerated research efforts in hydrogen energy (*18*, *19*). PEMFCs exhibit high power densities, quiet operation, generate zero pollution and have higher efficiencies compared to combustion energies that are limited by the Carnot factor (*20*). Hydrogen is abundant, produces environmentally benign by products upon combustion, and consists of a very high energy density between 120 MJ/kg and 144 MJ/kg (*16*, *21*). The major barrier in utilizing hydrogen energy is the lack of efficient means in which to store and transport it. Gaseous hydrogen requires excess pressures (>300 bar) for storage which, in and of itself is an energy intensive process requiring 1.36 kWh/kg H_2 to compress isothermally from to 20 to 350 bar (*22*). Liquefied hydrogen can reduce volume constraints but requires cryogenic cooling to -253°C (*16*, *22*, *23*). These technologies have been applied to some prototype vehicles, but ultimately these methods of storage do not meet the required gravimetric energy densities set by the US Department of Energy (DOE) (*9*, *24*, *25*). Thus, researchers have focused on developing hydrogen storage methods and materials to meet the 1.5 kWh/kg H_2 gravimetric capacity for onboard hydrogen storage set by the US DOE for 2020 (*24*). Of course, hydrogen fueling stations and also be proposed in lieu of hydrogen powered vehicles (*11*, *25*). Additionally, hydrogen is a primary candidate in the zero-energy concept, which has been introduced in energy policy and investigates the concept of buildings generated as much renewable energy as they consume (*17*). Therefore, it obvious that there are many advantages and interest in integrating hydrogen into existing energy infrastructure and as an alternative, carbon free energy source, but efficient storage and conversion solutions must be addressed.

Solid hydrogen storage materials generally consists of metal organic frameworks (MOFs), metal hydrides or borohydrides that can physically or chemical store hydrogen (*16*, *26*–*28*). Currently these systems fail to have appreciable hydrogen sorption properties, slow kinetics, or require harsh operating temperatures. Hydrogen stored in methane, natural gas or methanol are obvious efficient methods for hydrogen storage and transportation. In fact, the majority of hydrogen production currently comes from the steam reforming of methane (*21*, *29*, *30*). Ammonia for hydrogen storage is a promising, carbon free alternative that satisfies the DOE targets for physical storage of hydrogen (*23*). Ammonia can be readily decomposed at atmospheric pressure to form molecular hydrogen and nitrogen, and current infrastructure for transportation already exists. Ammonia has a high hydrogen content, a comparative energy density to some fossil fuels (3.5 kWh/kg compared to 5.6 for methanol, and 7.2 for ethanol) and is easily liquefied (*31*, *32*). In fact, ammonia as a direct fuel source has been studied in both laboratories and pilot plants either through ammonia fuel cells or combustion, and ultimately may be a more attractive and economically feasible fuel source than hydrogen (*33*–*39*). Most importantly, the cost of anhydrous ammonia is lower than that of pure hydrogen, making this an economically feasible process (*40*, *41*). Ammonia could be disregarded as a potential hydrogen carrier because of its toxicity, but recent studies have found that reversible ammonia storage in the form of metal ammine salts can dramatically reduce the hazards and smells associated with handling ammonia, while preserving the high hydrogen storage capacity (*28*, *42*). Additionally, the Advanced Research Project Agency-Energy (ARPA-E) has launched its

“Renewable Energy to Fuels through Utilization of Energy-Dense Liquids” REFUEL program aimed to develop scale up energy generation processes from carbon neutral fuel sources to make electricity of hydrogen (*43*). These projects include ammonia cracking membrane reactors, electrochemical membrane reactors for ammonia, H_2 generation from catalytic ammonia cracking, direct ammonia fuel cells and wind energy to ammonia synthesis to name a few. Ultimately, these points indicate that ammonia is an excellent candidate for hydrogen storage and transportation.

While decomposing ammonia to generate hydrogen is a carbon neutral process, ammonia is primarily produced from the steam reforming of methane and coal gasification (*29*, *30*, *38*). Ammonia alone is responsible for 1% of the world’s CO_2 emissions and 1.8% of the world’s consumption of fossil fuels (*38*, *44*, *45*). This is not surprising since it is the second largest production process in the world (*46*). Even without facilitating ammonia for hydrogen transport, there is a need to decarbonize ammonia synthesis and ultimately hydrogen production. Very recently, a massive number of projects have been announced for carbon free ammonia production. For example, Saudi Aramco and the Institute of Energy Economics announced its first shipment of “blue” ammonia, a process which generates hydrogen from natural gas and then captures the CO_2 emissions to be used further for methanol synthesis and enhanced oil recovery (*47*, *48*). Air Products has also recently signed an agreement to begin building a 4 GW ammonia production facility powered by renewable energy in 2025 (*49*). They propose to produce 650 tons per day of hydrogen through water electrolysis. Monolith Materials will produce carbon free ammonia by their proprietary technology that converts natural gas into hydrogen and carbon black, instead of CO_2 (*50*). This demonstrates that there will be a market and supply for “green” ammonia and hydrogen production in the near future. Yara also announced plans to continue to build upon their existing fleet of solar powered ammonia production plants from water electrolysis (*36*, *39*). The decarbonization and green production of ammonia and hydrogen is a promising step forward towards reducing our impact on the environment, but the long-term implications of water as a source of fuel should be further debated considering the growing demand and scarcity of fresh water sources (*51–53*). Currently, ammonia as a hydrogen storage and transportation molecule is seeing significant growth in research and industry sectors. While these points indicate that ammonia is a good candidate for the storage of hydrogen, the conversion of ammonia to hydrogen is yet to be addressed.

1.2 Catalytic Ammonia Decomposition

Hydrogen liberation from ammonia occurs through a thermal catalytic cracking process occurring at atmospheric pressure and requiring temperatures upwards of 550°C for complete conversion (*23*, *32*, *54*). The efficiency and cost at which current catalysts can decompose ammonia is the main drawback for utilizing ammonia for hydrogen storage. Additionally, the feasibility of ammonia for hydrogen storage depends upon realistic alignment between the temperature of decomposition with that of the PEMFC (~200°C) (*55*) so that the two technologies can be integrated. Using thermodynamic equilibrium data, we calculated the equilibrium conversion of ammonia at 1 bar, as shown in Figure 1.1. At 200°C, the equilibrium conversion for ammonia is roughly 89%, which is not adequate conversion for the low ammonia tolerance of PEMFCs (0.1 ppm) (*20*, *56*). This can be mitigated by using commercially available adsorbents, high-temperature PEMFC, alkaline fuel cells, or implementing membrane reactors during ammonia decomposition (*20*, *57*, *58*). Metals for ammonia decomposition typically include Fe, Co, Ni and Ru, which will

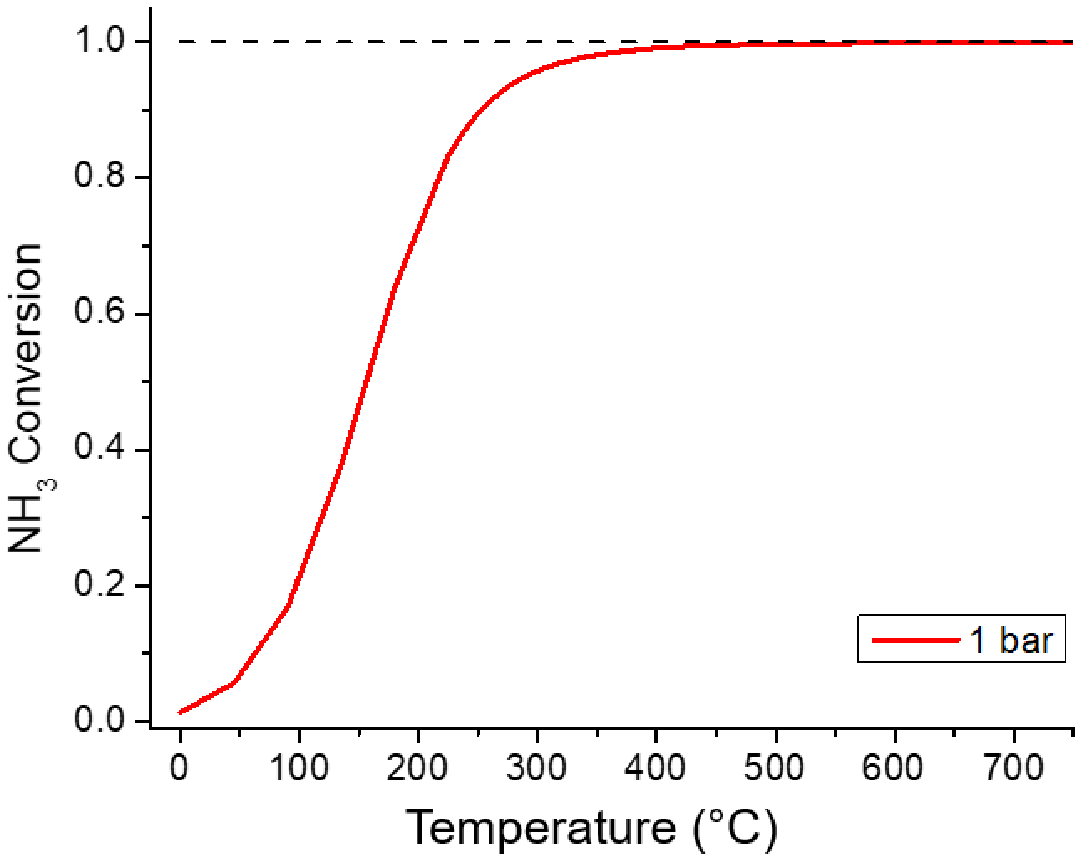

Figure 1.1. Equilibrium conversion of ammonia at atmospheric pressure

be elaborated on in later sections. Currently, the most effective catalysts consist of Ru nanoparticles supported on carbon nanotubes (CNT) (*59–63*). Of these, the commonly cited “state of the art” catalyst achieves less than 10% conversion at 200°C, and reaches 60% conversion of ammonia at roughly 400°C, using 7% Ru/CNT promoted with 4% Cs (*63*). While the Ru loading was considerably high and the inlet ammonia concentration was not reported, these results were some of the first to demonstrate that high ammonia conversions can be achieved at more mild temperatures. Typically, Ru based catalysts require upwards of 550°C to obtain high activity. Thermodynamically, 98% conversion can be achieved at 350°C, and 99.1% at 400°C, at which the reaction is essentially irreversible. Below 400°C, the conversion becomes more dependent on the kinetics of the reaction on the catalyst surface. The scarcity and cost of using high loadings of Ru also limits the economic feasibility of the decomposition reaction. A compilation of some of the ammonia decomposition literature shown in Figure 1.2 from 2001 to 2018, highlighting the active metal used in different studies for this reaction. Interestingly, this demonstrates that research efforts that are geared towards finding or utilizing alternative catalysts to Ru are extremely scarce. Instead, most studies focus on the optimization of existing Ru based catalysts through manipulation of Ru particle size, support and promoters. Therefore, it is pertinent to focus research efforts on cost reduction of the active metal component while simultaneously enhancing the reactivity at lower operating temperatures. Thermodynamically, this could be achieved at very mild temperatures, however diminishing the gap that exists between the thermodynamic and kinetic limitations will require more complex and broader research strategies than which currently exist.

1.2.1 A Brief History on Ammonia

Ammonia decomposition has been studied since the early 19th century as a convenient test reaction, and to better understand the ammonia synthesis reaction, which had had very little success up until this point (*46*, *64*, *65*). After the formulation of the van't Hoff equations for thermodynamic equilibrium, Fritz Haber discovered that a combination of high pressure and low temperatures were necessary for appreciable ammonia synthesis rates (*65*). Carl Bosch was then able to successfully scale up this reaction and discovered the technology for high pressure flow reactors. In the 1950's, Alwin Mittasch underwent one of the most comprehensive screening of over 2,500 different catalyst combinations to discover that fused Fe promoted with Al_2O_3, CaO and K was highly active for ammonia synthesis (*65–67*). Ammonia synthesis had a monumental impact on how we study,

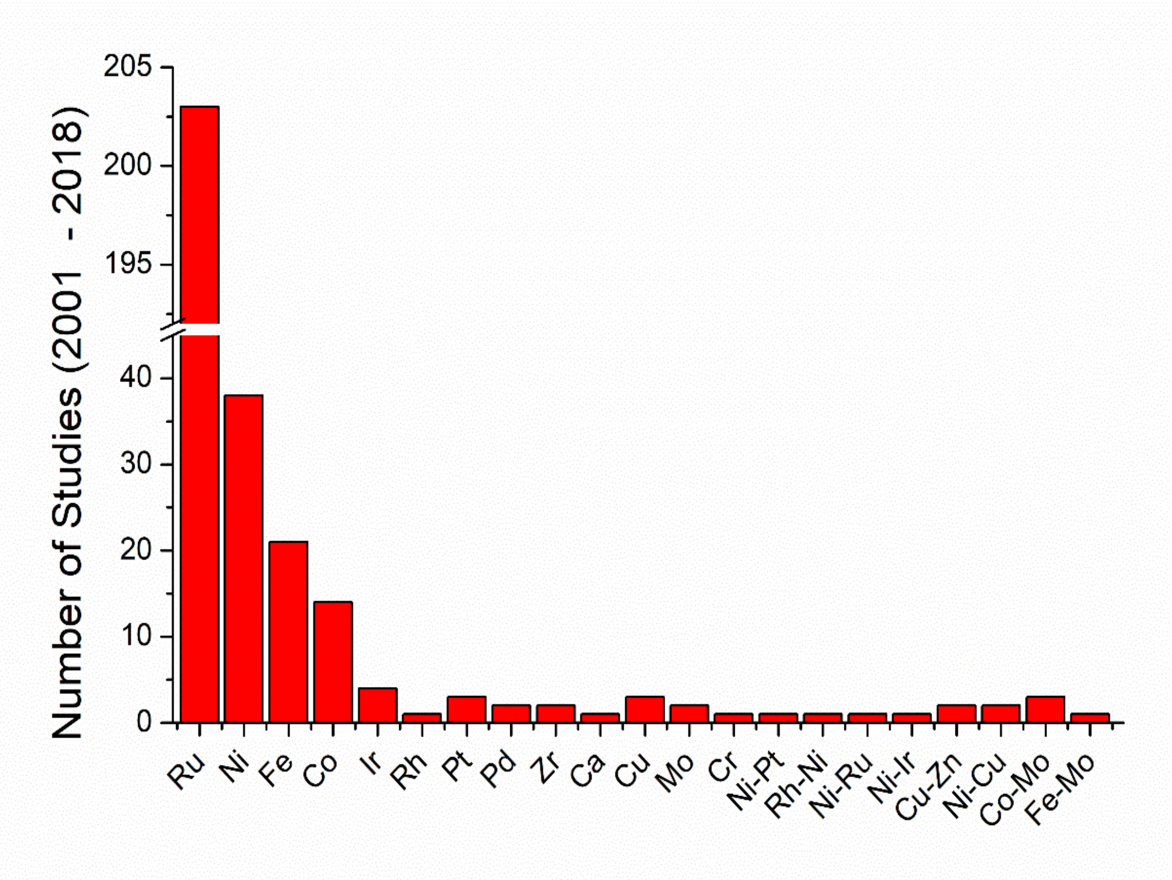

Figure 1.1. A compilation of some of the ammonia decomposition literature from 2001 – 2018 highlighting the active metal studied during the catalytic reaction.

investigate and go about catalytic materials and reactions. Industrially, the current ammonia synthesis catalyst is still relatively unchanged from the composition discovered by Mittasch. Regardless of these advances, mechanistic understanding was still very unclear due to the complexity of the reduction of Fe under reaction conditions, the surface coverage of K species that would change the electronic environment of the multiple different Fe crystal planes present (*68*). With the onset of ultrahigh vacuum (UHV) technologies, it became possible to simplify the complexity of catalysts by studying how the reaction proceeds over different crystal orientations.

The ammonia synthesis reaction has basically formulated all general concepts related to heterogeneous catalysis because of its apparent simplicity and the range of conditions and equilibrium situations in which it can be studied (*64*). The reaction is also well suited for surface science studies to determine how different atomic surface structures and composition influence activity (*69*). These efforts were led by Ertl and Somorjai to improve understanding of ammonia synthesis (*70*). For example, Somorjai et al. demonstrated how promoting three different basal planes of Fe with K could enhance the sticking coefficients of nitrogen. The rates of ammonia formation varied significantly over the different basal plans and with the addition of K (*71*). Additionally, the elementary reactions for ammonia synthesis could be studied on single crystal surfaces, which can provide the basis for microkinetic models to furth describe the behavior of a catalyst under more technical operating conditions.

1.2.2 Kinetics and Reactivity of Ammonia Decomposition

It was originally thought that the best catalyst for ammonia decomposition would also be the best catalyst for ammonia synthesis due to the principle of microscopic reversibility. Curiously, it is now widely accepted and demonstrated within one body of work this is not the case, due to differences in operating conditions and rate determining steps (adsorption vs. desorption of molecular nitrogen) (*72*). The original paper compares ammonia synthesis and decomposition rates as a function of dissociative nitrogen adsorption energy and makes the claim that the optimal ammonia decomposition catalyst will not be the optimal ammonia synthesis reaction based on this scaling relation. However, both reaction are enhanced by basic promoters and alkali and alkaline earth metal oxides and some examples of further catalyst systems used for both reactions can be found (*73–76*). The kinetics of ammonia decomposition have been shown to vary based on the temperature, concentration and active metal component (*77*, *78*). The most active metal for ammonia decomposition and ammonia synthesis is Ru, and therefore the kinetics and reactivity addressed here will be mainly focused on Ru based catalysts and surfaces. The Sabatier principle explains the reason between the high reactivity of Ru, for it can easily form stable intermediates, but not so stable as to retard the rate of reaction (*70, 79, 80*).

Ammonia decomposition occurs through sequential dehydrogenation steps, followed by the recombination and desorption of molecular N_2 and H_2 from the catalyst surface. The elementary steps for this reaction are as follows and are the reverse of the ammonia synthesis reaction:

$$NH_3 \leftrightarrow NH_{3,ads} \tag{1.1}$$

$$NH_{3,ads} \rightarrow NH_{2,ads} + H_{ads} \tag{1.2}$$

$$NH_{2,ads} + H_{ads} \rightarrow NH_{ads} + 2H_{ads} \tag{1.3}$$

$$NH_{ads} + 2H_{ads} \rightarrow N_{ads} + 3H_{ads} \tag{1.4}$$

$$2H_{ads} \rightarrow H_2 \tag{1.5}$$

$$2N_{ads} \rightarrow N_2 \tag{1.6}$$

Kinetic studies over Ru (0001) crystals have determined that the RDS is either the associative desorption of nitrogen atoms (eq. 1.6) or N-H bond cleavage (eq. 1.2-1.4) to be rate limiting (*81*, *82*) but no consensus on the rate determining step (RDS) or the most abundant reaction intermediate (MARI) have been established within the literature. Egawa et al., studied ammonia decomposition over Ru (0001) and stepped Ru (1110) single crystals and determined that the RDS may be a function of temperature, where below 650K, nitrogen desorption is rate limiting, and above 750K, N-H cleavage becomes rate limiting (*83*). They found that the rate of reaction increased up to ca. 560K, and then decreased at higher temperatures. At low temperatures when nitrogen desorption is rate limiting, they found that the kinetics were dependent on the ammonia and hydrogen partial pressures, and that the rate of nitrogen formation was one order of magnitude faster on stepped Ru (1110) than Ru (0001) crystal. Higher hydrogen partial pressures decrease the concentration of surface nitrogen and therefore inhibits the rate of reaction. This has been determined over various Ru catalysts by fitting rates of reaction to simple power law models (*84*, *85*). At higher temperatures, the reaction was found to be independent of hydrogen and nitrogen pressures and the amount of adsorbed hydrogen on the surface was found to be negligible (*83*). The activation energy for N_2 desorption on Ru (0001) has been determined to be 184-190 kJ/mol (*81*, *86*). However, differences in the RDS may appear under different reaction conditions (UHV conditions vs high pressures). Hinrichsen et al. (*87*) used microkinetic modeling to bridge the gap between UHV studies and high pressure studies, by probing the interaction of N_2 with Ru supported on Al_2O_3, MgO and Cs-Ru/MgO through N_2-TPD and isotopic exchange reactions. They determined that the desorption of N_2 from Ru/MgO resulted in new low temperature desorption peaks, which were not present in Ru/Al_2O_3. The Ru/MgO N_2 desorption event was attributed to electronic enhancement of the active site through oxygen vacancies that are exist at the interface between Ru crystallites and MgO. These sites were also present in Cs-Ru/MgO, and the addition of Cs lowered the activation energy for N_2 desorption from 158.0 to 137.0 kJ/mol.

Differences in RDS may be due to the support used as well as the dispersion and particle size and shape of the Ru particles. In fact, the dissociative adsorption of N_2 on Ru (0001) crystal has been shown to almost exclusively occur over Ru step sites (*88*). By preferentially blocking step sites on a Ru (0001) crystal through Au deposition, Dahl et al., showed that the N_2 sticking coefficient decreased by seven orders of magnitude. Additionally, N_2 desorption on Ru (0001) was strongly affected as exhibited by N_2-TPD, where the desorption of N_2 was shifted up roughly 150K with small amounts of Au. Egawa et al., found that the H_2 rate of formation was one order of magnitude higher on the stepped Ru (1110) single crystal (*83*). This demonstrates the structure sensitivity of the NH_3 decomposition reaction and may explain the differences in different RDS determined in various studies over Ru catalysts.

Therefore, it is clear that the rate of the reaction and kinetics of ammonia decomposition are heavily influenced by the support, promoter and operating conditions employed. In fact, experimental determination of the RDS using Al_2O_3 supported metal catalysts have shown that the RDS may be a function of the active metal (*78*). Ganley et al. (*78*) attempted to correlate TOF over 13 different metals with common models used to predict catalytic reactivity such as the energy of the center of the d-band relative to the Fermi level and heat of formation of the metal oxide. They determined that both the relative N-H bond cleavage and associative desorption of nitrogen were needed to predict the reactivity of the different metals, which resulted in a volcano plot relationship, where N-H cleavage is the RDS over precious metals like Ru, Rh, Pd, and Pt and the nitrogen desorption is the RDS over Fe, Co and Ni (*23*, *78*, *80*). The determined the order of activity Ru > Ni > Rh > Co > Ir > Fe. In contrast to Ganley et al., TAP experiments studying surface species and product formation during NH_3 decomposition over Ru/C catalysts determined that the RDS is associative desorption of N over Ru/C (*89*). Additionally, Yin et al. (*90*) determined the order of activity Ru > Rh > Ni > Pd = Pt > Fe.

Regardless of differences in the literature, theoretical calculations commonly utilize the N_2 binding energy of various metal surfaces as a descriptor to predict NH_3 decomposition reactivity (*80*, *88*). This method has identified various bimetallic catalysts such as Fe-Pt, Co-Pt, Cu-Pt (*89*, *90*) and Co_3Mo_3N (*80*) as promising cost effective catalysts. However, such highly defined systems such as Fe-Pt (111) will be difficult to experimentally synthesize and stabilize at more technical operating conditions. Yet there has been some success with CoMo catalysts for NH_3 decomposition (*91*), and most recently by using high entropy alloy catalysts composed of CoMoFeNiCu particles with various Co/Mo ratios (*92*).

1.2.3 Active Metals

While Ru is the most intrinsically active metal for ammonia decomposition, the cost associated with using Ru catalysts is a major drawback to the scaling of this process. In 2020, the cost of Ruthenium was 270 USD/oz, while that of Cobalt is only 0.21 USD/oz (*93*). This has motivated research for alternative catalysts based on metals that are more readily available and cost effective. These metals mainly consists of non-noble metals like Co, Fe, Ni as well as a variety of carbides and nitrides, based on their positioning in the volcano plot relationship describing ammonia decomposition rates of reaction with the N_2 binding energy (*78–80*). This body of work will discuss some of the results and variations in activity primarily in Fe, Ni and Co based catalysts.

Fe based catalysts have been extensively studied for ammonia decomposition because of their successful use in the ammonia synthesis reaction. However, under ammonia decomposition operating conditions, the formation of Fe nitrides is more prevalent, thus deactivating these catalysts at temperatures as low as 300°C (*23*, *88*). It has been demonstrated that encapsulating Fe nanoparticles in SiO_2 to create core-shell nanoparticles can show stability for up to 40 hours at 550°C and achieve a conversion of 60% at this temperature (*94*, *95*). Jedynak et al., showed that K promoted Fe catalysts supported on graphitized carbon with Fe nanoparticles resulted in higher turnover frequency (TOF) with decreasing Fe particle size, but that the apparent activation energy was significantly higher than that of K promoted Ru catalysts supported on carbon (166 kJ/mol compared to 139 kJ/mol) (*96*). Duan et al. (*97*, *98*) synthesized Fe particles on top of carbon nanofibers and achieved 51.3% conversion at 600°C in pure ammonia. On mica supported Fe/CNF catalysts, the activity was enhanced to 98.8% at the same temperature, due to the formation of small and highly dispersed Fe particles on top of the CNF. Lu et al. (*99*) synthesized Fe nanoparticles supported on CMK-5 carbon and SBA-15 and were found to be completely immobilized inside the channels of the supports. Fe/CMK-5 showed complete conversion of ammonia at 700°C. The addition of alkali metal promoters to Fe catalysts have been shown to prevent sintering of Fe nanoparticles (*100*), but overall, activities of Fe based catalysts normalized to the content of their active metal content are roughly two orders of magnitudes less activity than Ru based systems (*88*).

It has been shown that enhancing dispersion and reducing Ni particle size is the most effective method for enhancing the activity of Ni based catalysts (*88*). Ni based catalysts for ammonia decomposition have shown to be highly surface sensitive. This has been demonstrated by Li et al. (*101*) who studied ammonia decomposition over Ru and Ni catalysts supported on SiO_2, MCM-41 and SBA-15. The Ni catalysts with the highest dispersion were found to have the lowest number of active sites. This suggests that the different preparation methods used may have changed the Ni dispersion, morphology, and structure of the Ni nanoparticles. Additionally, they found that while K promotion greatly enhanced the activity of Ru based catalysts, K promotion had little effect on the Ni based catalysts supported on siliceous materials. Hu et al. (*102*) studied the effect of preparation method on Ni/ZSM-5 catalysts by synthesizing catalysts through wet impregnation, deposition-precipitation, solid state ion exchange, and modified solid state ion exchange methods. They found that the different preparation methods resulted in various Ni particle sizes, and that the smallest Ni particles were also the most active. They attributed the enhanced activity exhibited by the modified solid-state ion exchange synthesis method to the added dealumination process, which in turn allowed for framework Ni species to be confined in the ZSM-5. The Ni/ZSM-5 catalyst achieved almost complete conversion of ammonia at 650°C under pure ammonia. Lucentini et al. (*103*) achieved near complete conversion of ammonia at 550°C in 43% NH_3 using CeO_2 supported Ni catalysts, but these catalysts suffered from reoxidization to NiO at temperatures below 450°C. CeO_2 has also been shown to promote Ni supported Al_2O_3 catalysts (*104*). In 15% NH_3, a Ce/Ni ratio of 0.1 resulted in roughly 75% conversion at 500°C. Ce/Ni molar ratios greater than 0.1 resulted in a decrease in activity. The addition of CeO_2 to Ni/Al_2O_3 catalysts suppressed sintering of Ni nanoparticles and reduced the apparent activation energy compared to Ni/Al_2O_3 catalysts.

Co has also showed promise as a cost effect low temperature ammonia decomposition catalyst. Co has a calculated activation energy of 27 kJ/mol lower than Fe for ammonia decomposition and does not suffer from nitride formation (*105*). Czekajło et al. (*106*) studied the effect of synthesis conditions and promoters on catalytic activity of

Co based catalysts synthesized via precipitation method. Promotion by Ca, K, and Al acted to hinder sintering of Co nanoparticles and also had the highest number of active sites. Additionally, the found that higher precipitation temperatures resulted in smaller Co_3O_4 nanoparticles. Torrente-Murciano et al. (*107*) demonstrated that microporous carbon supports were able to stabilize small Co nanoparticles and that ammonia decomposition activity was hindered by the addition of Cs, which is similarly observed for other non-metal catalysts, but deviates from the relationships established for Ru based catalysts.

1.2.4 Surface Sensitivity

Both ammonia decomposition and synthesis are both structure sensitive reactions, which can be studied initially by measuring the reactivity of single crystals in ultra-high vacuum (UHV). Different surfaces will have different reactivities and product distributions reflect the difference active sites present on each surface. Strongin et al. (*108*) determined initial rates of ammonia synthesis over Fe(111), Fe(100) and Fe(110) surfaces and studied the effect of potassium over these crystal orientations under UHV reaction conditions.

Fe(110) showed no activity for ammonia synthesis with adsorbed K, and the addition of K drastically increased the reaction rates over the (111) and (100) surfaces by inducing changes in the reaction order with respect to hydrogen and ammonia. Dahl et al. (*109*) studied the dissociative chemisorption of N_2 on Ru (0001) surfaces in order to determine the influence of step sites on the N_2 sticking coefficient. This was accomplished sputtering Au onto a Ru (0001) metal surface. Typically, even clean metal surfaces will have some concentration of step sites present, especially those of high-index (*110*). They were able to isolate and measure reactivity over flat and stepped surfaces by depositing Au onto the Ru (0001), which would preferentially poisoning step sites. The N_2 sticking coefficient decreased by seven orders of magnitude with step sites were blocked, demonstrating that N_2 dissociation occurs exclusively over stepped sites. While geometries of step sites cannot be physically measured or observed, density functional theory (DFT) calculations can be used to determine N_2 dissociation energies over different geometric arrangements (*111*) and compared to the observed dissociation barriers from UHV experiments (Figure1.3a). These experiments formed the basis behind determining the most active site for ammonia decomposition. The site consists of an exposed threefold hollow site in close proximity to a bridge site, as seen in Figure1.3b. This configuration of Ru atoms is termed a B_5 site, by the nomenclature describing statistical arrangement of atoms first proposed by Hardeveld and Hartog (*112*). Since then, other works have proposed that statistically, different Ru shapes and sizes will more likely have more B_5 sites than others (*113–115*). However, many studies simply conclude that higher activity of a catalyst must be due to more B_5 sites present, either through electronic modification with a promoter or higher degree of metal dispersion.

1.2.5 Electronic and Structural Modification

The addition of different additives, specifically alkali metals, alkaline earth metals and lanthanide metals have shown to dramatically enhance activity. Ru catalysts promoted with K, Cs or Ba have shown to be very active for ammonia decomposition (*116–118*). The role of promoters is often unclear, whether they promote the formation of B_5 sites, accelerate the recombination and desorption of nitrogen, or some combination of the two (*119*). The role of the promoter also varies significantly based on the promoter precursor, metal precursor and support used during synthesis. One study has shown that K is the best

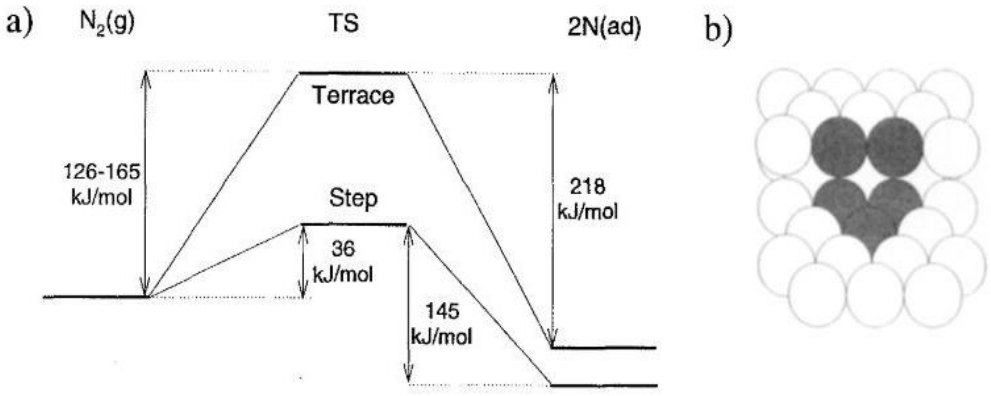

Figure 1.2. (a) Dissociation and desorption barriers for nitrogen interaction with Ru (0001) surface. TS is the transition state. (b) Sketch of the active site for nitrogen dissociation (black atoms) at the Ru (0001) step as found by DFT calculations. Adapted from ref (109).

promoter for Ru/Al_2O_3 catalysts (*118*), while another demonstrated that Na is most active for Ru/CNT (*120*). The acidity of the support can thus influence the interaction between the promoter and the support and also influence the optimal loading (*61*, *121*). Yu et al. (*122*) studied the effects of alkaline earth metal amides for ammonia decomposition and found that Ru-Ba$(NH_2)_2$ and Ru-Ca$(NH_2)_2$ had higher turnover rates and lower activation energies than Ru-Mg$(NH_2)_2$ and Ru/MgO. Yin et al. (*123*) demonstrated that KNO_3 modified Ru catalysts were highly efficient went supported on CNT, but not as effective supported on MgO. Zhang et al. (*124*) compared Ru/MgO catalysts promoted with Cs- or K- from carbonate or nitrate sources, and found that $CsNO_3$ resulted in the most active catalyst, albeit differences in the four promoted catalysts were very small. It is difficult to make direction comparisons across the literature due to the large differences in operating conditions and variations in synthesis parameters. For example, these two studies that both looked at KNO_3 modified Ru catalysts resulted in one with an activity of ~25% at 450°C, and the other 40% at the same temperature and space velocity.

The differences in promoter activities may be due to residual precursor ions present on the catalyst surface. Wang et al. (*61*) studied the effect of different electron withdrawing groups (F^-, Cl^-, Br^-, SO_4^{2-} and PO_4^{3-}) from different promoter precursors on ammonia decomposition for Ru/CNT catalysts. They found that KNO_3 had the highest activity and lowest activation energy, and activity trends were as followed: $NO_3^- > OH^- > CO_3^{2-} > F^- > Cl^- > Br^- > SO_4^{2-} > PO_4^{3-}$. Murata et al. (*121*, *125*) also studied the effect of residual Cl^- from $RuCl_3$ precursors and found that it was detrimental to activity, but that alkali or alkaline earth metal hydroxides can act as scavengers for the chlorine ions. This has led to the use of other Ru precursors like $Ru_2(CO)_{12}$ and $Ru(acac)_3$ which are more sterically hindered and will enhance the metal dispersion of the Ru particles compared to $RuCl_3$. The effect of lanthanides on Ru based catalysts have shown to have a stronger promoter effect than alkalis (*126*). Lanthanide promoter mechanism may involve anchoring Ru particles to the support while additionally providing electron donation.

1.3 High Throughput Experimentation (HTE)

Few studies are comprehensive enough to provide a legitimate comparison across different catalysts due to the broad variation that is present in operating conditions and synthesis parameters. The variables include but are not limited to catalyst structure, surface area, metal dispersion, and interactions between the metal, promoter and support. To further complicate matters, these variables are all intertwined and correlated, thus making it difficult to deconvolute and make viable comparisons through different literature studies. In addition to variables associated with catalyst synthesis, heterogeneous catalysis has the added complexity of operating and synthesis conditions that will also influence the activity, selectivity, and stability of various catalysts.

High throughout experimentation (HTE) and combinatorial sciences were first introduced to the field of materials by Hanak in the 1970s stressing the power of parallel synthesis techniques (*127*, *128*). These methods contrast the previous, one at a time approach to material discovery, commonly coined the “Edisonian” approach, due to the sequential nature of testing that Edison performed during his discovery of the incandescent light bulb filament. Over the following decades, these approaches to material discovery and synthesis were integrated into academic labs and companies. For example, Creer et al. (*129*) designed a multichannel microreactor for catalyst evaluation, where each of the 6 reactors were attached to a gas chromatograph. HTE can be used to rapidly synthesize, screen and analyze a large number of materials in a short amount of time. An intelligent design of experiment based on domain knowledge is pertinent to success. Combinatorial methods have also been recently developed that allow one to explore multidimensional catalyst composition and process parameter spaces at a high level of resolution. Initial high throughput studies suffered from poor data quality and was not considered to have low scientific value (*130*). However, methodologies to accurately quantify compositions, conversions, and selectivity’s of diverse catalyst libraries now exist.

1.3.1 HTE Screening Tools

Design of Experiments (DOE) is an essential tool to HT screening and experiments. The interactions between large number of variables and the different amounts of these variables that are present in a catalytic system have already been highlighted by reviewing ammonia decomposition catalysts. DOE techniques are a way to minimize the number of experiments needed while maximizing the amount of information acquired through a pre-determined number of variables and assessing the importance and interactions between multiple variables. DOE can be useful for comparing several factors, screening for which factors are important, determining interactions between variables, and optimizing a response, such as activity (*131*). Combinatorial approaches to catalyst discovery have been employed for reactions such as dehydrogenation (*132*), oxidative methane coupling (*133*, *134*), NO_x storage and reduction (*135*, *136*), CO oxidation (*137*) and ethylene epoxidation (*138*). DOE encompasses factorial designs, screening designs, response surface methodologies, and analysis of variance to name a few.

Machine learning (ML) has also been utilized to significantly increase the rate of material discovery. ML employs statistical algorithms to make connections between important features in a dataset and makes predictions from these learned relationships (*139*, *140*). Typically, a matrix of input features is constructed for which the algorithm can then construct qualitative or quantitative relationships between the features and the property of interest (*141*). In catalysis, ML techniques are often limited to computational data due to the massive number of datapoints necessary to generate an accurate model. These methods are capable of predicting a multitude of catalyst compositions (*142–144*). But experimentally, these catalyst compositions are not always physically feasible to synthesize. The limitation of time-at-a-time experimentation typical of experimental catalysis has previously limited the feasibility of ML in this field. But when coupled with data generated from HTE, accurate predictions of stable and synthesizable materials can be made (*145–147*).

1.3.2 HTE Analysis Techniques

Early HTE studies in catalysis often utilized scanning probe mass-spectrometry, infrared (IR) thermography or optical imaging techniques such as cataluminescence (CLT) or laser-induced fluorescence imaging (LIFI) for analysis (*148*, *149*). IR thermography is able to detect small changes in temperature at the catalyst surface, and thus can measure activity of exothermic reactions but cannot speciate between products. Similarly, CLT relies on detecting chemiluminescence emission of combustion reactions and LIFI relies on the breaking and forming of chemical bonds that can modify fluorescence of a molecule (*132*, *149–153*). Spatially resolved FT-IR is both quantitative and qualitative but can only be applied to products with an IR vibration, and only when product vibrations are not convoluted (*135*, *154*). The advantage of these optical imaging methods is that they offer parallel analysis of samples, but their uses are limited to specific cases. Scanning probe mass spectroscopy and gas chromatography have also been applied to HTE analysis for more complicated gas mixture, but can only be performed in a sequential manner, thus dramatically increasing the time for analysis and limiting them to only steady state applications (*148*, *149*, *155*).

1.4 Dissertation Scope

The work presented in this dissertation is motivated by the search for a low-cost ammonia decomposition catalyst that achieves high activity at temperatures at or below 450°C. Chapter 1 has reviewed the underlying reasoning for studying catalytic ammonia decomposition and has presented the issues in the current technology as well as a comprehensive review of our currently knowledge. Additionally, this chapter sets up HTE as the primary investigative tool for ammonia decomposition material discovery. In Chapter 2, the details are provided for the methods and theories behind the techniques that have been utilized for this work, which include catalyst synthesis, characterization techniques, and the various reactor configurations used throughout the work. Chapter 3 goes into depth describing a baseline, K promoted Ru catalyst and provides understanding of the structural and morphological changes of this catalyst before reaction, during the working conditions, after reaction and in different synthesis environments. Chapter 4 will discuss the selection of design catalyst design space, high throughput screening, and characterization of the ammonia decomposition catalysts and compare the activity of these to the baseline catalyst described in Chapter 3. General insight into the mechanism of the catalysts will be discussed based on previous work using machine learning algorithms, crystallite size analysis, and general trends in activity based on the different metals position on the periodic table. Lastly, Chapter 5 will conclude this body of work and give a conclusion and perspective on the future of this research and technology.

CHAPTER 2

THEORY & METHODS

2.1 NH_3 Decomposition Catalytic Activity Testing and Reactor Set Up

2.1.1 High Throughput Reactor Set Up

High throughput catalytic testing was conducted using a 16 channel parallel high throughput reactor which was previously built and optimized by the Lauterbach group (*149*). The reactor is composed of four ceramic radiant heaters (3 in ID, 6 in height), each of which heat four reactor tubes. Four on-off Proportional-Integral-Derivative (PID) controllers were used to control the power output of each of the heaters, which are controlled using an in-house written LABVIEW program. Additionally, the temperature in each furnace and reactor is measured using this software. A top view of the heater and reactor set up is shown in Figure 2.1.

Typically, each reactor is loaded with 50 mg – 500 mg of catalyst supported onto stainless steel frits (10µm pore size, Chand Metallurgical) to hold the catalyst powders in place within the reactor tube. In order to ensure even flow distribution between the 16 channels, a single gas inlet is split into 16 individual concentric capillary spirals and is fed to each of the reactor channels. The flow distribution system is contained inside a heated box. Further detailed information on this system can be found elsewhere (*135*, *138*).

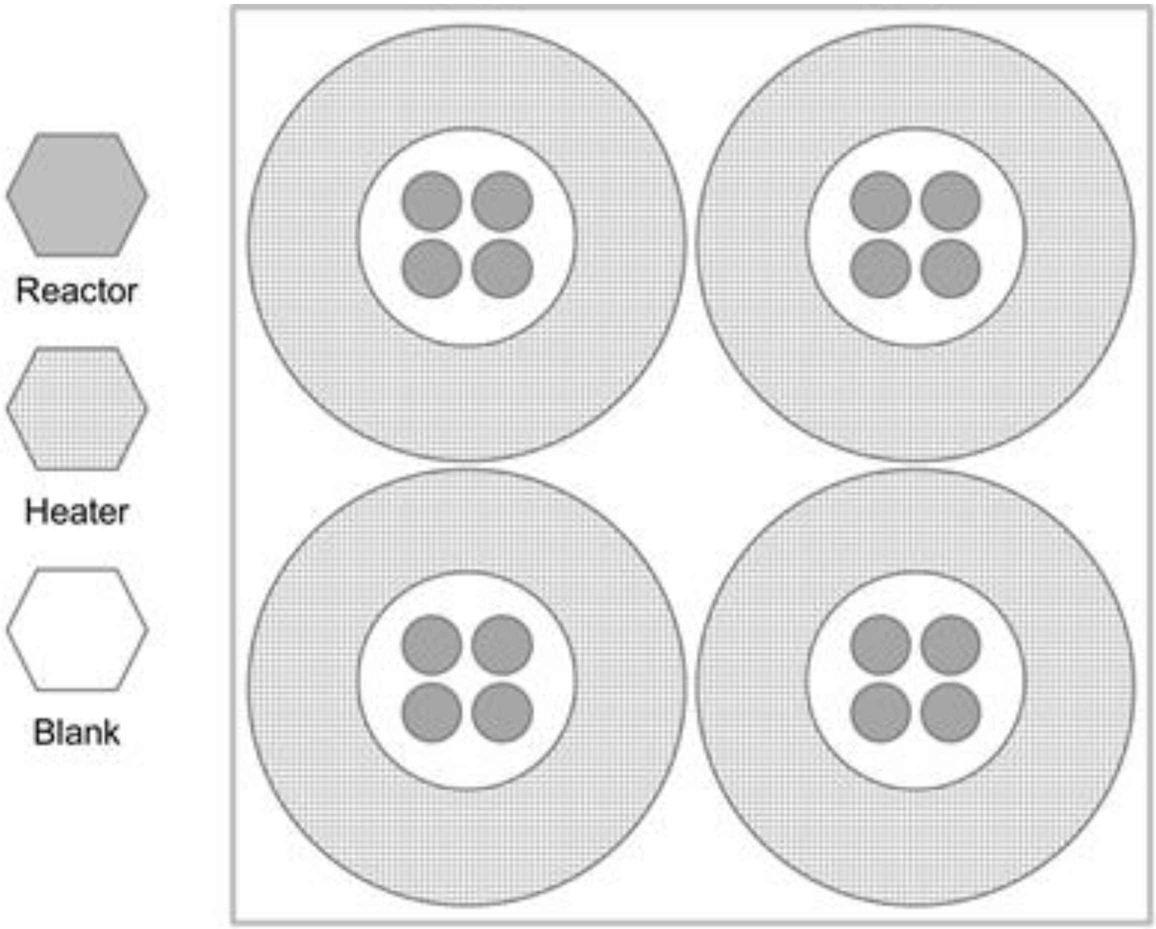

Figure 2.1. Top-view of the high throughput reactor. Adapted from ref (*138*).

2.1.2 Quantitative Analysis using Spatially resolved FTIR

In order to efficiently analyze the effluent from each reactor, parallel analysis of the product streams is required. Parallel analysis techniques primarily include optical screening methods, which include CTL, REMPI, ecIRT, FTIR and LIFI (*149*, *155*). Sequential analysis using GC and MS techniques have also been used for various high throughput systems (*128*, *156*, *157*). Unlike some optical screening techniques, FTIR permits species identification for molecules that are IR active. Additionally, gas phase concentrations can be measured as a function of absorbance at a given optical path length. The incorporation of focal plane array (FPA) detectors provides the spatial resolution necessary for parallel analysis using FTIR, and thus offers an instrumental multiplex advantage. Array detectors are massively multiplexed versions of single-element detectors, composed of individual detectors known as pixels.

Previously, our group has developed a unique way to interface rapid-scan interferometers with a HgCdTe (MCT) FPA detector that allows for faster acquisition and data processing without sacrificing data quality (*135*, *149*, *158*). The imaging system consists of a Bruker Equinox 55 FTIR spectrometer, a 128x128 MCT FPA detector (Santa Barbara Focalplane, Goleta, CA, USA) operated at 1610 Hz and an integration rate of 0.046 ms. Spectra are taken from a range of 4000-1000 cm^{-1} with a spectral resolution of 8 cm^{-1}. A gas phase array sampling cell has been developed to ensure that each reactor stream is kept separated, and that no cross talk between streams is possible during data acquisition. The sampling cell consists of 16 stainless steel tubes, each capped with a ZnSe window sealed with o-rings. The effluent from the high throughput reactor enters and exists the sampling cell through tubing welded to the sampling cell. The tubes are then fitted with stainless steel rectangles at both ends, with sixteen holes cut out of each side, allowing the IR beam to enter only through the 16 stainless steel tubes. Specifically, an infrared source is generated within the spectrometer and exits through a side port, where it is then collimated, and expanded to enter the gas phase array. The infrared radiation exiting the gas phase array is then focused on the FPA. More information on the design of the sample cell as well as the optical set up can be found elsewhere (*126*, *138*, *159*). During data acquisition, an image of the reactor gas outlet is taken, as shown in Figure 2.2. The image contains 16,384 individual MCT detectors, or pixels, and each contains information for an interferogram. Here, each colored circle represents photon intensity corresponding to one

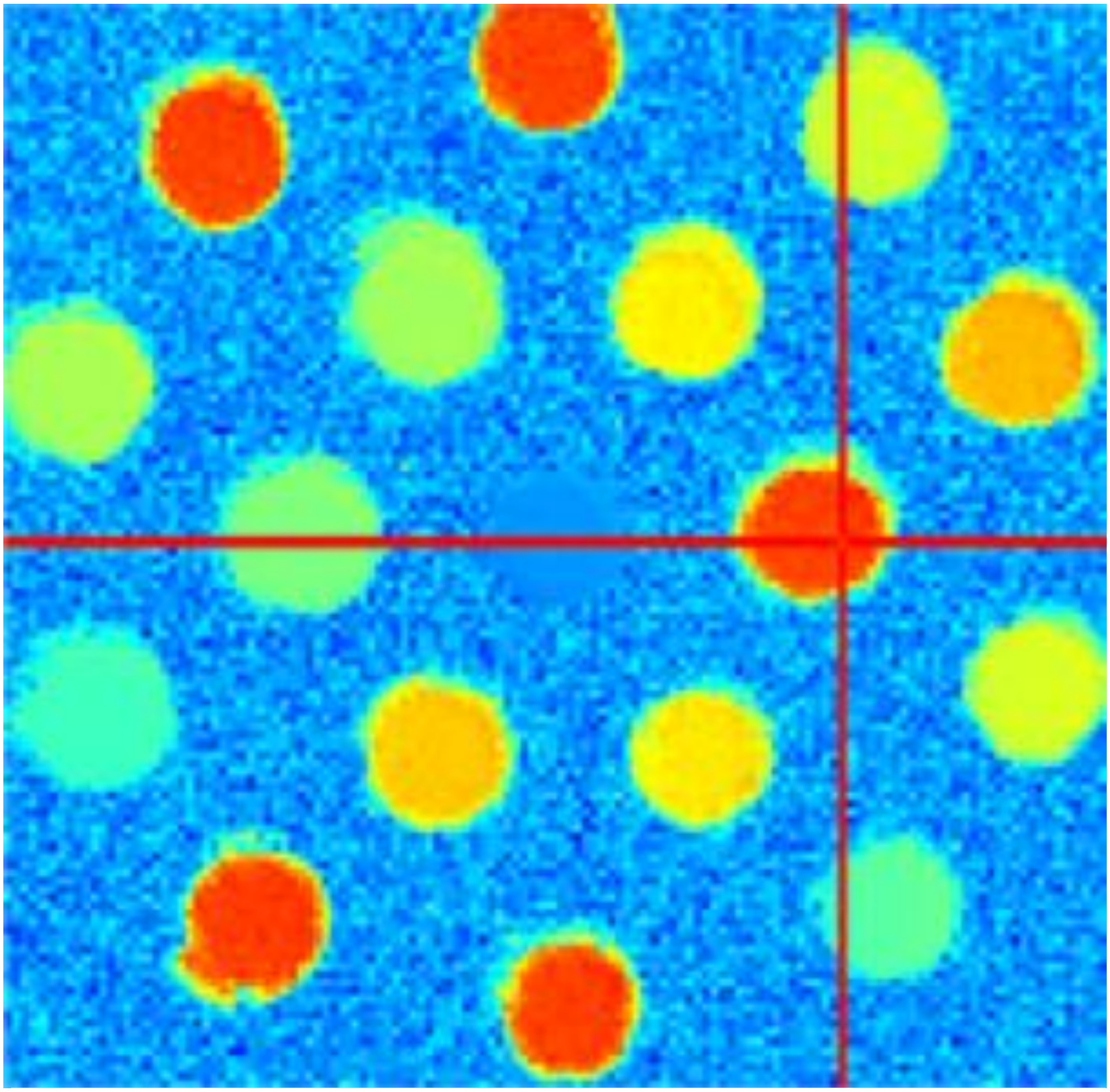

Figure 2.2. Image of raw data collected using spatially resolved FT-IR. Each colored pixel correlates to a single interferogram.

of the sixteen reactor channels. Data acquisition is controlled through an in-house written software named JAIMP (Just Another Image Processor) and images are recorded using WinIR 2009 software. During acquisition, 32 frames are captured within a single image in order to increase the signal to noise ratio. A Fourier Transform is performed on each individual frame, and the 32 IR spectra are averaged together to obtain the final image for one data point. Then, multiple IR spectra are averaged over for each reactor channel to obtain the final IR spectrum for each reactor channel. Figure 2.3 shows the FT-IR spectra for the NH_3 v_4 deformation mode for reactor 0 from 0.1% to 1.0% NH_3 after processing of the raw data.

After data acquisition and processing, the spectra are then quantified using the relationship established through Beer's Law, shown in Equation 2.1.

$$A(\bar{v})=a_i(\bar{v})bc_i \tag{2.1}$$

The linear dependence of absorbance ($A(\bar{v})$) as a function of wavenumber ($\bar{v}$), can be correlated to the concentration of a species (c_i), and allows for IR spectra to be quantified within a linear regime. However, nonlinearities begin to arise when larger values of absorbance are measured, but in general remans linear for measured absorbance units less than 2 (*160*, *161*). FTIR calibrations for ammonia decomposition were carried out via GRAMS software and the PLS-1 regression model. Calibration points were collected in 0.1 % increments from 0.1% to 1.0% NH_3 in balance Ar. The model utilizes the IR active vibrations of NH_3 that result from the symmetric and antisymmetric deformation modes that occur at roughly 1627 cm^{-1}. The FT-IR spectra were integrated from 1925 cm^{-1} to 1350 cm^{-1} for calibrations. Figure 2.4 shows the model results for reactor 0 and demonstrated an R^2 value of 0.997. Statistical outliers were determined for each model by determining the Mahalanobis distance for each data point (*162*). Each reactor channel exhibited an R^2 value of >0.99 demonstrating an excellent goodness of fit. After a calibration model was completed for each reactor channel, the models were validated by collecting FTIR of three randomly selected NH_3 concentrations between 0.1% and 1.0%. The results of the model validation for each reactor channel are shown in Figure 2.5. The average relative error ranged from 1.24% to 6.7% over the three validation points.

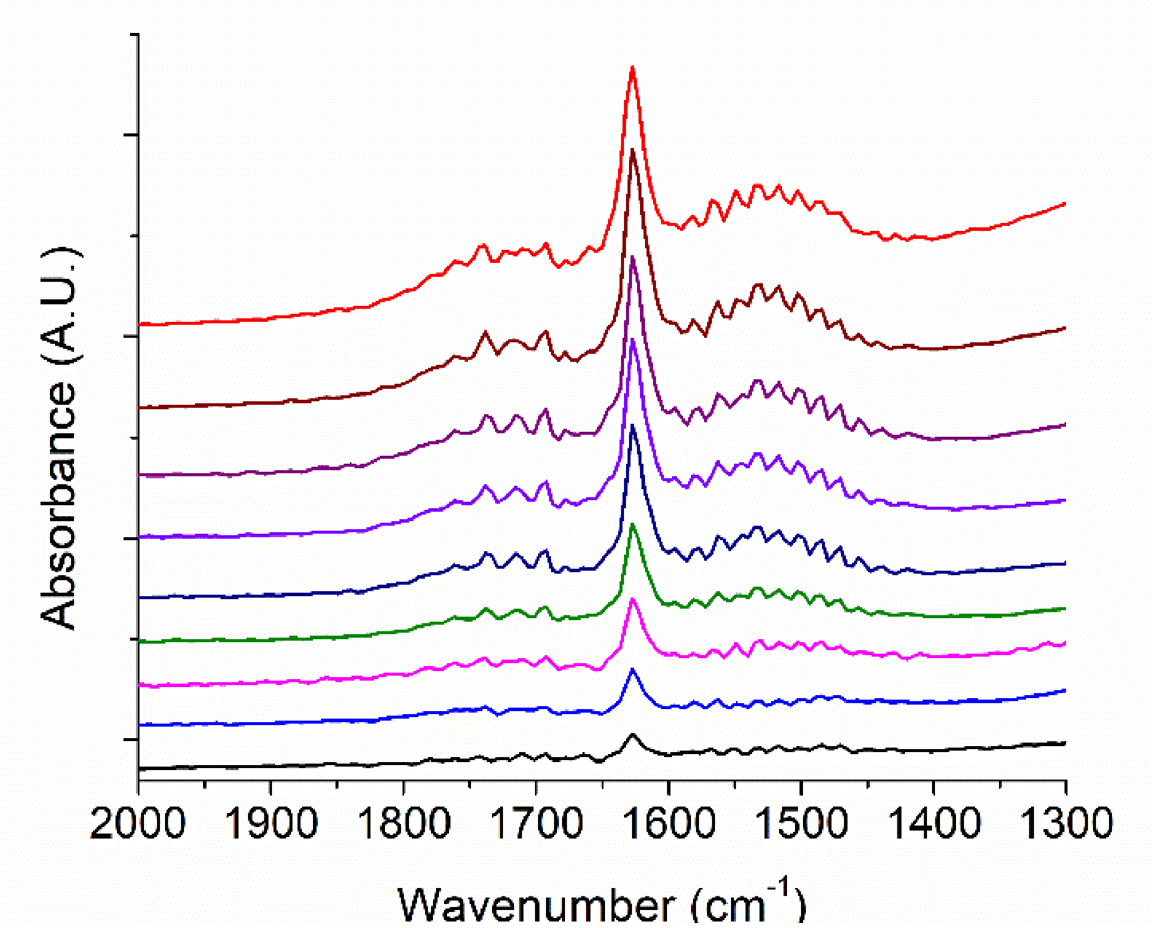

Figure 2.3. FT-IR spectra of the v_4 vibrational mode of NH_3 from 0.1% (bottom) to 1.0% (top).

The reproducibility of the high throughput reactor has also been tested by first running a set of reactions for their ammonia decomposition activity from 250°C to 400°C. Next, the catalysts were randomized in different channels and the reaction was run once more. The error between the measured activity for each catalyst at 300°C was taken to be the standard deviation of the two different randomized reactions. The activity measurements can be found in Table 2.1. The temperature 300°C was chosen because of the largest distribution of temperatures that was exhibited by the catalysts. The error at lower and at higher temperatures were much smaller than those shown at 300°C. The smallest error was found to be 0.6% and the largest error was found to be 8.9% which can

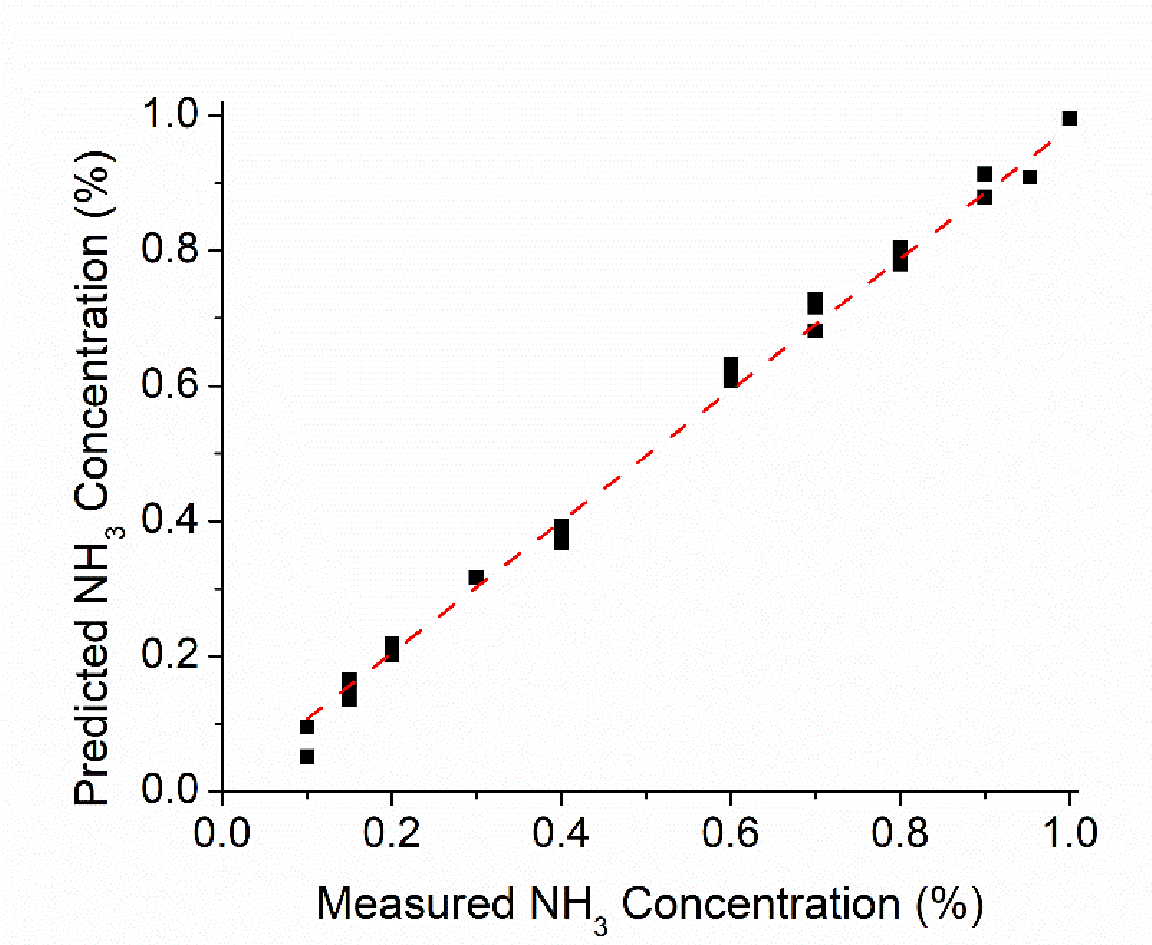

Figure 2.4. Measured vs. Predicted NH_3 concentrations from 0.1 – 1.0% for reactor 0 using PLS-1 regression model.

then be assumed to be the relative error between runs using spatially resolved FTIR for quantification of the ammonia concentration in the reactor effluent.

2.1.3 PID Tuning

A PID controller works by reading a sensor, and then computing the desired output to control a process variable by calculating the appropriate proportional, integral and derivative response and summing those three components to determine the output. PID controllers have a wide variety of applications and the tuning will depend greatly on what response is being measured and the characteristics of the output. In this case, the

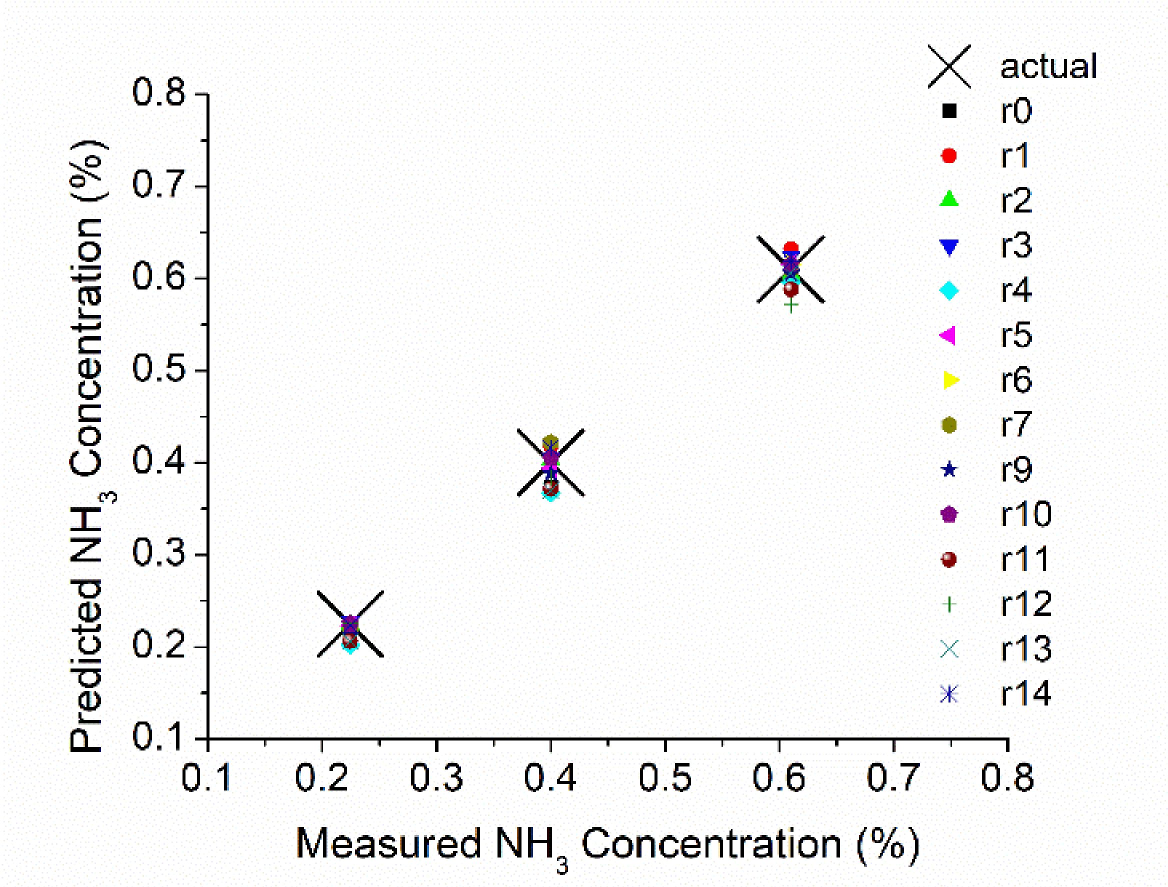

Figure 2.5. Model validation for each reactor channel. The black X corresponds to the measured concentration value.

temperature of each furnace is being read and the output is the power output of the solid-state relays used to supply power to the furnaces. Duty cycle refers to the ratio of the pulse width and period of a signal. Therefore, the PID controllers regulate the duty cycle of the solid-state relays, which in turn regulates the temperature of each furnace. The goal of the PID controllers is to quickly heat the furnaces without overshooting the desired temperature, and to regulate the temperature of each furnace. Accurate tuning is required in order to confirm that wild fluctuations in temperature are minimized. Figure 2.6 shows a block diagram for a typical closed loop system. The process variable is what is to be controlled, such as pressure, temperature, or flow rate. A sensor is used to measure this

Table 2.1. The standard deviation (Error %) between the same catalysts after they have been tested for ammonia decomposition at 300°C in two different randomly selected reactor channels where the reaction conditions are: T = 300°C, 10%NH_3/Ar, 30,000 mL/hr/g_{cat} and atmospheric pressure.

Catalyst #	**Activity – 1**	**Activity – 2**	**Std %**
1	40.2	51.1	5.45
2	33.5	51.2	8.85
3	44.0	42.9	0.55
4	6.0	21.1	7.55
5	43.9	54.6	5.35
6	61.4	52.5	4.45
7	38.9	42.4	1.75
8	46.9	31.8	7.55
9	56.9	42.5	7.2
10	15.9	26.6	5.35
11	43.9	51.9	4
12	42.1	44.8	1.35
13	35.9	34.6	0.65

variable and provide feedback to the control system. The PID controller tries to minimize the error between the process variable and the setpoint. The compensator refers to the control system algorithm and determines the system output, which in this case drives the heaters. This ultimately results in a closed, constant feedback loop system. The control performance will depend on the system, but in this case, it is desired to avoid dramatically overshooting the setpoint, which can occur with very fast initial heating. An example of the PID tunning for one of the four furnaces (Furnace 3) when heating from room temperature to 340°C is shown in Figure 2.7.

The Proportional, Integral and Derivative components are manipulated until the desired response is given. Here, the red trace is the process variable (PV Sensor) and the white trace is the temperature of the furnace (Setpoint). The temperature of the furnace exhibits ±2°C about the setpoint after settling time with this tuning setup. Furthermore, the duty cycle of the solid-state relay exhibits a steady and constant sinusoidal response. Additional theory behind PID control as well as heuristics for tuning can be found elsewhere (*163*). However, we found that patience and trial and error approach resulted in the best tuning of each of the individual furnaces. Additionally, we want to minimize the percent overshoot over the set point and settling time of the process variable.

2.1.4 High Throughput Screening of Ammonia Decomposition Catalysts

Ammonia decomposition activity tests were carried out for the Ru substituted catalysts using 200 mg of catalysts per channel under 1%NH_3 in balance Ar, and a space velocity of 30,000 ml-hr^{-1}-g$_{cat}$$^{-1}$. In some instances, 10% NH_3 in balance Ar was used as the inlet concentration, and a separate calibration file for was made for each reactor channel for this concentration of ammonia. All reactions took place under atmospheric pressure. The reactor effluent was measured via FT-IR at intervals of 50°C from 250°C to 400°C. For each temperature, three data points were taken, and the reported activity is the average of these three data points, and the standard deviation is reported as the error. Catalyst bed

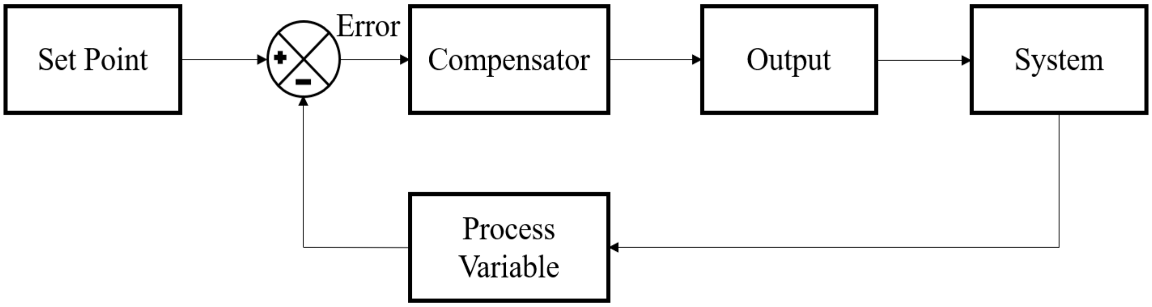

Figure 2.6. Block diagram of a typical closed loop system.

temperatures were measured using K-type thermocouples. A randomly selected channel was left empty during each experiment to ensure the accuracy of the calibration files and that zero conversion is observed in the empty reactor channel. NH_3 conversion was calculated using the inlet and effluent concentration of NH_3 as shown in Equation 2.2.

$$NH_3\text{Conversion }(\%)=\left(1-\frac{NH_{3_{outlet}}}{NH_{3_{inlet}}}\right)*100\% \qquad (2.2)$$

Prior to activity measurements, catalysts were first heated under Ar to 450°C, and then exhibited to a H_2 reduction in 10% H_2/Ar for 1 hour. Catalysts were then cooled to 250°C under Ar, where they were then exposed to NH_3 and data collection took place after ten minutes to allow the system to equilibrate.

2.1.4 Plug Flow Reactor Setup and Activity Testing

A horizontal tube furnace (MTI Corporation) was utilized as the basis for a plug flow reactor system. The tube furnace is fit with a 3/8” OD stainless steel reactor tube. A 1/8” diameter stainless steel tube is placed inside of the reactor tube at a set distance in order to maintain the same height of the catalyst bed for each experiment. The reactor tube is then packed with quartz wool, followed by 250 mg – 2 g of catalyst, and topped with quartz wool. The reactor system reaches temperatures up to 1250°C and allows for multiple

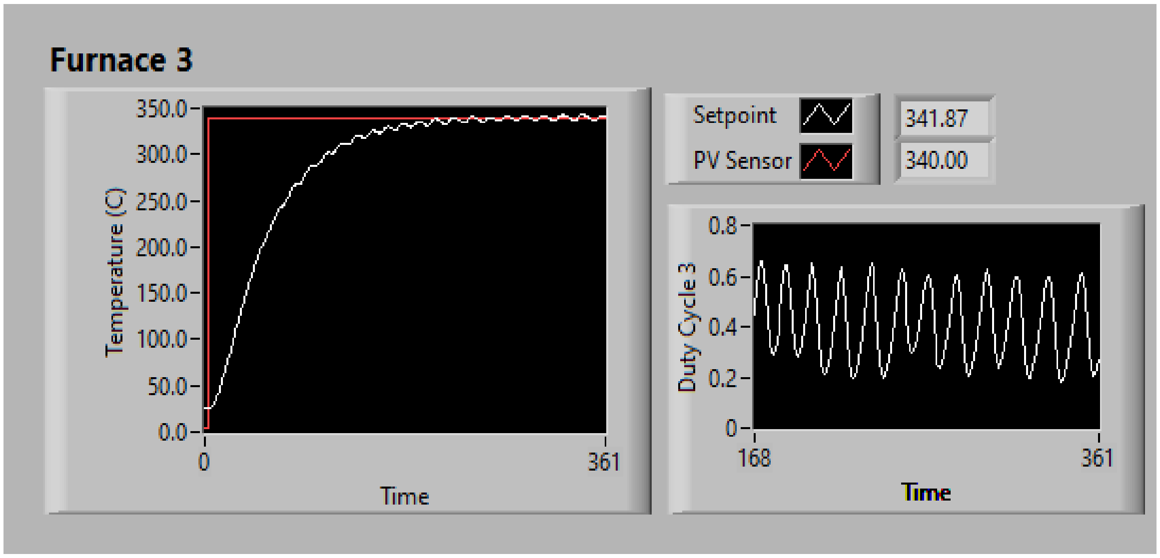

Figure 2.7. Response of the PID closed loop system as a function of time for Furnace 3 and the duty cycle output of the solid-state relay.

types of gases and concentrations to be flow through. Brooks 5850e mass flow controllers (MFCs) were used to regulate the flow of each individual gas velocity. Additionally, the reactor is outfitted with a back pressure regular (Swagelok) on the effluent side of the reactor and can be pressurized up to 10 bar. The temperature of the catalyst bed is monitored during experiments with a K-type thermocouple situated directly inside the catalyst bed. The composition of the product gas stream was analyzed using a Shimadzu 2014 gas chromatogram (GC), equipped with a thermal conductivity detector (TCD). The GC is equipped with a Mol Sieve 5A plot column for H_2 and N_2 separation. The concentration of H_2 and N_2 in the product stream were used to calculate the NH_3 conversion at each temperature and were always found to be in stoichiometric proportions. In order to determine the NH_3 conversion, the extent of reaction (X_e) was first calculated based off of the H_2 concentration in the outlet and the inlet concentration of NH_3 ($C_{NH3,in}$) as shown in Equation 2.3. More information on the extent of reaction can be found elsewhere (*164*).

$$C_{H2,\ out}=\frac{\frac{3}{2}*X_e}{C_{NH3,in}+X_e} \qquad (2.3)$$

After the extent of reaction was determined, the mole fraction of NH_3 in the outlet ($C_{NH3,out}$) could be determined through Equation 2.4 and the conversion could then be calculated following Equation 2.4.

$$C_{NH3,\ out}=\frac{C_{NH3,in}-X_e}{C_{NH3,in}+X_e} \qquad (2.4)$$

Prior to activity measurements, catalysts were first heated to 450°C in Ar and then subjected to a 10% H_2 reduction for one hour. For catalyst activity, NH_3 conversion was then measured in 50°C increments from 250°C to 400°C. The catalyst bed temperature was measured using a K-type thermocouple and the space velocity was kept constant for each reaction at 5,400 ml/hrg$_{cat}$. NH_3 conversion using the support material ɣ-Al_2O_3 was first measured under these conditions and found to be negligible at all temperatures.

Reaction orders were calculated by using a standard power law kinetic model as shown in Equation 2.5, where P_i indicants the partial pressure for i=NH_3, H_2, N_2.

$$r=A*\exp\left(\frac{-E_a}{RT}\right)*P_{NH3}^{\alpha}P_{H2}^{\beta}P_{N2}^{\gamma} \qquad \mathbf{(2.5)}$$

The order for each component can then be measured by varying the concentration of each component and measuring the rate of reaction. The power law model can then be linearized, such that the plot of the natural log of the rate of reaction as a function of the partial pressure of each component can be used to estimate the reaction order of each component from the slope. Through this method, one can determine the negative or beneficial effect the reactants and products have on the rate of reaction at a given temperature.

2.2 Catalyst Synthesis

2.2.1. Impregnation Methods

Impregnation methods for catalyst synthesis is achieved by contacting a solution containing active metal precursors with the support material, which is then dried to remove the solvent. This can be achieved either through the incipient wet impregnation (or dry impregnation) method or wet impregnation method (*165*, *166*). The defining difference between the two methods is that an excess of solution is used during wet impregnation, so that a slurry type mixture containing the solvent, active metal precursors and support is created, and are mixed and constantly heated. Diffusion is the main method in which the precursors are deposited onto the support. In incipient wetness impregnation, a volume of solution containing the active metal precursors and solvent equal to approximately the pore volume of the support material is added to the dried support, where capillary action then draws the solution into the pores of the support.

During this process, the impregnated support maintains a dry look on the macroscopic scale. The catalyst is then dried until the solvent has evaporated from the pores, and this process is repeated multiple times. Insufficient drying times or adding larger amounts of solution than that of the support pore volume will change the method of deposition from capillary action to diffusion, since there is no longer a capillary pressure difference present. The process of diffusion is much slower than the rate at which liquid is sucked into the pores of support through capillary action (*166*), and thus could lead to insufficient uptake of the active metal precursors.

Catalysts used for the high throughput screening of ammonia decomposition were synthesized using the incipient wetness impregnation technique and supported on SBA-200 γ-Al_2O_3 (Catalox, 99.99%, 192 ± 20 m^2/g). KCH_3COO (Fischer Scientific, 98% purity), anhydrous $RuCl_3$ and anhydrous chloride salts of the following: Mg, Ca, Sr, Sc, Y, Zr, Hf, Nb, Ta, Cr, Mo, W, Mn, Re, Fe, Os, Co, Rh, Ir Ni, Pd, Pt Cu, Ag, Au, Zn, Cd, In, Sn, Pb, and Bi (Sigma Aldrich, $\geq$ 95% purity) were used without further modification. The support was first dried at 120°C for 2 hours before impregnation. An appropriate amount of $RuCl_3$, secondary anhydrous chloride salt, and KCH_3COO were mixed to obtain 3:1:12, 2:2:12 or 1:3:12 weight ratios of Ru:M:K (where M = Mg, Ca, Sr, Sc, Y, Zr, Hf, Nb, Ta, Cr, Mo, W, Mn, Re, Fe, Os, Co, Rh, Ir Ni, Pd, Pt Cu, Ag, Au, Zn, Cd, In, Sn, Pb or Bi) and dissolved in DI water. An aliquot of solution equal to the pore volume of the support was slowly added to the dried support until incipient wetness was achieved. The impregnated support was then dried at 120°C for 30 minutes, after which the process was repeated until the entire solution was deposited onto and in the support. The catalysts were then ground, and heated at 200°C for 2 hours, and subsequently calcined in air at 550°C for 3 hours. This synthesis procedure was adapted from previous work performed by our group, where for a 4 wt% Ru, 12 wt% K catalyst supported on SBA-200 γ-Al_2O_3 was optimized by varying calcine temperature and time, and then measuring their ammonia decomposition activity. Details of this study can be found elsewhere (*126*).

Further catalyst studies were done in order to determine the effect of the precursor on ammonia decomposition activity. KNO_3 (Sigma-Aldrich, >95% purity), KOH (Sigma-Aldrich, >95% purity), $Ru(C_5H_7O_2)_3$ (Sigma-Aldrich, 97%), and $Ru_3(CO)_{12}$ (Sigma

Aldrich, 99%) were used in lieu of the above Ru and K precursors and were synthesized following the same synthesis procedure.

2.2.2 Strong Electrostatic Adsorption (SEA)

SEA is a unique wet impregnation synthesis technique that is used to maximize the interactions between the precursors and support by manipulating the pH of the solution. This enhances the dispersion of the deposited metals onto the surface support and thus increases the amount of usable metal surface area for catalytic reactions. Ion adsorption will be dependent on the charging of the support in aqueous solutions and can be measured with a variety of methods (*167*). This is achieved by first measuring the point of zero charge (PZC) of the support used. Below the PZC, the hydroxyl groups present on the surface of a support will become protonated and thus positively charged at these pH values. Above the PZC, the hydroxyl groups will become deprotonated and thus negatively charged. Thus, by manipulating the pH of the solution, different metal cation or anion adsorption can occur with the support's surface hydroxyl groups (*168*). The adsorption of these anions or cations occurs via strong electrostatic adsorption, hence the name of the synthesis method. The pH where the electrostatic interaction is strongest is the targeted pH range during synthesis. Through this method, a monolayer of precursor can be adsorbed onto the surface of the support, which can produce incredibly small and highly dispersed nanoparticles after reduction, which removes the precursor ligands.

Here, SEA synthesis was used to synthesize a catalyst containing 1% Ru, 12 % K supported on γ-Al_2O_3 and a 4% Ru and 12% K catalyst, in order to determine the effect of higher dispersion of ammonia decomposition activity, and to isolate the Ru species present on the catalyst, as the wet impregnation methods (as will be shown later) produces a variety of Ru species on the catalyst surface, and isolation of one proves to be difficult. Therefore, SEA synthesis helps us target small, isolated Ru clusters during synthesis which can then be contrasted with the activity of various Ru species made through wet or dry impregnation techniques. The SEA catalyst was synthesized by the Regalbuto group following a previously outlined method (*169*, *170*). Briefly, Catalbox brand SBA-200 γ-Al_2O_3 was used as a support, potassium hexacyanoruthenate (II) hydrate (Sigma-Aldrich) and potassium nitrate (Fischer Scientific) were used as the precursors. The alkali metals are first introduced by dry impregnation and then the Ru was introduced in sequential SEA steps with intermittent drying and reduction at 250°C to decompose the adsorbed precursor.

2.3 Characterization of Catalysts

2.3.1 X-ray Diffraction (XRD)

XRD is a powerful tool used to determine crystal structure and various crystal imperfections. For powdered and polycrystalline samples, a large number of randomly oriented tiny crystals should be present for phase identification and to determine crystallite size, strain, and faulting (*171*). In order for X-rays to be diffracted, materials must exhibit long range periodic arrangement of one or more atoms which are known as crystal lattices. There are 7 crystal families composed of triclinic, monoclinic, orthorhombic, tetragonal, cubic, trigonal and hexagonal, and 14 possible crystal lattices, known as the Bravais lattices which can be generated from 3-unit vectors and a set of integers commonly referred as *hkl* values. Therefore, different families of crystals will result in different diffraction patterns, allowing for phase identification based on the spacing between different layers of atoms (d spacing) in the crystal and angle of diffraction. Constructive inference of monochromatic X-rays occurs when successive planes of atoms separated by a distance d, in multiples of n wavelengths, thus satisfying Bragg's Law, shown in Equation 2.6. A countertop diffractometer (MiniFlex II, Rigaku) was used for XRD measurements using a Cu-Kα X-ray (λ=1.542 Å) source. The diffracted X-rays are collected in a small receiving slit located on a moving counter arm. During the measurement, the counter arm turns at constant angular velocity about the fixed sample, determined by user-defined instrument conditions. The detector position is recorded as the angle 2theta, (the angle between the incoming and outgoing x-rays) and records the number of X-rays at each angle that are diffracted from a crystal. In this study, XRD patterns were typically collected between 10 and 60 2θ at a rate of 1.5°/min and at a step scan size of 0.02°. XRD patterns were collected for each catalyst synthesized in order to perform phase identification and to determine the average crystallite size of the Ru species in each catalyst.

Particle size broadening can be determined using the Scherrer's Equation shown in Equation 2.7, where K is the shape factor, λ is the X-ray wavelength, L is the crystal dimension, and B(2θ) is the full-width half max (FWHM).

$$B(2\theta)=\frac{K\lambda}{L\cos\theta} \qquad \textbf{(2.7)}$$

Although Scherrer's equation was originally derived for cubic crystal systems, it can be used as approximation for non-cubic systems when the crystal dimension L is interpreted as the average crystallite size, since peak breadth increases as a function of 1/cosθ, and thus becomes more pronounced at larger 2theta values. Therefore, the major *hkl* reflections present at lower 2θ values were used when possible, to determine the average crystallite size. In order to determine the FWHM, a curve fitting and data analysis program Fityk

(1.3.1) was used for profile fitting and baseline subtraction for each of the XRD patterns. XRD reflections were fit using the Pseudo-Voigt approximation since peak broadening of each reflection contains both a Gaussian (particle broadening) and Lorentzian contribution (strain broadening).

2.3.2 Scanning Electron Microscopy/Energy Dispersive X-ray Spectroscopy (SEM/EDX)

SEM is an electron microscopy technique that uses a beam of high-energy electrons (typically between 5 keV – 20 keV) that are dissipated when the incident electrons hit a solid sample and decelerate. Secondary electrons produce SEM images that can provide information on particle morphology and texturing, as well as crystallinity and chemical composition. Chemical compositions can be determined from photons generated from the sample. Each element generates a characteristic X-ray when inelastic collisions occur between the incident electron beam and electrons in discrete orbitals of an atom. The characteristic X-ray is produced when an excited electron returns to lower energy state and is related to the differences in energy levels of the electron, and thus is unique for each orbital and for each element.

2.3.3 Transmission Electron Microscopy (TEM)

In contrast to SEM, TEM is an electron microscopy technique that uses a high voltage beam that is either scattered by the sample or passes through it. The electrons that pass through the sample are collected onto a fluorescent screen to produce an image of the sample. The samples must be very thin in order to let electrons pass through the sample.

2.3.4 Fourier Transform Infrared Spectroscopy (FTIR)

FTIR is a spectroscopic technique used to obtain an infrared (IR) spectrum of a sample or molecule. IR radiation may induce vibrational excitation, at which point a molecule will absorb IR radiation that corresponds to the energy of these vibrations, i.e., resonant frequencies. Molecular vibrations are only IR active if they induce a change in the molecule's dipole moment. The amount of energy absorbed by the sample can be determined by analyzing the transmitted light. Historically, an IR spectrum was collected by passing a monochromatic beam through a sample and determining the amount of IR radiation absorbed at each individual wavelength using a dispersive spectrometer (*172*). FTIR differs by utilizing a broadband light source to collect information from all wavelengths simultaneously. A comprehensive discussion on the FT-IR can be found elsewhere (*173*).

Generally, FTIR utilizes a broadband radiation source which passes through a Michelson interferometer, through the sample and finally to the detector. The Michelson interferometer is responsible for modulating the polychromatic light, so that a different combination of wavelengths is produced at each moment. A schematic of a Michelson interferometer is shown in Figure 2.8. A Michelson interferometer is a device that can split a beam into two separate paths and then recombine them after a path difference as been introduced for one of the beams. This is achieved by splitting the radiation source using a beam splitter, where the beam is partially reflected to a fixed mirror, and partially transmitted to a moving mirror. The moveable mirror is moved at a constant velocity, and both beams are reflected off of the mirrors and back to the beam splitter, where the combined beams will be reflected back to the detector. There, the two beams experience

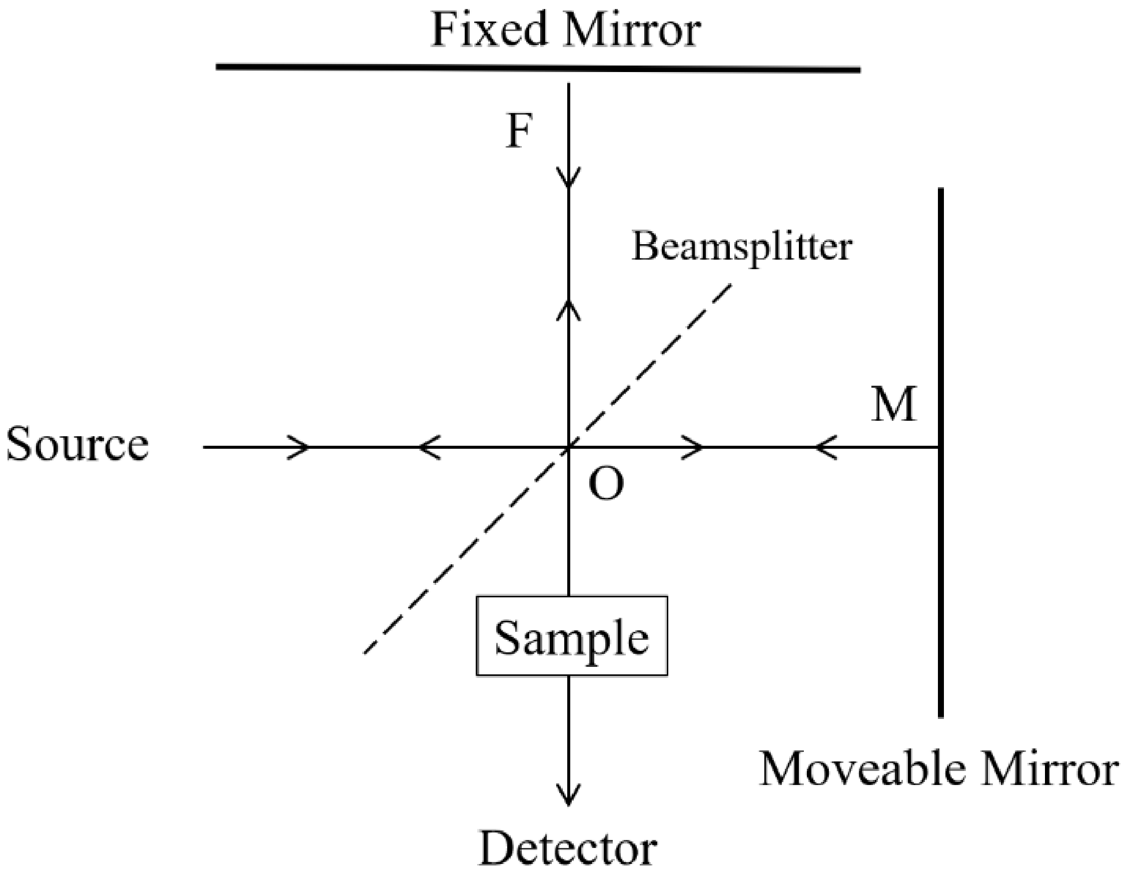

Figure 2.8. Michelson Interferometer

either constructive interference or destructive interference based on the path of the two beams before recombination. The path difference between the two beam is 2(OM-OF) and is the optical path difference (OPD). At a constant wavelength and an OPD of zero or any multiple of the wavelength, the two beams are in phase and constructive interference occurs. At any other OPD, the two beams are out of phase and destructive interference occurs. Therefore, the maximum intensity at the detector will occur at an OPD equal to *n* multiples of the wavelength. The detector can record the intensity of the beam as a function of OPD (cm) or as a function of time (s) for mirrors moving at a constant velocity. The interferogram is then converted into a spectrum by performing a Fourier transform, which converts the measured light absorption at each OPD into the absorption at each wavelength. The Fourier transform and Michelson interferometer dramatically decreases the time of acquisition needed to collect an IR spectrum, and eliminated the need for a monochromator. For polychromatic radiation sources, the measured interferogram is the result of the interferograms corresponding to each wavelength in the radiation source.

2.3.4.1 Diffuse Reflectance Infrared Spectroscopy (DRIFTS)

DRIFTS is a technique that analyzes IR radiation that is scattered from a sample, typically a fine powder or rough surface. Diffuse reflection refers to the scattering of light from a surface in many directions, instead of at a specific angle. For a fine powder or small particles, an incident beam can either be reflected off of the surface of a particle or transmitted through it. A transmitted beam can then pass through another particle where it can again be reflected or further transmitted. This method is primarily used when the transmission of an infrared beam through a sample is not feasible.

2.3.4.2 CO Adsorption

DRIFTS can be used to investigate the nature of adsorbed species on metal surfaces in order to gain insight into the metal surface configuration (*174*). The resultant stretching frequency of CO will depend on the bonding mode of CO, the electron density of the adsorbing metal and the metal surface configuration (*175–178*). Binding of CO to a metal surface can occur either through donation of an electron pair from CO to a metal orbital forming a σ-bond, or through π-backdonation from a metal d orbital to CO (*179–182*). The later requires the metal to have d electrons and for the metal to be in a low oxidation state. CO adsorption through π-bonding weakens the CO bond in relation to gas phase CO as electrons fill the π-antibonding orbital of CO. This results in a decrease in the CO stretching vibrational frequency compared to gas phase CO. The degree of weakening will depend on the metal and the geometry of the adsorption site, and thus provides detail information of the catalyst surface and can identify ensembles of catalytically active sites (*183*). In other cases, the vibrational frequency of CO can increase with respect to gas phase CO with increasing charge on the metal center, indicating a strengthening in the CO bond. Therefore, the number of carbonyl stretches, their position and relative intensities will provide insight into the nature of the atomic surface configuration of the catalyst.

For this study, a Bruker Vertex 70 spectrometer equipped with a Mercury Cadmium Telluride detector (MCT), Bruker Praying Mantis diffuse reflection attachment and a high temperature, low pressure reaction chamber were used to collect infrared spectra. Spectra were typically collected from 4000 cm^{-1} to 1000 cm^{-1} at a spectral resolution of 4 cm^{-1} and averaged over 512 scans. The reaction chamber consists of ZnSe windows and allows for gas flow through the chamber, as well as heating up to 1000°C. The reaction chamber was used to probe the interaction between various gas adsorbates and metal nanoparticles. Catalyst powders were first ground with a mortar and pestle and packed into the sampling cup (10mm dia.) without further modification. The powders are held in place with a small stainless-steel mesh.

Prior to adsorption of CO, catalysts were first heated under He (99.999%, Airgas) to 450°C and then subjected to a hydrogen reduction in 10% H_2/He for one hour. The catalyst was then further heated to 460°C under He for ten minutes in order to remove any H_2 than may have adsorbed onto the metal surface during the reduction pre-treatment. Then, the powders are cooled to 50°C under inert gas where a background scan is taken.

Next, the catalysts are subjected to 1000 ppm CO in balance He for ten minutes. The reaction cell was then flushed with He and an IR spectrum was collected and averaged with the background.

2.3.5 Raman Spectroscopy

Raman spectroscopy is a vibrational technique that relies on inelastic light scattering, or Raman scattering (RS) to gain insight into a material's chemical structure. A comprehensive text on Raman Spectroscopy can be found elsewhere and used primarily for discussion here (*184*). In contrast to FTIR, Raman active vibrations occur based on a molecule's polarizability. Additionally, photons do not need to have an energy that matches the difference in energy levels of a molecules ground state and vibration state in order to be scattered. Raman spectroscopy utilizes a monochromatic radiation source which interacts with a molecule by distorting its electron cloud. The polarized molecule is promoted to a virtual energy state and the photon is then re-emitted. If the incident photon induces nuclear motion from the molecule, energy will be transferred from the photon to the molecule or, from the molecule to the photon and RS occurs. The strength of RS is proportional to the fourth power of the excitation frequency. RS measures the differences in energy between n and m vibrational states by subtracting the energy of the scattered photon from that of the incident photon. Stokes scattering occurs when RS from the ground vibrational state leads to absorption of energy by the molecule promoting it to a higher excited vibrational state, n. If a molecule is present initially in an already excited state, then this process is referred to as anti-Stokes scattering and the molecule returns to its ground vibrational state, m and results in a negative Raman shift. Anti-Stokes scattering can be of interest if the molecule exhibits fluorescence but is typically much weaker than Stokes scattering. Intense RS occurs from vibrations which cause a change in the polarizability of the molecule's electron cloud. RS can also occur due to lattice vibrations of a crystal either longitudinally or perpendicularly to the perturbation.

Raman spectra were collected using a Horiba XploRA Plus Raman spectrometer equipped with a light microscope with 10x, 20x and 50x magnification. The spectrometer is equipped with a Linkim TMH600 environmental cell so that in-situ and operando studies of catalyst surfaces can be conducted. Typically, a monochromatic laser is focused onto a sample and the scattered light is focused onto a charged couple device (CCD) that is cooled to -70°C to reduce background noise. As mentioned previously, RS is measured as the difference between the energy of the incident photon and the photon scattered by the same. The intensity is measured as a function of Raman shift (Δ cm^{-1}) at a constant excitation source. The powder was loosely packed into the quartz crucible of the TH600 environment cell and packed down to create as flat a surface as possible. Care must be taken in choosing the correct excitation source, laser power, exposure time and working distance especially in Raman experiments involving elevated heating. Since RS is proportional to the fourth power of the excitation source, shorter wavelengths will provide stronger Raman signal. Additionally, longer wavelengths will penetrate deeper into the sample and thus could provide more signal from the substrate or holder than from the materials of interest.

A 437 nm excitation source was used at 15 mW. Spectra were collected by irradiating the same for 15 seconds, followed by 15 seconds of delay to allow the sample to cool and avoid localized heating. Five spectra were collected at each point and then averaged together to increase the signal to noise ratio.

2.3.6 Temperature Programmed Reduction (TPR)

TPR is a technique that monitors a chemical reaction as a function of temperature. The temperature is ramped linearly, and typically the gas content both before and after the reaction is measured. In the case of TPR, typically, a known amount of diluted H_2 is introduced to the catalyst, and reduction events will occur with increasing temperature when a reducible metal is present on the catalyst. After the reduction occurs, the reaction between the metal oxide and H_2 gas will produce H_2O, and the amount of consumed H_2 is measured using a thermal conductivity detector. Heating rates are generally between 0.1°C/min and 20°C/min. Insight into the temperature at which supported metal oxides occur can ensure that sintering is avoided, and complete reduction is reached during any reduction pretreatment steps that occur before a chemical reaction takes place. Variations in strong metal support interactions and the crystallite size of the supported metal oxide will influence the temperature at which reduction events occur.

Additionally, TPR patterns can provide insight into whether the precursor salt is still present in the catalyst. For example, TPR of Rh/SiO_2 made with chloride precursors will exhibit a higher temperature reduction of Rh-O bonds and a lower temperature reduction of Rh-Cl bonds. Additionally, the area under the TPR curve represents the amount of H_2 consumed by the catalyst per mole of metal atoms. TPR can also indicate whether two metals are in contact or not, specifically in the case of bi-metallic catalysts (*185*).

For this work, an AutoChem II 2920 benchtop instrument was used for H_2-TPR experiments. A glass U-tube was used as the reaction vessel, which is first loosely packed with quartz wool, followed by 100 – 200 mg of catalyst, and then topped with loosely packed quartz wool. A K-type thermocouple is placed inside the catalyst bed in order to measure the temperature of the catalyst during reaction. Before the TPR experiment, the catalysts are first dried at 120°C for 60 minutes under Ar to remove any physisorbed water from the surface that may misconstrue the TPR measurement. After the drying process, the catalysts are cooled to 50°C, and subjected to 10%H_2/Ar. A ramp rate of 10°C/min is typically used, from 50°C to 600°C. H_2 consumption is determined based on the moles of metal and using AgO standard sample for calibration of the TCD.

2.3.7. Pulse Chemisorption

Chemisorption is a technique that can be used to determine active metal surface area, crystallite size, number of active sites and metal dispersion over a support. Commonly used gases include H_2 and CO for chemisorption onto metal surfaces and knowledge on the number of H_2 or CO atoms that one active site can adsorb is necessary for analysis and for choosing which gas to use for chemisorption experiments. The rate of uptake of a probe gas will simply the product of the flux and sticking coefficient, assuming that the process is non-activated. Pulse chemisorption to measure active sites and metal dispersion should be a non-dissociative adsorption process.

Pulse chemisorption experiments are carried out on an AutoChem II 2920. samples are first heated to 450°C under inert and exposed to a hydrogen reduction pretreatment at 450°C for one hour in 10%H_2/Ar. Next, the temperature is increased slight to 460°C in order to remove any strongly bound H_2 leftover from the reduction. The samples are then cooled to 50°C in Ar for the chemisorption experiment. A known amount of reactant gas is pulsed over the sample and the amount of H_2 adsorbed is measured using a TCD. The pulses of reactant gas continue until the amount of H_2 measured by the TCD is constant, indicating that the active sites of the sample are completely saturated with reactant gas. The result from a typical pulse chemisorption experiment is shown in Figure 2.9 for H_2 chemisorption over a 4 wt% Ru, 12 wt% K catalyst supported on ɣ-Al_2O_3. Each pulse gets progressively bigger until all active sites have reacted, and the pulsed gas leaves the sample unchanged. Knowing the weight loading of the active metal in the sample, as well as the atomic characteristic of the metal, can then be used to calculate average crystallite size (assuming spherical particles), % metal dispersion, exposed metal surface area and the number of active sites in a catalyst sample.

2.3.8 Arrhenius Plot

For elementary reactions, the temperature dependence on the rate constant is given by the Arrhenius equation shown in Equation 2.8, where r is the rate of reaction (mol/kg/s), A is a pre-exponential factor, and E_a (kJ/mol) is the apparent activation energy.

$$r=A*\exp\left(\frac{-E_a}{RT}\right) \tag{2.8}$$

The apparent activation energy was measured in a diffusion limited regime and was calculated by linearizing the Arrhenius equation and plotting the natural log the rate of reaction as a function of inverse temperature. Due to the various diffusion and adsorption steps associated with heterogeneous catalysis, various regimes can control the rate of reaction, including diffusion through a boundary layer, intraparticle diffusion and finally a

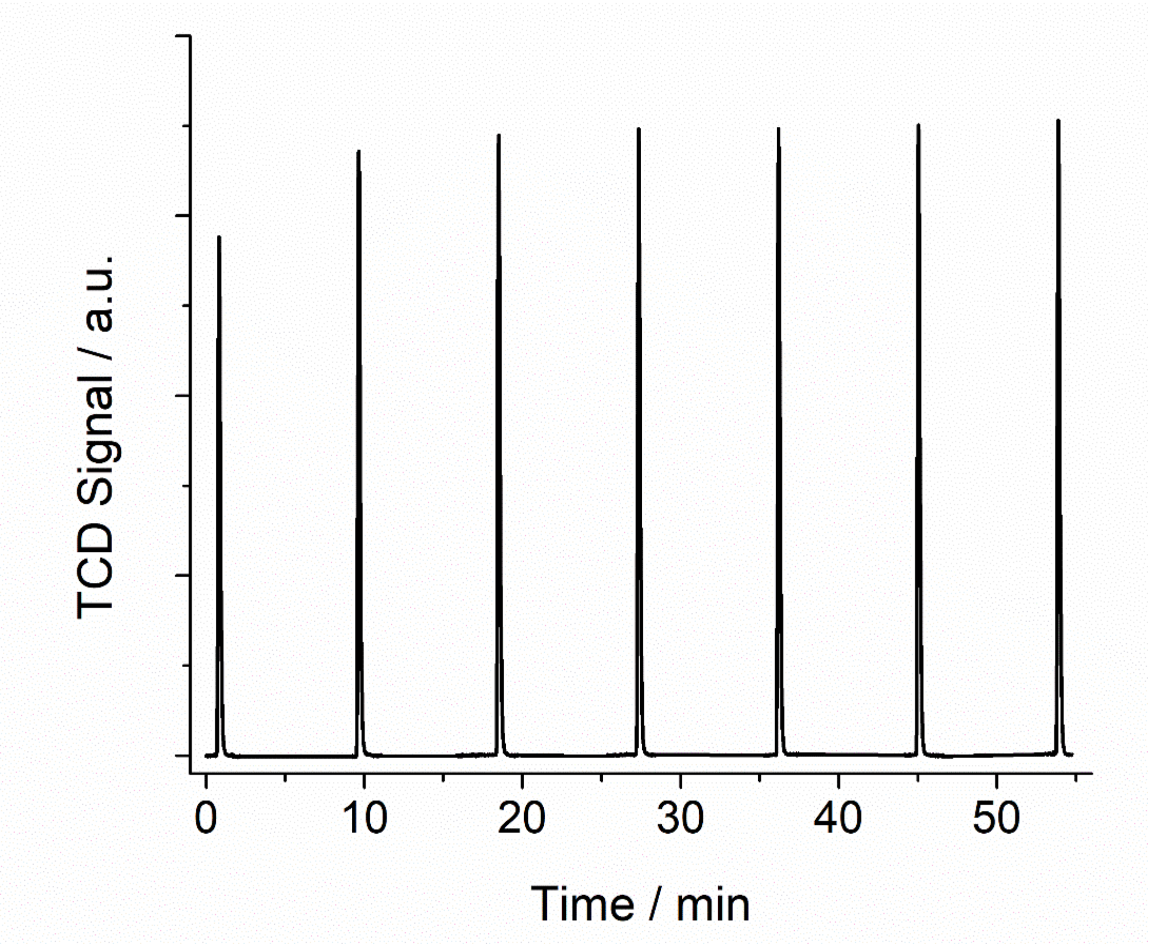

Figure 2.9. H_2 Pulse Chemisorption over 4 wt% Ru, 12 wt% K catalyst supported on ɣ-Al_2O_3.

combination of adsorption, surface reactions and desorption of products. Therefore, it is important to measure the apparent activation energy at lower temperatures, where diffusion of the reactants through the boundary layer and through the pores is fast compared to the rates of the surface reactions. This ensures the measured rate of reaction used to calculate the apparent activation energy is controlled by the intrinsic reaction kinetics (*46*).

A lack of linearity can be observed in the linearized Arrhenius equation when the regime which controls the rate of reaction changes reaction kinetics (*46*). A lack of linearity can be observed in the linearized Arrhenius equation when the regime which controls the rate of reaction changes. In this study activation energies were calculated in 100% NH3 at a space velocity of 5,400 mL/hr/g_{cat} between 2 – 15 % conversion. Catalysts were tested for activation energies in two separate experiments. The standard deviation between the two calculated apparent activation energies is given as the error, and the average of the two measurements is reported as the apparent activation energy for each catalyst.

CHAPTER 3

INVESTIGATION OF THE FORMATION AND WORKING STATE OF K-RU HOLLANDITE CATALYSTS FOR AMMONIA DECOMPOSITION

While the activity of Ru based catalysts for ammonia decomposition is well known to be enhanced by alkali metals and alkaline earth metals, typically these promoters are in the range of ppm levels up to 3%. Previously we have shown that promotion of large amounts of K (up to 36%) can be beneficial for low temperature ammonia decomposition for Ru catalysts supported on γ-Al_2O_3 (*118*, *126*). The enhanced activity was contributed to the formation of K and Ru based hollandite structures on the surface of the catalyst. While very little is known about supported hollandite catalysts, let alone the catalytic properties of K-Ru hollandites, unsupported Mn based hollandite catalysts have been thoroughly studied for a variety of oxidation reactions (*186–189*). Additionally, these structures are typically synthesized via solid state reactions or through hydrothermal synthesis methods (*190–196*). Therefore, it is interest to better understand the formation mechanism of K-Ru hollandite during various impregnation synthesis techniques, variables that influence the formation of hollandite, the working state of the K-Ru hollandite catalysts, and whether or not the formation of the hollandite structure is beneficial to the reaction, compared to the "ideal" Ru nanoparticle size of 1.8 to 2.5 nm, suggested in the literature. Additionally, we determined that K act to promote the reaction by chemically modifying the Al_2O_3 support surface, and by also acting as a Cl^- scavenger, thus, mitigating the negative effect on reactivity that free Cl^- are known to exhibit for ammonia decomposition.

3.1 Hollandite Background

Hollandite (often referred to as OMS-2 or cryptomelane type materials) refers to both the Ba Mn oxide mineral and to a specific crystal structure that can form with various metal cations and transition metals. These crystal structures consist of a one-dimensional tunnel structure, where a cation such as K, Na or Ba ion occupies the tunnel sites. The tunnel themselves are composed of 2x2 MO_6 (where M = transition metal) octahedrons that are connected through edge sharing and corner sharing oxygens and can be doped with various transition metals. The hollandite family has stoichiometry of $A_x(B, M)_8O_{16}$ where A is an alkali or alkaline earth cation, B is a trivalent cation which may or may not be present, and M is a transition metal such as commonly used Ti and Mn. Examples include Na-TiO_2 hollandite (*197*), K-MnO_2 hollandite (*187*, *194*, *195*, *198–200*), Li-TiO_2 (*201*), K-Ti,FeO_2 (*202*), Ag-MnO_2 (*203*) and Na-VO_x (*204*) to name a few. Hollandites have been used for a variety of chemical reactions due to their mild surface acid-base properties and ion-exchange properties. K-MnO_2 hollandites are highly active for a variety oxidation reactions such as CO oxidation (*205–207*), oxidation of ethyl acetate (*208*, *209*), partial oxidation (*210–212*) due to the presence of Mn in different oxidation states and highly mobile lattice oxygen species (*213*). However there is very little information present on K-RuO_2 type hollandite aside from the crystal structure and electronic properties (*214*). For simplicity, K-MnO_2 type hollandites will be discussed moving forward.

Typically, hollandite can be synthesized through hydrothermal methods (*186*, *198*, *215*, *216*) and solid state reactions. The mechanism for formation is generally thought to occur through initial nucleation and phase ordering of the K and Mn precursors into a layered structure, where the layers then collapse to form the 2x2 tunnel structure. Portehault et al. (*217*) reported the synthesis of K-MnO_2 hollandites through low temperature routes and studied the growth mechanism. After initial mixing of the precursors for a few hours at room temperature, the initial precipitate was found to be poorly ordered and no hollandite peaks were from XRD analysis. After mixing at 60 or 95°C, the pH fell below 2.0 and characteristic hollandite reflections appeared in the precipitate XRD patterns. They determined that high acidity increased the kinetics of phase transformation. Performing the synthesis with a mixture pH > 2.0 resulted in the early precipitate not transforming into hollandite after one week of aging. The precipitate was indexed to the layered MnO_2 birnessite phase. The authors state that growth occurs through a dissolution-crystallization process which is pH dependent. As the pH becomes more acidic, the Mn species become more soluble thus promoting the growth of the nanowires. However, proton chemisorption stabilizes small particles that initially form and can limit the growth state and limit longitudinal growth. Liu et al. (*215*) have also indicated that a thin, layered precursor forms during the early stages of synthesis followed by the appearance of lattice fringes, which indicate the formation of the hollandite tunnel structure. They conclude that the tunnel formation occurs when some of the Mn (III) octahedra from the layered structure migrate into the interlayer region and become corner-sharing octahedra, thus making the "walls" of the tunnel. Gao et al. (*218*) performed in-situ and ex-situ studies to determine the structural and morphological formation of β-MnO_2 and K-MnO_2 hollandite materials under hydrothermal reaction conditions. They found that γ-MnO_2 spheres with poorly defined 1x2 tunnel structures first formed and grew in size with increasing reaction time. The spheres began forming rod like structures on the peripheral of the particles that further grew in length with increasing reaction time and finally transformed into β-MnO_2 after 240 minutes. The phase transformation was thought to occur through the collapse of the 1x2 tunnel framework of γ-MnO_2 and rearrangement of the MnO_6 octahedra to form a 2x2 tunnel framework.

Shen et al. (*219*) studied mixed valent Mn oxides through in-situ XRD. They determined that, beginning with a layered structure precursor, the layers first compressed and simultaneously formed a 1x 2 tunnel structure, of which increased with increasing reaction time. After 75 minutes and reaction temperature of 180°C, some of the 1x2 tunnels began to transform to the 1x1 tunnel structure (β-MnO_2) and was completely transformed after 150 minutes. They further studied the phase transformation of MnOOH precursor to form K-Mn hollandite, which formed within ten minutes at 120°C. Chen et al. (*220*) proposed a framework to predict the formation and mechanism for growth of different MnO2 polymorphs based on particle size and solution composition by using in-situ X-ray scattering. They determined that the hydrothermal synthesis of MnO_2 proceeds through different crystallization routes under different K ion concentrations. Wang et al. (*186*) studied the reduction profiles for K-MnO_2 (K-Hol), H-MnO_2 (H-Hol) and β-MnO_2 (1x1 tunnel structure). β-MnO_2 exhibited three reduction peaks at 320, 350 and 450°C which corresponded to the reduction of MnO_2 to Mn_2O_3 to Mn_3O_4 to finally MnO. H-MnO_2 showed two reduction peaks at 330 and 490°C which was assigned to the reduction of H-

Hol to Mn_3O_4 and then to MnO. K-Holl exhibited reduction peaks at much lower temperatures, between 200 – 370°C.

3.2 Modification of Al_2O_3 with K

Alkali promoted Al_2O_3 catalysts are commonly used for the transesterification of palm kernel oil, sunflower oil, coconut oil and rapeseed oil The supported alkali catalysts can be synthesized via incipient wetness impregnation using nitrates, fluorides, iodides, and carbonate based potassium precursors after calcining to temperatures around 450-550°C (*221–225*), where K aluminates are formed as the active site for these reactions. Potassium carbonate is commonly used to modify the acid-base properties of alumina, as it reacts with the surface hydroxyl groups to readily form Al-OK compounds (*226*). K^+ ions derived from K_2CO_3 supported on alumina have been shown to replace the surface hydroxyl groups to form O-K compounds, but no Al-OK compound formation was observed up to 900°C (*227*).

Iordan et al. (*228*) that K_2CO_3 modified alumina resulted in the uptake of K^+ on through cation exchange with isolated Al-OH groups to form Al-OK surface species. They determined that most of the surface hydroxyl species had been eliminated by 120°C and $KAl(CO_3)(OH_2)$ surface species formed. Additionally, as the amount of potassium salt exceeded the saturation uptake of K^+, bulk potassium salts were found to form on the alumina surface. Wang et al. (*229*) studied the effect of loading K_2CO_3, $KHCO_3$ and KOH on alumina and their ability to generate superbasic sites, which pH as great as 33. For K_2CO_3 loadings below 10%, XRD patterns showed that no bulk K_2CO_3 or Al-OK species formed, indicating a high dispersion of K. At 10 wt%, $KAl(OH)_2CO_3$ was formed, and bulk K_2CO_3 began to form at loadings greater than 20%. As for $KHCO_3$, the same Al-OK compound formed as with K_2CO_3 between 10 -20%. Through TG-DTA and TPDE analysis, the authors determined that the $KAl(OH)_2CO_3$ compound decomposes between 225 – 350°C, which was accompanied by the evolution of CO_2 and H_2O within the same temperature regime. The authors determined that $KAl(OH)_2CO_3$ thus decomposes to form $KAlO_2$, H_2O and CO_2.. The formation of Al-OK compounds from wet impregnation has been proposed to occur in two different manners: in one mechanism, the non-specific adsorption of K cations occurs through electrostatic attraction to deprotonated Al-O^- surface groups, which then forms an ion pair with the positively charged K. Secondly, specific adsorption can occur through cation exchange with Al-OH surface groups which can form chemical bound Al-OK groups (*228*, *230*).

Sun et al. (*231*) attempted to create superbasic sites on TiO_2, ZrO_2 and SiO_2 by loading these supports with KNO_3. They were able to determine that dispersion of K nitrate was not a function of support surface as, the highest dispersion was exhibited on the lowest surface area, and the lowest dispersion on the highest surface area support, silica. They determined that octahedral vacant sites present on the various supports determined dispersion of KNO_3 and proposed that K^+ deposit onto the support through insertion into the surface vacant sites which agrees with the previously cited literature. The authors determined that only alumina and zirconia exhibit the necessary characteristics needed to form superbasic sites.

Zaki et al. (*232*) found that functionalization of alumina with K resulted in the formation of Al-OK groups, which stabilized Rh^0 and prevented Al-OH reformation under hydrolysis conditions. Additionally, they determined that the Al-OK groups were stable during hydrogen reduction at 200°C and under exposure to H_2O and O_2.

Due to the large loading of K promoter used during this study, we investigated the effect of K on the surface of support. Figure 3.2 shows the XRD pattern of 12 wt% K supported on ɣ- Al_2O_3. KCH_3COO was used as the K precursor and synthesized as described in Chapter 2.2. In the absence of Ru, we clearly see the formation of $KAl(OH)_2CO_3$ with the addition of K to the support (*228*, *233*). To the best of our knowledge, there is no information of K supported Al_2O_3 catalysts from using KCH_3COO as a precursor, as commonly used precursors as K_2CO_3 and $KHCO_3$ as discussed previously. Due to the variety of different vacancies that may be present in ɣ-Al_2O_3, the unidentified XRD reflections may be due to different Al-OK species with different carbonate or carbonyl type ligands, which may occur due to the two different mechanisms of K^+ adsorption that can occur on ɣ-Al_2O_3. No reflections related to K_2CO_3, $KHCO_3$, KOH or KCH_3COO were observed. The surface area of the ɣ-Al_2O_3 support used here is 192±8 m^2/g and has a maximum surface hydroxyl coverage of 11 OH^{-1} nm^{-2} (*228, 230*). This value is an estimation of the total number of surface lattice sites present on the alumina (100), (111) and (110) planes, assuming a defect spinel structure. It has also been reported that the maximum uptake of K^+ on alumina through deprotonation of surface hydroxyl groups to be 13 K^+ nm^{-2} (*228, 229*). Based on these theoretical values, the maximum uptake of K in our system is 3.56 mmol, which corresponds to 42% of the total K content in the catalyst. Figure 3.2 shows the Raman spectra for the K promoted Ru catalyst (red trace) compared to that of the 12%K on alumina (black trace). There are few reports indicating the Raman vibrations for the $KAl(OH)_2CO_3$ compound, however Raman shifts above 700 cm^{-1} have been reported, indicating that scattering from the K-Al bond occurs at 1097 cm^{-1} and 728

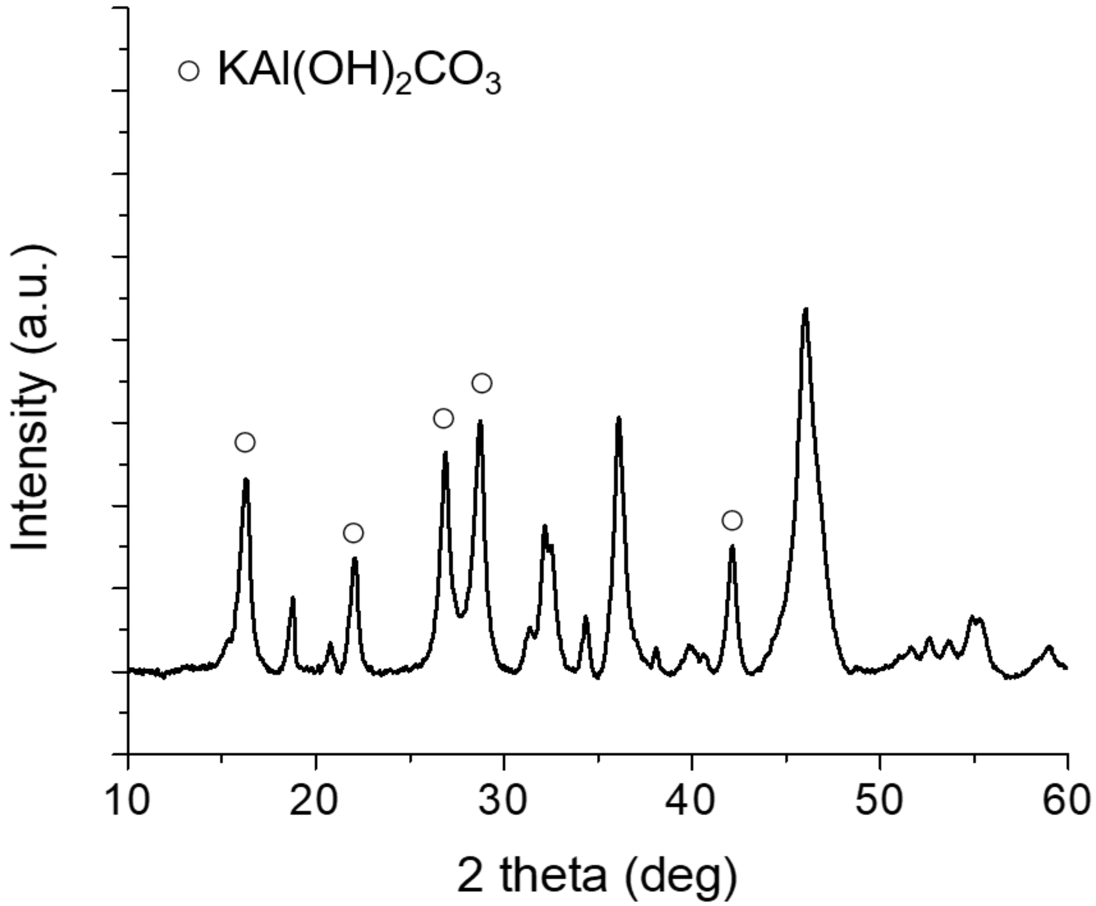

Figure 3.1. XRD pattern of 12 wt% K supported on ɣ- Al_2O_3. The circles indicate reflections corresponding to $KAl(OH)_2CO_3$

cm^{-1}, which are indicated in both Raman spectra, further indicating that the 4,12 RuK catalyst contains the K-Al compound when Ru is added to the catalyst during synthesis. The functionalization of the support with K gives insight in how such high loadings of promoter are not detrimental to the catalyst activity. Typically, large loadings of promoter are detrimental to activity, because it will begin to cover or block the active metal sites.

Instead, functionalizing the support surface with K actually enhances the basicity of the support, which will further enhance ammonia decomposition activity (*75*, *124*, *231*, *234–236*). To the best of our knowledge, using a promoter to enhance the basicity of the

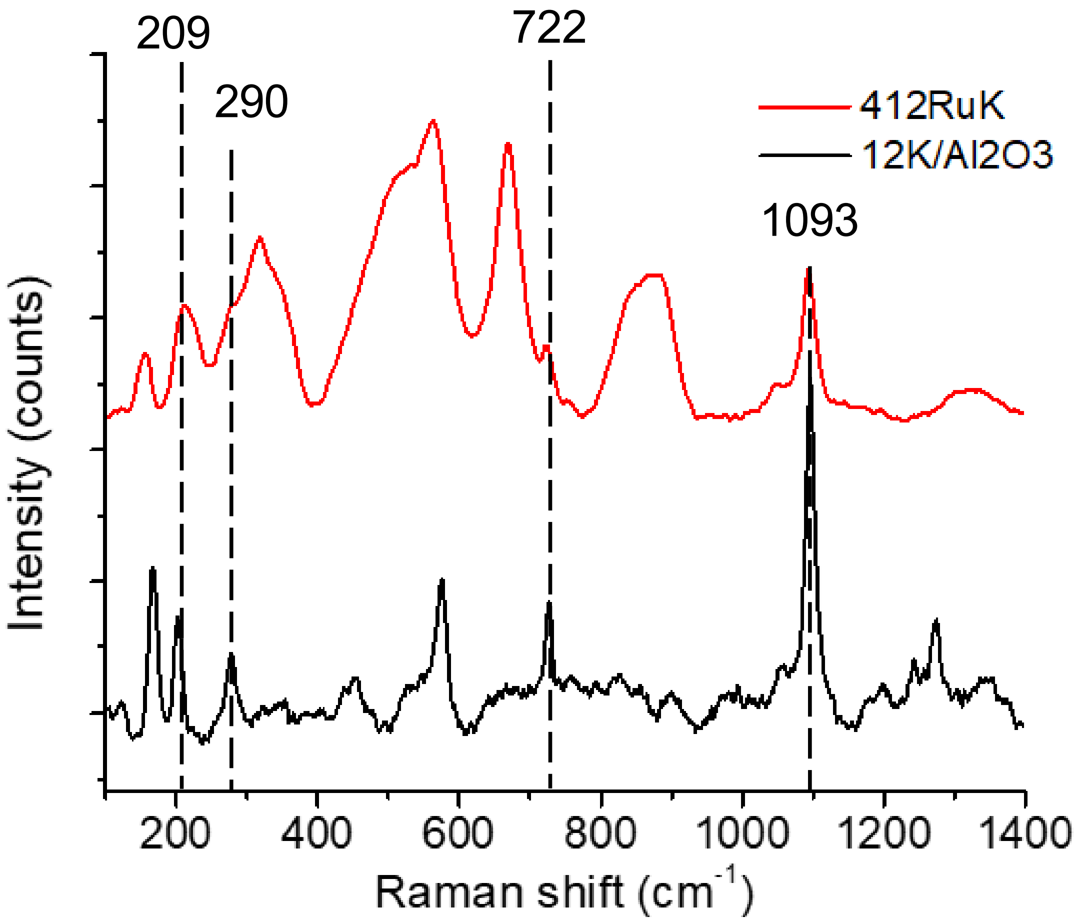

Figure 3.2. Raman Spectra of (top) 4,12 RuK/Al_2O_3 and (bottom) 12K/Al_2O_3.

support has not been investigated in this manner previously. It would be of interest to further explore the use of other alkali or alkaline earth metals deposited onto alumina in order to enhance the basicity of the catalyst. However, this study is outside the scope of this work.

3.3 Investigation of Hollandite Formation

Figure 3. shows the SEM and TEM images of two different catalysts, a baseline 4 wt% Ru supported on γ-Al2O3 catalyst (a, b) and a 4 wt% Ru promoted with 12 wt% K

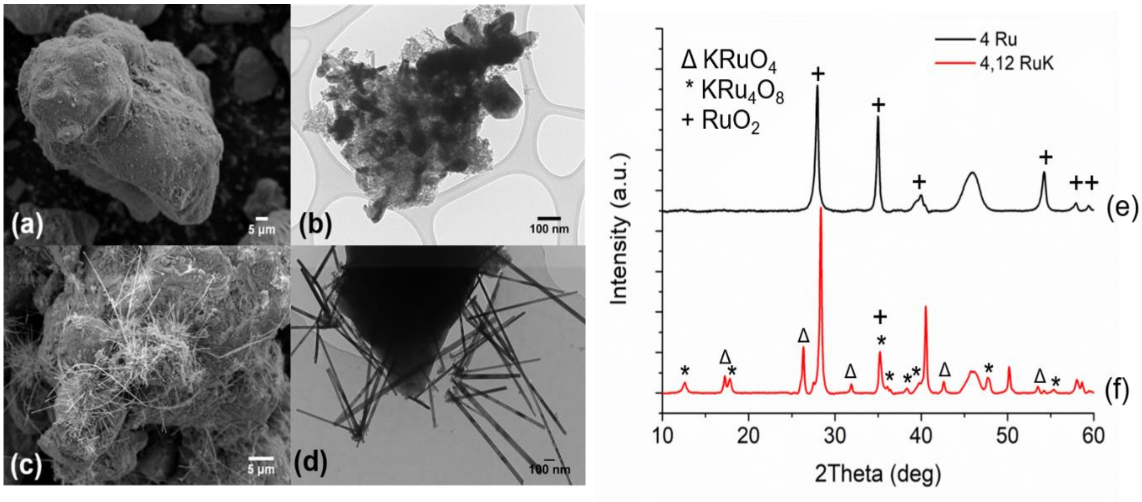

Figure 3.3. Left panel: SEM images of (a) 4 Ru/Al_2O_3 and (b) 4,12 RuK/Al_2O_3. TEM images of (b) 4 Ru/Al_2O_3 and (d) 4,12 RuK /Al_2O_3. Right panel: corresponding XRD patterns of (e) 4 RuK/Al_2O_3 and (f) 4,12 Ru/Al_2O_3.

catalyst (4,12 RuK) (c,d). These catalysts were synthesized using the incipient wetness impregnation technique. It is quite clear to see that with the addition of K, the catalyst morphology dramatically changes. While the 4 Ru catalyst exhibits large nanoparticles that can be indexed to RuO_2, the 4,12 RuK catalyst displays nanorod structures that have been previously been determined to be K-Ru hollandite (KRu_4O_8). The synthesis of this structure through impregnation techniques has not previously been investigated. Therefore, this section is dedicated to exploring under what conditions the hollandite structure can form in both wet and dry impregnation.

The apparent activation energy for the 4 Ru and 4,12 RuK catalyst were measured under differential conditions (2-12% conversion) under 100% NH_3 and at a space velocity of 5,400 mL/hr/g_{cat}. The Arrhenius plot for both the 4 Ru and 4,12 RuK catalysts is shown in Figure 3.. The 4 Ru catalyst had an apparent activation energy of 125.2 ± 8.9 kJ/mol, while the 4,12 RuK catalyst had an apparent activation energy of 65.7 ± 7.7 kJ/mol. Other

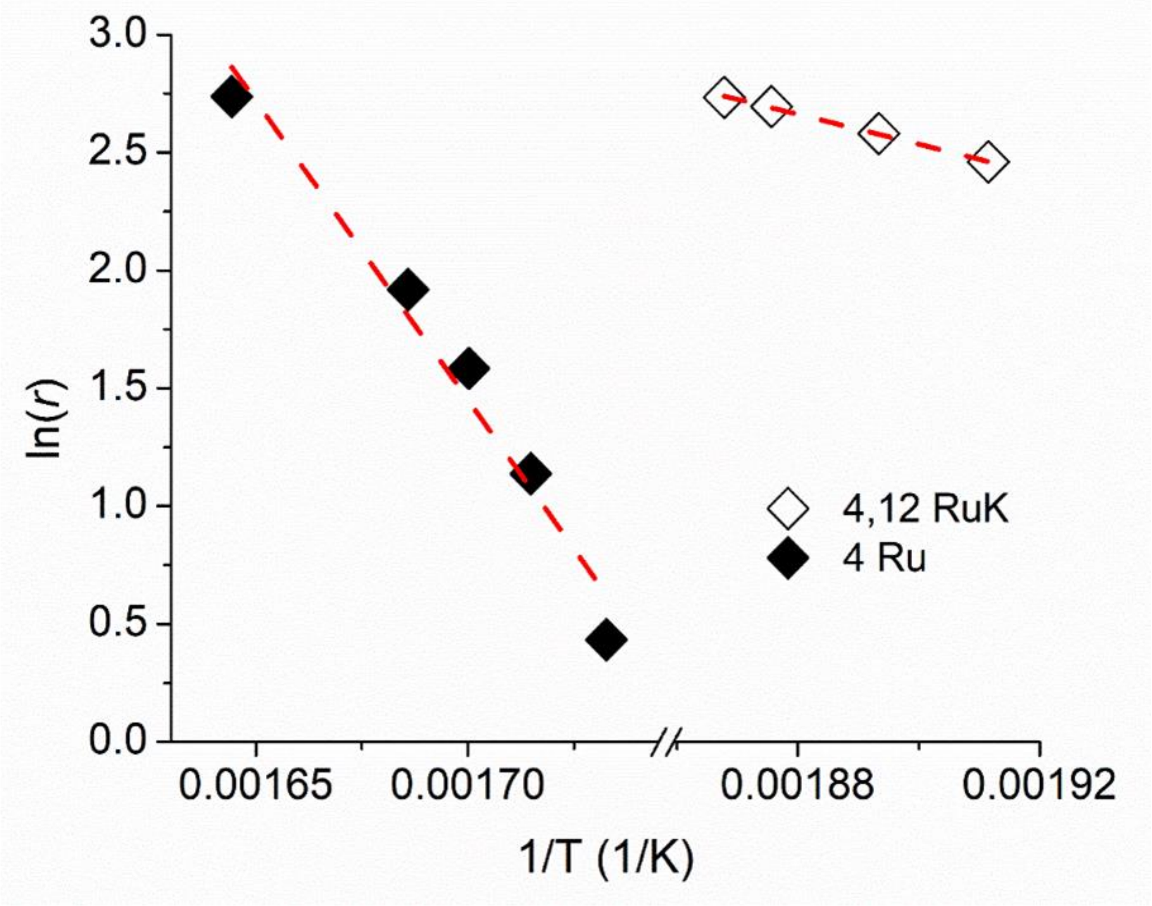

Figure 3.4. Arrhenius plot for 4 Ru (filled diamonds) and 4,12 RuK (open diamonds). Reaction conditions: 100% NH_3, 5,400 mL/hr/gcat and atmospheric pressure. Measurements were conducted under differential conditions.

apparent activation energy for Ru based catalysts have been reported within the range of 87.9 – 155 kJ/mol (*82*, *237–239*). The decrease in the apparent activation energy with the addition of K suggests that K electronically modifies the Ru active sites.

3.3.1 Effect of Precursors on Catalyst Composition and Activity

Different precursors were chosen in order to determine which K and Ru precursors would result in hollandite formation following the incipient wetness impregnation method. Specifically, two Ru precursors, ruthenium acetylacetonate ($Ru(acac)_3$) and ruthenium chloride ($RuCl_3$) and three K precursors, potassium acetate (KCH_3COO), potassium

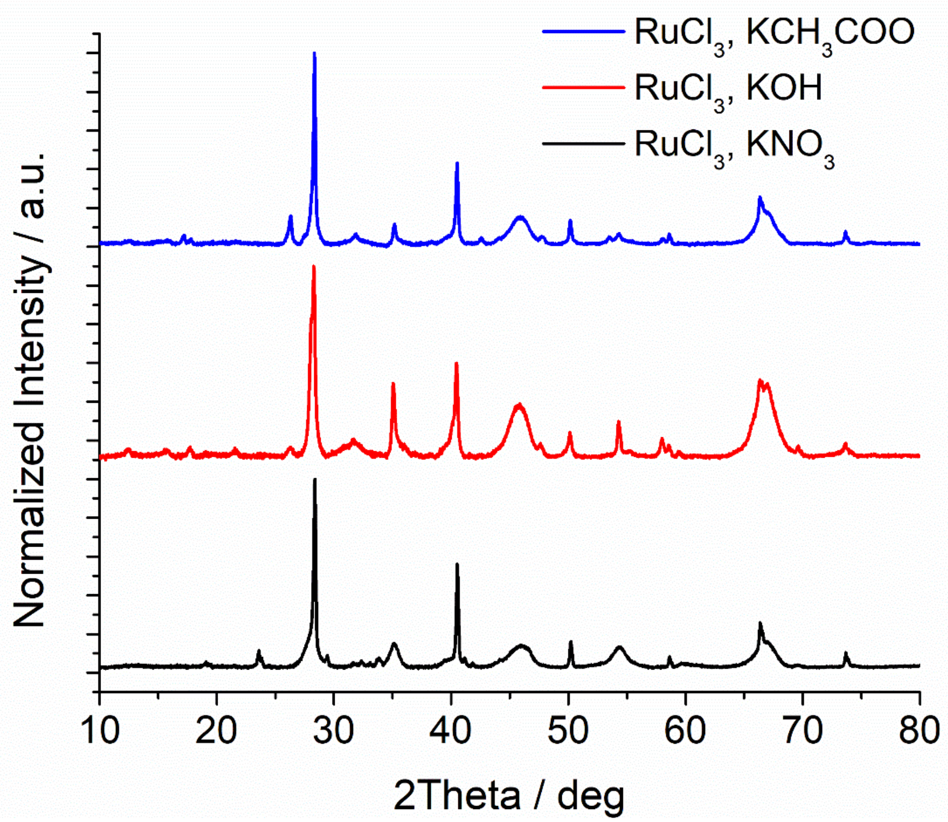

Figure 3.5 XRD patterns of 4,12 RuK catalysts synthesized with (blue trace) $RuCl_3$, KCH_3COO, (red trace) $RuCl_3$, KOH and (black trace) $RuCl_3$, KNO_3

hydroxide (KOH) and potassium nitrate (KNO_3) were chosen and each combination of the six different precursors were investigated through XRD for phase identification and were also subjected to activity measurements. Due to the complexity and polycrystallinity of the patterns, phase identification was primarily determined using the major phases for the variety of components in each catalyst. When necessary, the minor reflections at higher 2Theta values were used to conclusively determine phases. Highly crystalline KCl is seen in each pattern synthesized using $RuCl_3$ as the Ru precursor, as indicated by reflections at 28.33°, 40.49°, 50.14°, 58.6° and 66.36° (*54*). Additionally, the broad reflections located at roughly 46.1° and 67.3° are from the amorphous alumina support. The major reflections for KRu_4O_8 hollandite occur at 12.58° (110), 17.81° (200), and 35.15° (121)) (*54*, *118*, *126*, *200*, *240*). These reflections are exhibited in the $RuCl_3$, KCH_3COO catalyst as well as the $RuCl_3$, KOH sample. Additionally, these two catalysts contain a secondary phase $KRuO_4$, which exhibits major reflections at 17.18° (011), 26.28° (013) and 31.84° (020). Neither $KRuO_4$ nor hollandite appear in the $RuCl_3$, KNO_3 XRD pattern. Surprisingly, only reflections corresponding to RuO_2 are present in the $RuCl_3$, KOH pattern, indicated at 28.13°, 34.93°, 54.15°, 57.83° and 59.28°(*241*, *242*).

Very broad reflections appear in the $RuCl_3$, KNO_3 at 28.0° and 35.1° which may indicate highly dispersed RuO_2 nanoparticles. While Pyrz et al.(*118*) reported the formation of Ru hollandite using KNO_3 and $RuCl_3$ precursors, these results were not able to be reproduced here. Instead, reflections at 18.9°, 23.4°, 29.4°, 32.33°, 33.06°, 34.04°, and 41.8° appear due to KNO_3. Therefore, on the basis of XRD analysis, we concluded that Ru type hollandite can be formed using both KCH_3COO and KOH as precursors under the synthesis conditions studied here. Figure 3.6 shows the XRD patterns for the three catalysts synthesized using $Ru(acac)_3$ with KCH_3COO, KOH or KNO_3. As with the $RuCl_3$, KNO_3 catalyst, the $Ru(acac)_3$, KNO_3 catalyst indexes to KNO_3 but does not contain broad reflections corresponding to RuO_2. Catalysts containing KOH and KCH_3COO both contain $KRuO_4$ and also exhibit peak broadening in the range of 50.5° to 57.1°. This may be due to highly crystalline RuO_2, however the main reflections at 28.1 and 35.0° are not present in either pattern. No catalyst exhibited the major reflections related to hollandite while using the $Ru(acac)_3$ precursor.

The morphological properties of each of the six catalysts was determined using SEM and are shown in Figure 3.7. The top figures (a), (b), and (c) correspond to catalysts

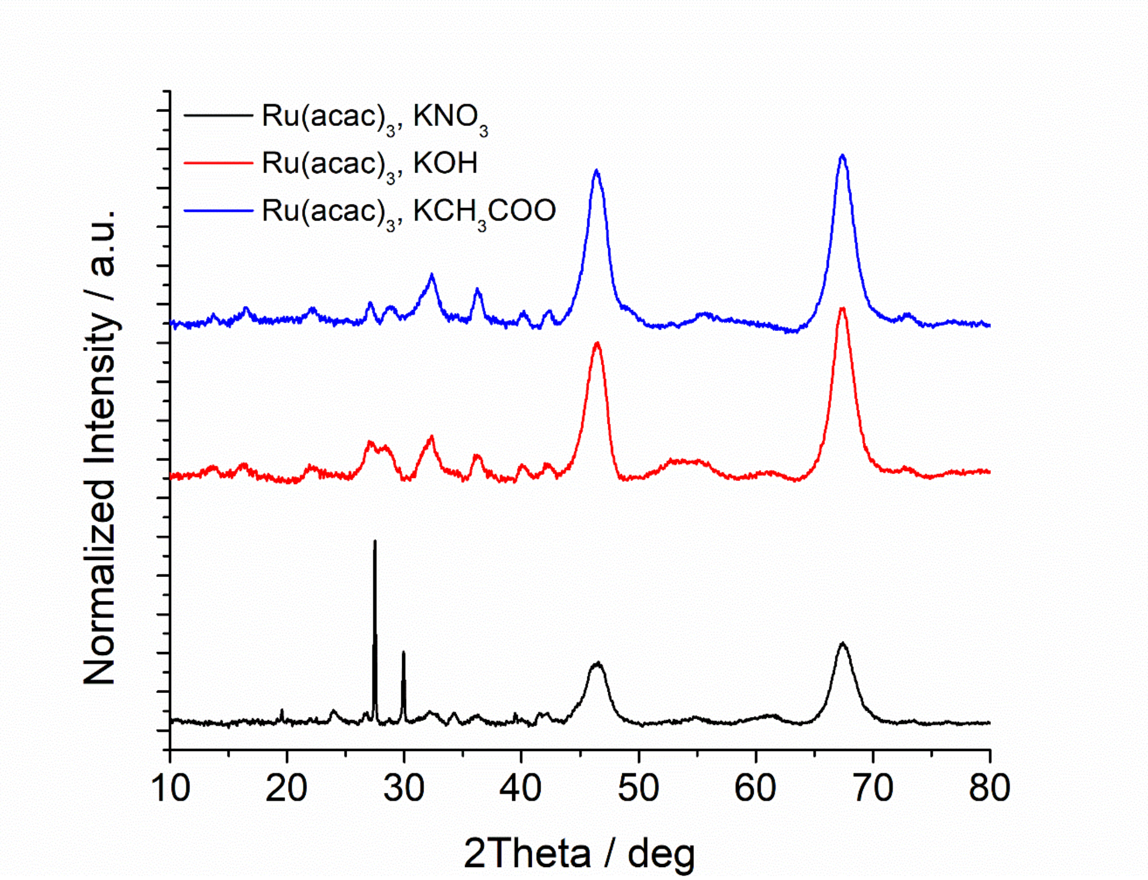

Figure 3.6 XRD patterns of 4,12 RuK catalysts synthesized with (blue trace) $Ru(acac)_3$, KCH_3COO, (red trace) $Ru(acac)_3$, KOH and (black trace) $Ru(acac)_3$, KNO_3.

made with $RuCl_3$, while the bottom figures (d), (e), and (f) correspond to catalysts made with $Ru(acac)_3$. For catalyst containing Ru type hollandite ($RuCl_3$, KCH_3COO and $RuCl_3$, KOH), we expect to see nanowhisker type structures, while those containing $KRuO_4$ exhibit wispy, sheet like structures instead. Figure 3.7a and Figure 3.7b shows the SEM images for catalysts synthesized with $RuCl_3$, KCH_3COO, and $RuCl_3$, KOH respectively. Both images show the nanowhisker structure indicative of hollandite, while Figure 3.7c ($RuCl_3$, KNO_3) does not indicate any KRu_4O_8 or $KRuO_4$ structures as confirmed by the XRD. The small white spheres seen in the image are related to the morphology of the support and are not due to Ru nanoparticles. This has been confirmed by SEM images of the bare ɣ-Al_2O_3 support. As for the $Ru(acac)_3$ catalysts, flat nanoneedles are seen in

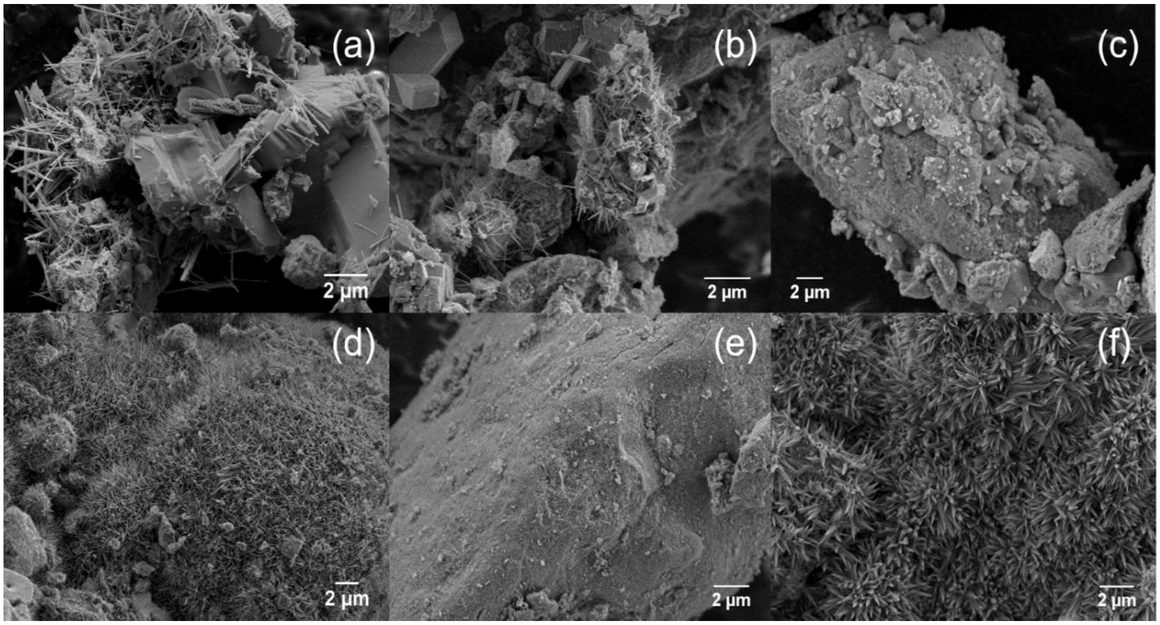

Figure 3.7. SEM images of 4,12 RuK supported on ɣ-Al_2O_3 made with (a) $RuCl_3$, KCH_3COO, (b) $RuCl_3$, KOH, (c) $RuCl_3$, KNO_3, (d) Ru(acac)$_3$, KCH_3COO, (e) Ru(acac)$_3$, KOH, and (f) Ru(acac)$_3$, KNO_3.

abundance in Figure 3.7d, and much more sparingly in Figure 3.7e. Interestingly, Figure 3.7f (Ru(acac)$_3$, KNO_3) also shows an abundance of nanoneedles (albeit wider in diameter compared to Figure 3.7d), even though no crystalline Ru phase could be determined from the XRD pattern. Therefore, these structures may correspond to KNO_3.

Finally, these six catalysts were tested for their ammonia decomposition activity under 10% NH_3 and at a space velocity of 45,300 mL/hr/$g_{cat.}$. The NH3 conversion from 250° to 400°C is shown in Figure 3.. The most active catalyst at all temperatures was the Ru(acac)3, KNO_3 which obtained 97% conversion at 400°C. The high activity of this catalyst may be due to the formation of highly dispersed Ru particles, such that could not be observed via XRD. Other studies have shown that using Ru(acac)$_3$ as a precursor can increase the Ru dispersion by 10% and enhance activity (*123*) which is most likely due to the size of the precursor ligand, which would create highly dispersed Ru nanoparticles due

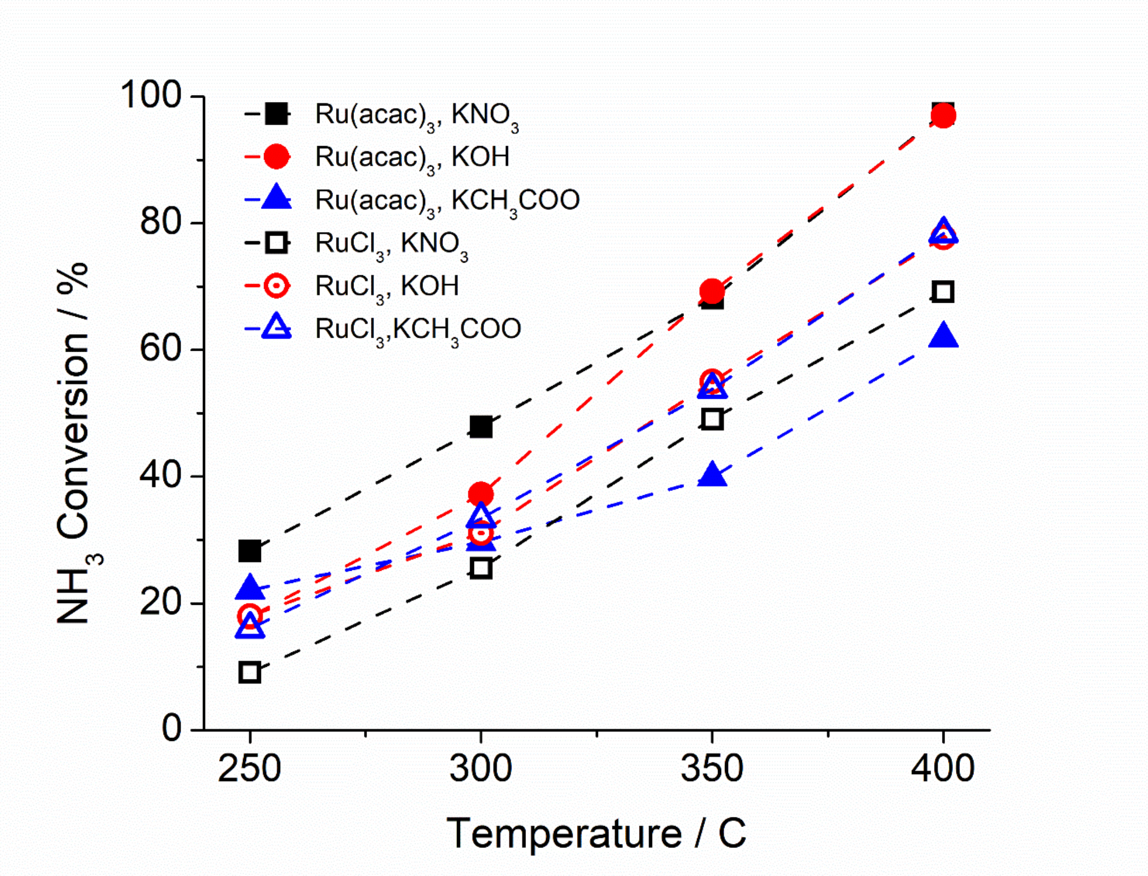

Figure 3.8. NH_3 conversion of various 4,12 RuK catalysts synthesized with different precursors. Reaction conditions: 10%NH_3/Ar, 45,300 mL/hr/g_{cat} and atmospheric pressure.

to the steric hindrance of the large ligands. The next most active catalyst was also synthesized using $Ru(acac)_3$ and KOH, while the least active catalyst was made with $Ru(acac)_3$ and KCH_3COO. A different trend was observed with the $RuCl_3$ based catalysts. The catalysts containing hollandite ($RuCl_3$, KOH and $RuCl_3$, KCH_3COO) showed roughly similar performance at all temperatures, and ultimately obtaining 77% and 78% conversion, respectively. The $RuCl_3$, KNO_3 catalyst however showed the poorest activity of the $RuCl_3$ catalysts. Ultimately, we see here that the effect of the precursor will greatly influence the activity depending on which Ru precursor is used. Insight into why this may be the case is beyond the scope of this study. Here, we are further interested in studying the precursors that are able to form hollandite, and that are also inexpensive. The high cost of the Ru(acac)$_3$ precursor limits its practical application and thus $RuCl_3$ will be continued to be used in combination with KCH_3COO precursor herein.

3.3.2 Influence of Synthesis Method

Three different synthesis methods were investigated for hollandite formation. Hollandites are typically synthesized via molten salt reactions, solid state reaction, flux method or through hydrothermal synthesis methods. Additionally, there is only a single report of hollandite synthesized for support catalysis. Typically, hollandite structures are utilized for various oxidation reactions but are not supported (*195*, *201*, *206*, *243*, *244*). Therefore, we further investigated under what conditions the hollandite structure could form with supported catalyst synthesis methods. These include wet impregnation method (WI), incipient wet impregnation (IWI) and strong electrostatic adsorption (SEA). The methods for each of these synthesis procedures can be found in Chapter 2.2. After synthesis, XRD patterns of each of the three catalysts made with the three different synthesis methods were collected and are shown in Figure 3.. We see with the incipient wet and wet impregnation methods, we are able to form the KRu_4O_8 hollandite phase, but is not the case with the SEA synthesis method. The SEA synthesis catalyst instead exhibits a strong KNO_3 reflection at 28.02°. This indicates that the reduction of the precursor ligands was not complete during the synthesis method.

The primary difference between the SEA synthesis method with the dry and wet impregnation method is the fact that the two precursors are deposited at two separate times and not at the same time, as with the dry and wet impregnation methods. This opens up a

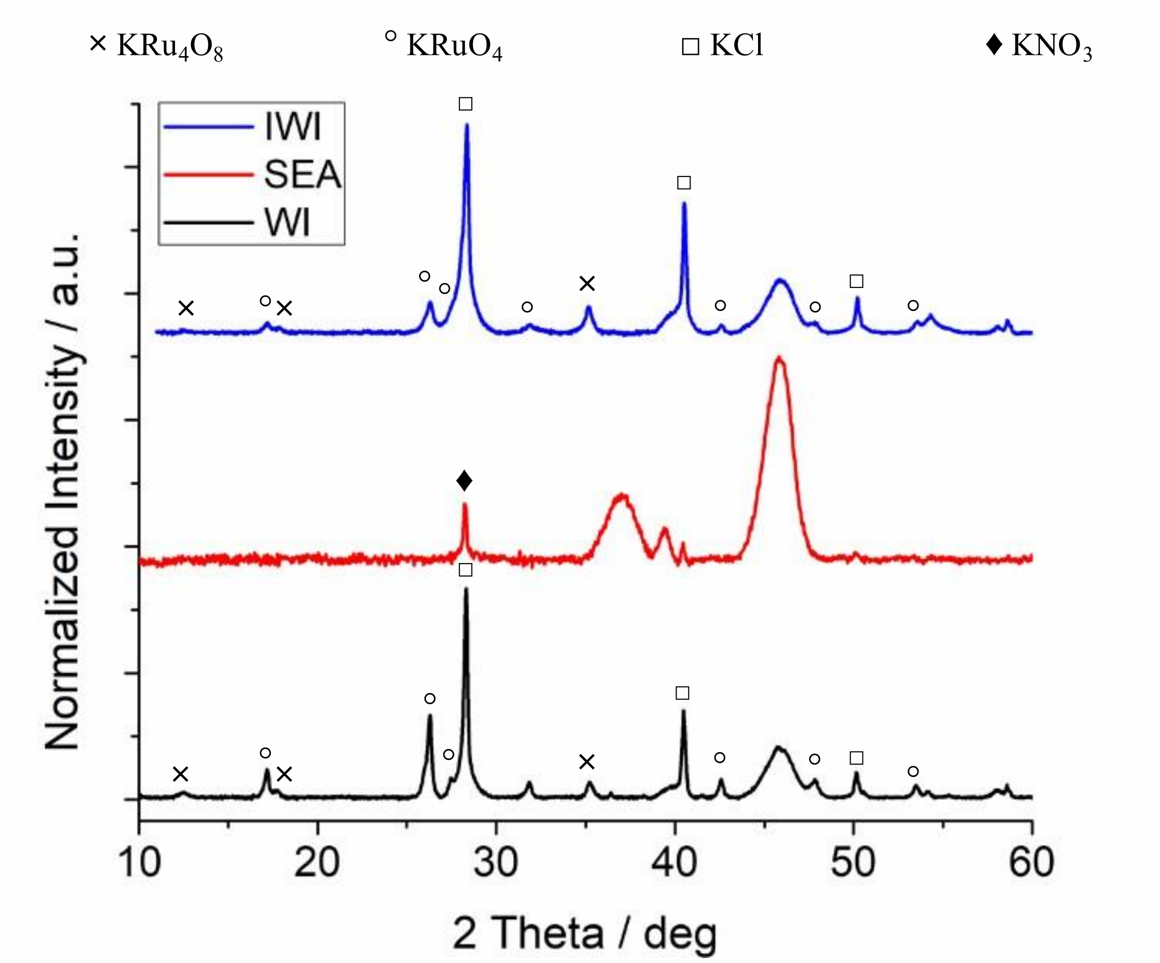

Figure 3.9. XRD patterns for the three different synthesis methods of 4,12 RuK. From top to bottom: incipient wetness impregnation (IWI), strong electrostatic adsorption (SEA) and wet impregnation (WI).

variety of questions that will be explored in later sections. Primarily, we are interested in determining whether or not sequential impregnation can also result in hollandite formation, as is seen with the co-impregnation synthesis used with the incipient wet and wet impregnation methods here. Additionally, we want to further understand of certain parameters specific to each the dry and wet impregnation influence the formation of the hollandite structure and will be the focus of the rest of this section.

3.3.3 Effect of Dilution Volume

The effect of the metal concentration impregnated during each aliquot of the incipient wetness impregnation method was investigated to determine if this variable influences the active metal phase formation or the ammonia decomposition activity. As the solution volume increases, the number of impregnations increases, and the amount of metal deposited per impregnation will decrease. This may help enhance the dispersion of the active metal or limit the formation of hollandite. The volume of the impregnation solution was varied from 5 mL, 6 mL, 8 mL, 12 mL and 20 mL, for a catalyst containing 4 wt% Ru and 12 wt% K using $RuCl_3$ and KCH_3COO precursors. Table 3.1 shows the amount of each metal contained within one aliquot of solution, and the total number of impregnations performed for each catalyst synthesis. The volume for one aliquot of solution (one impregnation) is determined by the pore volume of the support used. Figure 3. shows the XRD patterns for the five different catalysts. It is obvious that the solution volume influenced the formation and relative amounts of $KRuO_4$, and Ru based hollandite KRu_4O_8. This is highlighted in the insert, which shows that the KRu_4O_8 (200) plane increases with increasing solution volume in relation to the $KRuO_4$ (011) plane, and then disappears at the highest solution volume of 20 mL. The average crystallite size for $KRuO_4$ and KRu_4O_8 was calculated for each of the XRD patterns using Scherrer's equation given in Equation 2.7.

The FWHM was determined by fitting each reflection to a pseudo-Voigt profile using Fityk peak fitting software. The average crystallite size and the ratio of the FWHM of $KRuO_4$ (001) to KRu_4O_8 (200) are given in Table 3.. Interestingly, the largest crystallite size of 34.38 nm was observed in the 20 mL catalyst, which also had the lowest

Table 3.1. Average crystallite size for various 4,12 RuK catalysts synthesized with different impregnation volumes

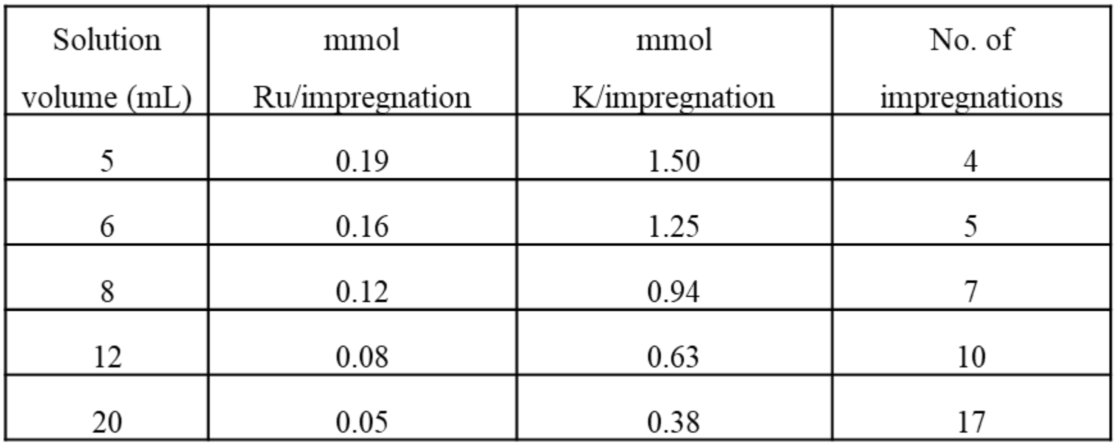

Solution volume (mL)	mmol Ru/impregnation	mmol K/impregnation	No. of impregnations
5	0.19	1.50	4
6	0.16	1.25	5
8	0.12	0.94	7
12	0.08	0.63	10
20	0.05	0.38	17

concentration of metal per impregnation. This suggests that after evaporating the water out of the pores of the support, the metals become mobile and agglomerate during the subsequent impregnation after water is reintroduced into the system. Alternatively, large particles may form from Oswalt ripening during the calcine process. The smallest crystallite size for both $KRuO_4$ (28.50 nm) and KRu_4O_8 (18.09 nm) was observed in the 6 mL solution volume catalyst. The relative ratio of the FWHM of the two Ru species gives us insight into the relative composition of each in relation to each other. The 6 mL sample also exhibited the lowest ratio, indicating more KRu_4O_8 present than $KRuO_4$, while the largest ratio was seen in the 5 mL solution volume sample. There did not seem to be a direct correlation between either particle size or Ru species formation to the dilution volume, although it heavily influenced the presence of each. However, due to the anisotropic nature of these particles, averaging the various planes may not result in useful crystallite information. Instead, the ratio of the FWHM of the KRu_4O_8 (110) to the (200) plane shows that as the solution volume increased, the ratio of the two planes decreased until the hollandite was no longer formed. XRD can only provide information on the various crystallites that are present within the hollandite particles and does not give us

Table 3.2. Average crystallite size for various 4,12 RuK catalysts synthesized with different impregnation volumes.

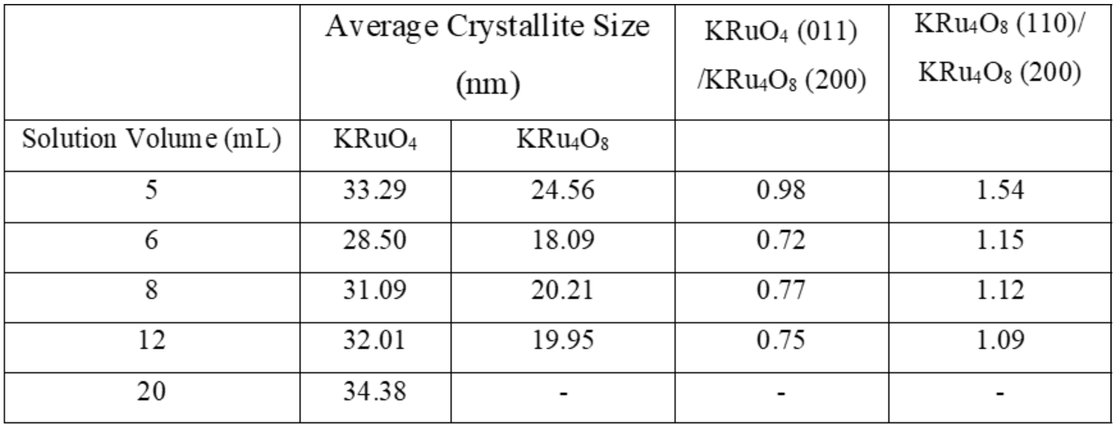

	Average Crystallite Size (nm)		$KRuO_4$ (011) /KRu_4O_8 (200)	KRu_4O_8 (110)/ KRu_4O_8 (200)
Solution Volume (mL)	$KRuO_4$	KRu_4O_8		
5	33.29	24.56	0.98	1.54
6	28.50	18.09	0.72	1.15
8	31.09	20.21	0.77	1.12
12	32.01	19.95	0.75	1.09
20	34.38	-	-	-

insight into the variation in the hollandite morphology, and how the aspect ratio changes as a function of solution volume. Further insight into the morphological changes of the Ru species can be observed in the SEM images shown in Figure 3.11.

The K promoted catalysts are shown against a unpromoted 4 wt% Ru catalyst supported on γ-Al_2O_3 (4 Ru, Figure 3.11a). The aspect ratio of the nanowires (Figure 3.11b-f) dramatically changes with increasing solution volume. At low solution volumes, the hollandite becomes thick and more rod like, and gradually takes on a nanowhisker morphology, becoming more pliable, longer, and thinner. At 20 mL (f), where only $KRuO_4$ forms, flat, short nanorods are present. The polydispersity may be due to the lower rate of reactants mixing with higher dilution volume, or dependent on the concentration of K^+ which could vary depending on the concentration of Al-OK and KCl that forms (*217*). It has also been shown that the crystallization process for Mn tunneled structures is highly dependent on the ratio of MnO_4^- to Mn^{2+} (*245*). Figure 3.a shows the activity of the five different 4,12 RuK catalysts compared to an unpromoted 4 Ru catalyst. The activity measurements were conducted under 1% NH_3 in balance Ar at a space velocity of 30,000

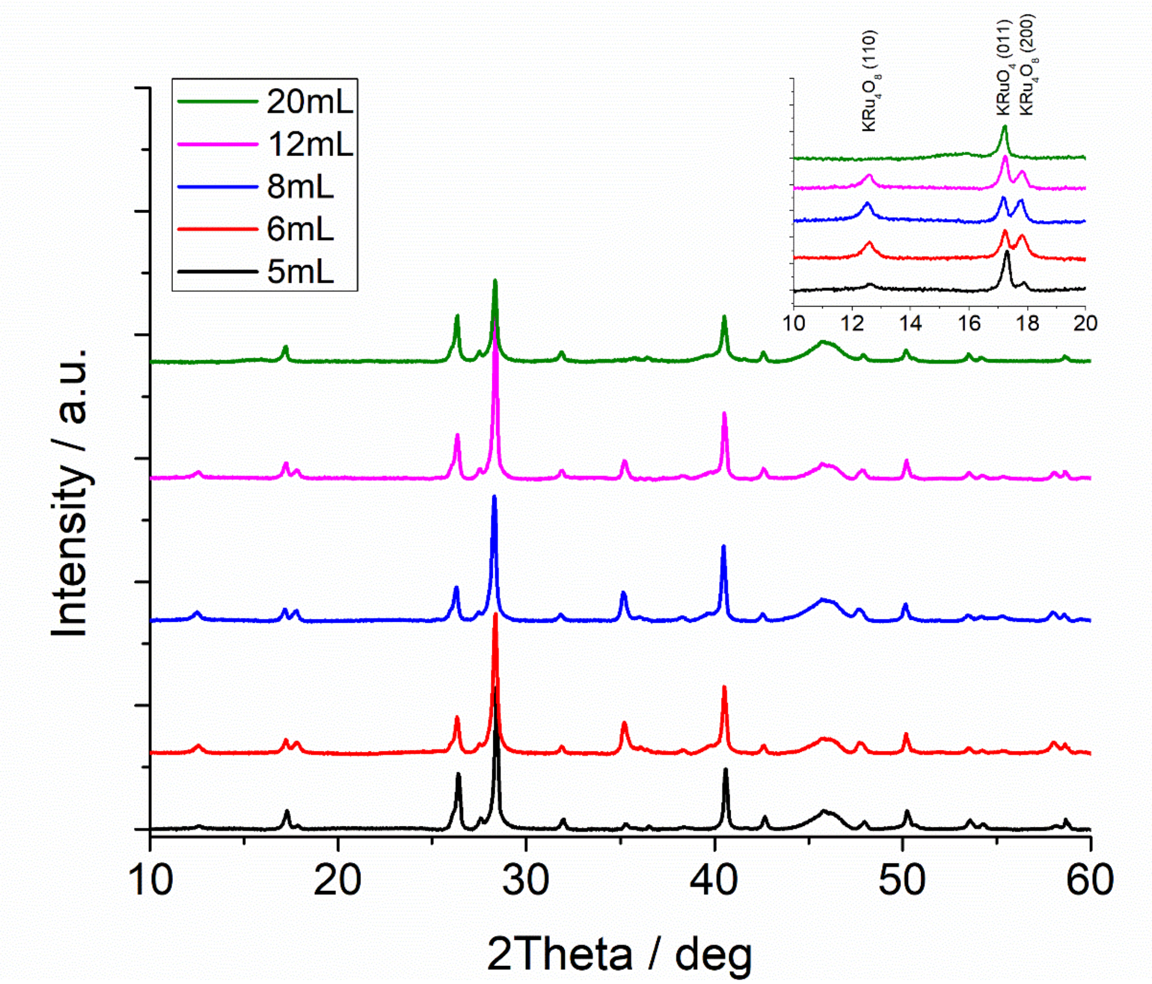

Figure 3.10. XRD patterns for the 4,12 RuK catalysts synthesized with different solution volumes from top to bottom: 20 mL, 12 mL, 8 mL, 6 mL, and 5 mL. The insert shows the 2 Theta values from 10 – 20 deg to highlight the relative intensity of $KRuO_4$ and KRu_4O_8.

mL/hr/g_{cat} and at atmospheric pressure. Figure 3.b shows the relationship between activity and the dilution volume for the five different 4,12 RuK catalysts. At all temperature, the 6 mL catalyst showed the best performance, which coincided with the smallest average particle size and smallest ratio of $KRuO_4$ to KRu_4O_8. At 300°C, the activity begins to decline at dilution volumes greater than 6 mL, indicating an optimal dilution volume for this system under study.

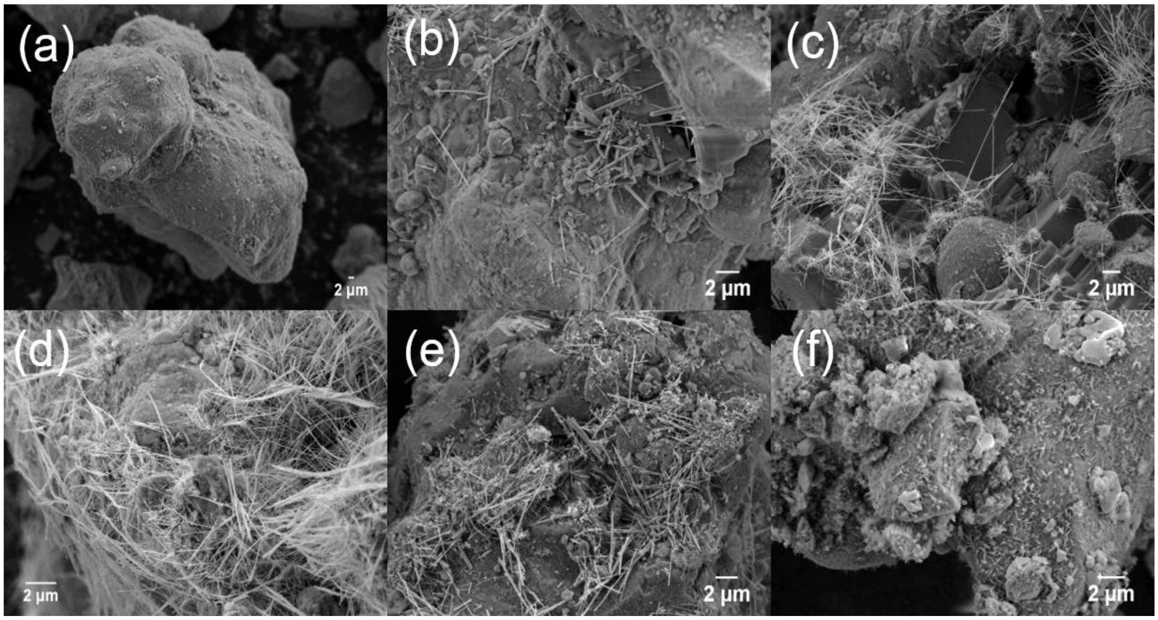

Figure 3.11. SEM images of 4,12 RuK catalysts compared to (a) unpromoted 4 wt% Ru. Synthesized with (b) 5 mL, (c) 6 mL, (d) 8 mL, (e) 12 mL or (f) 20 mL of solution during the incipient wetness impregnation synthesis.

3.3.4 Effect of Impregnation Order

During the co-impregnation synthesis method, the active metal Ru and promoter K are typically impregnated together. In order to determine if a synergistic effect occurs from mixing of the two components during synthesis, we conducted sequential impregnation of K followed by Ru and sequential impregnation of Ru followed by K onto γ-Al_2O_3. For sequential impregnation, either Ru or K only was first impregnated onto γ-Al_2O_3 following the synthesis procedure outlined in Chapter 2.2. After the calcine step, the second metal was then impregnated onto the calcined support and was then again dried at 200°C for 2 hours, and subsequently calcined in air at 550°C for 3 hours. The nomenclature for these two catalysts will include brackets to indicate which metal was impregnated first. For example, 4,12 (Ru), K indicates that Ru was first impregnated, calcined, and then impregnated with K and calcined again. The effect of impregnation order on catalyst

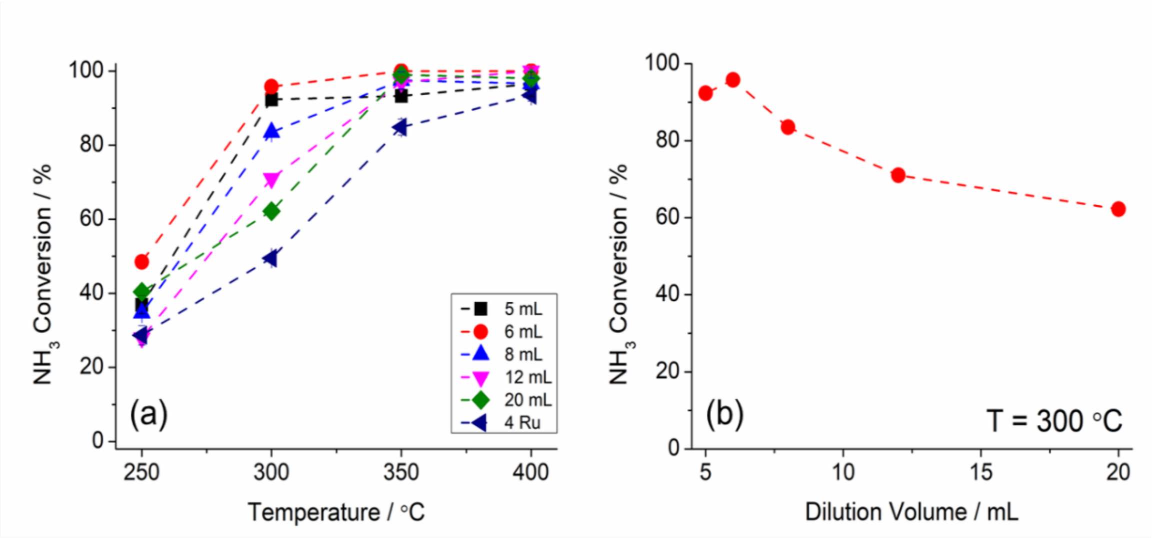

Figure 3.12.(a) Activity of the 4,12 RuK catalysts synthesized with different dilution volumes, compared to unpromoted 4 wt% Ru. Reaction conditions: 1% NH_3/Ar, 30,000 mL/hr/g_{cat} and atmospheric pressure. (b) Ammonia conversion as a function of catalyst dilution volume at 300°C and identical reaction conditions.

morphology was investigated using SEM and XRD. Figure 3.a shows the XRD patterns for 4,12 (Ru)K (red trace) and 4,12 Ru(K) (black trace) compared to the typical co-impregnated 4,12 RuK catalyst (blue trace). The 4,12 (Ru)K catalyst showed reflections corresponding to KRu_4O_8 as well as $KRuO_4$ and RuO_2. Interestingly, the relative intensity of the RuO_2 reflections is much larger than that of KCl, which is typically the most intense and sharp reflection exhibited in the XRD patterns. Interestingly, the XRD pattern for 4,12 Ru(K) shows that no KCl formed during the synthesis, even though $RuCl_3$ was used as the Ru precursor. This is highlighted in Figure 3.b, where the tailing on the left side of the KCl (110) peak in the 4,12 RuK catalyst may be from very small, highly dispersed RuO_2 nanoparticles, while the 4,12 Ru(K) catalyst shows no indication of KCl formation, but also shows highly dispersed RuO_2 in relation to the 4,12 (Ru)K catalyst. Additionally, the catalysts synthesized from sequential impregnation show more prominent reflections from

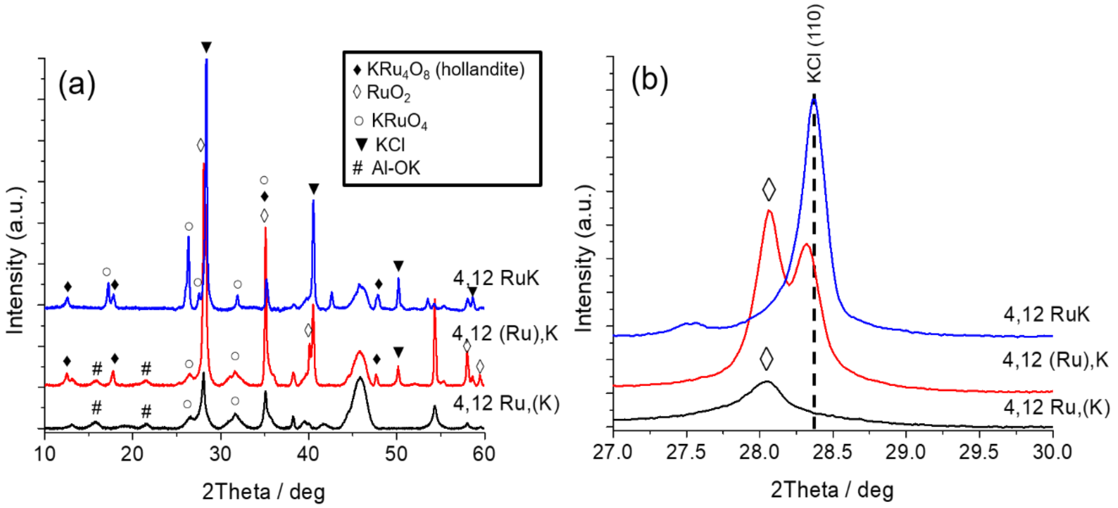

Figure 3.13. (a) XRD patterns of 4,12 RuK catalysts synthesized by sequential impregnation compared to co-impregnation method (blue trace) and (b) enlargement of the XRD patterns to highlight the KCl (110) reflection.

the Al-OK species discussed in Chapter 3.2. The intensity of these peaks is overshadowed by the formation of KCl and KRu_4O_8 and $KRuO_4$ in the co-impregnated catalyst.

Varying the impregnation method gives us insight into how the hollandite may form during the impregnation synthesis method. In typical hollandite hydrothermal synthesis for KMn_4O_8, it has been shown that a layered precursor phase is first formed that transforms to KMn_4O_8 or in some cases different polymorphs of MnO_2 (*218*, *220*, *246*, *247*). Due to the chain like nature of the precursor $RuCl_3$, this may be a feasible mechanism of formation for Ru based hollandite synthesized through incipient wetness impregnation. $RuCl_3$ will be partially hydrolyzed in water, and the negatively charged ligands could form an ion pair with K^+ in solution, forming the basis for a layered Ru-K compound. This would suggest that the support does not provide nucleation sites for the formation of hollandite. However, the formation of hollandite by sequential impregnation of Ru followed by K, suggests that this may not be the case. Gao et al. (*218*) showed the structural evolution of MnO_2 materials prepared at 140°C at different reaction times. They observed that spherical particles first formed and grew in size with increasing reaction time. Over time, short rod-like structures began to protrude from the surface of the spheres which grew in size with increasing reaction time, to finally transform from ɣ- (MnOOH) to β-MnO_2 (1x1 tunnel). Figure 3. shows the SEM images of the 4,12 Ru(K) (Figure 3.a) and 4,12 (Ru)K catalysts (Figure 3.b), where a similar phenomenon was seen when Ru was first impregnated onto the support followed by K. RuO_2 nanoparticles can act as nucleation sites for the formation of hollandite, or further react with the addition of K to form hollandite and $KRuO_4$.

3.3.5 Effect of Evaporation Temperature and Calcine Duration

Next, we determined whether or not the temperature at which the solution was allowed to evaporate as well as the duration of the calcine treatment had any effect on the catalyst activity, morphology, Ru species formation and average crystallite size. D'Addio (*126*) studied the effect of calcine temperature and time on ammonia decomposition activity for 4,12 RuK catalysts, and found that 550°C was an optimal calcine temperature that resulted in the highest ammonia decomposition activity, of 350°C, 550°C and 750°C. Therefore, the calcine temperature was kept constant in all cases at 550°C. However, the study did not further investigate which Ru phases were present at each calcine temperature or time. In order to study this, 4,12 RuK catalysts were synthesized using the wet impregnation synthesis method and allowed to evaporate at either 60°C, 90°C, 120°C and 150°C. Each sample individual sample was then separated into four crucibles, and each was either heated under air to 550°C for either 0 hr (no calcine treatment), 1 hr, 3 hr or 5 hr. Each catalyst was first heated to 200°C and held for 2 hours before being heated at

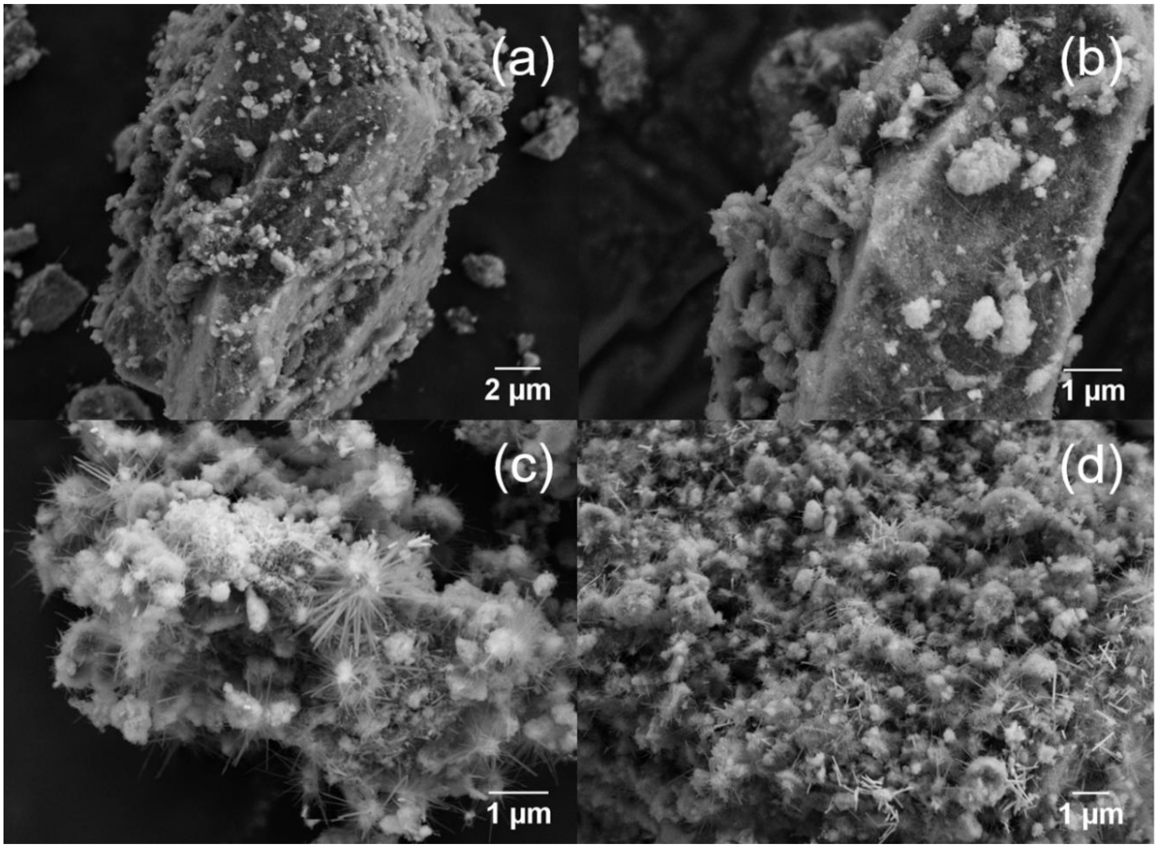

Figure 3.14. SEM images of (a,b) 4,12 Ru(K) and (c,d) 4,12 (Ru)K

550°C for the aforementioned times. Each sample was then cooled to room temperature and XRD was performed on each sample as well as ammonia decomposition activity measurements.

The XRD patterns for all 12 catalysts are shown in Figure 3.. From this figure it is clear that the formation of hollandite only occurs only with specific environmental factors. Only under mild evaporation temperatures of 60°C and 90°C, was the hollandite structure KRu_4O_8 able to be produced. Calcining these catalysts for up to five hours did not result in the degradation of the hollandite. In all cases $KRuO_4$ is present. This indicates that $KRuO_4$ is thermodynamically favorable phase under all conditions studied. Additionally, prior synthesis methods for $KRuO_4$ formation have reported that the compound can be easily

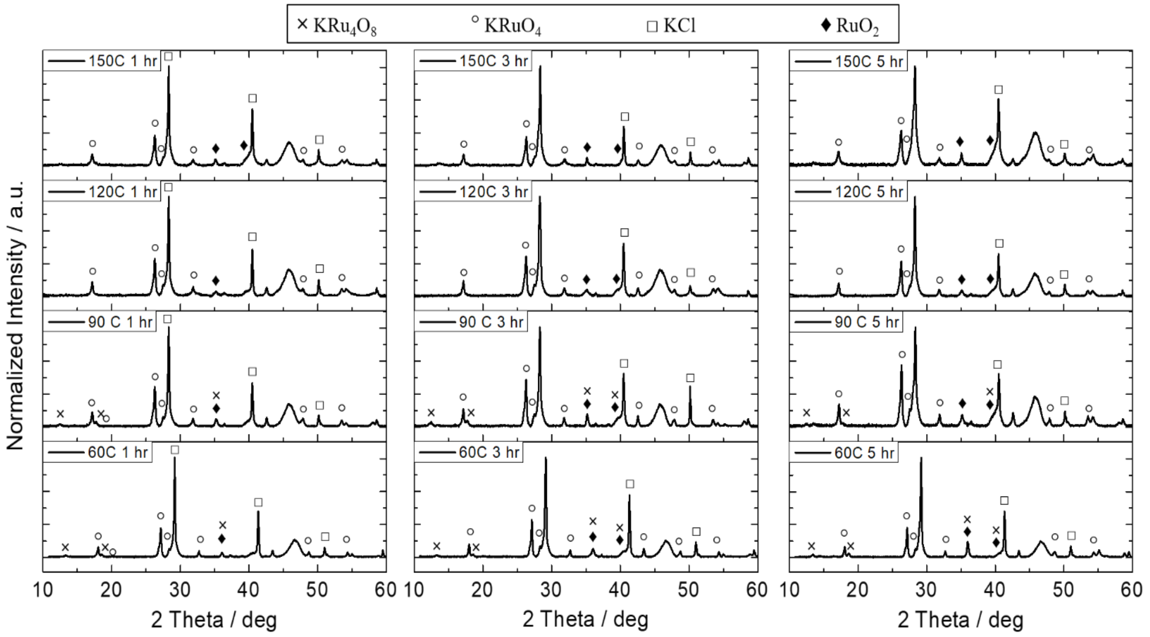

Figure 3.15. XRD patterns of (left) catalysts calcined for 1 hr, (middle) catalysts calcined for 3 hr, and (right) catalysts calcined for 5 hours. The temperature listed refers to the evaporation temperature during the wet impregnation synthesis.

prepared from $[Ru(OH)_2O_3]^{2-}$ in the presence of chlorine in basic solution (*248*). The Ru hydroxy complex can be easily formed from $RuCl_3$ dissolved in water (*249*, *250*) which would produce Cl^- anions, and the KCH_3COO precursor acts as the base in this specific synthesis method. In addition, KCl is easily formed, and is present both before and after the calcine procedure. Next, the activity of each of the catalysts was tested in 10% NH_3/Ar and 30,000 mL/hr/g_{cat} for their ammonia decomposition activity. The purpose of this measurement was to determine whether or not the formation of some Ru species and not others heavily influenced the reactivity. The catalysts were first reduced under 10% H_2/N_2 for one hour at 450°C and then allowed to cool to 250°C under inert before activity measurements. The results are shown in Figure 3. from 250°C to 400°C (left) followed by a contour plot showing the effect of both the calcine duration and the evaporation temperature on activity at 300°C. The legend uses the nomenclature where the first number indicates the evaporation temperature, and second number indicates the calcine duration.

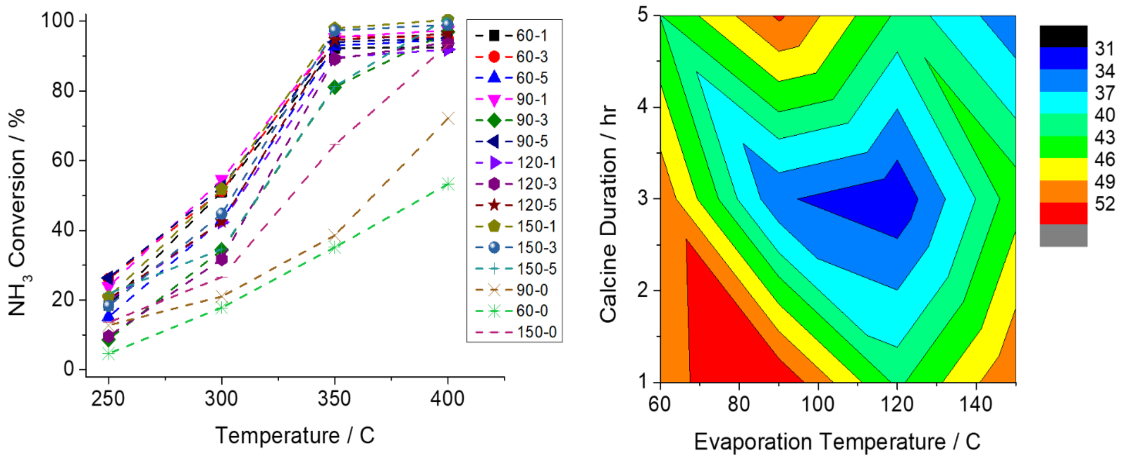

Figure 3.16. (Left) Activity of the 4,12 RuK catalysts synthesized using the wet impregnation technique where the evaporation temperature and calcine duration were varied. The legend indicates first the evaporation temperature of each catalysts (°C) followed by the calcine duration (hr). (Right) Contour plot showing the relationship between evaporation temperature, calcine duration and ammonia decomposition activity at 300°C. The legend indicates the NH_3 conversion (%) at 300°C. Reaction conditions: 10%NH_3/Ar, 30,000 mL/hr/g_{cat} and atmospheric pressure.

The contour plot showcasing activity at 300°C was chosen due to the largest variation in activity exhibited by the catalysts, and because we are interested in optimizing a catalyst for low temperature ammonia decomposition activity. Here we see that the highest activity was exhibited by the catalyst that was synthesized at 90°C and calcined at 1 and 5 hours.

Both catalysts contained a mixture of $KRuO_4$ and KRu_4O_8. The other catalyst containing KRu_4O_8 was synthesized at 60°C and was in the highest relative abundance at 1 and 3 hours, and the lowest abundance with a 5 hour calcine duration. The contour plot shows that the next highest activity catalysts were made at 60°C with calcine durations of 1 and 5 hours. Interestingly, there seems to be the poorest activity exhibited by the catalyst synthesized at 120°C and at 3 hours, which contained RuO_2 and $KRuO_4$ and further increases in the evaporation temperature above 90°C seemed to result in a catalyst with poorer activity regardless of the calcine duration. Additionally, the uncalcined catalysts

(Figure 3., 60-0, 90-0 and 150-0) were tested to determine if the calcine treatment was even necessary, and it does seem that calcining to produce the oxide phases of Ru is indeed and unsurprisingly necessary for high activity catalysts. Interestingly we do see that the catalyst evaporated at 150°C with 0 hr calcine time resulted in much higher activity than the other two catalyst with no calcine time. This may be due to the fact that the precursor Ru phases that will produce the RuO_2 and $KRuO_4$ phases are more easily reduced in the highly reducing atmosphere of NH_3 than the catalysts evaporated at 90°C and 120°C.

3.4 Influence of K Loading

While Pyrz et al. (*118*) discussed the effect of large loadings K on the morphological changes of the hollandite rods as well their implications to ammonia decomposition activity, there was little work involving the use of K loadings below 12%. Normally promoter loadings are in the range of ppm to levels to roughly 3% or 5% of the total weight of the catalyst. With higher loadings of promoter with respect to the active metal component, there is a risk of covering the surface of the active metal with the promoter, and thus lowering the activity by blocking the active sites. This has been exhibited in Cs promoted Ru decomposition catalysts where the Cs/Ru ratio was varied from 0 to 5, and the activity increased up until Cs/Ru = 2, and then further decreased with increasing Cs/Ru ratios (*235*). Therefore, the high loading of 12% K is relatively unique, as this a very high loading of promoter in relation to what is normally studied within the literature. Typically, promoters may be structural promoters, in that they increase the number of active sites present, or may be electronic promoters, in which the number of active sites stays relatively the same, but their intrinsic activity is increased. As mentioned in Chapter 3.2, K may act to promote the reaction may enhancing the basicity of the support in addition to electronically modifying the Ru active sites (as seen by the decrease in the apparent activation energy given in Figure 2.17).

Therefore, we did a systematic study of varying the K from 0.5% to 15% for a 1% Ru and a 4% Ru catalyst supported on γ-Al_2O_3. Figure 3.17 shows the ammonia decomposition activity of the 12 catalysts studied. The six different K loadings studied were 0.5%, 1%, 3%, 6%, 12% and 15 % each at either 1% Ru loading or 4% Ru loading. Two Ru loadings were chosen in order to see if the optimal K/Ru ratio varied based on the amount of Ru for the reasons mentioned earlier. Ultimately, we would expect to see that this ratio would be a function of the Ru loading, as the loading of Ru will affect the crystallite size and the dispersion of the metal. Thus, lower loadings of Ru may be more easily covered with higher loadings of K. The catalysts were run under 10%NH_3, with a space velocity of 30,000 mL/hr/g_{cat} and at atmospheric pressure from 250°C to 450°C. The filled symbols referred to the 4% Ru catalysts and the open symbols are the activity of the 1% Ru catalysts.

The catalysts containing 1% Ru generally were less active than the 4% Ru catalyst on an activity basis. Figure 3.18 shows the activity as a function of the K to Ru ratio for (a) catalysts containing 1% Ru and (b) catalysts containing 4% Ru. Interestingly we see that for both loadings of Ru, the most optimal loading of K is 12% as previously confirmed by Pyrz et al. (*118*). The most active catalyst was the 4,12 RuK catalyst composition, and the 1,12 RuK catalyst was the first most active catalyst. Interestingly, we find that the optimal K loading is independent on the Ru loading. This suggests that the modification of support with the K is highly beneficial to the ammonia decomposition reactivity. Pyrz et al. (*118*). determined that the next optimal K loading was 18% for a 4% Ru catalyst, while we found

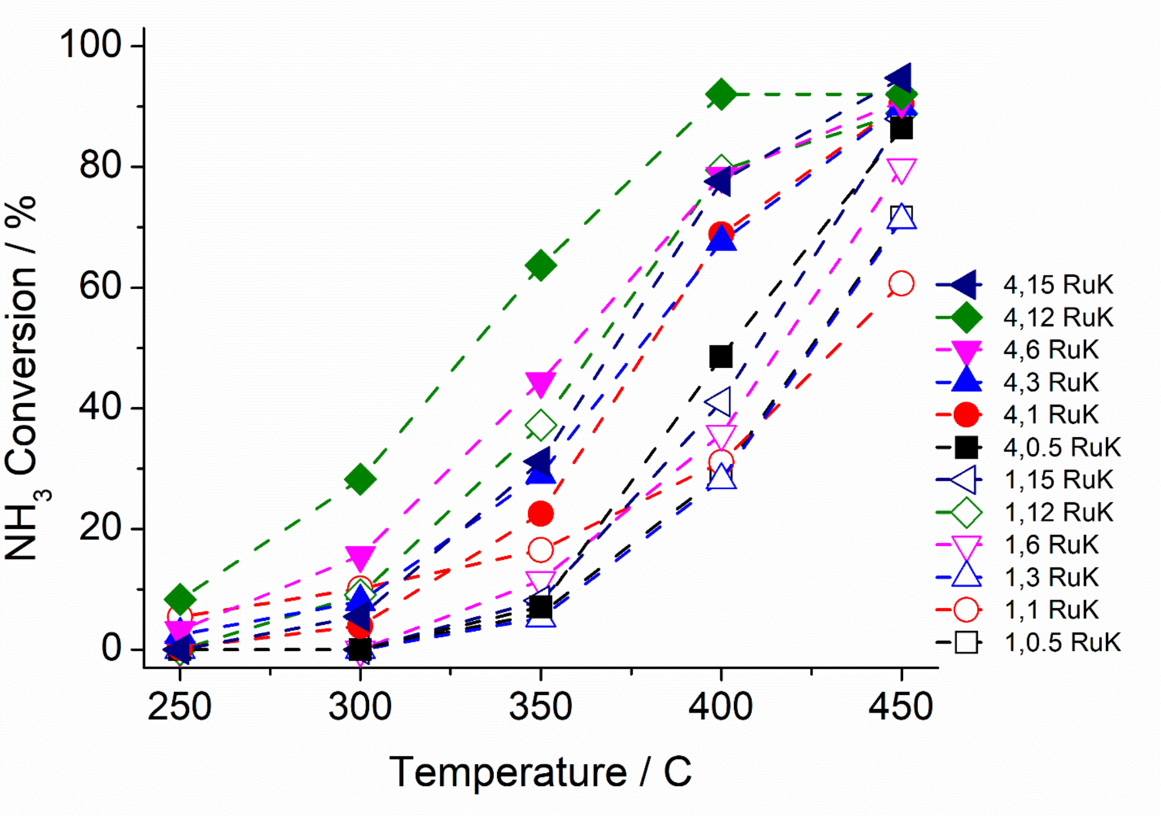

Figure 3.17. Ammonia decomposition activity of catalysts with various potassium loadings from 0.5% to 15 % in combination with either 1%Ru (1,X RuK) and 4% Ru (4,X RuK) supported on γ-Al_2O_3, where X = K loading. Reaction conditions: 10% NH_3/Ar, 30,000 mL/hr/g_{cat} and atmospheric pressure.

that 6% promotion resulted in higher activity than with 15% K. The larger loadings of K may act to block the Ru active sites or may cause bulk crystallization of K_2CO_3 or other K carbonate species as previously mentioned. If the hydroxyl groups located on the surface of the Al_2O_3 can participate in ion exchange with the K cations in solution, then by utilizing the same support, the same interaction and utilization of K will occur regardless of the Ru loading. This will help mitigate the blocking of active sites. Theoretically, the $[OH]^-$ concentration on γ-Al_2O_3 has been calculated to 11 OH/nm^2 (*229*, *230*) and the theoretical maximum K+ uptake has been calculated to be 13 K^+/nm^2 (*228*). The support used here had a measured BET surface area of 192 ± 8 m^2/g. Therefore, the theoretical maximum

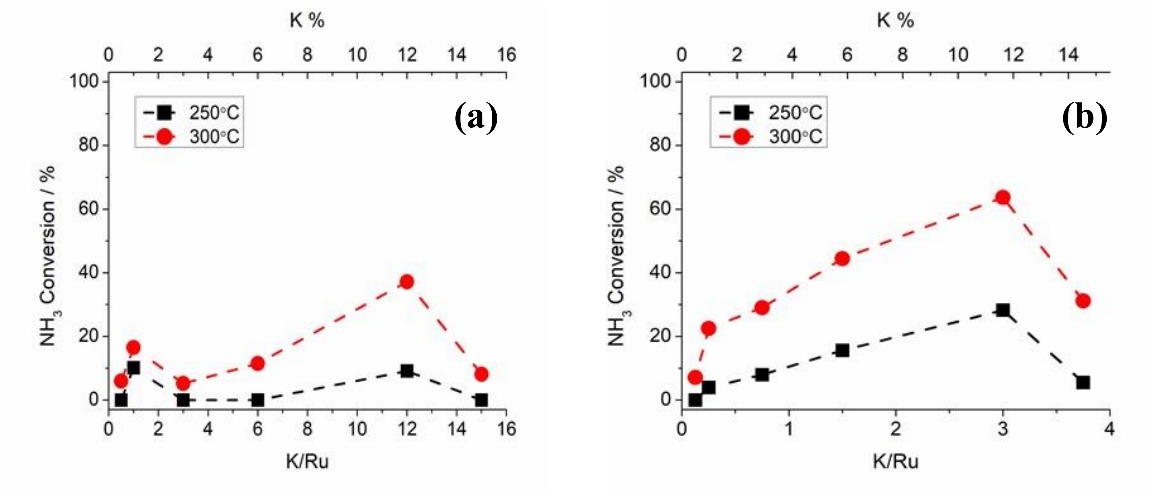

Figure 3.18. K/Ru ratio as a function of ammonia decomposition for catalysts containing (a) 1%Ru and (b) 4 % Ru supported on γ-Al_2O_3. Reaction conditions: 10% NH_3/Ar, 30,000 mL/hr/g_{cat} and atmospheric pressure.

uptake of K^+ during our synthesis is 3.56 mmol of K^+, which is roughly 58% of the total K^+ present in the synthesis. Because the K^+ can also readily interact with the Cl^- ions present from the Ru precursor, large agglomerations of crystalline K species are most likely not deposited onto the Al_2O_3 as seen with other K modified Al_2O_3 reports at higher K loadings. If all Cl^- ions were utilized in the form KCl, that would result in an additional 2.37 mmol of K utilized, which accounts of 39% of the total K ions in solution. Therefore, the amount of K cations that are present to deposit near Ru is not nearly as high as the actual loading of K, as the purpose of the promotional effect of K is multifaceted and encompasses may different aspects.

3.5 Working State of the Catalyst

While we have a better understanding under what conditions the hollandite structure will form, we want to understand the role of the structure during the ammonia decomposition reaction, and more importantly, what the working of the state of the catalyst looks like and what the active site is. In order to answer these questions, a 4,12 RuK catalyst

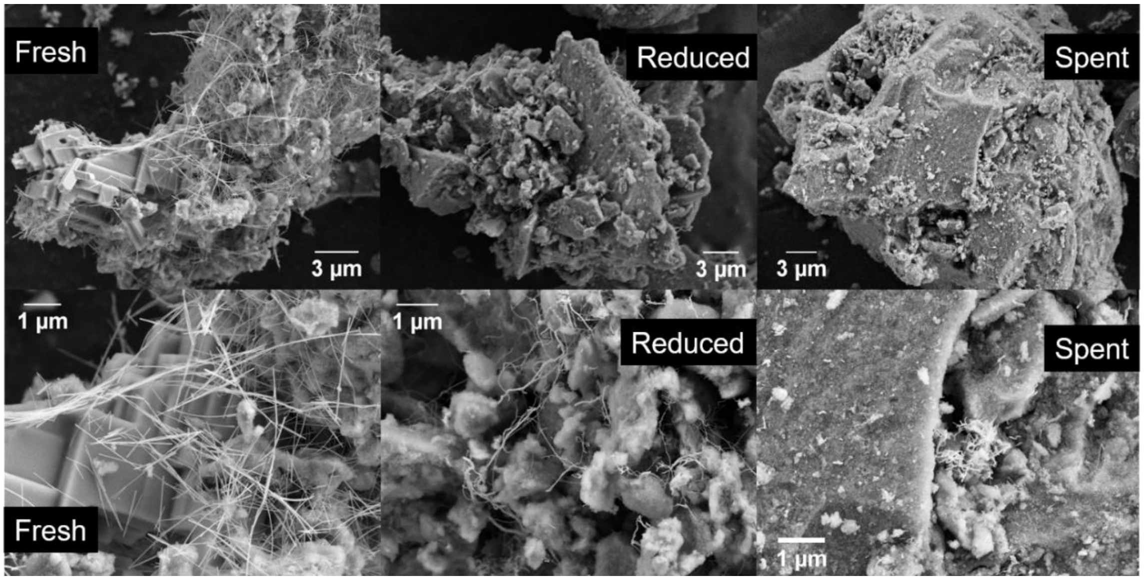

Figure 3.3. SEM images of 4,12 RuK catalysts (left) fresh, (middle) reduced and (right) spent at two different scales (top) 3 μm and (bottom) 1 μm.

was synthesized and then characterization was performed on the fresh catalyst, the catalyst have it has been reduced at 450°C in 10%H_2/Ar for 1 hr to understand the working state before exposure to ammonia, and after exposure to ammonia (spent). Figure 3.3 shows SEM images of the three different states of the catalyst: fresh, reduced and spent. In the fresh catalyst we see nanowhisker formation indicative of hollandite formation. The fresh image also shown highly crystalline block structure which have been identified as KCl from EDX mapping (not shown).

From the fresh to the reduced images, very small, fragmented nanowires are now present. At first glance, they are not present at the 3µm scale, but require much larger magnification to see. The wires are segmented and much more wormlike in nature. Additionally, in these reduced images we cotton ball like structures on the surface of the support. These have been separately identified to be apart of the support, as they are also present in SEM images of just the bare γ-Al_2O_3 without any modification. In order to determine the nature of these segmentations, elemental analysis was performed. The results of the mapping are shown in Figure 3. following the characteristic X-rays of Al, O, Cl, K and Ru. The segments are composed primarily of Ru, which exhibits the most intense signal from the mapping, and interestingly the segments are also covered in Cl. Additionally we see that after the H_2 reduction is K is littered all about the surface of the catalyst, which is to be expected as the K modifies the surface of the support as discussed previously. Lastly, we can determine from the mapping that the nanowire structure is not in an oxide phase, as the only O signal present is from that of the support.

This provides some information on the working state of the catalyst already. After the H_2 reduction, the well structure nanorods presumably decompose into Ru and Cl containing nano worms. After exposure to ammonia, the worm shapes further break apart into small segments and clusters as seen in Figure 3.3 spent. The corresponding TEM images for the fresh, reduced and spent nanorods are shown in Figure 3. where two different scales are shown. The TEM images further highlight the structuring the nanorods in each of the three cases. The fresh nanorods exhibit for well-defined and straight ordering, while dendritic like branching and clear segmentation is exhibited in the reduced nanorods.

Lastly the spent rods show much more agglomeration compared to the reduced rods, however the segmentation persists. This demonstrates that further that the segmentation is present after exposure to ammonia and the structural changes may be the reasoning for the enhanced activity of these structures. In order to determine differences in the three different states, the average diameter of the nanorod in each of the three cases was determined by measuring the multiple nanorods via TEM for each sample. Figure 3. shows the distribution of rod diameter for the fresh, reduced and spent catalysts, where an average of 100 rods were counted for each case. Each histogram is then fitted with a

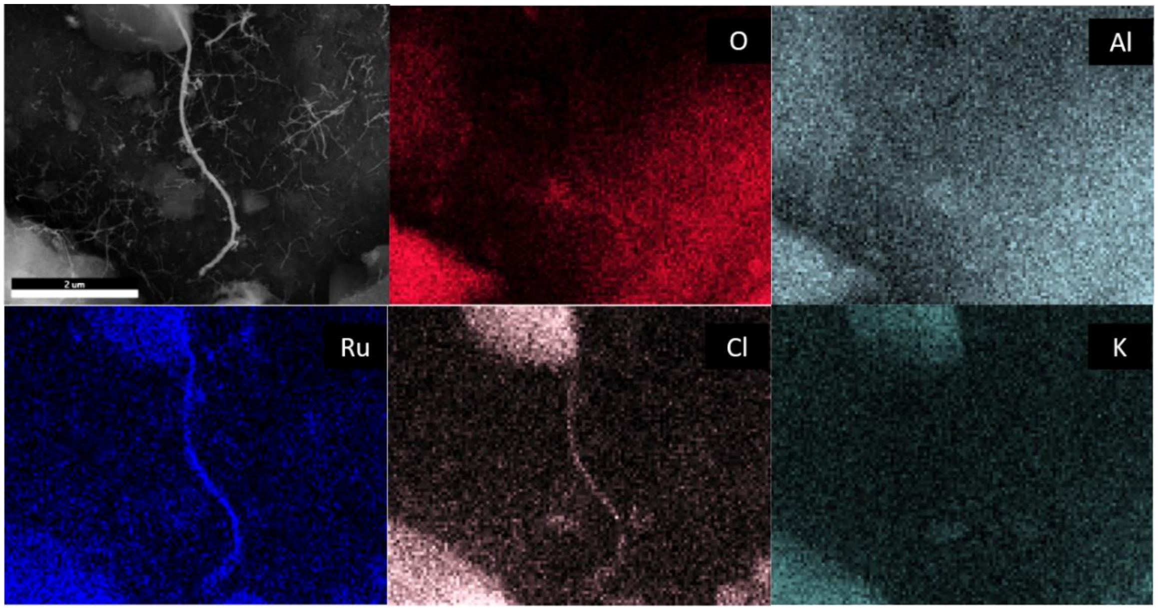

Figure 3.20. Elemental mapping of reduced 4,12 RuK catalyst.

Gaussian curve to visualize the distribution of diameters. The average diameter decreases from the fresh to the reduced case from 28.0nm to 23.7 nm, and then stays relatively the same after exposure to ammonia with a diameter of 24.0 nm. This reduction in diameter suggests that the initial hollandite nanorods decompose during the reduction to produce metallic Ru rods. This would occur via migration of K^+ out of the center of the tunnels. The diameter of the reduced state and that of the spent state suggests that the morphology of these segmented rods is highly stable during the reaction conditions since we do not see dramatic differences in the sizes. The elemental mapping in Figure 3. does indeed suggest that the surface of the Al_2O_3 is littered with K^+ after reduction.

Figure 3. shows the XRD patterns for the three catalysts. It is obvious to see that the hollandite whose major reflections are initially present at 12.47° (110) and 17.73° (200), are no longer visible in the reduced and spent patterns. The same goes the $KRuO_4$

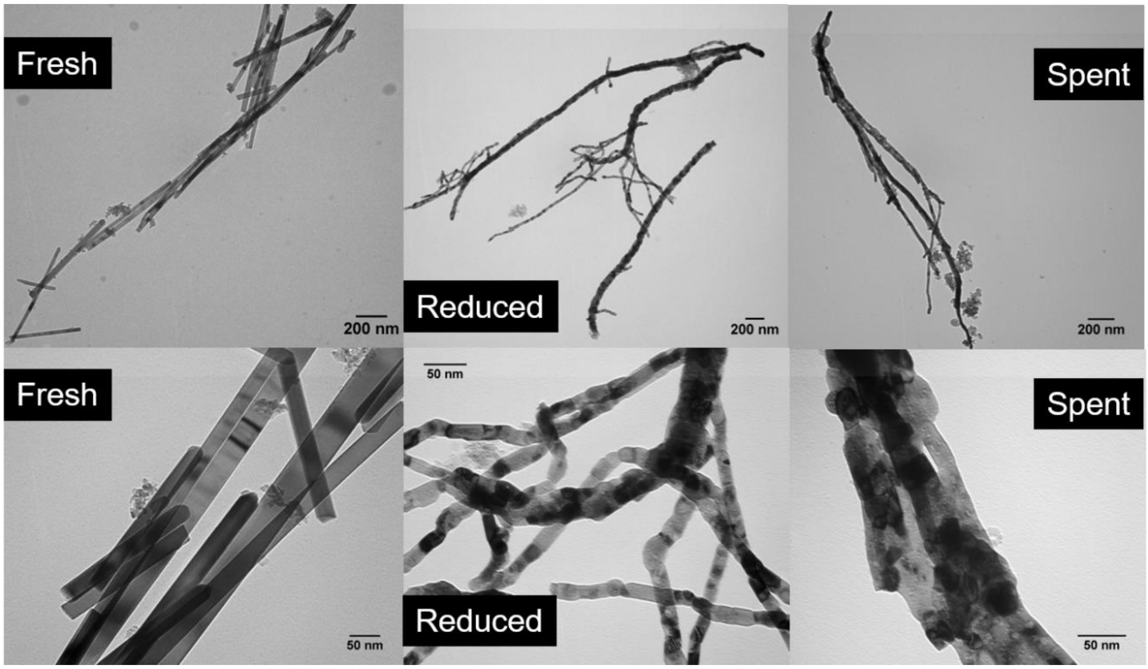

Figure 3.21. TEM images of 4,12 RuK catalysts (left) fresh, (middle) reduced and (right) spent at two different scales (top) 200 nm and (bottom) 50 nm.

reflections, which indicates that these structures are not the active sites during the ammonia decomposition reaction. After the catalysts are reduced, reflections belonging to highly crystalline KCl are still present, and reflections indicative of metallic. Ru appear at roughly 42.38° (002) and 44.07° (002). This indicates that both species reduce to metallic Ru during the reduction pretreatment and that metallic Ru is the active phase during the ammonia reaction. Additionally, the dendritic nanorods have been shown to be composed to Ru, and thus are most likely where the reaction occurs. Additionally, the crystallite size of the Ru (002) and Ru (101) facet for the reduced and spent patterns were calculated using Scherrer's equations. For the reduced catalyst, the Ru (002) facet was 16.2 nm, while that of the spent catalyst was 14.1 nm. The Ru (101) facet for the reduced catalyst was measured to be 15.1 nm, while that of the spent catalyst was 14.7 nm.

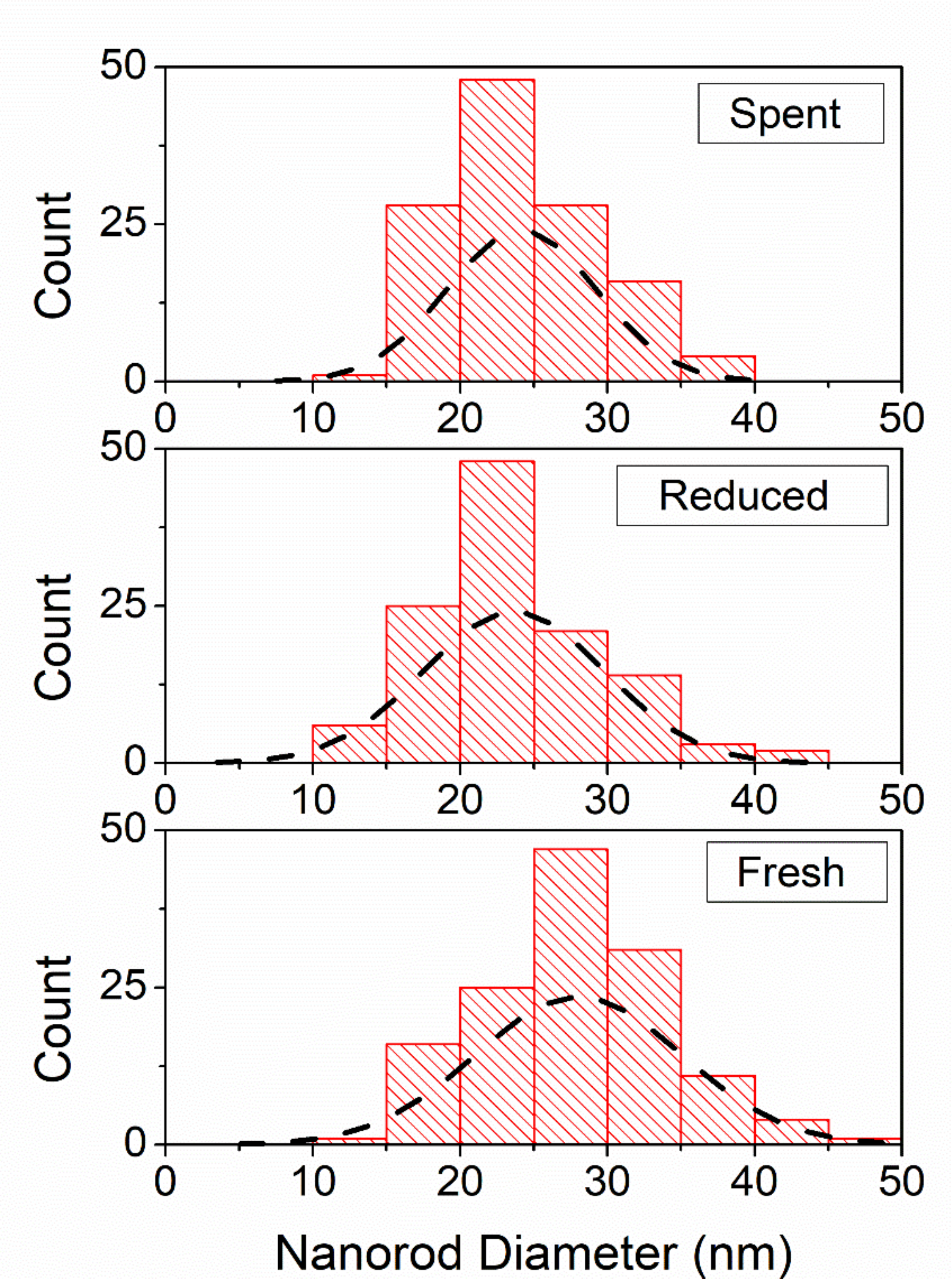

Figure 3.22. Nanorod diameter distribution for 4,12 RuK catalysts (bottom) fresh, (middle) reduced and (top) spent. Each distribution is fit with a Gaussian function.

The relatively similarity of the crystallites further suggests that these segmentations are stable during reaction, and that bulk restructuring of the Ru segments does not occur after the reaction was finished. Prior work in our group *(127)* has conducted further imaging on the spent Ru nanorods using dark fielding imaging and focusing the diffracted electrons from the Ru (002) and Ru (100) facets and have determined that the segmentations are composed of individual crystallite grains as shown in Figure 3.24. These segments are connected through grain boundaries, which were proposed to possibly contain a higher number of B_5 sites, which may enhance the rate of reaction.

3.6 Catalyst Reducibility

While we now have a better understanding of the working state of the catalyst during the reaction, we want to better understand the metal oxide redox properties of the catalyst. H_2-TPR is a technique that is useful in determining the correct reduction temperature for reaction pretreatments, to determine the mechanism of reduction of single metal catalysts, to understand the redox properties of reducible supports and the interactions between supports and active metals. Figure 3. shows the H_2-TPR profiles of 4% Ru/γ-Al_2O_3 (4 Ru, black trace) and of 4% Ru, 12%K/ γ-Al_2O_3 (4,12 RuK, red trace).

A H_2-TPR profile was also taken for bare γ-Al_2O_3, and no reduction peaks were exhibited (not shown). The 4 Ru catalyst exhibits three reduction events at 138°C, 165°C and at 194°C. The position of the reduction events can be influenced strongly by the particle size of the reducible metal oxide as well as the interaction between the support and the metal oxide. The low temperature peak at 138°C can be assigned to the reduction $RuCl_3$ (*251*) which indicates that the $RuCl_3$ is not completely removed at the calcine temperature

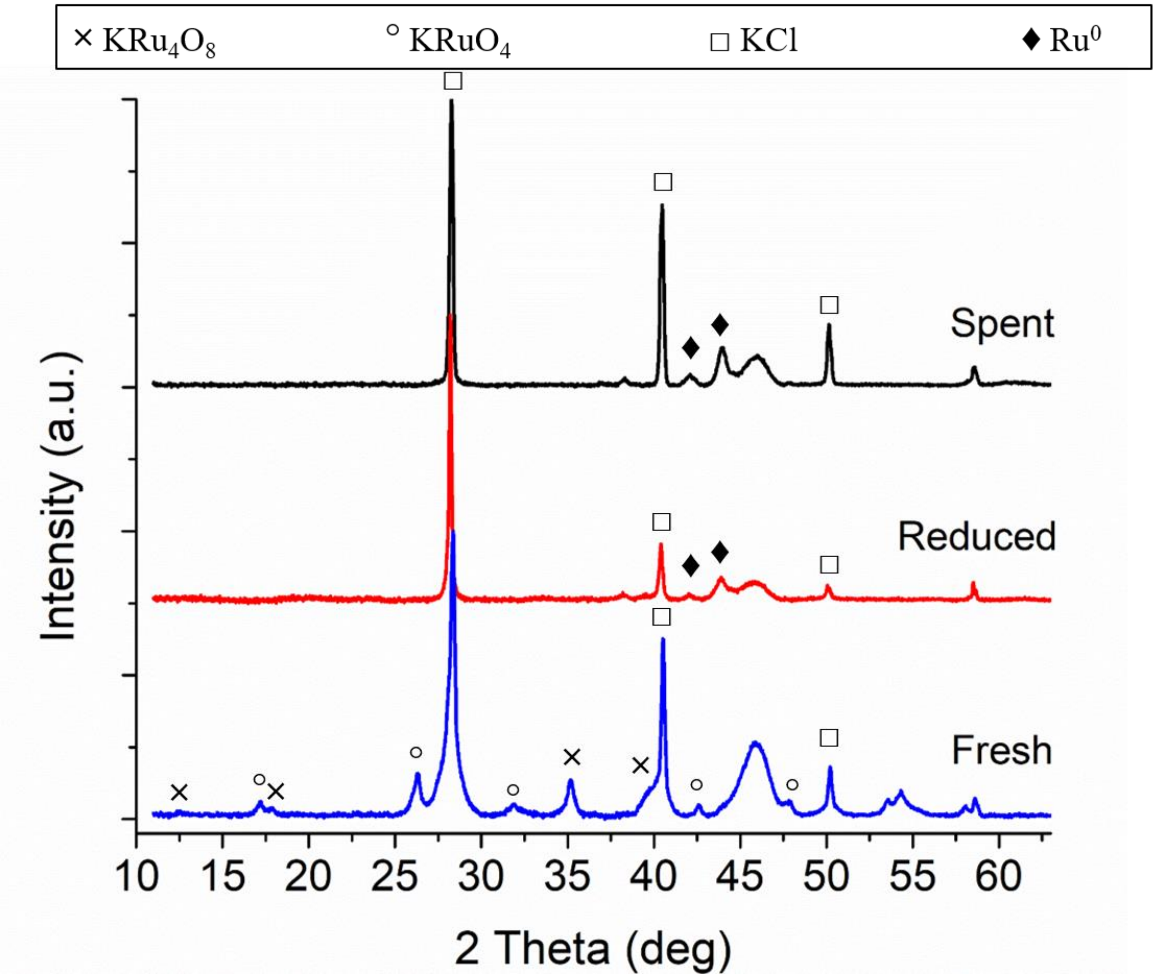

Figure 3.23. XRD patterns of 4,12 RuK catalysts (blue trace) fresh, (red trace) reduced and (black trace) spent.

of 550°C. The reduction of RuO_2 nanoparticles can be assigned to the high temperature peak at 194°C (*251*, *252*), where the reduction of RuO_2 has been reported between 450K and 470K. The intermediate reduction temperature peak at 165°C may be due to the reduction Ru oxychloride. Interestingly, another variable that can change not just the redox properties, but other chemical and physical properties of a catalyst is the use of chlorine salt precursors, and the residual Cl that is leftover on the catalyst surface after the calcine.

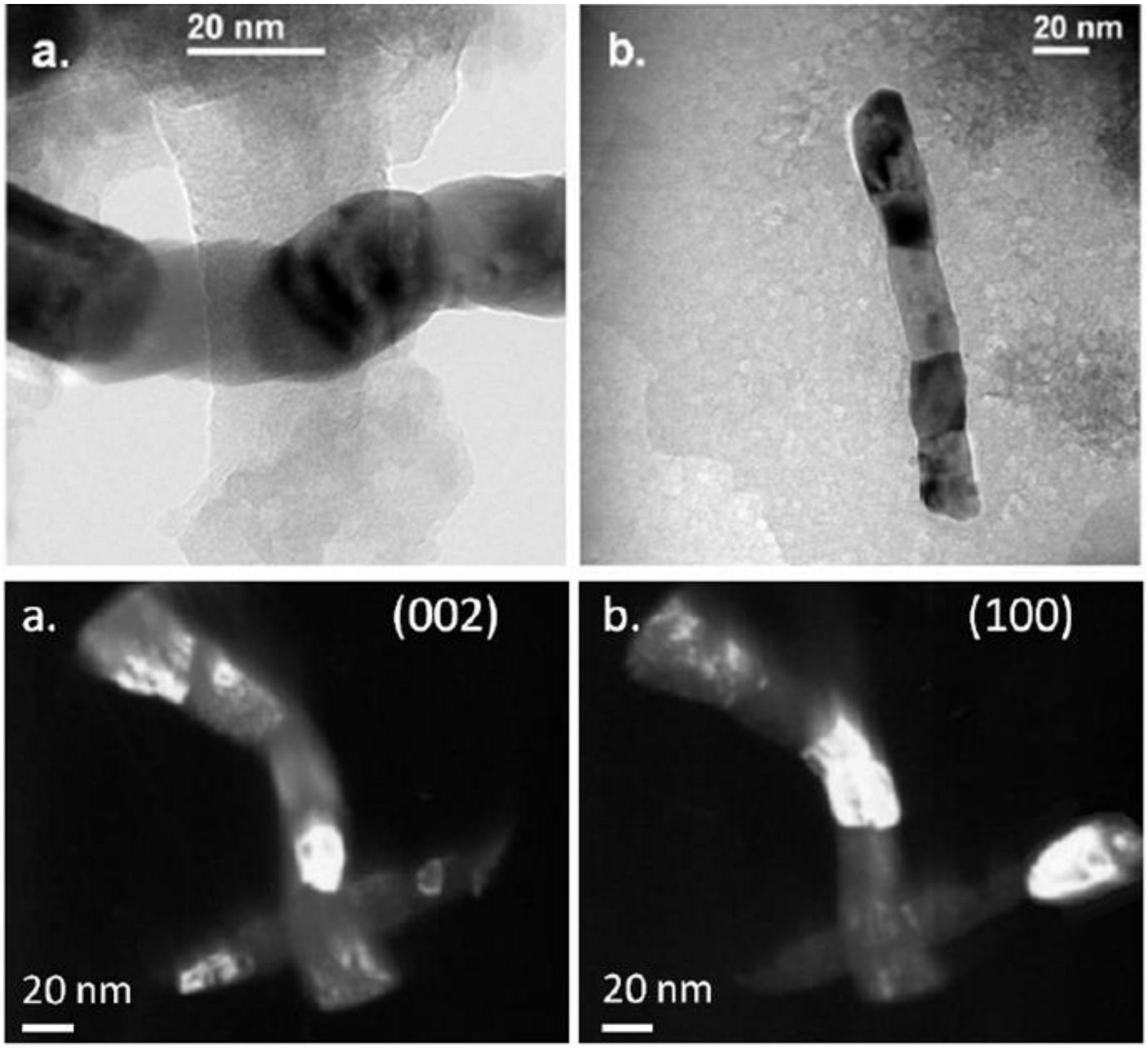

Figure 3.24. Top (a,b) TEM images of spent Ru nanorods and bottom (a,b) dark field imaging of the same area containing Ru nanowires. Aperture was placed over different bright spots to illuminate corresponding crystal grains. Adapted from ref *(127).*

Chlorine has been found to have both negative and positive aspects to catalytic activity depending on the reaction being studied (*125*, *253, 254*)

Chlorine has been found to increase the dispersion of the active metal particles, change the catalyst selectivity and activity and also can affect the rate of adsorption over different metal surfaces (*121*, *125*, *255*). As shown in Figure 3., the working state of the 4,12 RuK catalyst is covered completely with residual chlorine. With the addition of K, the

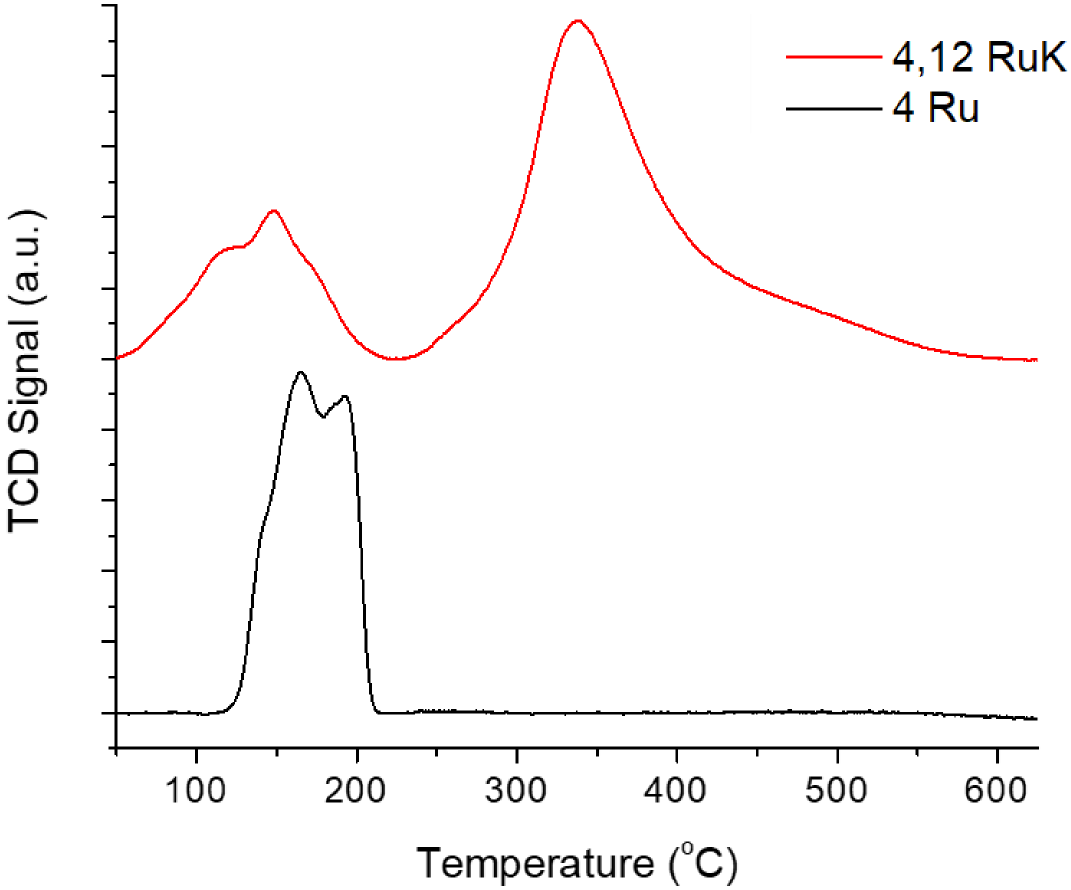

Figure 3.25. H_2-TPR profile of 4 Ru (black trace) and 4,12 RuK (red trace) supported on γ-Al_2O_3.

H_2-TPR profile becomes very different from that of the unpromoted 4 Ru catalyst. Two distinct regions appear in the 4,12 RuK profile. The first low temperature region consists of peaks located at 120°C, 144°C and 156°C. The second, high temperature region has a main reduction even occurring at ~345°C, with a peak shouldering the left side at ~287°C and a much broader shouldering on the right-hand side around 350°C and an even more broad and long reduction even at ~397°C. These high temperature reduction peaks are not indicative or RuO_2 reduction or from surface or bulk reduction of hydroxyl groups from Al_2O_3. Indeed, the profile is further complicated by the fact the catalyst contains multiple mixed metal oxides. The reduction of $KRuO_4$ and KRu_4O_8 have not previously been reported. In typical cases, the addition of a promoter does not change the structural arrangement of the metal oxide. Here, from the XRD analysis, we can clearly see that $KRuO_4$ and KRu_4O_8 hollandite are two of the primary reductive metal oxides present in the 4,12 RuK catalyst. Additionally, very small RuO_2 particles may be present that are either convoluted within other XRD reflections or are too small to be visible using XRD.

The addition of promoters to a catalyst has the capability of changing the reducibility of the active metal when they are in close proximity to one another. Similar to strong metal support interactions, where the charge state of the metal is altered by interactions with the support, the charge state of the metal can also be altered by a promoter. This is typically one reason why promoters are highly electropositive or electronegative. Therefore, we expect to see major differences in the TPR profile with such high loading of K present in the catalyst. With the extreme broadening exhibited, it is highly probable that there are multiple reduction events occurring within one or both of the low and high temperature reduction areas. Some studies have shown that low loadings of K may not affect the reducibility of metals below 2% (*256*), but that higher loadings of K indeed completely change the TPR events and add to the complexity of the profile. External H_2-TPR measurements of $KRuO_4$ purchased from Sigma-Aldrich were taken, and multiple reduction events between 50°C and 150°C were seen (not shown). The TPR profile for $KRuO_4$ exhibited multiple peak maxima at 77°C, 124°C, 145°C and 167°C. In addition, we see with the 4Ru sample that the reduction of RuO2 also occurs within this temperature range. The identification of the high temperature reduction events was not straightforward.

The TPR profiles of K-Mn based hollandite show that the reduction of K-Mn hollandites occurs via the reduction of MnO_6 octahedrons to Mn_3O_4, Mn_2O_3 and finally to MnO_2 (*220*). However, the Ru_3O_4 and Ru_2O_3 oxidation state are extremely uncommon (*248*, *257*) and therefore it is unlikely the reduction of K-Ru hollandite occurs through a similar mechanism. However, it is possible that Ru based hollandite reduces by transitioning through multiple oxidation states. From the H_2-TPR the hollandite reduction event may occur at the high temperature reduction event between 287°C and 397°C, however further experimentation is needed in order to determine this. To begin, the H_2-TPR profile of $12K/Al_2O_3$ should be probed in order to determine if the carbonates from the $KAl(CO_3)OH_2$ compound are responsible for the high temperature reduction peaks.

In order to gain insight into the reduction mechanism of the catalyst, *in-situ* XRD was performed to follow the reduction of the hollandite KRu_4O_8 and $KRuO_4$ complexes by monitoring the major phases of both complexes as a function of time. The measurements were taken while flowing a stream of $5\%H_2/Ar$ over the catalyst bed. The temperature of the catalyst bed was increased in 25°C increments from room temperature to 450°C, and the temperature was held constant while each measurement was being performed. Next, the catalyst was allowed to dwell for 30 minutes at 450°C, where another measurement was taken. Finally. the catalyst was allowed to cool under inert back to room temperature where a final scan was taken. The XRD patterns are shown in Figure 3.. The XRD measurements were taken at a scan rate of 2°/min from 10° to 60°. Additionally, each pattern contains a major reflection of α-Al_2O_3 at 25.8° which is from the corundum sample holder.

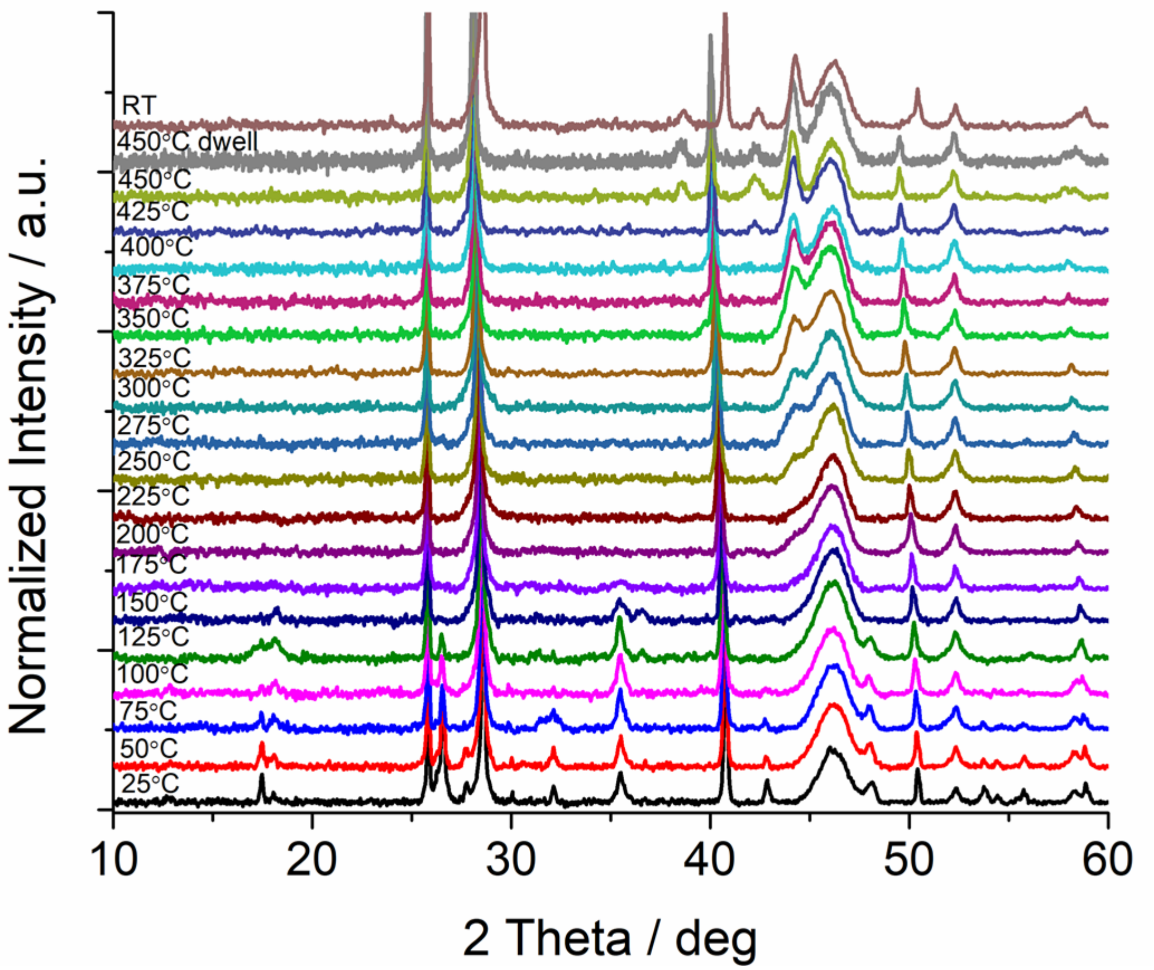

Figure 3.26. *in-situ* XRD patterns for 4,12 RuK during H_2 reduction in 5%H_2/Ar from 25°C to 450°C. After the last measurement at 450°C, the temperature was held for 30 minutes and a second measurement was taken. The catalyst was then allowed to cool to room temperature under inert and the final measurement was taken (RT).

The major reflections for $KRuO_4$ are present at 17.2°, 26.38° and 31.8°, while KRu_4O_8 reflections are present at 17.8°, 31.15° and 46.1°. The major reflections at the smaller 2 Theta values are overshadowed by the highly crystalline KCl, and therefore are shown more clearly in Figure 3.27. Additionally, we can see here that the reduction of these two Ru compounds occurs at relatively low temperature. We see a decrease in the relative intensity of these major reflections, which then completely disappear by 175°C. The disappearance of these peaks is also accompanied by the formation of a new reflection located at roughly 44.4°, which can be clearly seen in Figure 3.27. This reflection can be

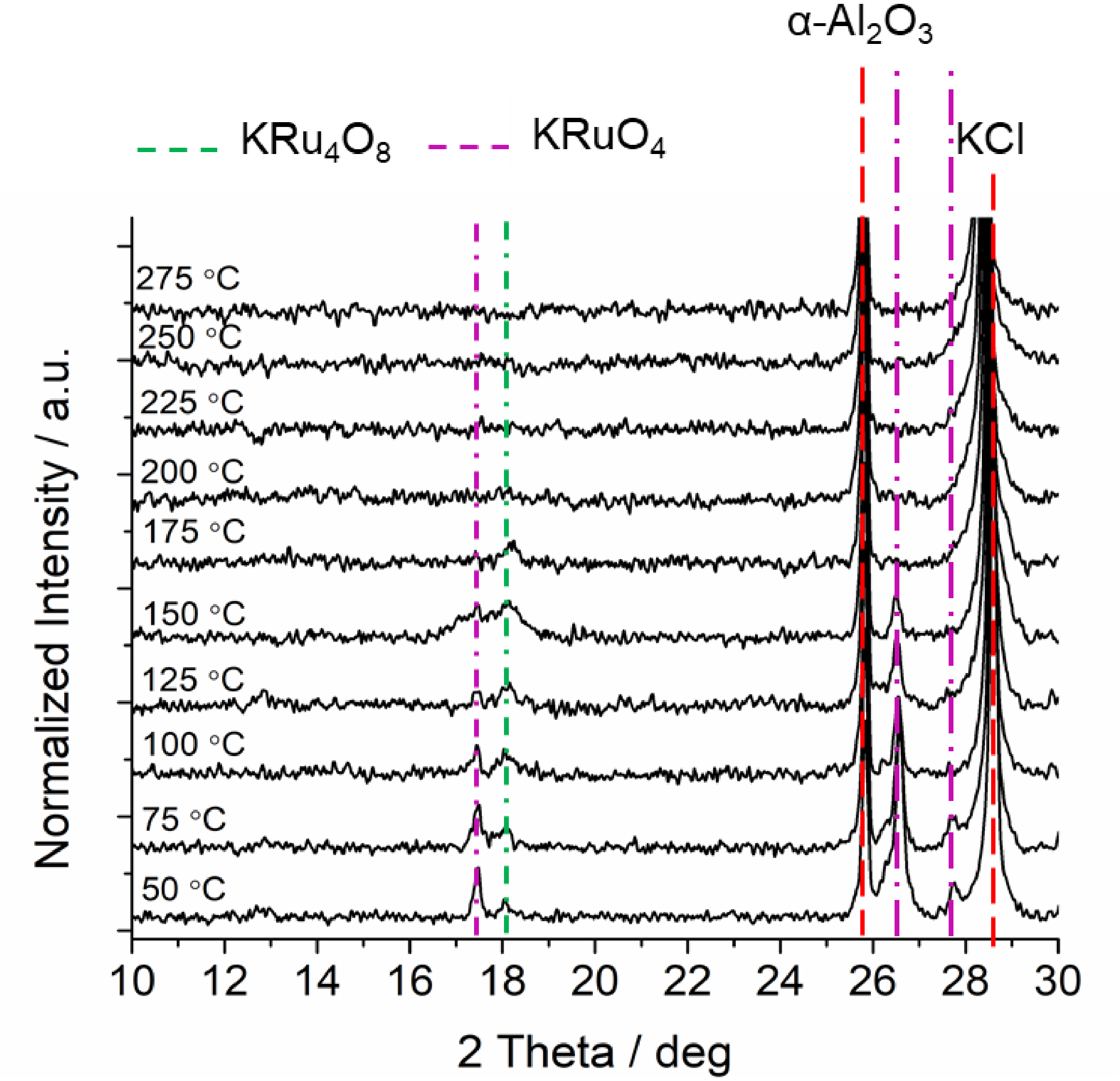

Figure 3.27. *in-situ* XRD patterns for 4,12 RuK during H_2 reduction in 5%H_2/Ar from 25°C to 275°C highlighting the major reflections of $KRuO_4$ and KRu_4O_8 and their disappearance from 10°- 30°.

attributed to the metallic Ru (101) crystallite facet, and begins to appear at roughly 175°C. This peak continues to grow in intensity all the way up to 450°C, where it then remains relatively constant after holding the catalyst bed temperature at 450°C for 30 minutes. In order to quantify the changes in the Ru crystallites as a function of temperature, the FWHM was fit for the Ru (101) facet from 175°C to 450°C and the crystallite size was calculated using Scherrer's equation.

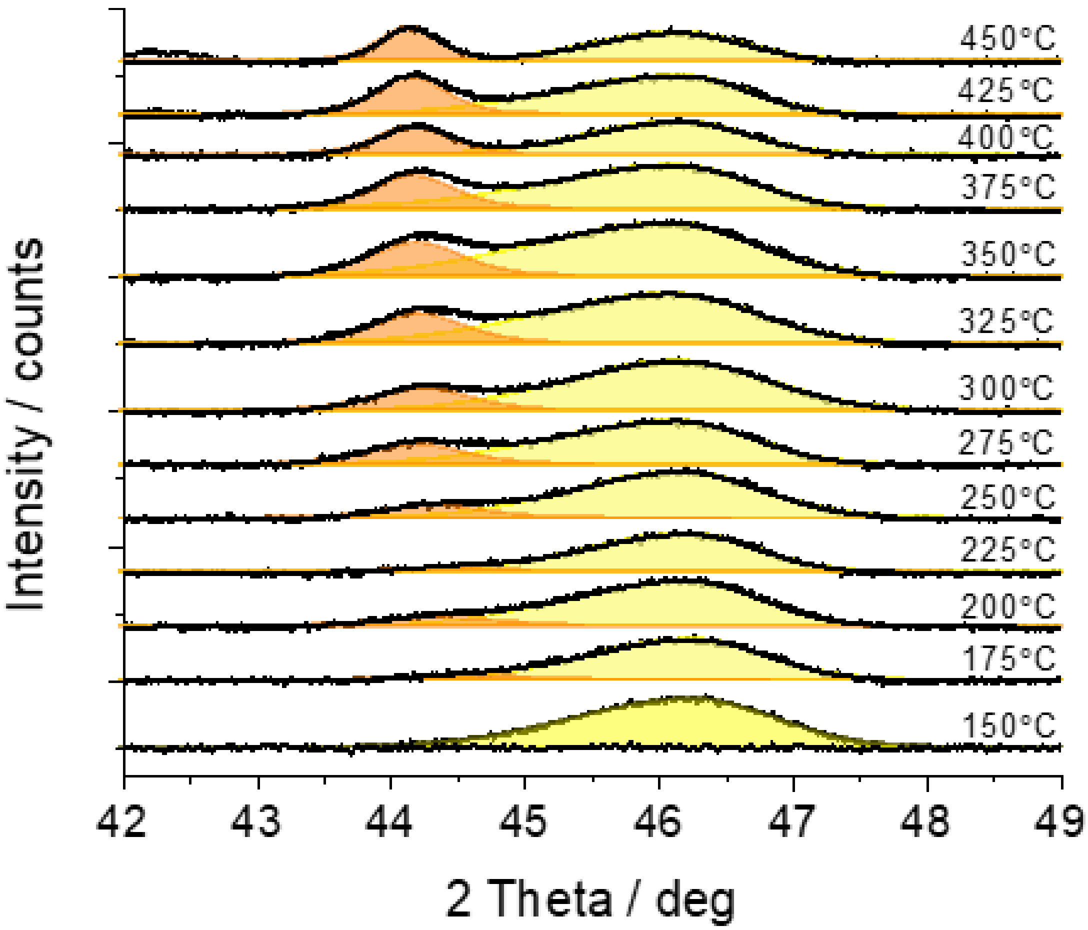

Figure 3.28. *in-situ* XRD patterns from 41° to 49° of 4,12 RuK under 5%H_2/He, showing the growth of the Ru^0 reflection as a function of temperature from 150°C to 450°C.

Interestingly, we also see that the FWHM of the metallic Ru reflection changes with increasing temperature. This suggests a change in the crystallite size. In order to determine this, profile fitting was conducted in order to fit the FWHM of the metallic Ru reflection, which was then used to calculate the average crystallite size using Scherrer's equation. Because of the peak convolution between γ-Al_2O_3 and metallic Ru, the γ-Al_2O_3 was also fit in order to properly determine the peak function for the metallic Ru. The alumina peak was first fit in a pattern where no metallic Ru was present, using a Split Pseudo Voigt function. An example of the fitting for the alumina peak is given in Figure 3.28, where the

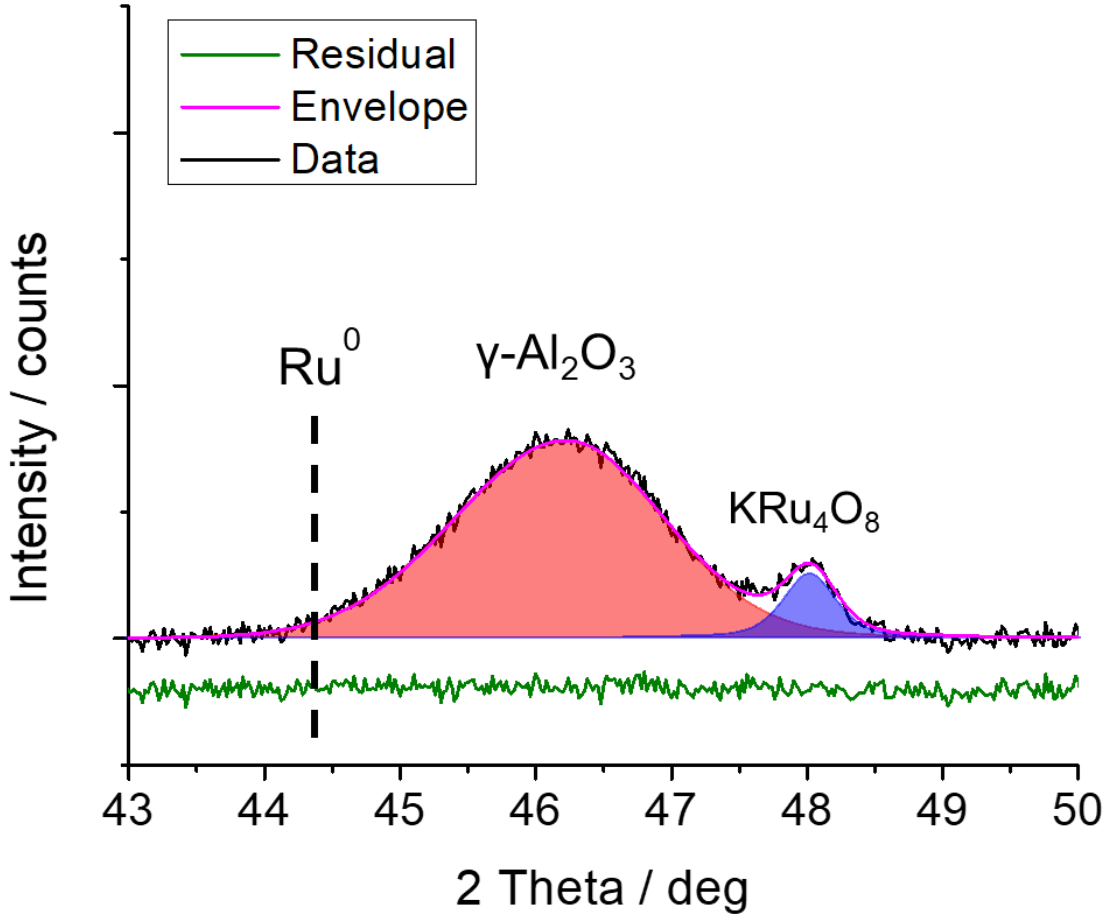

Figure 3.29. *in-situ* XRD pattern from 43° to 50° at 50°C, highlighting the fitting of the γ-Al_2O_3 peak before the appearance of the Ru (101) facet along with the residual of the fit. Profile fitting of the γ-Al_2O_3 peak was performed using a Split Voigt function.

position of the Ru (101) facet is indicated on the left-hand side of the alumina peak. Shape factor 1 was set constant to 0.0216 and shape factor 2 was set constant to 0.077 for each fitting of the alumina peak at each temperature in order to ensure accurate fitting of the Ru (101) facet. Next the Gaussian contribution was fit for both sides of the alumina peak at each temperature from 175°C to 450°C. Afterwards, the metallic Ru peak was fit using a Pseudo Voigt function. The residual is shown in order to represent the error in the fitting, which was roughly 1 nm. The fitting for both the alumina and the metallic Ru peak from 175°C to 450°C can be seen in Figure 3.29, where the light-yellow area corresponds to the alumina, and the orange area corresponds to the metallic Ru. Here we see in increase in the

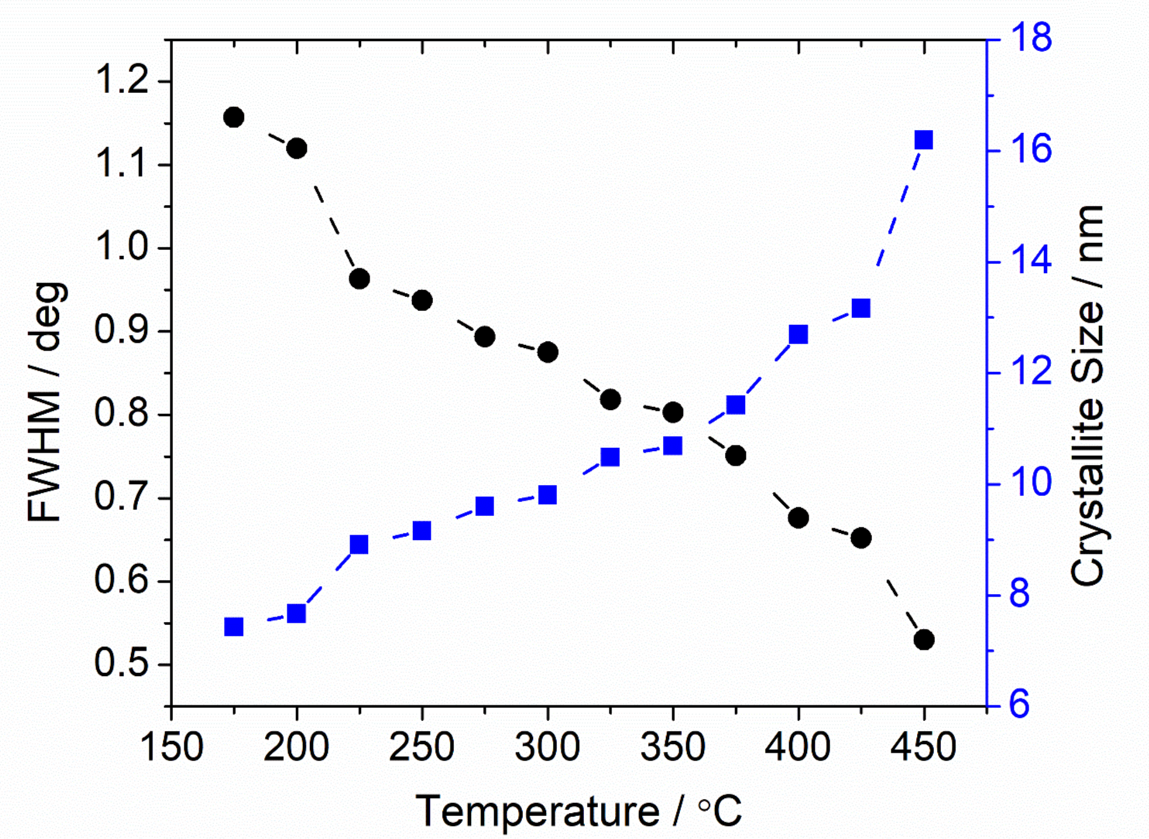

Figure 3.30. Full Width Half Max (FWHM) and crystallite size (nm) of the Ru (101) as a function of reduction temperature. Reduced under 5%H_2/He.

FWHM as a function of temperature, indicating crystal growth is a function of the reduction temperature. The calculated crystal size and the FWHM for the metallic Ru (101) reflection from 175°C to 450°C is given in Figure 3. as a function the reduction temperature. The crystallite size increases from 7.4 nm at 175°C to 16.8 nm at 450°C. After holding for 30 minutes at 450°C, the crystal size did not change much from 16.8 nm. After cooling to room temperature, the crystallite size decreased to roughly 15 nm.

Lastly, this experiment shows us that the large reduction even that occurs in the 4,12 RuK H_2-TPR profile from roughly 250°C – 500°C is not due to the reduction of a metal oxide. We have shown through *in-situ* XRD that the Ru metal oxides all reduce below 150°C, and thus the complex reduction peak in the H_2-TPR from 75°C to 220°C is from the reduction of $KRuO_4$ and KRu_4O_8. Additionally, we were able to ascertain that the particle size of the resultant active site can be controlled through the reduction temperature of the catalyst. However further understanding of what is occurring between the temperature ranges of 125°C to 175°C, and from above 250°C needs to be further elucidated. To begin with this, we performed *ex-situ* SEM imaging of the reduced 4,12 RuK catalyst at three different reduction temperatures, 250°C, 350°C and 450°C, each of which was subjected to a reduction in 10%H_2/Ar. The images for the three reduction temperatures are shown in Figure 3.31. At a reduction temperature of 250°C, the support shows a sparce and homogenous covering of short nanorods. As the reduction temperature increases to 350°C, these short rods begin to agglomerate and form more a more dendritic covering over the support particle.

Additionally, we see that the thickness of the rods has further increased. At the last temperature studied 450°C, the rods further agglomerate into more stalky and shorter nanorods. These images indicate that there are dramatic morphological differences in the active component of the catalyst as the reduction temperature changes. Even though the Ru mixed metal oxides are completely reduced by 250°C, the morphology of the metallic Ru species continues to change. In order to determine the consequence of these morphological changes, the activity of the 4,12 RuK catalyst at each of these reduction temperatures were determined. Figure 3.32 shows the ammonia decomposition activity of the catalyst reduced at 250°C, 350°C and 450°C. The catalysts were subjected to a flow of 100% NH_3 and a space velocity of 16,200 mL/hr/g_{cat} at atmospheric pressure. Interestingly, we see that the catalyst reduced at 250°C and at 350°C both exhibited very similar activities, while both having vary different crystallite sizes and morphologies, as indicated by the *in-situ* XRD

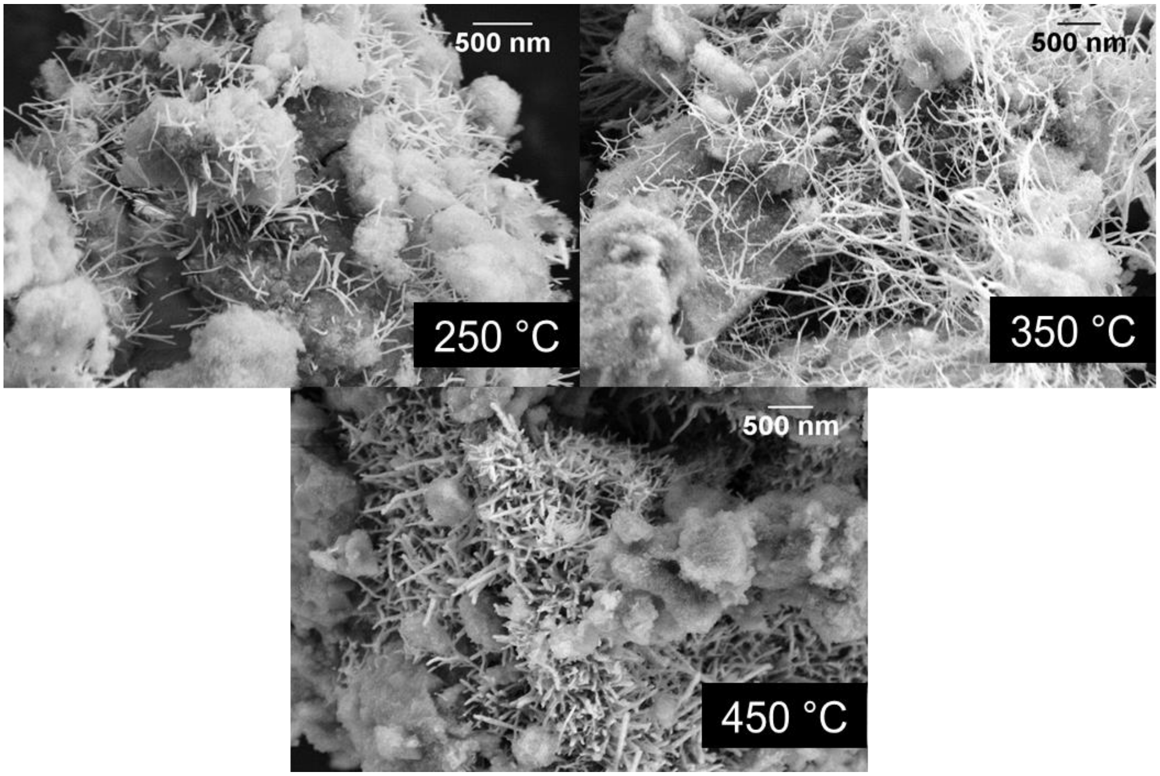

Figure 3.31. SEM images of the 4,12 RuK catalyst reduced *ex-situ* in 10% H_2/Ar at three different temperatures: 250°C, 350°C and 450°C.

measurements and *ex-situ* SEM images. At a reduction temperature of 450°C, the activity of the catalyst dramatically increases at all temperatures, while also exhibiting the largest crystallite size. Since the metal loading of the catalyst does not change for each of these activity measurements, the differences in activity must be due to more active sites being present after being reduced at 450°C. Additionally, in most particle size studies, the Ru particle size or crystallite size of interest is not studied above roughly 7 nm, while here we look at crystallite sizes between 9 and 17 nm. Further investigation into the working state of the catalyst at these three reduction temperatures should be done in order to determine how the nanorod diameter distribution changes, as well as H_2 chemisorption in order to determine the number of active sites present to determine the TOF.

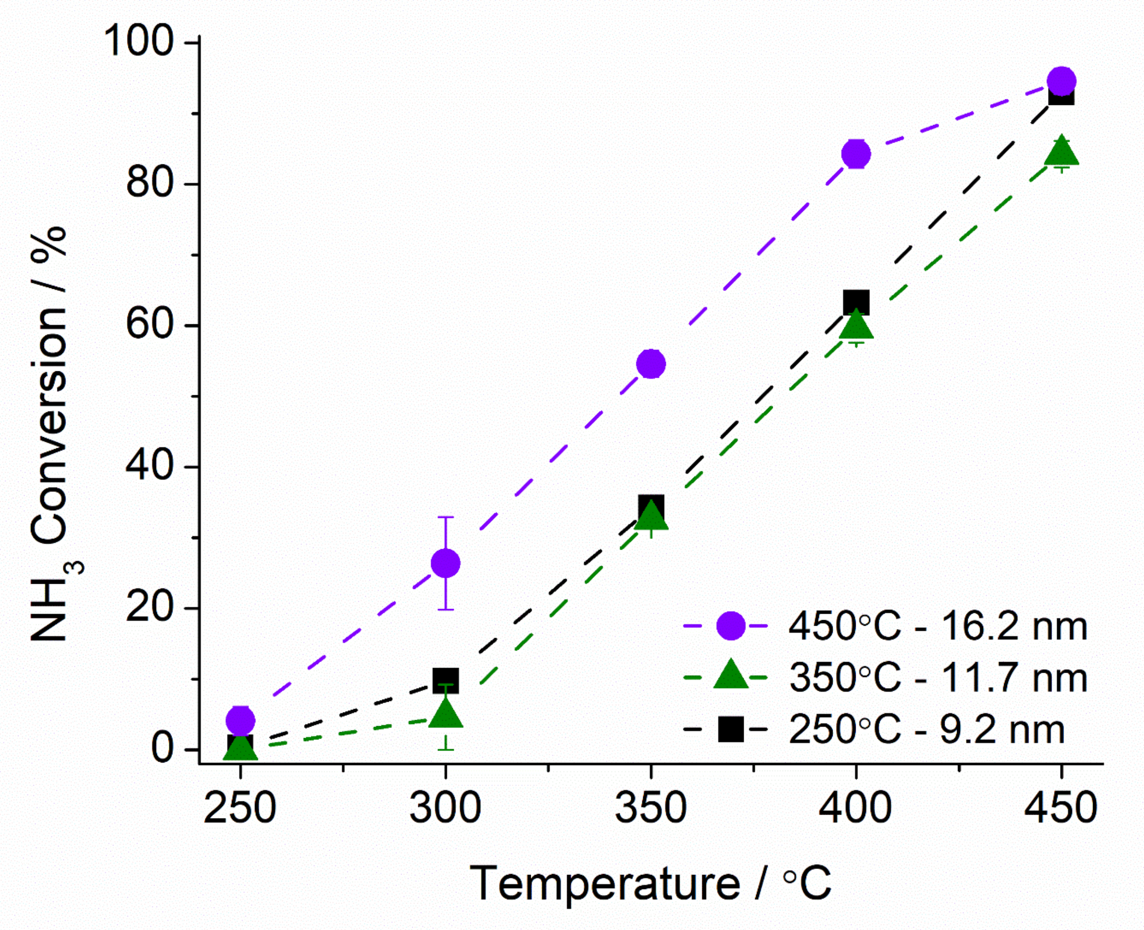

Figure 3.32. Ammonia decomposition activity of the 4,12 RuK catalyst reduced at three different temperatures: 250°C, 350°C and 450°C. The legend indicates the reduction temperature in 10%H_2/Ar, followed by the calculated Ru (101) crystallite size from the *in-situ* XRD measurements. Reaction Conditions: 100%NH_3, 16,200 mL/hr/g_{cat} and atmospheric pressure.

3.7 Activity Comparison of Mixed Metal Ru Oxide Catalyst to Highly Dispersed Ru Nanoparticles Synthesized via SEA

In order to make comparisons of our mixed metal oxide Ru based catalysts to the more idealized size and shape of Ru particles reported in the literature (1.8nm – 2.5nm), K promoted Ru catalysts were synthesized via SEA in collaboration with the Regalbuto group. The catalysts were synthesized using the same γ-Al_2O_3 support as those made through wet and dry impregnation methods. The SEA method allows us to control the particle size more efficiently, and thus in theory increase the number of edge sites present on the Ru particles, and in turn the number of highly active B_5 ensembles present, as discussed in Chapter 1. The SEA catalyst was synthesized with the same nominal loading as the catalyst synthesized via incipient wetness impregnation (4%Ru and 12%K) so direct comparisons could be made in activity based on the morphology and particle size.

Figure 3.33 shows the XRD patterns for 4,12 RuK SEA catalyst after synthesis, and after exposure to ammonia. In the fresh pattern (black trace), reflections corresponding to Ru metal are not present, which indicate that the Ru is highly dispersed in the catalyst and have a particle size that is below the limit of detection through XRD (< 3nm). Additionally, the spent pattern does not shown signs of Ru reflections, which indicates that sintering did not occur of the Ru particles after exposure to ammonia and to high temperatures. Next, the activity of the SEA synthesized catalyst was tested and compared to that of the incipient wetness impregnation catalyst (IWI) under identical operating conditions. Figure 3.34 shows both the activity of both catalysts as a function of temperature, as well as the long-term stability of both catalysts at 450°C. The catalysts were tested in 100% NH_3, at a space velocity of 5,400 mL/hr/g_{cat} and at atmospheric pressure. Interestingly, we found that under these conditions, both catalysts exhibited very similar reactivity, and were found to be stable for 10 hours at 450°C. At 450°C, the IWI catalyst exhibited slightly higher activity than the SEA catalyst of 94.2% conversion, while the SEA catalyst exhibited 93.8% conversion. These values are roughly within error of each other. In order to try to ascertain differences in activity between the two catalysts, the space velocity of the reaction was tripled from 5,400 mL/hr/g_{cat} to 16,200 mL/hr/g_{cat}. Due

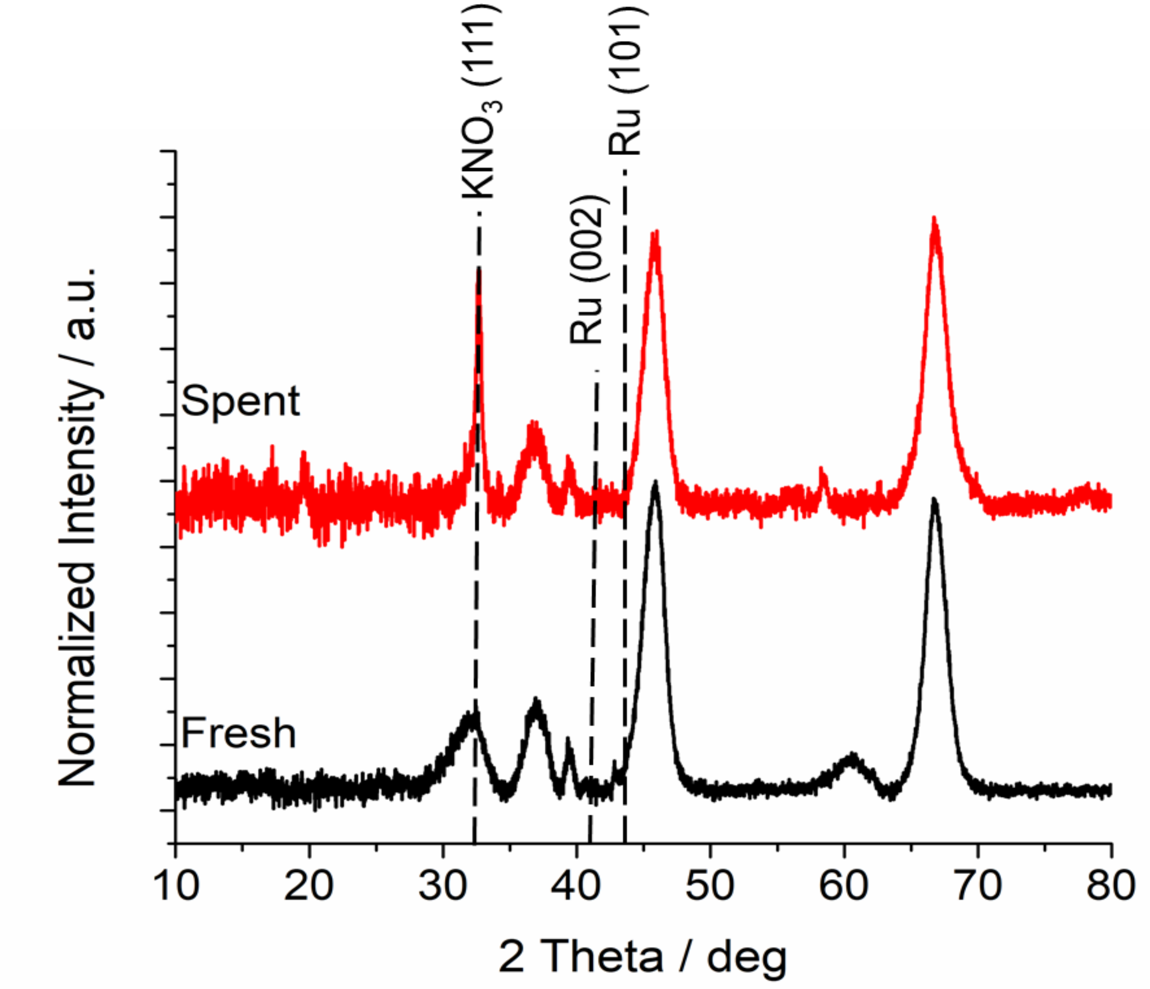

Figure 3.33. XRD patterns of (black trace) fresh and (red trace) spent 4,12 RuK catalyst after exposure to ammonia. Catalyst was synthesized via SEA method.

to the high reactivity of both catalysts, it may have been necessary to dramatically increase the space velocity to determine differences in the two catalysts.

Figure 3.35 shows the activity of the SEA and IWI catalysts with the higher space velocity, and in 100% NH_3 at atmospheric pressure. Here we see that with the increase in space velocity, there are dramatic differences in activity for the two catalysts. The SEA catalyst shows a dramatic decline in activity compared to the IWI catalyst. The IWI catalyst shows slightly lower activity at lower temperatures, but still maintains 94% conversion at 450°C. For the SEA catalyst, the activity at 450°C drops to roughly 80%. This shows that

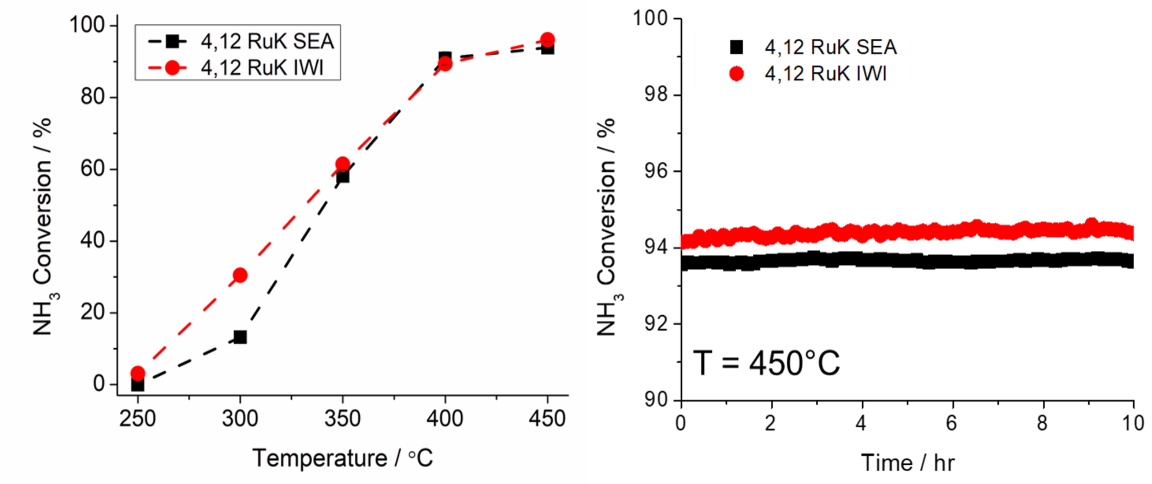

Figure 3.34. (left) Activity of the 4,12 RuK SEA (black squares) compared to the 4,12 RuK catalyst synthesized via incipient wetness impregnation (IWI) (red circles). Reaction conditions: 100%NH_3, 5,400 mL/hr/g_{cat} at atmospheric pressure and (right) long term stability of the 4,12 RuK SEA (black squares) and of the 4,12 RuK IWI (red circles) at 450°C over 10 hours.

our mixed metal oxides exhibiting large Ru particles, are more active than what is commonly referred to in the literature as the optimal Ru particle size for this reaction. However, to confirm these results H_2 chemisorption should be performed on both catalysts in order to compare the TOF of the two catalysts.

Lastly, to try to explain the differences in catalytic activity that is exhibited between the catalysts, the rate of reaction for each catalyst were fit to a simple power law model in order to determine the reaction order with respect to NH_3 and H_2. The reaction order with respect to N_2 was not considered here because it has been previously shown in multiple studies that there is no dependence on the N_2 partial pressure on the rate of reaction. Figure 3.36 shows the logarithmic dependence of the partial pressure of hydrogen (top) and the

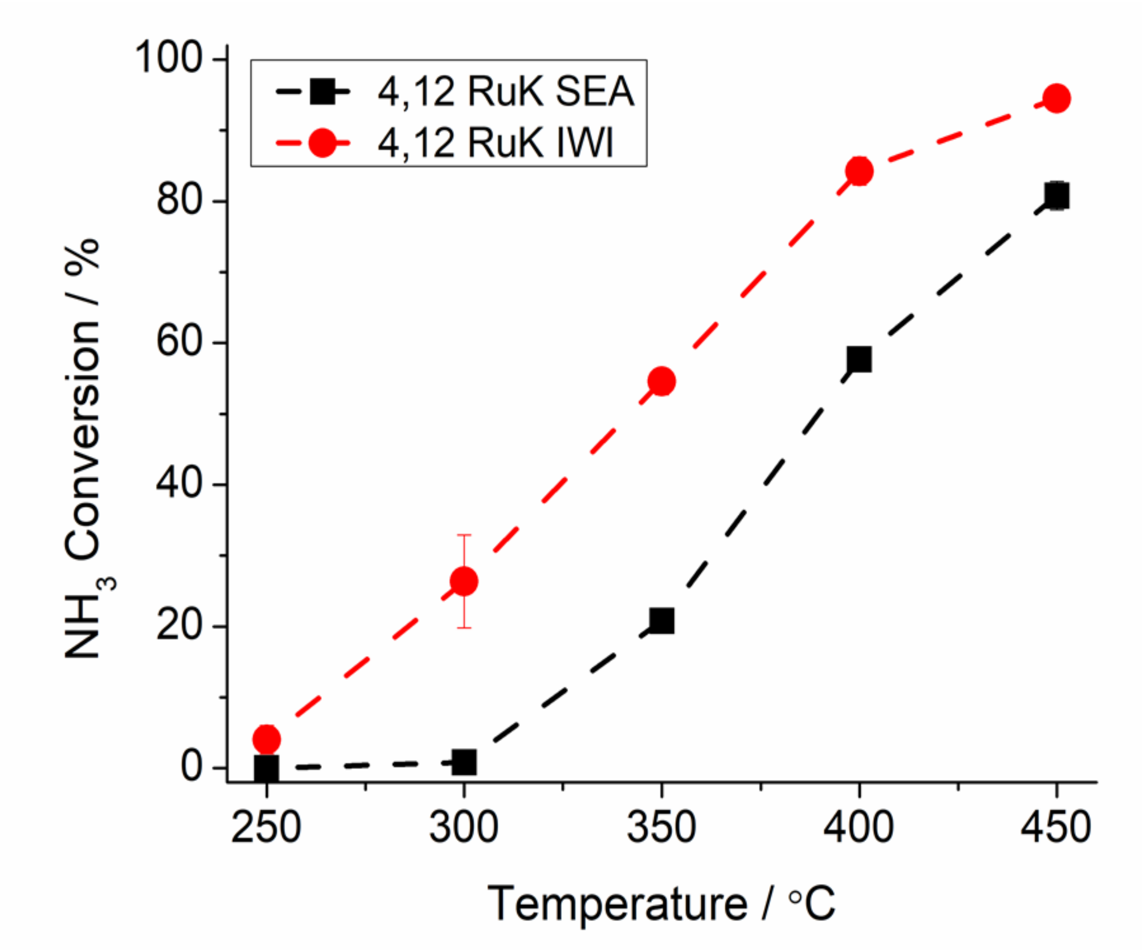

Figure 3.35. Activity of the 4,12 RuK SEA (black squares) compared to the 4,12 RuK catalyst synthesized via incipient wetness impregnation (IWI) (red circles). Reaction conditions: 100%NH_3, 16,200 mL/hr/g_{cat} at atmospheric pressure

partial pressure of ammonia (bottom) on the logarithmic rate of reaction. In order to determine the effect of the partial pressure of each gas on the rate of reaction, the inlet concentration of hydrogen and ammonia was varied between 10% and 30% with balance Ar, and the temperature and space velocity were held constant at 450°C and 5,400 mL/hr/g_{cat} respectively. Each catalyst was then fit with a linear regression and the R^2 value shows the goodness of fit of the experimental data. Additionally, the rate of reaction was fit for a 4 Ru catalyst in order to make comparisons of our values to those of the literature. We found that for a 4% Ru catalyst, there was a reaction order of -0.55 with respect to

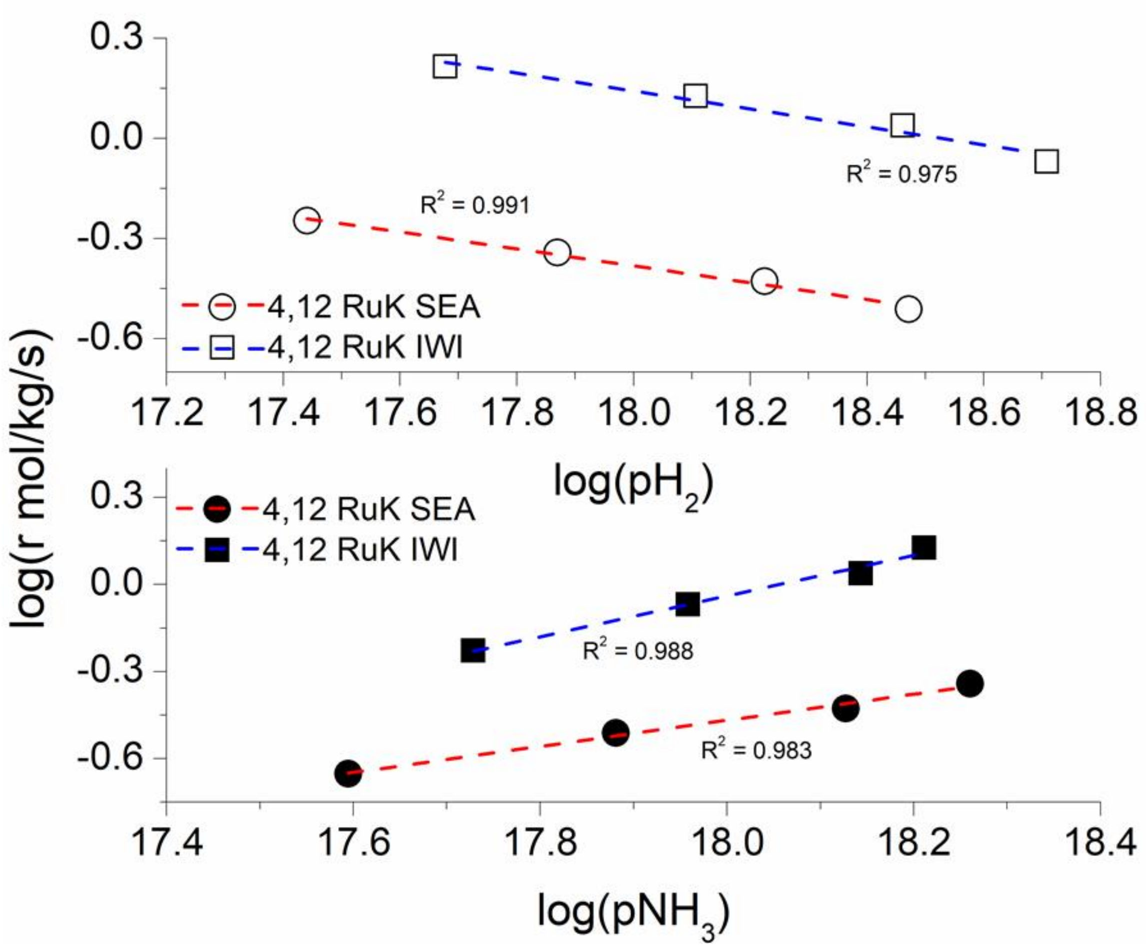

Figure 3.36. Reaction order determination for 4,12 RuK SEA (circles, red trace) and 4,12 RuK IWI (squares, blue trace) with respect to H_2 (top) and NH_3 (bottom). Reaction conditions: 100% NH_3, T= 450°C, 10-30% H_2, 10 – 30% NH_3 in balance Ar, 5,400 mL/hr/g_{cat} and atmospheric pressure.

hydrogen, and 0.40 with respect to ammonia. These correlate to similar values within the literature, where a value -0.60 with respect to hydrogen and between 0.0 – 1.0 with respect to ammonia have been measured in the literature (*82*, *83*, *258*). The SEA 4,12 RuK catalyst exhibited a reaction order of -0.28 with respect to hydrogen, and 0.49 with respect to ammonia. The IWI 4,12 RuK catalyst exhibited a similar reaction order with respect to hydrogen of -0.26 but a much higher reaction order with respect to ammonia of 0.70. The slight increase in the negative dependence on the hydrogen partial pressure indicates that the inhibitive effect of hydrogen is reduced on both catalysts in comparison to the 4 Ru catalyst. The dramatic differences in the dependence on the ammonia reaction order may indicate differences in the rate limiting step, and further experimentation should be done in order to elucidate the mechanistic differences.

3.7 Conclusions

This chapter investigated various synthesis methods and parameters that may influence the formation of hollandite for supported catalysts. Firstly, we discussed how the addition of K to γ-Al_2O_3 influences and chemically modifies the surface by ion exchanging with the surface hydroxyls and showed the formation of $KAl(OH)_2CO_3$ in a K/Al_2O_3 catalyst. Nextly, we discussed how the addition of K influenced the catalyst compared to a 4% catalyst through apparent activation energy required for ammonia decomposition as well as morphological differences and differences in crystalline phases present. The addition of K induced the formation of mixed metal oxides $KRuO_4$ and KRu_4O_8 which took the form of nanowires and sheets in the SEM/TEM images. Additionally, the apparent activation energy decreased from 125.2 kJ/mol to 65.7 kJ/mol with the addition of 12% K.

Next, we looked at which precursors were able to form the hollandite structure. These included $RuCl_3$, $Ru(acac)_3$, KNO_3, KOH and KCH_3COO. A total of six catalysts were synthesized and analyzed for their crystal structure, morphology and ammonia decomposition activity. We found that $RuCl_3$ in combination with KOH and KCH_3COO formed hollandite, but synthesis methods with KNO_3 failed to produce the hollandite structure. When $Ru(acac)_3$ was used, no combination of $Ru(acac)_3$ with K precursors produced the hollandite structure. This suggests that the chainlike nature of $RuCl_3$ is an important factor in forming the tunnel like hollandite structure during impregnation synthesis methods. These catalysts were tested for their ammonia decomposition activity in 10% NH_3/Ar at a space velocity of 45,300 mL/h/g_{cat} and at atmospheric pressure. The best performing catalyst was the $Ru(acac)_3$, KNO_3 catalyst at all temperatures, followed by $Ru(acac)_3$, KOH. The high activity of these catalysts may be attributed to the lack of Cl^- anions present which has been known to be detrimental to activity. Three different impregnation methods were looked at to determine when hollandite will form. We determined that dry impregnation, incipiently wet impregnation were viable methods to form hollandite, but SEA was not able to produce the hollandite structure.

Next, variables specific to both dry and incipiently wet impregnation were studied to further understand under what conditions hollandite can form in supported catalysts. Firstly, the effect of the volume of the solution used during incipient wet impregnation was investigated. The abundance of metal deposited per impregnation may have influenced the availability of Ru to interact with K and provided insight into the growth mechanism of hollandite. The number of impregnations was varied from 4 to 17 with a solution volume of 5 mL to 20 mL, respectively. XRD analysis showed that the dilution volume influenced the relative ratio of $KRuO_4$ to KRu_4O_8, and that a maximum ratio was obtained with a solution volume of 5 mL, and that the aspect ratio of the hollandite varied with the solution volume. The most diluted impregnation did not form hollandite structure. These catalysts were then tested for ammonia decomposition activity and a catalyst synthesized with a solution volume of 6 mL showed the highest activity at 300°C, while the catalyst synthesized with 20 mL of solution volume had dramatically lower activity.

Next the effect of the impregnation order was studied to see if both K and Ru needed to be deposited onto the catalyst in tandem for the hollandite to form. Sequential impregnation was performed so that K was first impregnated, calcined followed by an impregnation of Ru and a final calcine, and then the two precursors were reversed so that Ru was first impregnated. XRD analysis of the two catalysts showed that when first impregnated Ru, the hollandite structure would form, but not when K was first impregnated. Additionally, SEM images showed that the hollandite nanowhiskers seemed to nucleate out of a single point to first starburst structures.

The factors influencing dry impregnation were then studied. These included the temperature at which the solution was evaporated and the calcine duration. Temperatures between 60°C and 150°C and calcine durations between 1 and 5 hours were studied. We determined that at temperatures 60°C and 90°C, the hollandite structure would form regardless of the calcine duration. At higher evaporation temperatures, only $KRuO_4$ was present, and at 150°C, RuO_2 began to be present on the catalyst. These catalysts were tested for their low temperature ammonia decomposition activity in 10% NH_3/Ar and at a space velocity of 30,000 mL/hr/g_{cat} at atmospheric pressure. We found that catalysts synthesized at an evaporation temperature of 90°C and calcine duration of 1 hour showed the highest activity of the 12 catalysts at 300°C. The least active catalyst was synthesized with an evaporation temperature of 120°C and a calcine duration of 3 hours.

We also further varied the K loading of the catalyst to determine an optimal K loading for low temperature ammonia decomposition. K loadings were varied from 0.5, 1, 3, 6, 12 and 15% and in combination with either 1% Ru or 4% Ru, in order to find an optimal K loading for both a high and low loading of Ru catalysts. Interestingly, we found that for both 1% Ru and 4% Ru, 12% K was the optimal loading and produced the highest activity at all temperatures when tested in 10% NH_3/Ar and at a space velocity of 30,000 mL/hr/g_{cat} at atmospheric pressure.

The working state of the catalyst was investigated to determine what the active site during ammonia decomposition was. SEM/TEM analysis showed that there was a dramatic reducing in the nanorod diameter and that the rods became much more dendritic and segmented after H_2 reduction and after exposure to ammonia. XRD analysis and elemental mapping showed that the dendritic nanorods were composed of metallic Ru and contained residual Cl^- on the surface. XRD analysis showed that the hollandite and $KRuO_4$ had reduced to Ru^0 after the hydrogen reduction pretreatment, and this was the phase present after exposure to ammonia as well. H_2-TPR was performed to understand at what temperature the two structures reduce and compared to a 4% Ru catalyst. However, two large broad reduction events occurred between 75°C-175°C and between 350°C and 500°C. To further understand at what temperature $KRuO_4$ and KRu_4O_8 may reduce, in-situ XRD measurements were taken under 5%H_2/Ar. We determined that the two structures reduced well below 150°C, and the reflection of metallic Ru became visible at 175°C, and continued to become sharper and more intense with increasing temperature up to 450°C. We determined that the crystallite size of the metallic Ru continued to increase with increasing temperature, from 7.4 nm to 16.2 nm at 450°C and at room temperature after the catalyst was cooled down under inert. *Ex-situ* electron microscopy was performed on the catalyst after it was reduced at 250°C, 350°C and 450°C. The morphology of the catalyst was found to dramatically change at each reduction temperature in addition to the particle size. These catalysts were then tested for their ammonia decomposition activity in order to determine if the changes in the crystallite size and morphology had any influence on reactivity. While reduction temperatures of 250°C and 350°C resulted in similar activities, a reduction of 450°C resulted in a much more activity catalyst, even though this reduction temperature resulted in a catalyst with the most stalky like nanorods and largest crystallite size.

The catalyst reduced at 450°C was then compared in activity to that synthesized through SEA, in order to synthesize a catalyst was more along the lines of the ideal catalyst suggested in the literature. The SEA method was able to synthesize Ru nanoparticles that were highly dispersed on the support, and below the limit of detection via XRD. These ideal nanoparticles as suggested by the literature were then tested for ammonia decomposition and compared to the 4,12 RuK IWI catalyst under identical conditions and found to be highly activity at low space velocities, but to have much lower activities compared to the IWI catalyst at higher space velocities. We conclude that this may be due to differences in the measured dependence of the ammonia partial pressure on the rate of reaction. This was determined by fitting the rate of reaction to a simple power law model in order to determine the dependence of the reaction rate on the ammonia and hydrogen partial pressure for the SEA and IWI catalyst with identical weight loadings. Ultimately, the dependence on the hydrogen partial pressures was similar for both catalysts, but the IWI catalyst had a higher dependence on the ammonia partial pressure than the catalyst synthesized via SEA. This may indicate that there are differences in the rate limiting step over the two catalysts.

CHAPTER 4

HIGH THROUGHPUT SCREENING OF RU BASED CATALYSTS

There exists a lack of diversity in the literature for promotional and active metals for ammonia decomposition, despite the fact that this reaction has been studied for over one hundred years. Primarily, ammonia decomposition had been studied to better understand the ammonia synthesis reaction over Fe and Ru catalysts due to the milder operating pressure. Now, there interest in this reaction is motivated by the fact that ammonia can be used as a hydrogen storage and transportation device, which can catalytically decompose to provide a source of hydrogen for PEM fuel cells. In order for this to occur, a catalyst must be designed that is not only cost-effective but can exhibit high activity at temperatures below 450°C in order to avoid either poisoning of the membrane from ammonia in the effluent, or thermal degradation of the membrane from high operating temperatures. While Ru is intrinsically the most active metal for this reaction, current studies work to optimize Ru based catalysts through particle size and shape manipulation and investigating various supports and promoters. However, this is strongly limited alkali and alkaline earth metal promoters, and to basic supports such as MgO, and much more complicated supports such as carbon nanotubes and various spinel and perovskite supports.

Since the pioneering work performed by Mittasch and coworkers in the early 20th century (*66*) for discovery of ammonia synthesis catalysts, there has been a lack of exploration to further define combinations of elements that work either as doubly, or triply promoted catalyst systems or as a dual-active site catalyst to create a cost effective, highly active low temperature ammonia decomposition. This is mainly due to the time-consuming nature of a study of this magnitude. This is why the utilization of high throughput experimentation allows for the testing more exotic catalyst combinations in an efficient manner. Therefore, we sought to find a highly active low temperature ammonia decomposition by looking at K promoted catalysts that contained either 1, 2 or 3 wt% Ru and added one of 31 different metals to these three Ru weight loadings, in order to determine to what extent the Ru content could be reduced while still maintaining high activity at low temperatures. In total over 100 unique catalyst combinations were synthesized.

However, this can be further expedited with the use of machine learning algorithms. High throughput experimentation is perfectly suited as a means to provide large amounts of homogeneous data as an input for machine learning algorithms, which can then either guide a second iteration of catalyst design or provide more efficient means of screening catalysts by lowering the number of catalysts needed to be tested within a given design space, in order to predict the activity of the catalysts within the rest of the design space.

4.1 Ru Substitution by Transition Metals

In order to begin screening for bi-metal ammonia decomposition catalysts, various previous and non-precious metals were chosen to replace half of the Ru content in a 4 wt%

Ru catalyst supported on γ-Al_2O_3 (4 Ru). These included Co, Ni, Fe, Mn, Zn, Mo, Hf and Y transition and rare earth metals, the latter of which have very little information concerning their catalytic performance in the literature. Additionally, Pt, Os, Ir and Rh previous metals were also chosen. Very little experimental literature is available on Ru based bimetallic or bimetal catalysts for ammonia decomposition. Here we do not claim that these catalysts are in fact bimetallic, but simply that two metals were impregnated onto the support. Figure 4.1 shows the catalytic activity of these catalysts measured under 1% NH_3/Ar and at a space velocity of 30,000 mL/hr/hg_{cat}.

Except for 2,2 RuFe at 250°C, all catalyst performed poorly with less Ru compared to the baseline catalyst of 4 wt% Ru. However, the most promising catalysts were found to be those substituted with either Mg, Hf or Y which are not typically considered active for catalytic reactions. Interestingly, we see that the addition of Ni resulted in one of the worst catalyst activities, while previous literature suggests that Ni is one of the most promising non-precious ammonia decomposition metals. These studies typically report high activities between 550 – 650°C, and do not see appreciable activities within the ranges studied here (*103*, *259*).

Ultimately, substitution of Ru with a transition-based metal will result in a catalyst with less intrinsically active active sites as compared to the 4 Ru catalyst. For example, Chen et al. (*260*) synthesized bimetallic Ru-Fe nanoparticles on carbon nanotubes (CNT) and showed that these catalysts exhibited a fast desorption of N adatoms from the surface compared to Ru/CNT catalysts but ultimately resulted in similar activity as a Ru/CNT catalyst after H_2 reduction. Additionally, Fe has been shown to bind N_2 too strongly to be a good ammonia decomposition catalyst, and Co too weakly (*79*, *80*). This evident in the

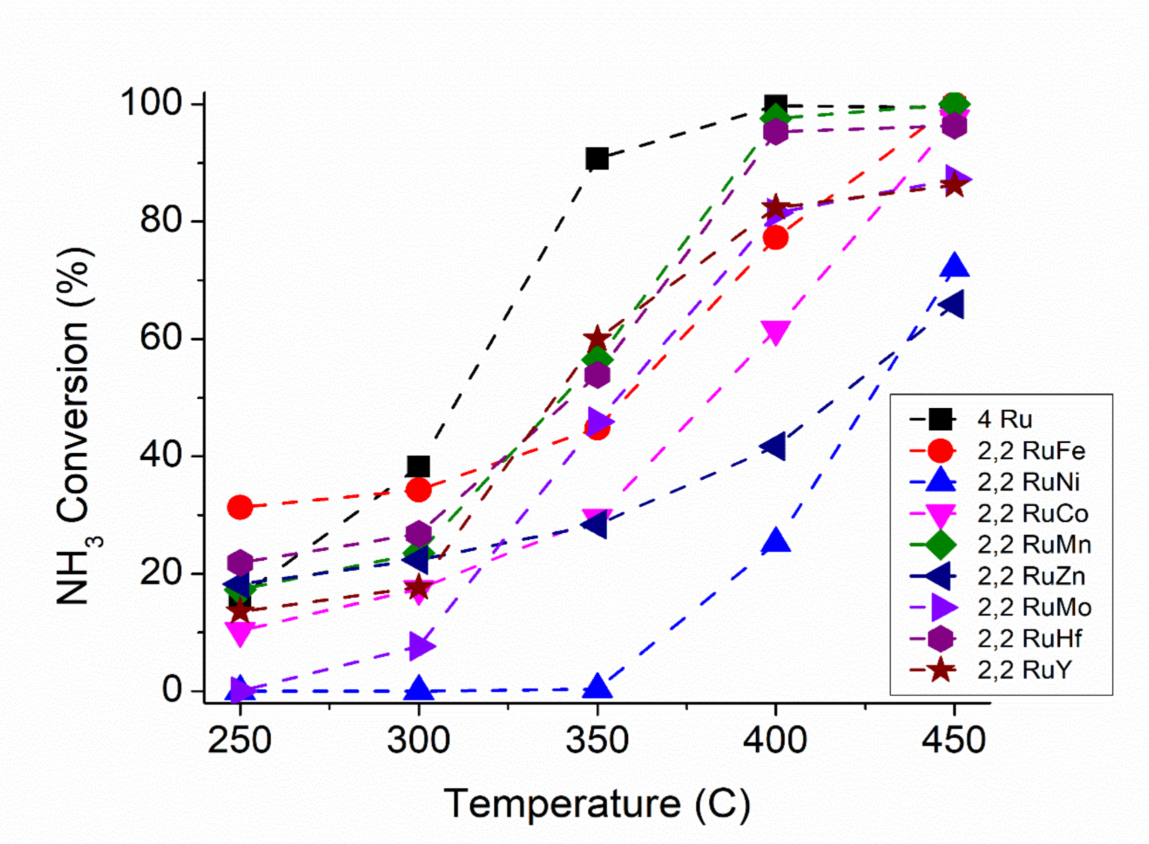

Figure 4.1. NH_3 conversion of 2,2 RuM (M= Fe, Ni, Co, Mn, Zn, Mo, Hf or Y) supported on γ-Al_2O_3. Reaction conditions: 1% NH_3/Ar, 30,000 mL/hr/hg_{cat} and atmospheric pressure.

reaction data at 250 and 350°C, where 2,2 RuFe shows higher activity compared to 2,2 RuCo at lower temperatures because it requires less energy to activate NH_3. While on the other hand, Co shows poor activity at these low temperatures since it requires more energy to bind N effectively. Zhang et al. (*261*) demonstrated that at 550°C, Fe/CNT catalysts had lower activity compared to Co/CNT, and that bimetallic nanoparticles of FeCo/CNT resulted in higher activity that just Fe/CNT. Three different bimetallic composition were studied but none of them performed better than Co/CNT at the given temperature. Lorenzut et al. (*262*) demonstrated that bimetallic FeMo nanoparticle supported on yttria-stabilized zirconia (YSZ) outperformed both of their monometallic counterparts Fe/YSZ and Mo/YSZ, but not until temperatures above 600°C. CoMo bimetallic catalysts have also been extensively studied, and have been shown to also be more active than their monometallic counterparts, but again require temperatures above 450°C for appreciable conversion to be achieved (*263–266*).

Additionally, Pt, Os, Rh and Ir precious metals were also studied due to the high activity of their monometallic counterparts. While the main objective of this work was to find a cost, effective catalyst compared a catalyst containing 4 wt% Ru, by substituting Ru with another precious metal, this may have resulted in such an active catalyst that the cost per hydrogen produced could have been lower than that of just a Ru supported catalysts. Figure 4.2 shows the activity results of precious metal substituted Ru catalysts compared to the baseline 4 Ru catalyst under identical reaction conditions. Here we see a similar trend as the non-precious metal catalysts, that regardless of the metal substituted, there is no enhancement in activity compared to the baseline catalyst with more Ru content.

We found here bi-metal Ru catalysts based off of transition metals to be poor substitutes to catalysts containing only Ru. While studies do in fact create successful bimetallic catalysts for ammonia decomposition, the comparisons are made between the bimetallic catalyst and a catalyst with Ru only. Therefore, for transition metals that are active for ammonia decomposition, it is no surprise they would be more active than a Ru only catalyst since the Ru content is constant in both cases and additional active metal is added to the bimetallic catalyst. Additionally, many of these studies include computational calculations of over various bimetallic crystal planes, which are not feasible to experimentally produce (*89*, *267*, *268*).

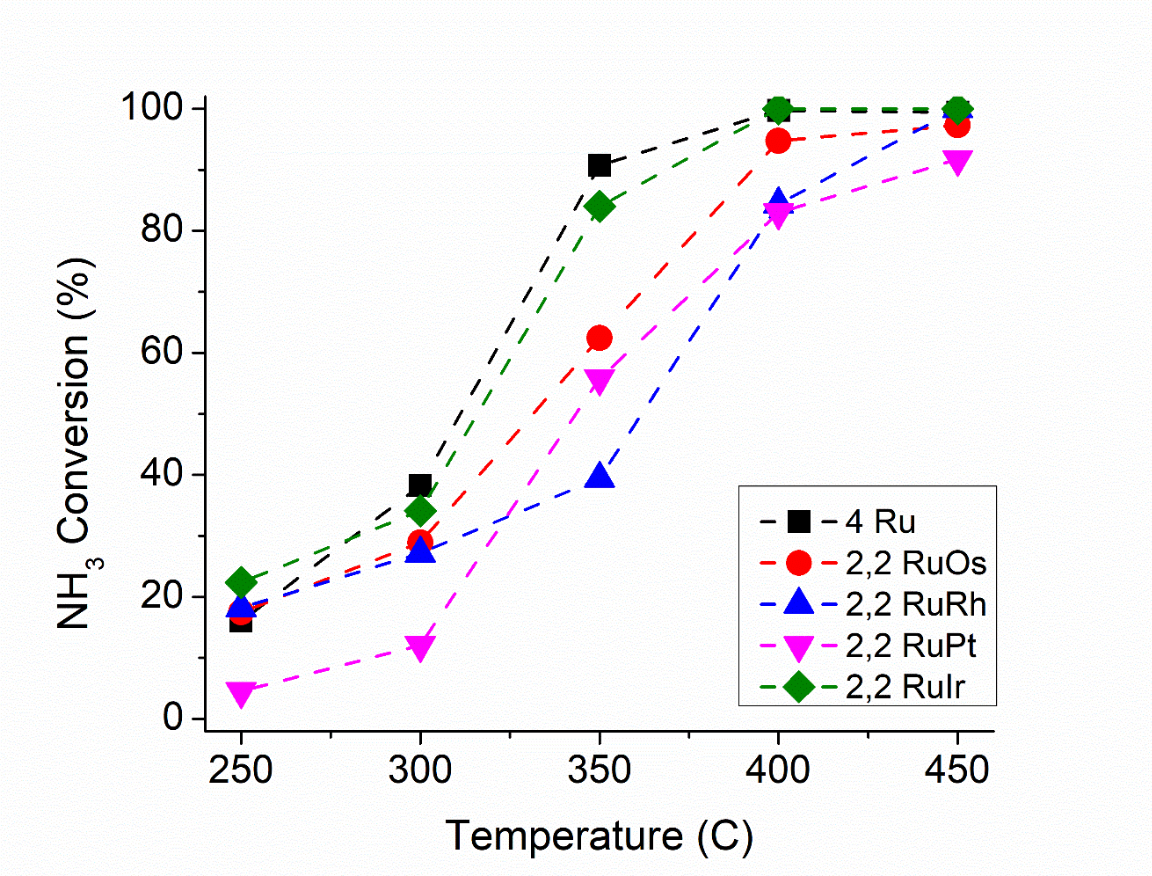

Figure 4.2. NH_3 conversion of 2,2 RuM (M= Os, Rh, Pt or Ir) supported on γ-Al_2O_3. Reaction conditions: 1% NH_3/Ar, 30,000 mL/hr/hg_{cat} and atmospheric pressure.

Due to the lack of success, we found in using previous literature as a basis for creating cost effective Ru based catalyst for ammonia decomposition, a more Edisonian approach was taken encompassing a broader scale of metals and weight loadings. Additionally, there are very few metals that show promise for ammonia decomposition at the low temperatures studied throughout this body of work.

4.2 Design Space for Ammonia Decomposition Catalysts

Previously, our group determined the effect of promoters and preparation solvents on ammonia decomposition activity for Ru supported catalysts (*118*). Of the following promoters, K, Cs, Ba, Sr, Rb, Ca, Na and Li, the most promising promoters were found to be K, Cs and Ba. The effect of these three promoters and the optimal promoter loadings was determined through response surface methodology, which was built around a 4 wt% Ru catalyst supported on ɣ-Al_2O_3. The weight loading of the three promoters was varied from 0 to 12% and either one or two promoters were used. A catalyst promoted by 12 wt% K was found to be the most active. For this reason, we chose a 4 wt% Ru, 12 wt% K catalyst supported on ɣ-Al_2O_3 as a baseline catalyst to make activity comparisons with catalysts containing less Ru. Using this catalyst as a basis, the total metal loading was held constant at 4 wt%, and the Ru content was reduced to either 3 wt%, 2 wt% or 1 wt% with the remaining metal loading be composed of either 1 wt%, 2 wt% or 3 wt% of one of the following elements: Mg, Ca, Sr, Sc, Y, Zr, Hf, Nb, Ta, Cr, Mo, W, Mn, Re, Fe, Os, Co, Rh, Ir, Ni, Pd, Pt, Cu, Ag, Au, Zn, Cd, In, Sn, Pb or Bi. These will be referred to as secondary elements. Lastly, each catalyst was promoted with 12 wt% K. This resulted in over 100 unique catalyst formulations. The nomenclature for catalyst loadings will first indicate the three weight loadings of Ru, the secondary metal and K, followed by the three elements that were used in that catalyst. For example, a catalyst could composed of 3 wt% Ru, 1 wt% Fe and 12 wt% K will be referred to as 3,1,12 RuFeK, and a catalyst composition of 1 wt% Ru, 3 wt% Mg and 12 wt% K would correspond to 1,3,12 RuMgK. All catalysts were supported on ɣ-Al_2O_3 (192 ± 8 m^2/g) for the purpose of the high throughput screening study.

While the K promoter used here was found to be the optimal loading for a 4 wt% Ru catalyst, this may not be the case for all of the catalysts studied here due to the variety of secondary metals probed. In fact, there is no agreement on what the most active promoter is for a Ru supported catalyst and is a function of the support and promoter precursor. Other studies have shown that LiOH was the most active promoter compared to CsOH and KOH on a ɣ-Al_2O_3 supported Ru catalyst (*269*, *270*) due to surface modification of the support with alkali hydroxides. However, here we have shown that K also modifies the ɣ-Al_2O_3 support by forming alkali aluminates in Chapter X. By using the same promoter and support throughout this study, we can ensure that changes in the rate of reaction will be due to the addition of the secondary element and not due to newly introduced promoter support interactions, which is beyond the scope of this work. Additionally, it would be time consuming and costly to reproduce the design space with a different promoter, effectively doubling or tripling the number of catalysts that would need to be synthesized and screened. However, it would be worthwhile to further investigate different promoters after promising catalysts have been identified.

4.2.2 Effect of Support on Ammonia Decomposition Activity

Various supports were probed in order to determine if ɣ-Al_2O_3 was the best support to use for this study, including TiO_2, SiO_2, α-Al_2O_3, CeO_2 and ZSM-5. These supports were chosen in order to probe the effects of surface area, strong metal support interactions (SMSI), oxide reducibility and mesoporosity on catalyst activity. The results of the various supports in relationship to ɣ-Al_2O_3 are shown Figure 4.3 for 3,1,12 RuHfK catalysts. The activity was measured in 100% NH_3 at a space velocity of 5,400 mL/hr/g_{cat} and atmospheric pressure. Interestingly we found low surface area α-Al_2O_3 to be almost as active as ɣ-Al_2O_3 at 400°C. However, very little information is available on α-Al_2O_3 as a support for ammonia decomposition due to its low surface area and inertness and is primarily used to carry out kinetic studies to minimize temperature gradients and to minimize channeling

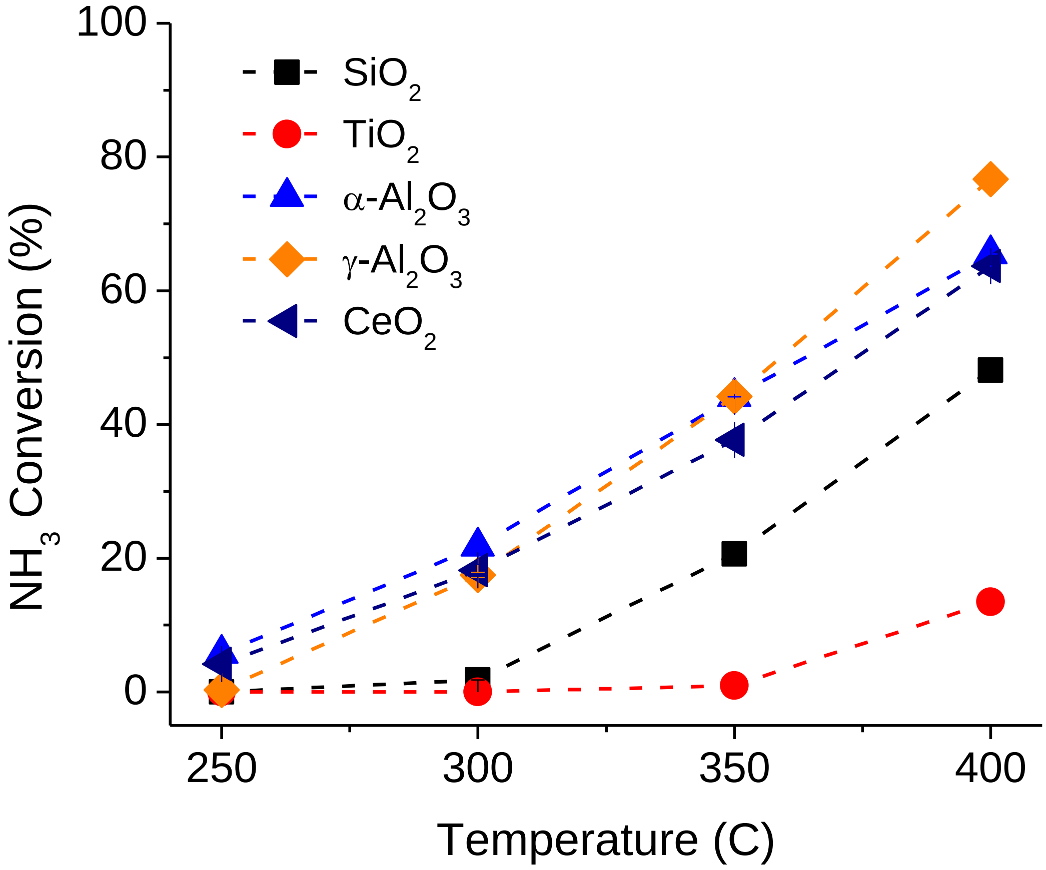

Figure 4.3. Ammonia decomposition activity of 3,1,12 RuHfK over various supports. Reaction conditions: 5,400 mL/hr/g_{cat}, 100% NH_3 and 1 bar.

(*269*). For ammonia synthesis, α-Al_2O_3 was shown to have the poorest performance compared to SiO_2, ZrO_2, ɣ-Al_2O_3, and MgO, regardless of the active metal (*271*). In contrast, a recent ammonia synthesis study varied the calcine temperature of alumina in order to study the different phases of Al_2O_3 for supported Ru-Ba catalysts (*272*). This study found that calcining the Al_2O_3 support to 980°C resulted in the formation of θ-Al_2O_3 and α-Al_2O_3 and resulted in the most active ammonia synthesis catalyst over α and ɣ phase alumina. Further heating to 1300°C resulted in the formation of α-Al_2O_3 and resulted in an increase in Ru particle size. The larger Ru particles may have a higher diffusivity over larger Ru particles compared to smaller Ru particles (*273, 274*). Additionally, α-Al_2O_3 also exhibited the least amount of surface OH groups. Hydrogen atoms that migrate to the support may interact with the surface OH groups and can cause hydrogen poisoning. Therefore, the lack of surface OH groups may reduce hydrogen poisoning and increase the rate of reaction at higher temperatures. Additionally, we observed high activity at low temperature on 3,1,12 RuHfK supported on CeO_2. Investigation into CeO_2 as a support is relatively new has been shown to prevent sintering of the active metal when used as a promoter for Ni supported catalysts (*275*). Recently Ru and Ni catalysts supported on CeO_2 have been tested for ammonia decomposition, and the activity was found to be greatly enhanced when Ru and Ni were supported on CeO_2, in relation to Al_2O_3 supported catalysts (*276*). However, the synthesized alumina support was found to be in the χ phase, instead of the commonly used and thermodynamically stable γ phase of alumina. This may lead to a misleading representation of the activity of CeO_2 supported catalysts in relation to alumina.

Titania was shown to be the least active support followed by SiO_2. Yin et al. (*277*) also observed TiO_2 to be a poor support for Ru catalysts compared to MgO, Al_2O_3 and CNT at temperatures up to 600°C. Choudhary et al. (*278*) synthesized Ni catalysts on HY zeolite, SiO_2, HZSM-5 and Al_2O_3 and found that the activity per metal site was greatest on SiO_2 supports. However, Li et al. (*101*) reported that the addition of K to Ru/SiO_2 catalysts did not result in a large improvement in catalytic activity compared to unpromoted the Ru/SiO_2 catalyst. Therefore, it is apparent that the optimal support will vary depending on the active metal and promotional environment. Previous literature has shown that strongly basic supports enhance the ammonia decomposition reaction. Surface modification of alumina with K has been shown to increase basicity of the support which may explain the enhanced activity of the two alumina supports. Sun et al. (*231*) showed that titania and silica lacked the proper vacant sites and ability to anchor KNO_3 that is necessary to generate basicity in other supports such as alumina and zirconia. This may explain the poor performance of the two supports. From this study, we concluded that high surface area ɣ-Al_2O_3 was the most effective support for Ru supported catalysts with very high loadings of K promoter and was utilized for all catalyst during the high throughput screening.

4.3. High Throughput Screening

The K promoted Ru based catalysts were screen for ammonia decomposition activity in 1% NH_3/Ar at 30,000 mL/hr/g_{cat} and at atmospheric pressure. Figure 4.4, Figure 4.5, Figure 4.6, and Figure 4.7 show the activity results at 250°C, 300°C, 350°C and 400°C respectively. In each figure, the top graph (a) corresponds to 1 wt% Ru substitution with a secondary metal (3,1,12 RuMK), the middle graph (b) corresponds to 2 wt% Ru substitution (2,2,12 RuMK), and the last graph (c) corresponds to 3 wt% Ru substitution (3,1,12 RuMK). The secondary metal substituted is label on the x-axis. Additionally, each figure has the activity of the baseline 4,12 RuK catalyst indicated by the black dashed line under identical operating conditions in order to make direct comparisons to activity at each catalyst weight loading. respectively. In each figure, the top graph (a) corresponds to 1 wt% Ru substitution with a secondary metal (3,1,12 RuMK), the middle graph (b) corresponds to 2 wt% Ru substitution (2,2,12 RuMK), and the last graph (c) corresponds to 3 wt% Ru substitution (3,1,12 RuMK). The secondary metal substituted is label on the x-axis.

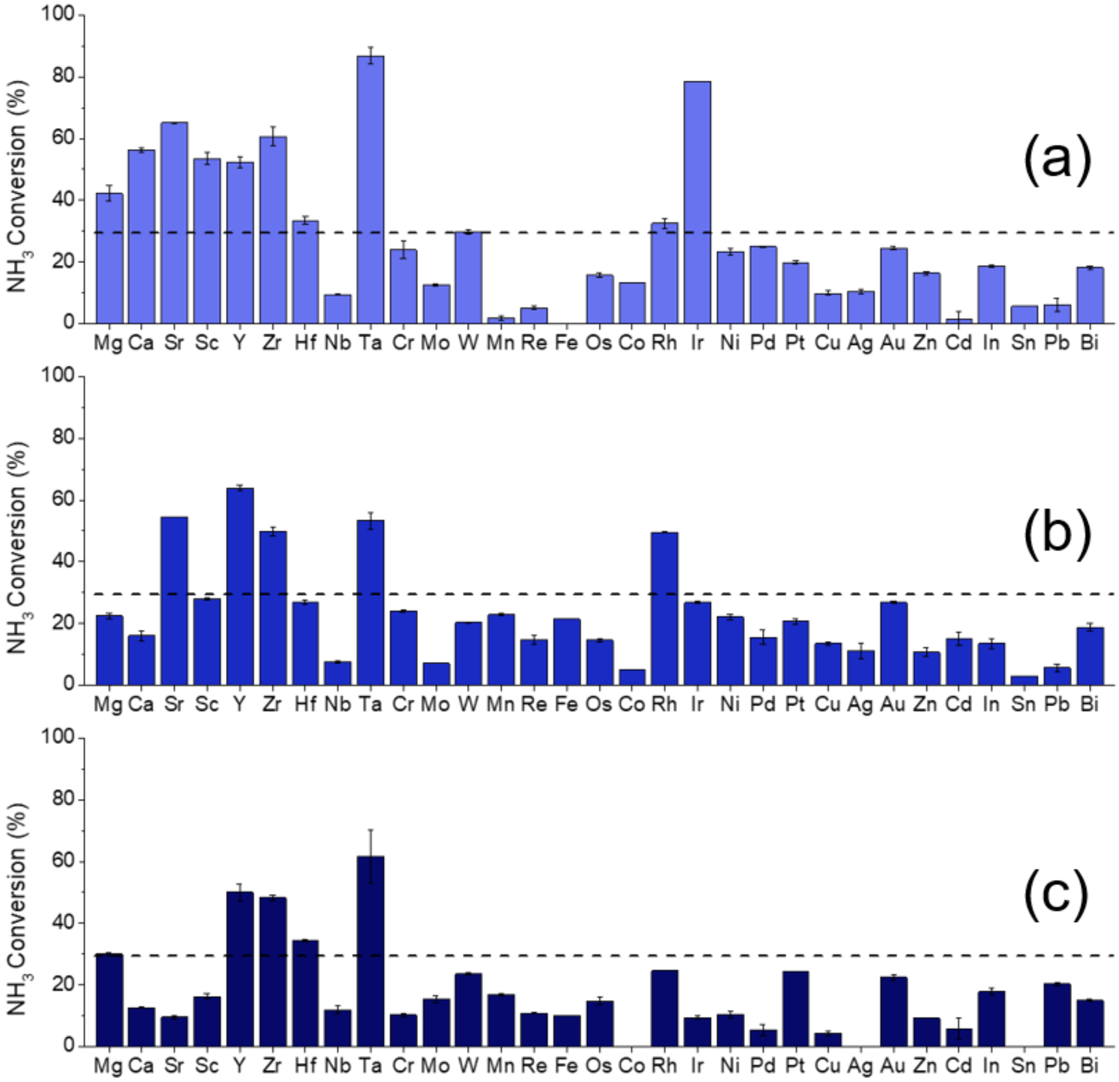

Figure 4.4. High throughput screening results at 250°C for (a) 3,1,12 RuMK, (b) 2,2,12 RuMK and (c) 3,1,12 RuMK, where the substituted metal M listed on the x-axis. Reaction conditions: 1%NH$_3$/Ar, 30,000 mL/hr/g$_{cat}$ and atmospheric pressure. The black dashed line corresponds to the activity of 4,12 RuK at identical conditions.

Because so many catalysts were able to achieve the same activity as the baseline catalyst at 400°C, we chose a milder temperature of 300°C to determine successful substitutions of Ru with a secondary metal. This is because we are interested in not only a low Ru content catalyst, but also a catalyst that has high activity at low temperatures. Additionally, these screening results utilized only 1% NH$_3$ in the feed gas. The rate of

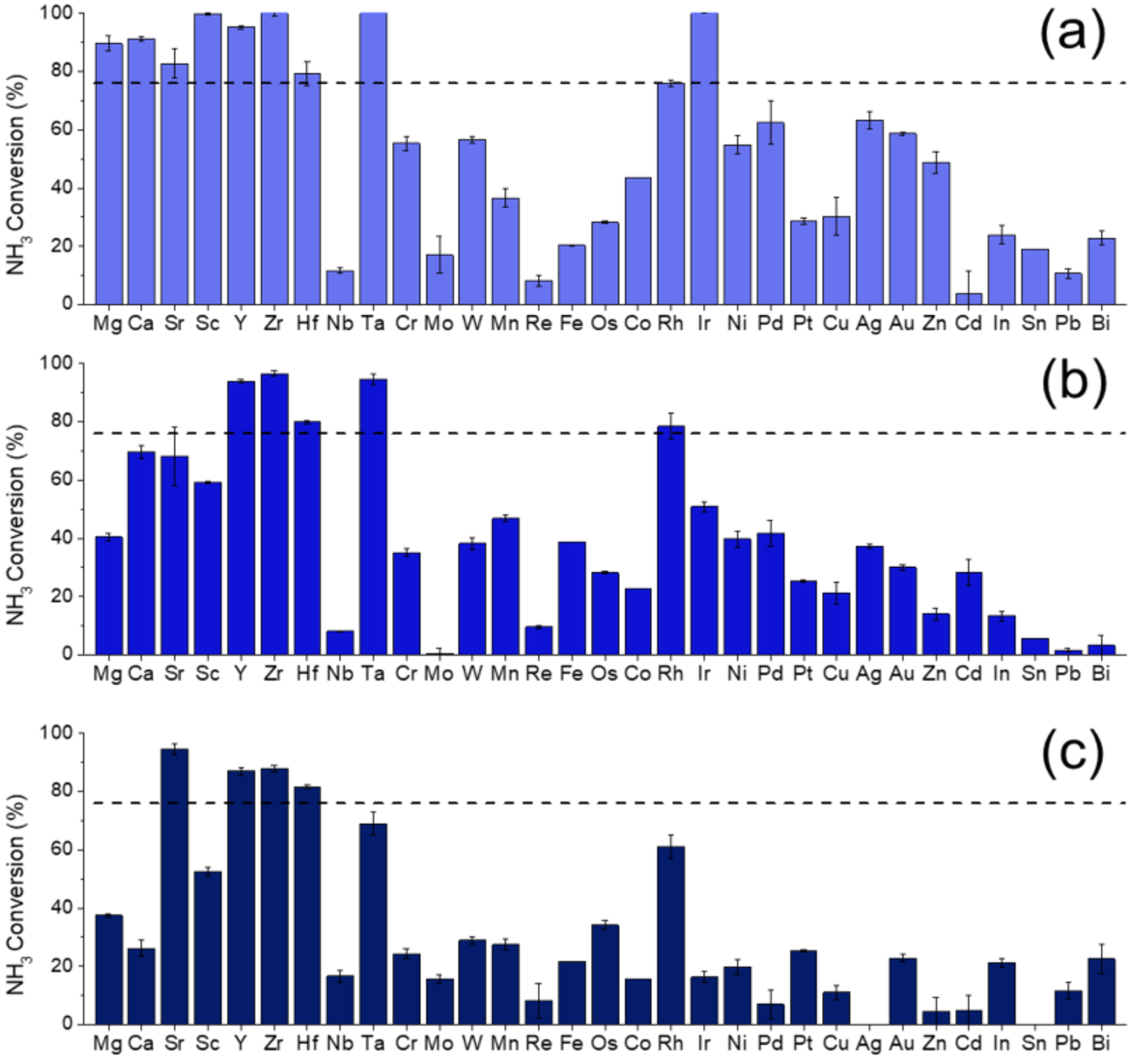

Figure 4.5. High throughput screening results at 300°C for (a) 3,1,12 RuMK, (b) 2,2,12 RuMK and (c) 3,1,12 RuMK, where the substituted metal M listed on the x-axis. Reaction conditions: 1%NH_3/Ar, 30,000 mL/hr/g_{cat} and atmospheric pressure. The black dashed line corresponds to the activity of 4,12 RuK at identical conditions.

reaction is known to have a negative dependence on the partial pressure of ammonia, so as the ammonia concentration increases, the rate of reaction should also decrease (*258*). Therefore, catalysts that do not perform well at 300°C with 1% NH_3 are not expected to perform well when the reaction conditions become harsher. Under these conditions, catalysts containing 3% Ru and 1% of either Mg, Ca, Hf, Sc, Ta, Zr, Ir or Y achieved

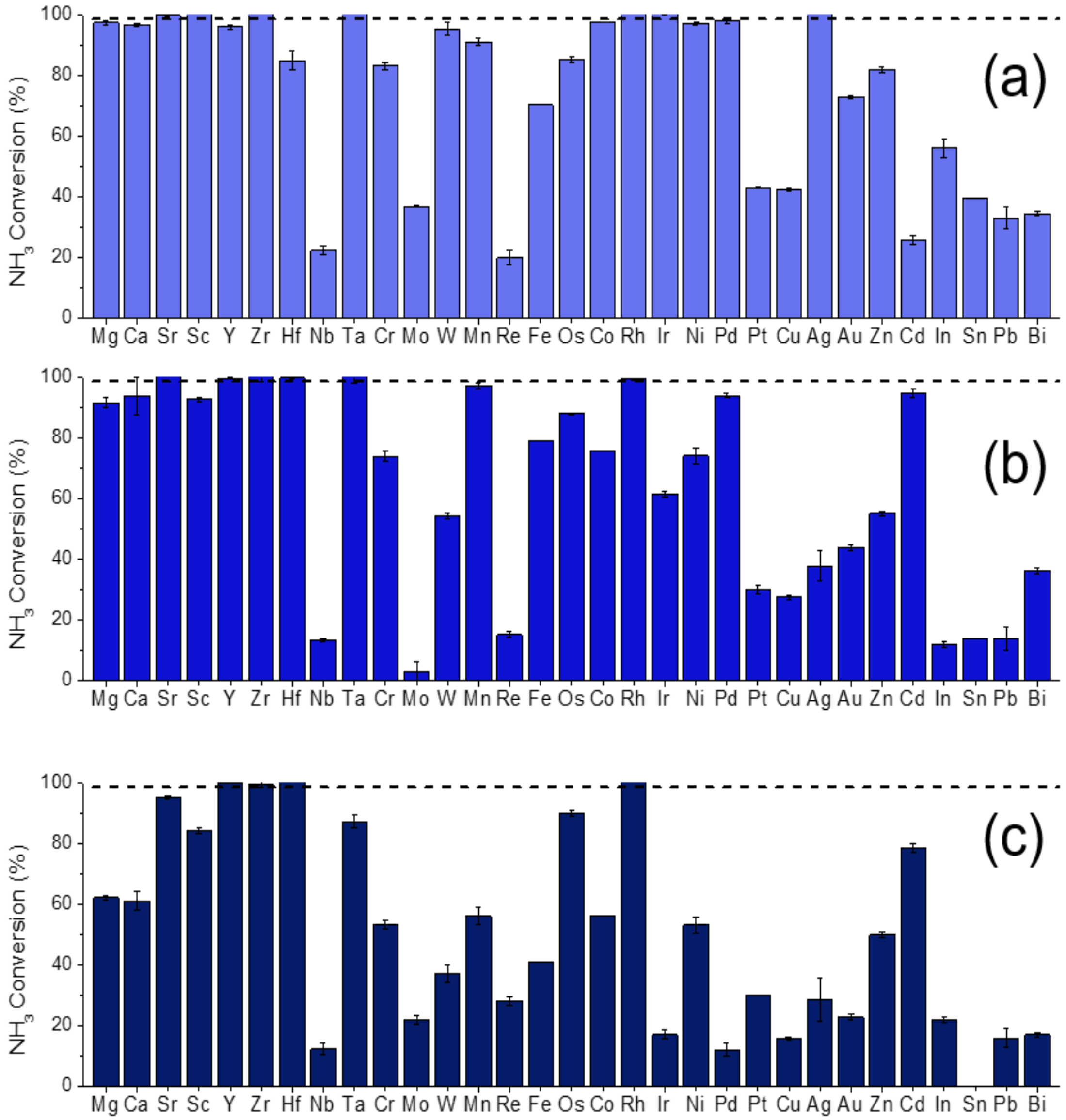

Figure 4.6. High throughput screening results at 350°C for (a) 3,1,12 RuMK, (b) 2,2,12 RuMK and (c) 3,1,12 RuMK, where the substituted metal M listed on the x-axis. Reaction conditions: 1%NH_3/Ar, 30,000 mL/hr/g_{cat} and atmospheric pressure. The black dashed line corresponds to the activity of 4,12 RuK at identical conditions.

greater than 80% conversion. As the ratio or Ru to secondary metal decreased from 2% Ru and 1% Ru, only Sr, Y Zr and Hf continued to exhibit excellent performance, while substitution with Bi, In, Mo, Nb, Cu, Re, Cd, Sn and Pb dramatically lowered the activity in relation to the 4,12 RuK catalyst regardless of the weight loadings.

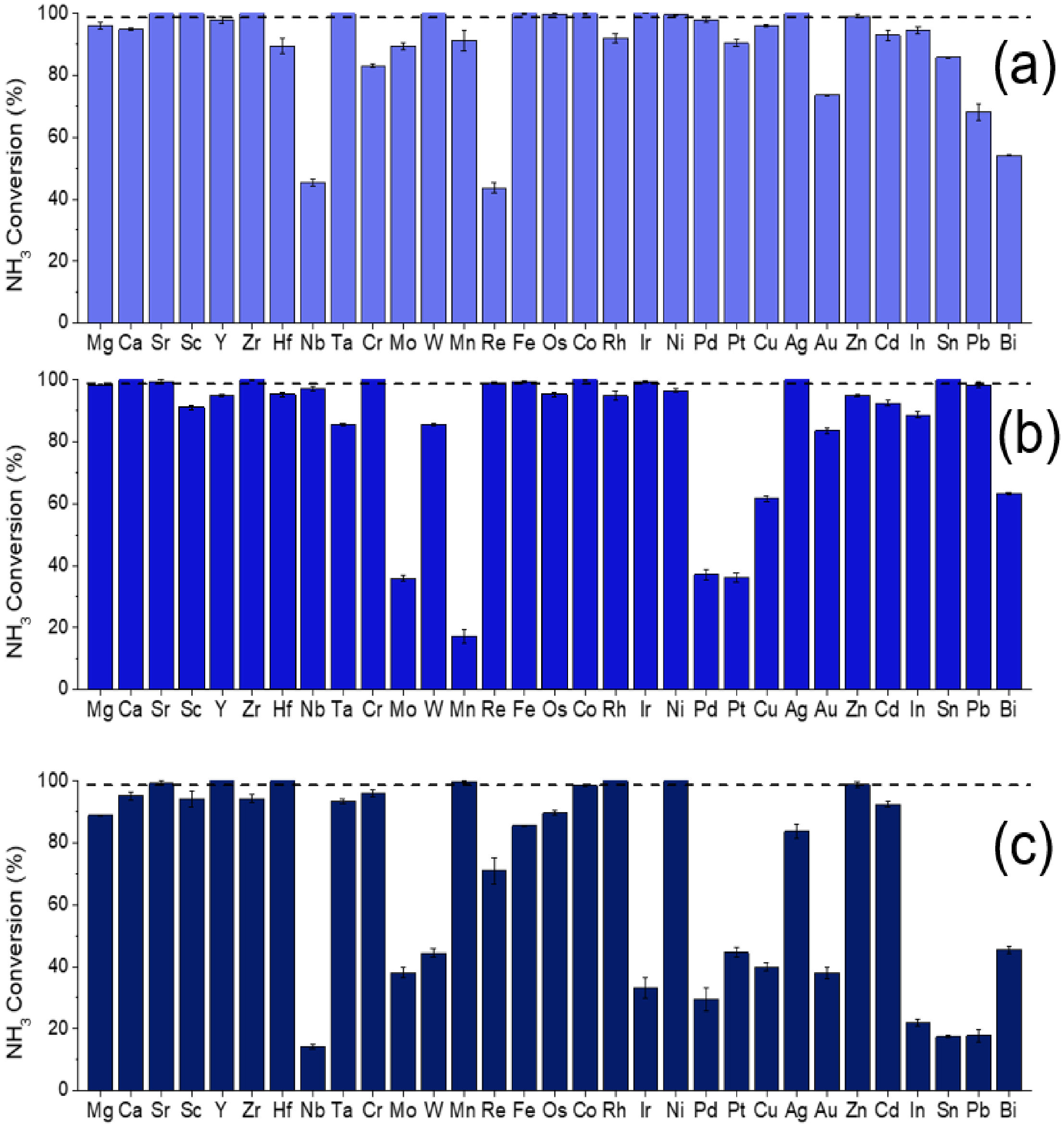

Figure 4.7. High throughput screening results at 400°C for (a) 3,1,12 RuMK, (b) 2,2,12 RuMK and (c) 3,1,12 RuMK, where the substituted metal M listed on the x-axis. Reaction conditions: 1%NH_3/Ar, 30,000 mL/hr/g_{cat} and atmospheric pressure. The black dashed line corresponds to the activity of 4,12 RuK at identical conditions.

At 250°C, multiple catalyst at each weight loading are able to outperform the 4,12 RuK baseline catalyst with less Ru. These include 3,1,12 RuMgK, 3,1,12 RuCaK, 3,1,12 RuSrK, 3,1,12 RuScK, 3,1,12 RuYK, 3,1,12 RuZrK, 3,1,12 RuHfK, 3,1,12 RuIrK, 3,1,12 RuRhK, 2,2, 12 RuSrK, 2,2,12 RuYK, 2,2,12 RuZrK, 2,2,12 RuTaK, 2,2,12 RuRhK, 1,3,12 RuMgK, 1,3,12 RuyK, 1,3,12 RuZrK, 1,3,12 RuHfK and 1,3,12 RuTaK. At this temperature, the Ta substituted catalyst resulted in the most active catalyst regardless of the compositional loading. At this low of temperature, the most active substituted catalysts were composed of alkali metals, alkali earth metals, rare earth metals and precious metals. Catalysts with 3 wt% Ru and 1 wt% of Mg, Sr, Ca, Hf, Sc, Ta, Zr, Ir or Y achieved greater than 83% conversion at 300°C. At 350°C and 1 wt% substitution of Ru with W, Mn, Co, Pd, and Ag begin to light-off, but decrease in activity with decreasing Ru loading in relation to the 4,12 RuK baseline activity. Interestingly, substitution with Cd shows excellent activity with lower loadings of Ru. Cd has been previously studied as a catalyst for hydrolysis, esterification and transesterification of triacylglycerides and fatty acids (*279*). Interestingly K supported catalysts have also been studied for transesterification reactions (*221*, *225*). Cd compounds are of interest because it can act as a Lewis acid, activating electronegative atoms such as N_2. Other common Lewis acids include Cu, Zn, and Sn, but we do not see a similar enhancement in activity with the addition of these metals. Again, we see that all of the alkali earth and alkaline earth metals achieve complete conversion at 350°C, but as the Ru loading decreases, the activity of Mg, Ca, Sr and Sc fall below the 4,12 RuK activity baseline, while Y, Zr, Hf and Rh substitution were still highly active with only 1% Ru. By 400°C, many more catalysts begin to reach the same activity as the baseline catalyst. With 1% Ru substitution, the worst catalysts contained Nb, Re and Bi, and at 3% Ru substitution, the worst catalysts contained Nb, In, Sn, Pb, Mo, W, Pd, Ir, Pt and Cu.

The substitution of Ru with transition-based metals generally resulted in a catalyst with poorer activity than the baseline. This was also observed in Figure 4.1 and Figure 4.2

when a promoter was not added to the catalysts. In general, this can be attributed to the replacement of highly active Ru active sites with intrinsically less ones. The Ru active sites are not being electronically or structurally modified, simply replaced. As for substitution with the noble metals Pt, Pd, Rh, Os, Ir, Pt and Au, these metals exhibited a strong correlation between and weight loading. Generally, we see that the activity decreases with increasing noble metal loading, while the activity was not as heavily influenced by variation in transition metal weight loadings. Higher weight loadings of noble metals would result in a stronger degree of hydrogen splitting and spillover. Hydrogen has been well known to be a poison to the ammonia decomposition reaction because it blocks the active sites of Ru for ammonia adsorption (*272*, *280–282*). So, increasing and noble metal loading while simultaneously decreasing the Ru loading and thus the number of active sites, could result in inhibition on the rate of reaction because of the hydrogen spillover effect (*283–286*). The most successful catalysts came from the substitution of Ru with alkali metals, alkali earth metals and rare earth metals. While alkali metals are generally considered to be electronic promoters, Mg and Ca have shown to provide structural enhancement (*115*, *122*, *287*), increasing the number of active sites present as opposed to making them more reactive. Recent work has investigating Sr niobates and titanates as supports for ammonia synthesis have shown that Sr niobate can enhance activity by inducing epitaxial growth of Ru (*288*) and that Sr titanate (*281*) can alleviate hydrogen poisoning and increase the electron density of Ru sites. Figure 4.8 shows SEM images of fresh and spent 3,1,12 RuCaK, 3,1,12 RuMgK and 3,1,12 RuSrK catalysts, highlighting the morphological differences of the Ru nanowhiskers both before and after exposure to ammonia, with the addition of different alkaline earth metals. All three catalysts exhibited

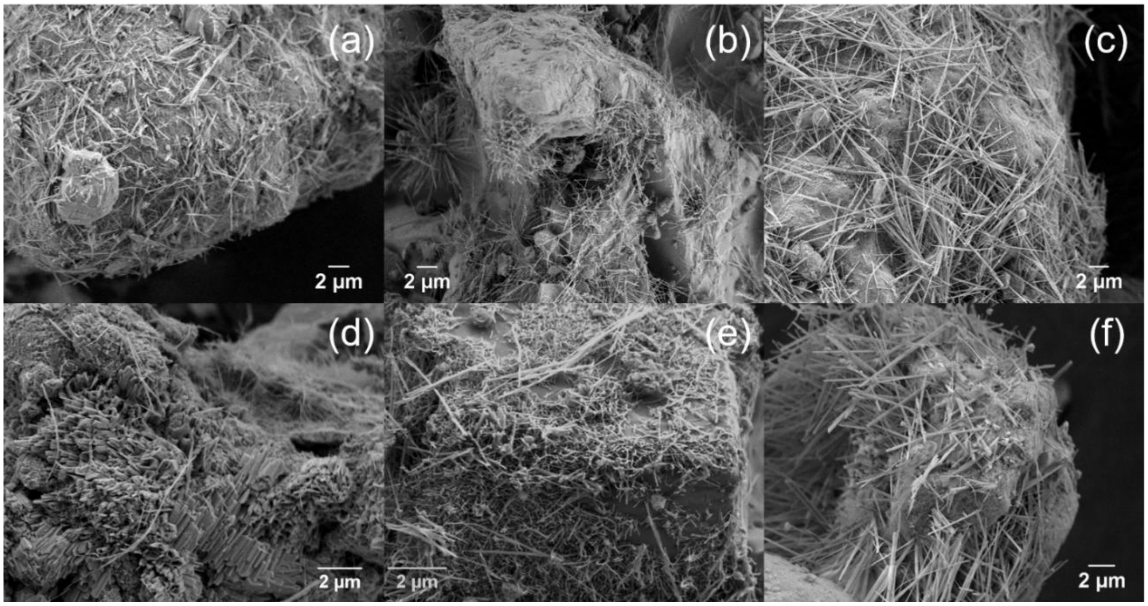

Figure 4.8. SEM images of fresh (a) 3,1,12 RuCaK, (b) 3,1,12 RuMgK, (c) 3,1,12 RuSrK and spent (d) 3,1,12 RuCaK, (e) 3,1,12 RuMgK and (f) 3,1,12 RuSrK.

XRD reflections indicative of hollandite crystal structure, and so the variation in the rod diameter and length is primarily due to the addition of the secondary element, which may in turn influence the pH of the synthesis solution for example.

Additionally, we wanted to determine the applicability of the results gathered through high throughput experimentation to those from a traditional plug flow reactor setup. Therefore, various 3,1,12 RuMK catalysts were chosen to be tested in a plug flow reactor under more realistic operating conditions. Specifically, the NH_3 concentration was increased from 1% to 100% and the space velocity was changed to 5,400 mL/hr/g_{cat} in order to meet H_2 productivity benchmarks set previously by ARPA-E (*289*) that can be financially feasible for upscaling the technology for H_2 production. Figure 4.9 shows the Arrhenius plot and calculated activation energies for randomly selected 3,1,12 RuMK

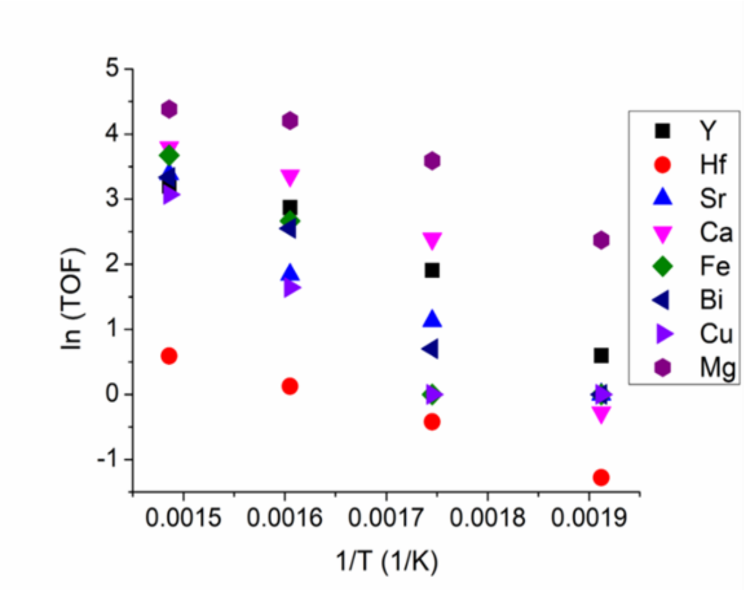

Catalyst	E_a (kJ/mol)
3,1,12 RuYK	61.75
3,1,12 RuHfK	36.22
3,1,12 RuSrK	62.93
3,1,12 RuCaK	79.11
3,1,12 RuFeK	78.65
3,1,12 RuBiK	69.00
3,1,12 RuCuK	61.82
3,1,12 RuMgK	39.80

Figure 4.9. Arrhenius plot of various 3,1,12 RuMK catalysts and calculated apparent activation energies. Turnover frequencies calculated from H_2 uptake and assuming a ratio of 1 H_2: 1 Ru active site. Reaction conditions: 100% NH_3, 5,400 mL/hr/g_{cat} and atmospheric pressure.

catalysts, where M = Y, Hf, Sr, Ca, Fe, Bi, Cu or Mg. The conversion was measured from 250°C to 450°C in 50°C increments, and the H_2 uptake was measured for each catalyst using H_2 chemisorption experiments. From these, the turnover frequency (TOF) for each catalyst was determined and the activation energy could be calculated for each catalyst. The catalysts with the lowest TOF were Bi and Cu, which correlates to what was exhibited in the high throughput screening experiments. Additionally, catalysts with the highest conversion were Mg, with Rh and Sr performing slightly behind these two catalysts.

From the measured activation energies, we can see that Hg and Mg substitution had dramatically lower activation energies than those with Bi, Cu, Sr or Y, and that Ca and Fe substitution had even higher activation energies than these. This suggests that the rate determining step may be changing with the various substituted metals (*78*). Because of this, we wanted to gain further insight into two specific substituted metal catalysts, Sr and Fe, of which were a good and bad performing catalyst. Additionally, we did further characterization and activity measurements on these catalysts in order to validate the findings of the high throughput screen.

4.4 XRD Analysis

4.4.1 Phase Identification

Due to the complexity of the catalysts studied here, XRD was performed on each catalyst in order to determine which Ru species were present and whether or not a crystalline secondary phase was present at the various weight loadings. Specifically, we identified the formation of RuO_2, $KRuO_4$ and KRu_4O_8 species in each pattern through phase identification and calculated the crystallite size of these Ru metal oxides using Scherrer's equation. The summation of the different Ru species in catalyst can be found in Table 4.. There were no obvious correlations made between Ru species present and the activity of each catalyst, most likely because the addition of the secondary metal was more influential in determining activity than the crystal phase. Future work We have demonstrated previously that the Ru species all reduce to metallic Ru during the H_2 pre-treatment.

Table 4.1. Summary of the Ru crystal phases present in each catalyst tested for low temperature ammonia decomposition where the first column indicates the composition weight loading, the second column indicates the secondary metal, and a “Y” indciates that the corresponding species is present.

Ru, Secondary Metal,K Weight Loading	Secondary Metal	RuO_2	$KRuO_4$	KRu_4O_8
3,1,12	**Mg**	Y		Y
2,2,12		Y		
1,3,12		Y		
3,1,12	**Ca**			
2,2,12				
1,3,12			Y	
3,1,12	**Sr**		Y	
2,2,12			Y	
1,3,12				
3,1,12	**Sc**	Y	Y	
2,2,12		Y		
1,3,12		Y		
3,1,12	**Y**		Y	
2,2,12			Y	
1,3,12			Y	
3,1,12	**Zr**	Y		
2,2,12		Y	Y	
1,3,12		Y	Y	
3,1,12	**Hf**			
2,2,12			Y	
1,3,12			Y	
3,1,12	**Nb**	Y		
2,2,12		Y		
1,3,12		Y		
3,1,12	**Cr**	Y		Y
2,2,12		Y		
1,3,12				
3,1,12	**Mo**	Y	Y	
2,2,12		Y		
1,3,12		Y		
3,1,12	**W**	Y		
2,2,12		Y		
1,3,12		Y		
3,1,12	**Mn**			Y
2,2,12				Y
1,3,12				Y
3,1,12	**Re**			

2,2,12		Y		
1,3,12		Y		
3,1,12	**Fe**			Y
2,2,12				Y
1,3,12				
3,1,12	**Os**			Y
2,2,12				Y
1,3,12				
3,1,12	**Co**			Y
2,2,12		Y		
1,3,12				
3,1,12	**Ir**			Y
2,2,12			Y	Y
1,3,12			Y	Y
3,1,12	**Ni**	Y		
2,2,12		Y		
1,3,12				
3,1,12	**Pd**	Y		Y
2,2,12		Y		Y
1,3,12		Y		Y
3,1,12	**Pt**	Y		
2,2,12		Y		
1,3,12		Y		
3,1,12	**Cu**	Y		
2,2,12		Y		
1,3,12				
3,1,12	**Ag**			
2,2,12				
1,3,12				
3,1,12	**Au**	Y		
2,2,12		Y		
1,3,12		Y		
3,1,12	**Zn**		Y	
2,2,12		Y		
1,3,12		Y		
3,1,12	**Cd**		Y	
2,2,12			Y	
1,3,12			Y	
3,1,12	**In**	Y		
2,2,12		Y		
1,3,12		Y		
3,1,12	**Sn**			
2,2,12		Y		
1,3,12				
3,1,12	**Pb**			

2,2,12				
1,3,12				
3,1,12	**Bi**			
2,2,12				
1,3,12				

4.4.2 Effect of Secondary Element and Crystallite Size on Activity

Due to the structure sensitivity of ammonia decomposition over Ru, previous studies have identified optimal Ru particle sizes between 3 and 5 nm (*113*, *290*). Within this regime, there is a higher probability of the occurrence of B_5 sites, which consist of ensembles of five Ru atoms that have a three-fold hollow site and a bridge site in close proximity (*112*). This B_5 site has been hypothesized to be the most active site for ammonia decomposition over Ru. While it is has been shown that Ru step sites are more active than flat surfaces, there is no direct way to measure the activity or number of B_5 sites that may be present in a catalyst. Other works suggest that the optimal Ru particle sizes are closer to 3-5 nm (*291*), while others have observed that hemispherical particles between 7 – 8.5 nm are much more active than Ru particles that are roughly 1.5 nm in size (*114, 115*). Other works suggest that a broad distribution of Ru particle sizes is necessary for high ammonia decomposition activity, due to a synergistic effect that occurs between large and small Ru particles and the migration of H atoms from large to small Ru particles, thus promoting the hydrogenation of adsorbed NH_x species (*273*, *274*). For these reasons profile fitting was performed on each XRD pattern in order to determine the average crystallite size of RuO_2, $KRuO_4$ and KRu_4O_8. The profile fitting was used in order to determine the full-width half max (FWHM) of each Ru species reflection, after which the the average crystallite size was determined using the Scherrer's Equation. The average crystallite size for each Ru species present in each individual catalyst composition was then averaged together to provide a representative crystallite size for each catalyst. An example of the profile fitting is given in Figure 4.10 showing part of the XRD pattern from for the 1,3,12 RuMoK catalyst. The reflections for the three Ru species were fitted, using the reflections located at roughly 12.4°, 17.7° and 47.6° for KRu_4O_8, reflections located at 28.2°, 35.1°, 39.2°, 58.3° and 59.7° for RuO_2, and reflections located roughly at 26.4°, 27.8° and 31.7° for $KRuO_4$ (*54*, *126*). The position of these reflections will vary slight based on the interatomic distances of these species, which may change based on crystal stress, strain, or imperfect stoichiometry (substitutional doping). Additionally, the peak width can provide information on the crystal defects. Diffraction peaks can be described as a combination of both Gaussian and Lorentzian functions (*292*, *293*). A diffraction peak will exhibit Gaussian line broadening based on crystal strain, and will exhibit Lorentzian line broadening due to crystal size (*294*). Therefore, a commonly used function to fit diffraction peaks is the pseudo-Voigt function, which is a linear combination of Gaussian and Lorentzian functions. In this work, each crystalline reflection was fitted using a pseudo-Voigt peak fit in order to fit both the profile shape and peak width. For the amorphous diffraction peaks (ɣ-Al_2O_3), a split-Voigt function was used in order to capture the peak asymmetry. This was performed for each of the 99 catalyst compositions studied in the high throughput screen. The crystallite size was then compared to the measured activity at 300°C and in 1% NH3 at 30,000 mL/hr/g_{cat}.

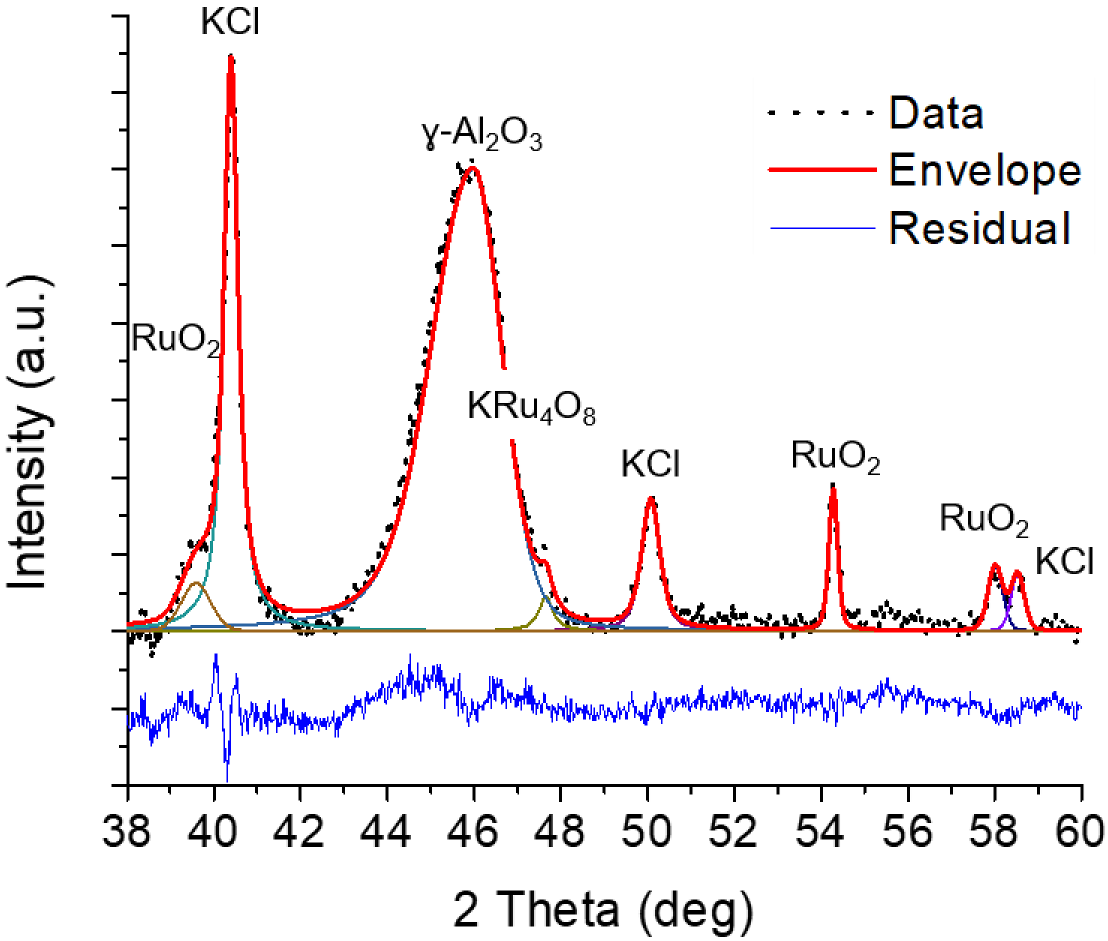

Figure 4.10. XRD pattern of 1,3,12 RuMoK showing the profile fit using Pseudo-Voight and Split-Voight fit and the residual after fitting from 38 – 60°.

Additionally, due to the variation in secondary metal, the effect of the catalyst composition was also probed to determine if particle size was dependent on the secondary metal or metal loadings. In order to make comparisons between activity and each catalyst, catalysts were grouped based on the weight loadings of each components, and then the atomic number of the secondary metal was used to differentiate between each of the catalysts within a constant weight loading. The average particle size as a function of NH_3 conversion for each catalyst is shown in Figure 4.1a for the 3,1,12 RuMK catalysts, Figure 4.1b for the 2,2,12 RuMK catalysts and Figure 4.1c for the 1,3,12 RuMK catalysts. Each figure contains a minimum of 17 data points. As the Ru loading decreased, in some instances the crystallite size becomes too small to accurately measure and identify due to the convolution of peaks.

For catalysts containing 3,1,12 RuMK weight loadings, the smallest Ru average particle sizes were catalysts containing Cu (average crystallite size = 9.85 nm, atomic # 29, NH_3 Conversion = 30%), Os (8.4 nm, #76, 28.2%), Pt (8.86 nm, #78, 28.5%), Au (8.48 nm, #79, 30.0%), and Ir (7.75 nm, #77, 100%). The largest particle sizes were those containing Y (29.51 nm, #39, 95.2%), Cr (28.06 nm, #24, 55.4%), Fe (26.45 nm, #26 and Co (31.46 nm, #27, 44%). For the higher weight loadings of Ru, those catalysts with smaller average crystallite size are also the most active over a broad range of secondary metals. Catalysts within the atomic # range of 30 – 40 exhibit poor performance at average particle size less than 15 nm. The catalysts within this atomic # range include Cd and Nb. There are other instances where we see that catalysts with larger particle sizes also perform well for ammonia decomposition, specifically substitution of Ru with Sc (24.28 nm, #30, 99.8%). As the amount of Ru decreases from 3% to 2% and then to 1%, we that the area of high activity becomes much more concentrated within a range of low average crystallite size and secondary metals with low atomic numbers.

Interestingly with the decrease in Ru weight loading, we do not see a consistent decrease in the average crystallite size. For example, catalysts containing Sc, the average particle sizes changes from 19.64 nm to 18.8 nm and the conversion decreases to 59.2% and then to 52.5% at 1,3,12 RuScK. For the Hf catalysts that exhibited very high activity (~80%) across all three catalyst compositions, but the average particle size increased from 8.46 nm to 16.33 nm and then decreased down to 7.94 nm at the 1,3,12 RuHfK catalyst.

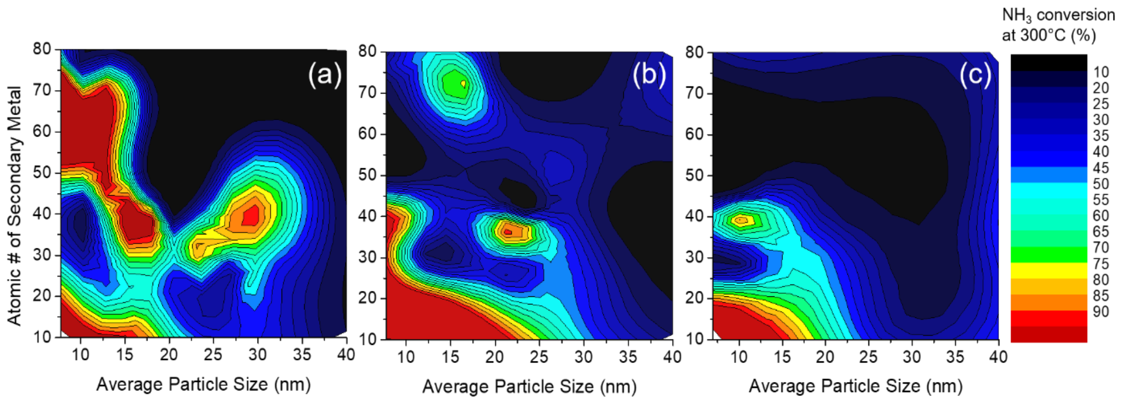

Figure 4.11. NH_3 conversion at 300°C as a function of average Ru particle size and the atomic number of the secondary metal. (a) 3,1,12 RuMK, (b) 2,2,12 RuMK and (c) 1,3,12 RuMK where M refers to the secondary metal.

So, there is a strong interplay occurring between the composition, secondary metal and average particle size in addition to a variety of other features, that makes elucidating trends in such a complicated data set very difficult.

For these reasons, machine learning (ML) has more recently began to be utilized to guide catalyst discovery and optimization for a few catalytic reactions including methane oxidative coupling, olefine epoxidation and propane ammoxidation (*295–298*). For studies targeted at discovering new catalyst compositions, rudimentary heuristics have been able to be determined to create better performing catalysts within very specific composition ranges and do not provide information outside of the original design space (*147*). Work in our group has recently shown that we can utilize experimental data to predict ammonia decomposition catalysts very accurately while using small amounts of data and outside of the range of compositions used in the training data set. Additionally, we can extract features from the data set in order to gain insight into what properties are important for influencing catalytic activity. The development, application and predicative capabilities of the machine learning algorithm developed for this purpose can be found elsewhere (*299*). The importance of the feature extraction will be briefly highlighted here.

4.5 Machine Learning for Catalyst Feature Extraction

Previously our group has developed a methodology that combines ML and high throughput experimentation to make catalyst predictions. We utilize a variety of operating parameters, catalyst synthesis conditions, and chemical features that can be easily found in databases. These include electronic, geometric, and atomic properties of elements used in order to describe each catalyst. These properties, or features, are then used to make predictions for catalyst activity and to predict active catalyst compositions that the algorithm does not have information about. The body of work demonstrates that we can utilize as little as three catalysts as input data to the algorithm to accurately predict the activity of other catalysts containing different metals for ammonia decomposition activity (*147*). Due to the complexity of the data set studied from the high throughput screening, machine learning feature extraction is a powerful tool that can help us ascertain which properties are most influential in determining catalytic activity. Figure 4. shows the highest rank features determined for a random forest model utilizing a leave one out cross validation to make predictions on catalyst activity. The determination for which values of feature importance denoted an actually meaningful feature can be found elsewhere (*147, 299*).

The algorithm determined that changes in temperature was the most important feature determining catalytic activity. As most all reactions exhibit endothermicity or exothermicity, this offers no new insight into the inner workings of the catalyst surface but does provide evidence in the correctness of the model to learn, as variation in temperature is indeed most influential to changes in activity. The next most important features include number of d-shell valence electrons, electronegativity, covalent radius, adjusted work function and the number of valence electrons. These features are all related to the electronic configuration of the catalysts. Correlations between reactivity of different metal surfaces and their electronic environment have been studied for decades. Changes in the catalysts composition and proximity to various promoters will affect the strength of the bond formed between a metal surface and the adsorbate which will influence the reactivity of that metal surface for different catalytic reactions (*300*, *301*). For example, the number of d-shell valence electrons for late transition and noble metal surfaces has been directly correlated to the reactivity of these metals to small probe molecules (*300*). However, this feature alone is not enough to predict catalytic activity, and this has been experimentally validated by Ganley et al. (*78*) over monometallic catalysts for ammonia decomposition. The position of the d-band of different metals relative to their Fermi levels have also been shown to accurately describe the reactivity of these metals (commonly referred to has d-band theory) (*79*, *80*, *141*, *302*, *303*). This theory has been extensively used in computational catalysis to predict reactivity of different metal surfaces. Exceptions to the d-band theory include situations where there are large differences in electronegativities between the adsorbate and the substrate when the substrate has a nearly full d-band (*304–306*). Modification of the adsorption energy calculations can be modified to include the Pauli repulsion, Pauli electronegativity, work function and various local chemical environment information in order to enhance the accuracy of these models (*307–309*). Interestingly, the algorithm was

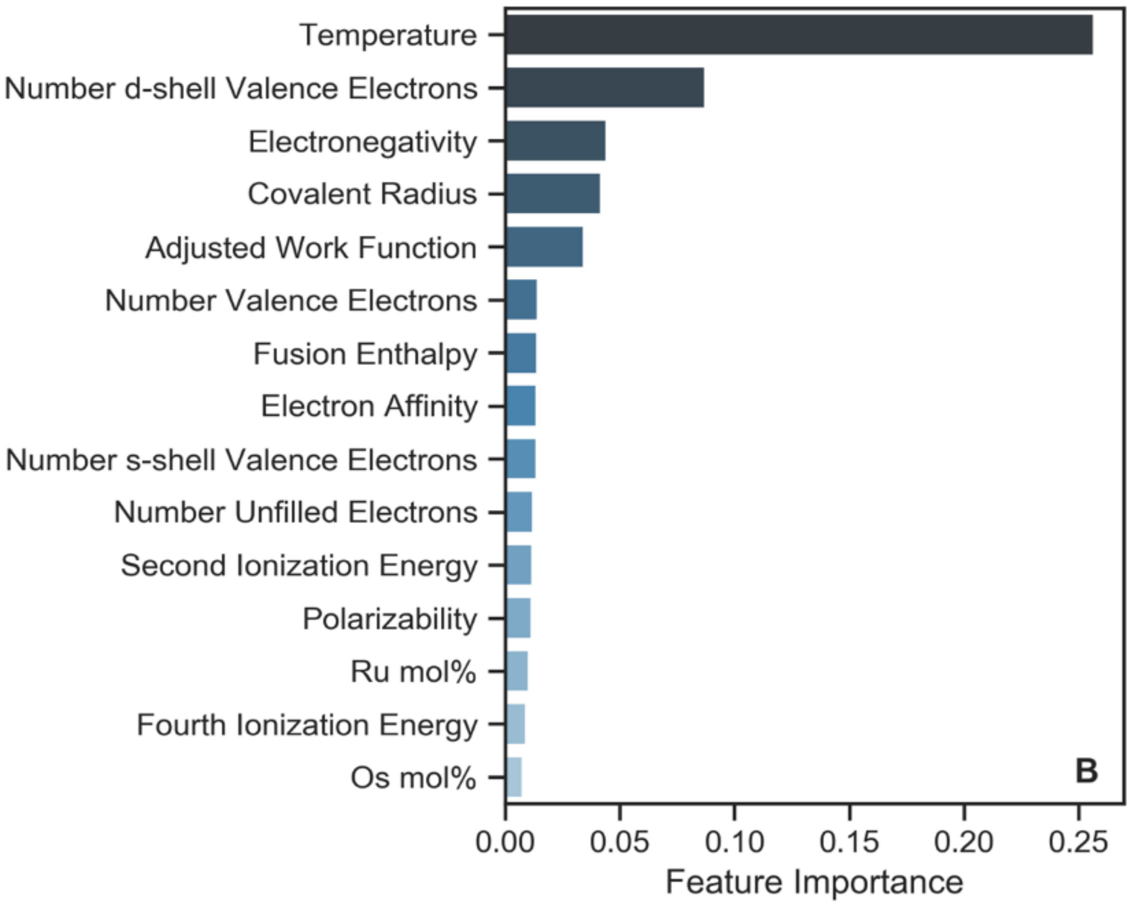

Figure 4.12. Highest ranked features according to their feature importance for determining ammonia decomposition activity for catalysts with 3,1,12 RuMK, 2,2,12 RuMK and 1,3,12 RuMK weight loadings. Adapted from ref *(77)*.

able to decipher these features as most important without have any prior knowledge on the reaction or information of the binding energies pertinent to ammonia decomposition. Since this study incorporates not only transition and noble metals but alkali, rare earth, and alkaline earth metals, this may result in bias towards more electronic features such as the electronegativity and covalent radius due to the different interactions between these elements with the active metal substrate and the adsorbate. The next 9 most important features include less easily correlateable features such as the Os mol%. We have seen that removable of these nine features very slightly decreases the overall accuracy of the machine learning algorithm predictions and provide little meaningful insight (*299*).

We have looked at some of these individual features and their 2-way interactions and have found some general trends within them, for example, a low mean absolute deviation (MAD) of the catalyst work function and a low MAD of the number of d-shell valence electrons results in a catalyst with higher activity. This is exhibited in the contour plot shown in Figure 4., which shows these two variables as a function of the NH_3 conversion measured at 300°C and 1% NH_3 concentration. However, as displayed in Figure 4.1, we also saw a general trend that decreasing particle size and lower atomic number of the secondary element also resulted in a catalyst with higher activity. The convolution of these multiple variables exhibits the power of machine learning to disseminate the relationship between activity and multiple variables, such to a degree that cannot be generalized by the human mind. However, with these conclusions, future iterations of catalyst design can be implemented based off these trends discovered here.

4.6 Investigation of Sr and Fe Catalysts

This section is dedicated to understanding the influence of Sr and Fe on ammonia decomposition kinetics and reactivity. Sr addition of the K promoted Ru based catalysts allowed for the Ru content to be decreased down to 1% Ru, while still maintaining extremely high activity at low temperatures and in a flow of 1% NH_3/Ar. While Mg, Ca and Ba have been thoroughly studied for ammonia synthesis, there is very little information about the other alkaline earth metals such as Sr. In contrast, the Fe containing catalysts became less active as the amount of Fe increased and the amount of Ru decreased, even though Fe has also been shown to be an effective ammonia decomposition catalyst. Typically, Fe containing catalysts are prone to forming nitrides and thus techniques such as core shell encapsulation of the Fe nanoparticles are taken to avoid this (*310*, *311*). For

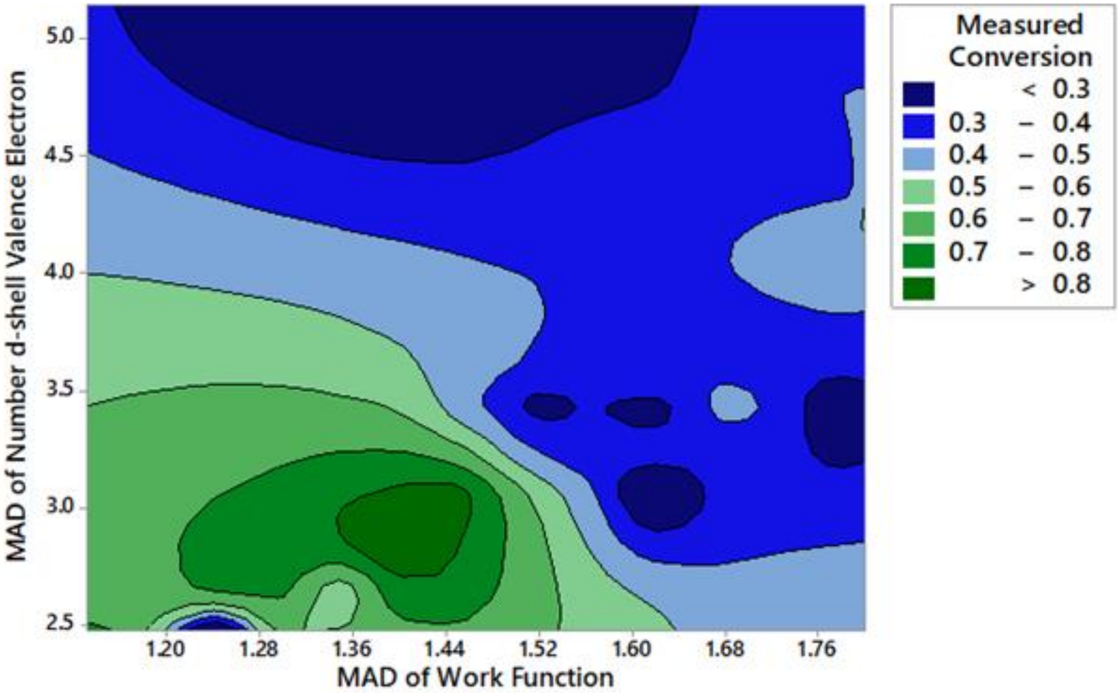

Figure 4.13. Ammonia decomposition activity at 300°C, 1% NH_3/Ar and 30,000 mL/hr/g_{cat} as a function of the mean absolute deviation (MAD) of the number of d-shell valence electrons and the MAD of the catalyst work function.

these reasons, Sr and Fe were chosen to discern trends in catalytic activity under high concentrations of ammonia, for their long-term stability, and to grasp a better understanding of the ammonia decomposition kinetics over the Sr and Fe containing catalysts.

The apparent activation energies were calculated for each of the 3 weight ratios of Sr and Fe catalysts under differential conditions (2 -12% conversion) and under 100% NH_3 at a space velocity of 5,400 mL/hr/g_{cat} and compared to the apparent activation energy of the 4 Ru and 4,12 RuK catalysts under identical conditions. Before measurements were taken, the Weisz-Prater criterion was used to determine the absence of internal mass transfer resistances (*312*, *313*). The Weis-Prater criterion was used to determine the absence of internal diffusion resistances. The Weis-Prater criterion is given by equation 4.1:

$$\frac{r'_A \rho_c R_P^2}{D_e C_{AS}} \ll 1 \qquad (4.1)$$

where r'_A= measured NH_3 reaction rate (mol/kg/s), ρ_c= catalyst pellet density (750 kg/m^3), R_P^2= pellet radius (2.25x10^{-5} m), D_e=effective diffusivity of NH_3 in the catalyst pellet and C_{AS} = NH_3 concentration at the pellet surface (16.7 mol/m^3). Effective diffusivity is calculated by equation 4.2:

$$D_e = \frac{D_{NH3\text{-}H2}\phi_p \sigma}{\tau} \qquad (4.2)$$

where ϕ_p= pellet porosity, σ is the constriction factor, and τ is the tortuosity. Typical values for a catalyst pellet are ϕ_p=0.4, σ=0.8, and τ= 3 (values adapted from ref. 64). D_{NH3-H2} is the diffusion coefficient of NH_3 in H_2 at 400°C and is given in equation (4.3):

$$D_{NH3\text{-}H2} = \frac{0.00266T^{3/2}}{PM_{NH3\text{-}H2}^{1/2}\sigma_{NH3\text{-}H2}^2\Omega_D} \qquad (4.3)$$

where T is the temperature (K), P is the pressure (bar), $M_{NH3\text{-}H2}=2*[(1/M_{NH3})+(1/M_{H2})]^{-1}$, M_{NH3}=molecular weight of NH_3, M_{H2} = molecular weight of H_2, σ_{NH3-H2} = characteristic length (Å) and Ω_D is the diffusion collision integral (dimensionless) (*313*). D_e was found to be 3.51 x10^{-4} m^2/s.

The measured reaction rate at 400°C for the unpromoted 4 Ru catalyst is 2.07 mol/kg/s. The LHS of the Weis-Prater criterion equates to 1.34x10^{-3} which is much less than 1. Therefore, the criterion is satisfied. Figure 4. shows the Arrhenius plots for the

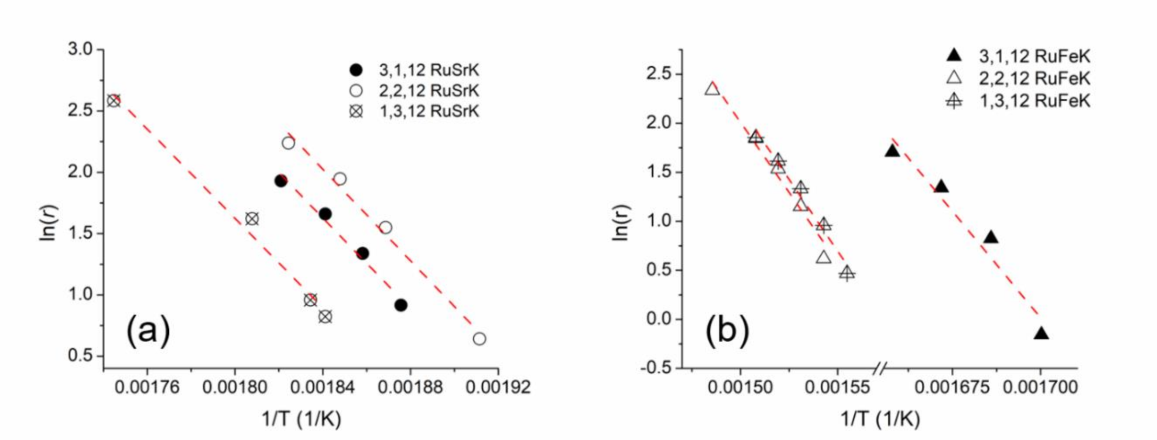

Figure 4.14. Arrhenius plot of (a) RuSrK and (b) RuFeK based catalysts. Reaction conditions: 100% NH3, 5,400 mL/hr/gcat and atmospheric pressure. Apparent activation energies were conducted under differential conditions.

RuSrK and RuFeK catalysts. Here, measurements were conducted under differential conditions in order to capture the kinetically limited regime of each catalyst. Additionally, H_2 chemisorption was performed on each catalyst in order to calculate the number of exposed active sites present. Turnover frequencies (TOF) were calculated at 350°C and 400°C by normalizing the rate of reaction to the number of exposed Ru atoms were gram of Ru, which was measured through H_2 chemisorption. The H_2 uptake, TOF and apparent activation energies are shown in Table 4.. The addition of either Sr or Fe to the Ru based catalyst resulted in an increase the apparent activation energy for each catalyst regardless of the compositional weight loadings. The 4,12 RuK catalyst exhibited an activation energy of 65.7 ± 7 kJ/mol, where the Sr containing catalysts had apparent activation energies between 149.6 and 156.4 kJ/mol, and the Fe containing catalysts had values vastly larger values between 248 and 251 kJ/mol. The apparent activation energies for the Fe containing catalysts is even higher than that which has been calculated for the rate determining step of the recombination and desorption of molecular N_2 on a Ru (001) crystal, of 184 kJ/mol (*81*). kJ/mol. Therefore, Fe dramatically inhibits the rate of reaction with even substitution of just 1% Ru with Fe in relation to the 4,12 RuK catalyst. However, an increase in the apparent activation energy may suggest that the rate determining step is changing with the addition of the second metal. The catalysts were run in 100% NH3, 5,400 mL/hr/g_{cat} and at atmospheric pressure. Comparing the TOF of the Fe based catalysts to those of the 4 Ru and 4,12 RuK at 350°C and at 400°C, we see that the TOF decreases from 0.97 to 0.41 and finally to 0.28 with decreasing Ru loading. The Sr based catalysts also increase the apparent activation significantly from the 4,12 RuK catalyst and only slight in regards to the unpromoted 4 Ru catalyst. Therefore, we can assume that the addition of Fe is indeed negative to the overall performance of the catalyst and does not seem to modify the Ru active sites in any matter. Instead, we see that the Ru active sites are simply being replaced with less active Fe sites for ammonia decomposition. In the case of Sr, the apparent activation energy slightly increased with increasing Sr loading from 149.6 ± 4.1 kJ/mol to 153.7 ± 2.4 kJ/mol to 156.4 ± 1.6 kJ/mol. These values are slightly lower than the 184 kJ/mol required for the recombinative desorption of N_2 from Ru stepped surfaces. Additionally, the TOF for each of the Sr catalysts actually increases with decreasing Ru loading from 0.88 s^{-1} for the 3,1,12 RuSrK catalyst, to 1.78 s^{-1} for the 1,3,12 RuSrK catalyst, which is dramatically more active than the 4,12 RuK catalyst. Additionally, the 1,3,12 RuSrK catalyst exhibits over twice the apparent activation energy of the 4,12 RuK catalyst. We also observe a decrease in the H_2 uptake of the Sr based catalysts with increasing Sr loading. This suggests that there are less Ru active sites exposed as the loading of Ru decreases. However, the apparent activation energy stays relatively unchanged while the TOF increases. This suggests that the Sr is electronically modifying the Ru active sites and may be changing the rate determining step from that of 4,12 RuK.

Table 4.2. H_2 uptake, turnover frequency (TOF) and apparent activation energies (Ea) for Sr and Fe containing catalysts compared to 4 Ru and 4,12 RuK catalysts where the H_2 uptake for each catalyst was calculated from H_2 chemisorption experiments assuming a 1:1 ratio.

Catalyst	H_2 Uptake (μmol H_2/g)	TOF (1/s)		E_a (kJ/mol)
		350°C	400°C	
4 Ru	6.50	0.00	0.14	125.2±8.9
4,12 RuK	4.70	0.26	0.33	65.7±7.7
3,1,12 RuSrK	1.90	0.43	0.88	149.6±4.1
2,2,12 RuSrK	0.90	0.81	1.38	153.7±2.4
1,3,12 RuSrK	0.75	1.10	1.78	156.4±1.6
3,1,12 RuFeK	0.76	0.35	0.97	248.1±3.0
2,2,12 RuFeK	0.10	0.03	0.41	226.6±2.9
1,3,12 RuFeK	1.20	0.00	0.28	250.9±7.6

For example, microkinetic modeling has calculated the dehydrogenation of adsorbed NH_3 to be roughly 44 kJ/mol, the dehydrogenation of NH_2 to be 65.3 kJ/mol and the hydrogenation of adsorbed NH to be the highest with 161.5 kJ/mol (*84*). Therefore, Sr seems to either change the rate determining step from the dehydrogenation of NH_2 species to the dehydrogenation of NH (or some combination thereof) or may act to electronically modify the Ru active sites. Further experiments have shown that Sr supported catalysts are not active alone for ammonia decomposition (not shown). The changes in rate limiting steps with different metal surfaces has previously been determined (*78*), however little work has been done on determining how the rate limiting step changes with the different one or multiple promoters.

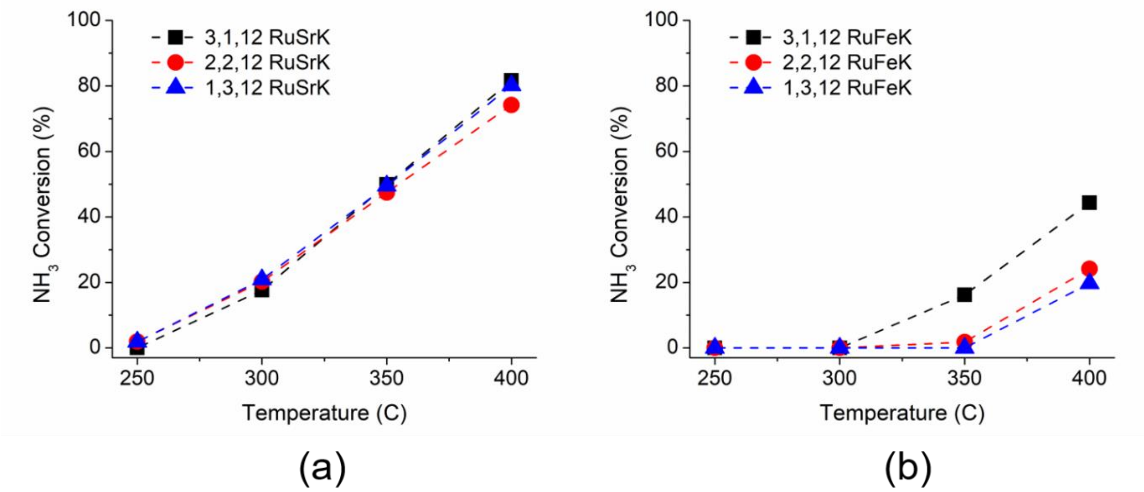

Figure 4.15. Ammonia decomposition activity of (a) 3,1,12 RuSrK (black squares) 2,2,12 RuSrK (red circles) and 1,3,12 RuSrK (blue triangles) and (b) 3,1,12 RuFeK (black squares) 2,2,12 RuFeK (red circles) and 1,3,12 RuFeK (blue triangles). Reaction conditions: 100% NH_3, 5,400 mL/hr/g_{cat} and atmospheric pressure.

Next, the ammonia decomposition activity of these Sr and Fe based catalyst was further tested in higher concentrations of ammonia, in order to determine the accuracy of fails and hits in the high throughput experimentation and also to determine how good these catalysts may be in more realistic conditions for H_2 generation from ammonia decomposition. The activity of the Sr and Fe containing catalysts under higher concentrations of ammonia in a plug flow reactor set up. The results are shown in Figure 4.. The catalysts were tested from 250°C to 400°C in increments of 50°C. The reactions were run under 100% NH_3 at a space velocity of 5,400 mL/hr/g_{cat} and at atmospheric pressure. It has been reported that there is a negative dependence on the partial pressure of ammonia on the rate of reaction (*84*). Therefore, in general we expect to see a decrease in the conversion as the inlet concentration of ammonia is increased. So, upon increasing the concentration from 1% NH_3 in the high throughput screen to 100% $NH_{3,}$ all catalysts shown a decrease in conversion. The Sr based catalysts exhibited similar performance to each other under these conditions, while the 3,1,12 RuFeK catalyst showed much better performance than the 2,2,12 RuFeK or the 1,3,12 RuFeK catalysts. Additionally, all six catalysts showed a marked decline in activity at the lower temperatures of 250°C and 300°C. However, we see similar trends compared to what was exhibited in the high throughput screening, where Sr based catalysts showed excellent activity at lower temperatures (≤ 400°C).

4.6.1 CO Adsorption over Ru based Catalysts

The adsorption configuration of CO onto a metal surface can provide insight into the strength of the bond between the metal and CO. Different metal sites will adsorb CO in various configurations, so CO adsorption can also provide insight into active sites that may be present in some catalysts and not others. CO adsorption was investigated through FTIR spectroscopy. The adsorption of CO at room temperature for 4 Ru, 4,12 RuK, 1,3,12 RuSrK and 1,3,12 RuFeK are given in Figure 4.16. The 1,3,12 RuSrK and 1,3,12 RuFeK were chosen to determine if there were different active sites present in the 1,3,12 RuSrK which exhibited high conversion and TOF, in contrast to the 1,3,12 RuFeK catalyst.

The baseline 4 Ru (black trace) catalyst exhibits three primary features: a weak band at 2135 cm^{-1}, a strong band at 2078 cm^{-1} and another weak band at 2015 cm^{-1}. Studies of CO adsorption on Ru often report a weak band at 2135 cm^{-1} in conjunction with a band at 2078 cm^{-1}, which is ascribed to the vibration of multicarbonyl surface species (*314–316*). The 2015 cm^{-1} exhibited in the 4 Ru catalyst has been attributed to the vibration of dicarbonyl species, as well as the adsorption of CO on low coordinated Ru or high energy defect sites (*316*). These bands are suppressed with the addition of K, which has been previously observed by other groups (*169, 317*). In contrast, with the addition of K, the

4,12 RuK catalyst (blue trace) exhibits bands at 2165 cm^{-1}, 2033 cm^{-1} and a broad feature from 1995 cm^{-1} to 1850 cm^{-1}. This broad feature is also present in the 1,3,12 RuSrK and 1,3,12 RuFeK catalyst, albeit the peak maxima shift slightly in each spectra. Alkali addition to metal catalysts have been known to largely affect the interactions of CO in the low frequency range. This is due to the interactions of CO with an electropositive center, this weakening the bond between C and O, and making it more reactive. For example, the adsorption of CO on K pre-covered Ru (0001) crystals have been shown to be a function of the CO and K coverage, and that K addition can shift the CO stretching frequency by as much as 600 cm-1 (materials 73-75). Other studies have reported that with the addition of K, bands become broader and more asymmetrical with bands located at 1995 cm^{-1}, 1950 cm^{-1} and 1940 cm^{-1} (*169*, *317*). The suppression of these bands with K has been hypothesized to be a consequence of blocking low coordinated Ru sites, which in turn suppresses hydrogen adsorption (*317*). With the addition of K, we do indeed see a decrease in the H_2 uptake at constant Ru loading during H_2 chemisorption experiments (Table 4.). For the 4,12 RuK catalyst, the band located at 2033 cm^{-1} may be attributed to linearly adsorbed CO. The position of this band has been shown to be a function of CO coverage over the metal surface (*169*, *314–318*), due to dipole-dipole interactions between neighboring CO molecules. This peak is not present in the 1,3,12 RuFeK catalyst, but is in the 1,3,12 RuSrK spectra. The addition of Fe may act to suppress the adsorption of CO on Ru, as this has been previously reported for Rh/SiO_2 catalysts when Fe was added to the catalyst (*319*, *320*). Furthermore, the 1,3,12 RuSrK catalyst shows maxima located at 1950 cm^{-1} and 1894 cm^{-1}, while the 1,3,12 RuFeK catalyst has maxima located at 1976 cm^{-1}, 1925 cm^{-1} and 1903 cm^{-1}. Additionally, both catalysts in addition to the 4,12 RuK catalyst

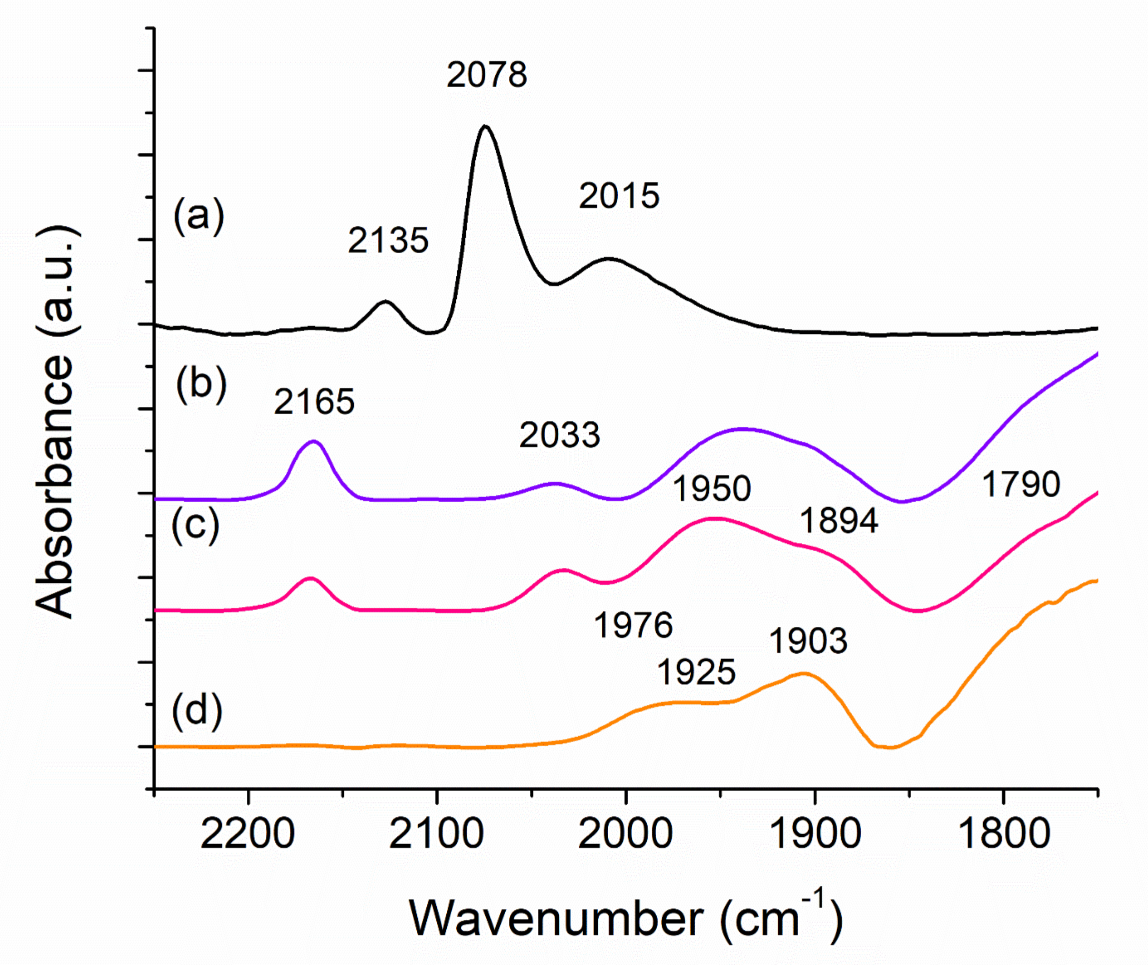

Figure 4.16. FTIR spectra of CO adsorbed on (a) 4 Ru (b) 4,12 RuK (c) 1,3,12 RuSrK and (d) 1,3,12 RuFeK.

exhibit a broad, intense shoulder at 1790 cm^{-1} which may be attributed to bridge bonded CO (*181*, *316*). This stretch is not observed in the 4 Ru catalyst and has previously been reported in K promoted Ru systems using 3% K (materials 68, 76). Single crystal studies have investigated bridge bonded CO on alkali promoted Pt (111) and Rh (111) surfaces and have found that the amount of bridge bonded CO increases with alkali coverage (*321*, *322*). Therefore, we may see a dramatic increase in intensity of this band as the alkali loading is much higher here than reported elsewhere. Ultimately, the electropositive nature of Sr may act to weaken the CO bond through further charge transfer resulting in a larger relative intensity of bridge bonded CO especially with the lower Ru content, with respect to the 4,12 RuK catalyst.

4.7 Conclusions

In this chapter we explored various catalysts geared towards lowering the loading of Ru content compared to a 4% Ru catalyst for ammonia decomposition at low temperatures. The baseline catalyst used for comparison was a previously optimized catalyst containing 4% Ru and 12% K supported on γ-Al_2O_3. Substitution of Ru was first carried out by using various transition and precious metal catalysts, however no combination of Ru with a second metal was able to perform better than a catalyst containing 4% Ru. This is because of the high intrinsic activity exhibited by Ru for this activity, as it is able to bind N_2 neither too strongly or too weakly and thus most easily facilitates the rate determining step for ammonia decomposition. Next, high throughput experimentation was used to explore an even wider parameter space for low Ru content ammonia decomposition catalysts by variously not only the secondar metal but also the composition of Ru and the secondary metal in combination with K. Catalysts contained the compositional loadings of either 1,3,12 RuMK, 2,2,12 RuMK or 3,1,12 RuMK, where M = Na, K, Mg, Ca, Sr, Sc, Y, Zr, Hf, Ta, Nb, Cr, Mo, W, Mn, Re, Fe, Os, Co, Rh, Ir, Ni< Pd, Pt, Cu, Ag, Au , Zn, Cd, In, Sn, Pb or Bi. This resulted in over 100 catalyst formulations, many of which have not previously been explored for ammonia decomposition. In order to quickly and accurately test this large number of catalysts, a 16-channel parallel plug flow reactor system was used for screening of ammonia decomposition catalysts in 1% NH_3/Ar from 250°C to 450°C. Quantification of each of the 16 reactors was performed in parallel by using spatially resolved FT-IR. A focal plane array based detector was used in order to gain the spatial resolution needed to quantify in parallel. The catalysts were compared to the activity of a 4,12 RuK catalyst under identical operating conditions, and catalysts that performed better than this baseline with less Ru were considered to be successful hits in the screen. These catalysts included many different substituted elements including Mg, Ca, Sr, Sc, Zr, Hf, Ta, Rh and Ir. With only 1% Ru, Sr, Y, Zr and Hf substitution were able to dramatically outperform the 4,12 RuK catalyst at 300°C with only 75% of the Ru content.

The comprehensive catalyst data set synthesized here was further investigated through XRD analysis, where XRD patterns for each of the 100 catalysts were collected and analyzed through profile fitting and crystal identification. While there was no correlation found between crystal phase present and ammonia decomposition activity, we found a general trend within average crystallite size, secondary element substation and ammonia decomposition activity. At 300°C, catalysts containing smaller average Ru crystallite sizes in conjunction with smaller atomic number secondary elements exhibited higher ammonia decomposition reactivity. This trend became more evident at each compositional loading, where the most active catalysts of the 1,3,12 RuMK catalysts had the smallest average particle size and the small atomic number of the secondary element.

However, due to the vast number of other variables present here that may be influencing activity, a random forest machine learning algorithm was developed to determine which features of the catalysts most heavily influenced the activity. The algorithm showed much promise in predicting catalytic activity by using only few catalysts as a training set. From this, we were able to determine that many electronic features were the most important in influencing the activity from catalyst to catalyst. These include number of d-shell valence electrons, electronegativity, covalent radius and work function.

Ultimately, we have shown that high throughput experimentation with an expertly chosen design space in combination with machine learning, can ultimately reduce the cost and time necessary for material discovery.

To better understand why some of these catalysts performed better than others, further investigation into Sr and Fe based catalysts was conducted by determining the apparent activation energy, measuring the TOF, H_2 uptake, and probing the kind of Ru active sites present through CO adsorption. With the 1,3,12 RuSrK catalyst, the TOF was increased to 1.78 s^{-1}, compared to 0.88 s^{-1} exhibited by the baseline 4,12 RuK catalyst. Additionally, the apparent activation energy was increased from 65.7 kJ/mol for 4,12 RuK to 149.7 kJ/mol for the 3,1,12 RuSrK catalyst. The apparent activation energy further increased with increasing Sr loading to 156.4 kJ/mol. With increasing TOF and increasing apparent activation energy, this suggests that Sr acts to electronically modify the exposed Ru active sites and may possibly result in a change in the rate determining step over Ru based on rate determining steps calculated through microkinetic modeling. By probing the metal surfaces with CO adsorption, we determined that the Sr based catalysts weakened the CO bonds on Ru sites, and also increased the relative intensity of strongly adsorbed linear CO. This may be analogous to the weakening of the N-H bonds of adsorbed ammonia and thus more easily facilitating the dehydrogenation steps.

CHAPTER 5

CONCLUSIONS & OUTLOOK

This body of work explored the discovery of ammonia decomposition catalysts using high throughput experimentation, as well understanding the use of hollandite as an ammonia decomposition catalyst. Ammonia decomposition is a viable solution to hydrogen storage and transportation, due to its high energy density, ease of transportation, and liquification at 8 bar and 298K. Currently, the issues with ammonia decomposition are that the cost of the Ru based catalyst are much too high for the large-scale manufacturing of the catalyst to be realistic. Additionally, these catalysts need to be able to reach near complete conversion at low temperatures, at or below 450°C, in order for this technology to be pair with PEMFC, which can utilize the liberated hydrogen as a source of energy. Ammonia decomposition occurs through sequential dehydrogenation steps, followed by the recombination and desorption of molecular hydrogen and nitrogen. Typically, the rate limiting step for this reaction is the recombination and desorption of molecular nitrogen. However, catalysts also suffer from hydrogen poisoning at higher rates of reactions when more hydrogen is generated from the decomposition of ammonia. The current body of literature has explored optimization of Ru based catalysts, but typically these loadings are in excess of 5% or more or require complex synthesis methods such as making carbon nanotubes for supports. Other transition metals for this reaction include Fe, Co, and Ni, however, these metals are intrinsically less active than Ru and exhibit poor performance at the temperatures of interest.

In most cases, complete conversion is not met until roughly 600°C. Ultimately, current catalysts are severely kinetically limited in the lower temperature range for this simple reaction. There has been little work involving the discovery of multi component catalysts for low temperature ammonia decomposition, and this fact is what motivated this body of work presented here.

Previous work from our group used response surface methodology to optimize the promoter and promoter loading for a 4% Ru catalyst. Through this study, they determined that 4% Ru 12%K catalyst was the most active for low temperature ammonia decomposition, and found that structurally, the catalyst consisted of KRu_4O_8 hollandite as the Ru structure. The body of work presented here was aimed at understanding under what conditions this structure could be form through impregnation techniques, as prior synthesis methods for this structure involve solid state reactions, flux methods and hydrothermal treatments. In Chapter 3, we investigated multiple variables involving the synthesis of hollandite, as well as determined what the working state of the 4% Ru 12% K catalyst was before ammonia decomposition reactions and began to unravel the reduction mechanism of the hollandite structure. First, we investigated three different impregnation methods, dry impregnation, incipiently wet impregnation, and strong electrostatic adsorption. We determined that both dry and incipiently wet impregnation was able to form the hollandite structure. The SEA method instead produced highly dispersed K on the alumina support, with very small RuO_2 nanoparticles. Additionally, we were able to determine that most of the K used in the 4,12 RuK catalyst chemically modifies the alumina support by interaction with the surface hydroxyl groups. This creates a $KAl(OH)_2CO_3$ compound that is known to enhance the basicity of the support. We found that the addition of K to the Ru based catalyst also lowers the apparent activation energy from 125.2 kJ/mol to 65.7 kJ/mol/. This is most likely due to the electronic enhancement of the Ru active sites by electron donation from K.

Next, we investigated whether or not which metal precursors were chosen for the incipient wetness impregnation synthesis had any effect of hollandite formation. This involved two different Ru precursors and three different K precursors. This study determined that hollandite is able to be formed with the use of $RuCl_3$ in combination with KCH_3COO and KOH, and not with $Ru(acac)_3$ in combination with either KCH_3COO, KOH or KNO_3. Next, we look at dilution volume use during the incipient wetness impregnation method on the relative abundance of hollandite and $KRuO_4$ formation on the 4,12 RuK catalyst. The impregnation solution varied from 5 mL to 20 mL, which correlates to 4 impregnations up to 17 impregnations. We were able to determine that with lower solution volumes, the ratio of hollandite to KRu_4O_8 was larger through the basis of XRD analysis and decreased with increasing solution volume. We tested these catalysts for their ammonia decomposition activity and an optimal dilution volume of 6 mL was determined to have the highest activity at 300°C. Next, we looked at the effect of impregnation order on the formation of hollandite. This provided insight into how the hollandite is formed, whether or not Ru and K require intimate mixing to form some sort of layered precursor structure to the hollandite or whether they grow epitaxially. The impregnation was changed from co-impregnation of Ru and K to sequential impregnation of Ru followed by K, and then K followed by Ru. These catalysts showed that when Ru was impregnated onto the catalyst first, we could forego the formation of KCl. Additionally, when Ru is impregnated first, hollandite was formed on the catalyst, but this was not the case when K was first impregnated. This suggests that Ru acts as nucleation sites for the formation of hollandite.

Next, we looked at variables concerning the wet impregnation synthesis, specifically the duration of the calcine treatment and also the temperature at which the solution is evaporated during the wet impregnation and whether or not these variables had any effect on the formation of hollandite for the 4,12 RuK catalyst. Specifically, we looked at evaporation temperatures of 60°C, 90°C, 120°C and 150°C and calcine durations of 1 hr, 3 hr and 5 hr. We determined that at lowering evaporation temperatures of 60°C and 90°C, the hollandite structure was able to be formed after calcining at 550°C for either 1, 3 or 5 hr, but at higher temperatures, the hollandite could not form regardless of the calcine temperature. The primary structure present instead of $KRuO_4$. When these catalysts were tested for ammonia decomposition, we found that an evaporation temperature of 90°C and a calcine duration of 1 hr resulted in the highest activity at 300°C in 10% NH3/Ar and at a space velocity of 30,000 $mL/hr/g_{cat}$. Lastly we looked at the effect of lowering the K loading on ammonia decomposition activity, as the original study did not investigate loadings below 12%, but looked at loadings up to 36%. Here, we synthesized 4% Ru catalysts with various K loadings from 0.5% to 15%, as well as 1% Ru catalysts with various K loadings from 0.5% to 15%. Interestingly, both the 1% Ru and 4% Ru had an optimal K loading of 12%. This is most likely due to the fact that K is utilized in the catalyst in multiple ways, and not simply deposited in close proximity to Ru to enhance activity. In addition to electronic enhancement, K also chemically modifies the surface of the alumina has previously mentioned, and also acts to alleviate poisoning from Cl anions leftover from the synthesis, by forming bulk KCl on the catalyst. Based on theoretical calculations of the uptake of K^+ on γ-Al_2O_3, the maximum uptake of K^+ on our support would be 3.56 mmol of K^+. In addition, if all the Cl^- interact to form KCl, that would account for an additional 2.37 mmol of K^+. These two uses of K would account for roughly 97% utilization of the K^+.

In Chapter 3, the working state of the catalyst was also investigated. Mainly, we wanted to determine whether or not the KRu_4O_8 hollandite structure was the active site during the ammonia decomposition reaction or not. To determine this, the 4,12 RuK catalyst after H_2 reduction was studied using SEM, TEM and EDX. From SEM analysis, the nanorod structures clearly underwent some degradation to form worm like structures on the surface of the catalyst, which were further degraded after exposure to ammonia. Elemental mapping confirmed that these worm-like structures were composed of Ru and Cl, with K being highly dispersed about the surface of the support. TEM imaging showed a clearer image of these rods in their fresh, reduced and spent state and measuring the diameter of the rods determined that they shrink from an average diameter of 27.5 nm to 23 nm after reduction. The size does not further decrease after exposure to ammonia. XRD analysis showed that the rods are composed of metallic Ru after reduction, and therefore we can safely confirm that they completely decompose before the ammonia decomposition reaction. H2-TPR was further used to reducibility of the hollandite structure compared to 4% Ru catalyst. While the 4% Ru catalyst showed typicaly reduction peaks for RuO2 as well as uncalcined RuCl3 between the range of 100 – 200 °C, the 4% Ru, 12%K catalyst had two major, broad reduction events. The low temperature event occurred between 75°C and 200°C with maxima located at 120°C, 144°C and 156°C, and an even larger high temperature event between 275°C and 500°C, with a maximum at 345°C. The reduction of hollandite and the secondary phase formed during synthesis $KRuO_4$, is not known.

Therefore, we further probed the reducibility of the catalyst through *in-situ* XRD measurements to corroborate the reduction events with the disappearance of the major XRD reflections of the two Ru species. Interestingly, we found that both the $KRuO_4$ and hollandite structure reduce by 150°C, and that metallic Ru did not appear until roughly 200°C, indicating that some sort of intermediary phase occurs before the hollandite reduces to metallic Ru. Alternatively, the crystallite size of the Ru particles could have been too small to be seen with XRD. Regardless, this gave us inside into the reduction temperature of the catalyst, and that all of the metal oxides species reduce by 150°C. Additionally we saw that the crystallite size of metallic Ru increases with increasing temperature all the way up to our typical reduction temperature of 450°C. The particle size increased from 7.4 nm to 16.2 nm. The morphology of catalysts reduced at 250°C, 350°C and 450°C was analyzed using SEM. We found that the metallic Ru nanosegments became much more stalky with increasing reduction temperature. Additionally, the effect of reduction temperature of the ammonia decomposition reactivity of the catalyst was measured. Catalysts reduced at 250°C and 350°C showed the same activity, even with differences in morphology and crystallite size. The catalyst when reduced at 450°C, showed dramatically higher activity than the other two reduction temperatures. This may be due to the fact that this catalyst had a higher fraction of B_5 ensembles.

In Chapter 4, high throughput experimentation was used in order to find new low temperature ammonia decomposition catalysts that contained less Ru than the previously discussed catalyst containing 4% Ru and 12%K supported on γ-Al_2O_3. Ultimately the goal here was to produce a catalyst with dramatically lowered Ru content, that also exhibited high ammonia decomposition reactivity at low temperatures. High throughput experimentation gives us the unique ability to test multiple catalysts in parallel, in order to save on the cost of experimentation as well as time. This gives us the ability to test more exotic and unique catalyst combinations than a typical single reactor plug flow reactor would give. When high throughput experimentation is paired with machine learning algorithms, one has the capability to dramatically reduce the amount of time and experimentation required for new material discovery. Currently, most literature has only been able to interpolate within specific ranges of compositions for catalyst discovery or require complex density functional theory calculations or compiled literature data as a training data set. Very few studies have the capabilities to generate the large amount of data required for machine learning algorithms. Firstly, we attempted to find low Ru content catalysts by adding secondary transition metals to 2% Ru. These included Co, Ni, Fe, Mn, Zn Mo, Hf, Y and the precious metals Os, Rh, Pt, and Ir. In all cases, the addition of 2% of these transition metals to a 2% Ru catalyst resulted in poorer activity than a 4% Ru catalyst under identical conditions. This was not surprising, as similar results have been achieved in the literature.

Therefore, a different approach was taken to new catalyst discovery. The previously optimized catalyst containing 4% Ru and 12% K was used as a baseline and further modified in two ways. Firstly, a secondary metal was introduced into the catalyst, of which spanned the entire periodic table. Secondly, the total metal weight loading was held constant at 4%, and varied such that either 1, 2 or 3% of Ru was replaced with one of the secondary metals. These metals included Ca, Sr, Sc, Y, Zr, Hf, Nb, Ta, Cr, W, Mn, Re, Fe, Os, Co, Rh, Ir, Ni, Pd, Pt, Cu Ag, Au Zn, Cd, In, Sn, Pb or Bi, which are denoted by the letter "M". The weight loadings were then either composed of 3%Ru, 1%M, 12%K (3,1,12 RuMK), 2%Ru, 2%M, 12%K (2,2,12 RuMK) or 1%Ru, 3%M, 12%K (1,3,12 RuMK) and supported on γ-Al_2O_3. These catalysts were tested for low temperature ammonia decomposition using a 16-channel parallel plug flow reactor and spatially resolved FTIR for quantification of all 16 reactions in parallel.

The catalysts were then compared to the baseline 4,12 RuK catalyst tested from 250°C to 450°C under 1 %NH_3/Ar at a space velocity of 30,000 mL/hr/g_{cat}. Successful "hits" were determined at 300°C that, which is an extremely mild ammonia decomposition temperature and also produced the widest variety of responses from the 99 catalysts studied. The successful catalysts were those that showed a higher activity than the baseline catalyst at these conditions. From this study we found that substitution of Ru with Mg, Ca, Sr, Sc, Y, Zr, Hf, Ta, Rh and Ir with less Ru. It is obvious that this approach was much more successful than studying simply bi-metal catalyst systems. With as little as 1% Ru, substitution with Sr, Zr, Y and Hf resulted in a much more active catalyst than the 4,12 RuK baseline. In order to better understand the relationship between catalyst composition, present metal oxides and activity, XRD patterns were taken for each catalyst in the data set. To this end, compositional analysis as well as peak fitting to determine the crystallite size of each crystalline Ru component was performed to determine the average crystallite size for each catalyst. The activity of each of the three weight loadings as a function of the average particle size, secondary metal atomic number and ammonia decomposition activity were then compared. With compositions of 3,1,12 RuMK we found that catalysts with smaller particle sizes had higher activity, but that the atomic number of the secondary metal was not much a factor. As the compositional loading decreased from 2,2,12 RuMK to 1,3,12 RuMK, the atomic number of the secondary element became a larger factor in determining trends in the ammonia decomposition activity at 300°C. The catalysts with the highest activity exhibited the smallest average Ru particle size and the smallest atomic number of the secondary element. However, we found no discernible trends in Ru metal oxides and secondary oxides present and ammonia decomposition activity. This may be due to the strong interplay present between the composition, secondary metal and average particle size in addition to a variety of other factors that makes elucidating trends not as straight forward.

For these reasons, we introduced a framework combining high throughput experimentation with machine learning algorithms using the experimental data collected here. The purpose of this algorithm was to show that we can use small sets of data (hundreds of points) to make predictions on catalyst activity and also to determine which features of the catalyst are the most important in determining activity. These features include structural, geometric and general chemical data describing metals. Additionally, we added features that pertained to the synthesis parameters and operating conditions for each catalyst such as moles of chlorine present, space velocity and ammonia concentration. A random forest machine learning algorithm was developed for this purpose, and ultimately, we determined that the most important features describing ammonia decomposition activity across this range of catalysts was temperature, number of d-shell valence electrons, electronegativity, covalent radius, work function and number of valence electrons. While it was obvious that temperature is the most influential variable in determining activity, this serves as a confirmation that the algorithm can indeed accurately choose variables that influence activity.

Chapter 4 also provided further insight into two catalysts from the high throughput screen, mainly one good performing set of catalysts containing Sr, and a poor performing set of catalysts containing Fe. This served as a confirmation that the high throughput was a good screening tool to find catalysts that can operate under more realistic conditions, and also to under why one catalyst performed well while the other on did not. Firstly, the apparent activation energy for each of the 3,1,12 RuSrK, 2,2,12 RuSrK, 1,3,12 RuSrK, 3,1,12 RuFeK, 2,2,12 RuFeK and 1,3,12 RuFeK catalysts was determined in 100% NH_3 at a space velocity of 5,400 ml/hr/g_{cat} and under differential conditions. These values were then compared to the 4 Ru and 4,12 RuK baseline catalyst. We found that the addition of Sr increased the apparent activation energy from 65.7 kJ/mol (4,12 RuK) to 149.6 kJ/mol for the 3,1,12 RuSrK catalyst. The apparent activation energy continued to slightly increase with increasing Sr loading up to 156.4 kJ/mol. The Fe containing catalysts exhibited a much higher apparent activation energy between the range of 226.6 kJ/mol and 250.1 kJ/mol. The TOF for each catalyst was also determined under the same conditions. The 1,3,12 RuSrK catalyst had the highest TOF of 1.78 s^{-1}, over twice as active as the 4,12 RuK catalyst with a TOF of 0.88 s^{-1}. Ultimately, we determined that the substitution of Fe with Ru replaced the active Ru sites with intrinsically less active Fe sites, while Sr instead seemed to electronically modify the Ru active sites on the basis of the increasing TOF with increasing Sr loading and the H_2 uptake as determined through H_2 chemisorption experiments. Comparing the activation energy needed for various steps in the ammonia decomposition reaction, it seems that the addition of Sr may act to change the rate limiting step from the recombination and desorption of N_2 to some combination of the dehydrogenation of NH_x species. CO adsorption was performed on 4 Ru, 4,12 RuK, 1,3,12 RuFeK and 1,3,12 RuSrK to further confirm whether Sr modifies or produces different sites on the Ru catalysts based on the different adsorption configurations of CO on Ru. We determined that the addition of Sr produced relatively more linearly adsorbed CO and acted to weaken the CO triple bond on Ru sites, which analogously which could facilitate the dehydrogenation steps during ammonia decomposition.

Ultimately this work has shown that high throughput experimentation gives us a unique ability to generate massive, multidimensional datasets that are not typical for heterogeneous catalysis. Here, we demonstrated the synthesis and catalytic screening of over 100 different Ru based bimetallic catalysts for low temperature ammonia decomposition. The aim of this study was to discovery novel elements and catalyst formulations that could result in a less expensive and highly active ammonia decomposition catalyst at temperatures below 450°C. We showed that high throughput experimentation can be a powerful for new catalyst discovery when an appropriate design space is chosen based on domain knowledge for the reaction in hand. Additionally, when combined with machine learning, the efficiency of screening and catalyst discovery can maximize further.

BIBLIOGRAPHY

1. BP, “Statistical Review of World Energy” (2020), (available at www.bp.com/statisticalreview.).
2. D. H. Vo, A. T. Vo, C. M. Ho, H. M. Nguyen, The role of renewable energy, alternative and nuclear energy in mitigating carbon emissions in the CPTPP countries. *Renew. Energy*. **161**, 278–292 (2020).
3. S. J. Zinkle, G. S. Was, Materials challenges in nuclear energy. *Acta Mater.* **61**, 735–758 (2013).
4. K. Menyah, Y. Wolde-Rufael, CO2 emissions, nuclear energy, renewable energy and economic growth in the US. *Energy Policy*. **38**, 2911–2915 (2010).
5. A. S. Iyer, S. J. Couch, G. P. Harrison, A. R. Wallace, Variability and phasing of tidal current energy around the United Kingdom. *Renew. Energy*. **51**, 343–357 (2013).
6. S. Guo, Q. Liu, J. Sun, H. Jin, A review on the utilization of hybrid renewable energy. *Renew. Sustain. Energy Rev.* **91** (2018), pp. 1121–1147.
7. E. Kabir, P. Kumar, S. Kumar, A. A. Adelodun, K. H. Kim, Solar energy: Potential and future prospects. *Renew. Sustain. Energy Rev.* **82** (2018), pp. 894–900.
8. S. A. Sherif, F. Barbir, T. N. Veziroglu, Wind energy and the hydrogen economy-review of the technology. *Sol. Energy*. **78**, 647–660 (2005).
9. E. L. V. Eriksson, E. M. A. Gray, Optimization and integration of hybrid renewable energy hydrogen fuel cell energy systems – A critical review. *Appl. Energy*. **202** (2017), pp. 348–364.
10. A. Chapman, K. Itaoka, K. Hirose, F. T. Davidson, K. Nagasawa, A. C. Lloyd, M. E. Webber, Z. Kurban, S. Managi, T. Tamaki, M. C. Lewis, R. E. Hebner, Y. Fujii, A review of four case studies assessing the potential for hydrogen penetration of the future energy system. *Int. J. Hydrogen Energy*. **44** (2019), pp. 6371–6382.
11. A. Midilli, M. Ay, I. Dincer, M. A. Rosen, On hydrogen and hydrogen energy strategies I : Current status and needs. *Renew. Sustain. Energy Rev.* **9** (2005), pp. 255–271.
12. J. D. Fonseca, M. Camargo, J. M. Commenge, L. Falk, I. D. Gil, Trends in design of distributed energy systems using hydrogen as energy vector: A systematic literature review. *Int. J. Hydrogen Energy*. **44**, 9486–9504 (2019).

13. J. O. M. Bockris, The hydrogen economy: Its history. *Int. J. Hydrogen Energy*. **38**, 2579–2588 (2013).

14. G. W. Crabtree, M. S. Dresselhaus, M. V. Buchanan, The hydrogen economy. *Phys. Today*. **57**, 39–44 (2004).

15. J. Bockris, A. . Appleby, The Hydrogen Economy - An Ultimate Economy? *Environ. This Mon.*, 29 (1972).

16. L. Ouyang, K. Chen, J. Jiang, X. S. Yang, M. Zhu, Hydrogen storage in light-metal based systems: A review. *J. Alloys Compd.* **829** (2020), doi:10.1016/j.jallcom.2020.154597.

17. K. Alanne, S. Cao, Zero-energy hydrogen economy (ZEH2E) for buildings and communities including personal mobility. *Renew. Sustain. Energy Rev.* **71** (2017), pp. 697–711.

18. Y. Wang, D. F. Ruiz Diaz, K. S. Chen, Z. Wang, X. C. Adroher, Materials, technological status, and fundamentals of PEM fuel cells – A review. *Mater. Today*. **32** (2020), pp. 178–203.

19. G. Karanfil, Importance and applications of DOE/optimization methods in PEM fuel cells: A review. *Int. J. Energy Res.* **44** (2020), pp. 4–25.

20. S. Chiuta, R. C. Everson, H. W. J. P. Neomagus, P. Van Der Gryp, D. G. Bessarabov, Reactor technology options for distributed hydrogen generation via ammonia decomposition: A review. *Int. J. Hydrogen Energy*. **38** (2013), pp. 14968–14991.

21. R. Pinsky, P. Sabharwall, J. Hartvigsen, J. O'Brien, Comparative review of hydrogen production technologies for nuclear hybrid energy systems. *Prog. Nucl. Energy*. **123** (2020), , doi:10.1016/j.pnucene.2020.103317.

22. DOE, DOE Hydrogen and Fuel Cells Program: Hydrogen Storage. *U.S Dep. Energy*. **25**, 6 (2009).

23. S. Mukherjee, S. V. Devaguptapu, A. Sviripa, C. R. F. Lund, G. Wu, Low-temperature ammonia decomposition catalysts for hydrogen generation. *Appl. Catal. B Environ.* **226**, 162–181 (2018).

24. DOE Technical Targets for Onboard Hydrogen Storage for Light-Duty Vehicles | Department of Energy, (available at https://www.energy.gov/eere/fuelcells/doe-technical-targets-onboard-hydrogen-storage-light-duty-vehicles).

25. T. Hua, R. Ahluwalia, L. Eudy, G. Singer, B. Jermer, N. Asselin-Miller, S. Wessel, T. Patterson, J. Marcinkoski, Status of hydrogen fuel cell electric buses worldwide. *J. Power Sources*. **269** (2014), pp. 975–993.

26. K. Young, M. Young, T. Ouchi, B. Reichman, M. A. Fetcenko, Improvement in high-rate dischargeability, activation, and low-temperature performance in multi-phase AB 2 alloys by partial substitution of Zr with y. *J. Power Sources*. **215**, 279–287 (2012).

27. B. Sakintuna, F. Lamari-Darkrim, M. Hirscher, Metal hydride materials for solid hydrogen storage: A review. *Int. J. Hydrogen Energy*. **32**, 1121–1140 (2007).

28. A. Klerke, C. H. Christensen, J. K. Nørskov, T. Vegge, Ammonia for hydrogen storage: challenges and opportunities (2008), doi:10.1039/b720020j.

29. S. K. Seo, D. Y. Yun, C. J. Lee, Design and optimization of a hydrogen supply chain using a centralized storage model. *Appl. Energy*. **262**, 1–20 (2020).

30. R.-Y. Chein, Y.-C. Chen, C.-S. Chang, J. N. Chung, Numerical modeling of hydrogen production from ammonia decomposition for fuel cell applications. *Int. J. Hydrogen Energy*. **35**, 589–597 (2009).

31. A. Valera-Medina, H. Xiao, M. Owen-Jones, W. I. F. David, P. J. Bowen, Ammonia for power. *Prog. Energy Combust. Sci.* **69** (2018), pp. 63–102.

32. K. E. Lamb, M. D. Dolan, D. F. Kennedy, Ammonia for hydrogen storage; A review of catalytic ammonia decomposition and hydrogen separation and purification. *Int. J. Hydrogen Energy*. **44** (2019), pp. 3580–3593.

33. A. Patil, L. Laumans, H. Vrijenhoef, in *Procedia Engineering* (Elsevier Ltd, 2014), vol. 83, pp. 322–327.

34. A. Valera-Medina, H. Xiao, M. Owen-Jones, W. I. F. David, P. J. Bowen, Ammonia for power. *Prog. Energy Combust. Sci.* **69** (2018), pp. 63–102.

35. D. W. Kang, J. H. Holbrook, Use of NH3 fuel to achieve deep greenhouse gas reductions from US transportation. *Energy Reports*. **1**, 164–168 (2015).

36. A. Tullo, Yara plans to make green ammonia in Norway. *c&en* (2020), (available at https://cen.acs.org/business/petrochemicals/Yara-plans-make-green-ammonia/98/web/2020/12).

37. J. R. Bartels, “A feasibility study of implementing an Ammonia Economy,” (available at https://lib.dr.iastate.edu/etd).

38. L. Ye, R. Nayak-Luke, R. Bañares-Alcántara, E. Tsang, Reaction: “Green” Ammonia Production. *Chem.* **3** (2017), pp. 712–714.

39. T. Brown, Yara: solar ammonia pilot plant, for start-up in 2019. *Ammon. Ind.* (2018), (available at https://ammoniaindustry.com/yara-solar-ammonia-pilot-plant-for-start-up-in-2019/).

40. Fertilizer prices fall to lowest levels in a decade, economist says | Successful Farming. *Success. Farming* (2020), (available at https://www.agriculture.com/news/crops/fertilizer-prices-fall-to-lowest-levels-in-a-decade-economist-says).

41. J. Reed, “DOE Hydrogen and Fuel Cell Technical Advisory Committee Hydrogen Energy Storage Activities” (2015).

42. C. H. Christensen, R. Z. Sørensen, T. Johannessen, U. J. Quaade, K. Honkala, T. D. Elmøe, R. Køhler, J. K. Nørskov, Metal ammine complexes for hydrogen storage. *J. Mater. Chem.* **15** (2005), pp. 4106–4108.

43. REFUEL | arpa-e.energy.gov, (available at https://arpa-e.energy.gov/technologies/programs/refuel).

44. Trevor Brown, Ammonia production causes 1% of total global GHG emissions. *Ammon. Ind.* (2016), (available at https://ammoniaindustry.com/ammonia-production-causes-1-percent-of-total-global-ghg-emissions/).

45. H. Bielawa, O. Hinrichsen, A. Birkner, M. Muhler, The Ammonia-Synthesis Catalyst of the Next Generation: Barium-Promoted Oxide-Supported Ruthenium. *Angew. Chemie Int. Ed.* **40**, 1061–1063 (2001).

46. G. Ertl, H. Knozinger, F. Schuth, J. Weitkamp, *Handbook of Heterogenous Catalysis Vol. 1* (ed. 2, 2011).

47. Saudi Aramco, World's first blue ammonia shipment opens new route to a sustainable future. *Saudi Aramco* (2020), (available at https://www.aramco.com/en/news-media/news/2020/first-blue-ammonia-shipment).

48. T. Brown, Saudi Arabia ships low-carbon ammonia to Japan - Ammonia Energy Association. *Ammon. Energy* (2020), (available at https://www.ammoniaenergy.org/articles/saudi-arabia-ships-low-carbon-ammonia-to-japan/).

49. Air Products, Air Products, ACWA Power and NEOM Sign Agreement for $5 Billion Production Facility in NEOM Powered by Renewable Energy for Production and Export of Green Hydrogen to Global Markets. *Press release, Air Prod. Chem. Inc.* (2020), (available at https://newsroom.neom.com/air-products-acwa-power-and-neom-sign-agreement-for-5-billion-production-facility-in-neom-powered-by-renewable-energy-for-production-and-export-of-green-hydrogen-to-global-markets-321553).

50. Monolith, Monolith Materials Plans to Build Country's First Large Scale Carbon-Free Ammonia Plant (2020), (available at https://monolithmaterials.com/news/monolith-materials-carbon-free-ammonia-plant).

51. V. Chaturvedi, M. Hejazi, J. Edmonds, L. Clarke, P. Kyle, E. Davies, M. Wise, Climate mitigation policy implications for global irrigation water demand. *Mitig. Adapt. Strateg. Glob. Chang.* **20**, 389–407 (2013).

52. V. Chaturvedi, P. N. Koti, R. Sugam, K. Neog, M. Hejazi, Cooperation or rivalry? Impact of alternative development pathways on India's long-term electricity generation and associated water demands. *Energy*. **192**, 116708 (2020).

53. A. Boretti, L. Rosa, Reassessing the projections of the World Water Development Report. *npj Clean Water*. **2**, 1–6 (2019).

54. K. McCullough, P. H. Chiang, J. D. Jimenez, J. A. Lauterbach, Material discovery and high throughput exploration of Ru based catalysts for low temperature ammonia decomposition. *Materials (Basel).* **13**, 1–19 (2020).

55. T. E. Bell, H2 Production via Ammonia Decomposition Using Non-Noble Metal Catalysts: A Review. *Top. Catal.* **59**, 1438–1457 (2016).

56. R. Halseid, Ammonia as Hydrogen Carrier: Effects of Ammonia on Polymer Electrolyte Membrane Fuel Cells. **089**, 1–264 (2004).

57. J. N. Armor, Overcoming equilibrium limitations in chemical processes. *Appl. Catal. A Gen.* **222**, 91–99 (2001).

58. A. Di Carlo, A. Dell'Era, Z. Del Prete, 3D simulation of hydrogen production by ammonia decomposition in a catalytic membrane reactor. *Int. J. Hydrogen Energy*. **36**, 11815–11824 (2011).

59. S.-F. Yin, B.-Q. Xu, C.-F. Ng, C.-T. Au, Nano Ru/CNTs: a highly active and stable catalyst for the generation of CO x -free hydrogen in ammonia decomposition. *Appl. Catal. B Environ.* **48**, 237–241 (2004).

60. W. Zheng, J. Zhang, B. Zhu, R. Blume, Y. Zhang, K. Schlichte, R. Schlögl, F. Schüth, D. S. Su, Structure-Function Correlations for Ru/CNT in the Catalytic Decomposition of Ammonia. *ChemSusChem*. **3**, 226–230 (2010).

61. S. J. Wang, S. F. Yin, L. Li, B. Q. Xu, C. F. Ng, C. T. Au, Investigation on modification of Ru/CNTs catalyst for the generation of COx-free hydrogen from ammonia. *Appl. Catal. B Environ.* **52**, 287–299 (2004).

62. S. F. Yin, Q. H. Zhang, B. Q. Xu, W. X. Zhu, C. F. Ng, C. T. Au, Investigation on the catalysis of CO x -free hydrogen generation from ammonia. *J. Catal.* **224**, 384–396 (2004).

63. A. K. Hill, L. Torrente-Murciano, Low temperature H2 production from ammonia using ruthenium-based catalysts: Synergetic effect of promoter and support. *Appl. Catal. B, Environ.* **172–173**, 129–135 (2015).

64. R. Schlögl, "Part B 2.1. Ammonia Synthesis," (available at www.fhi-berlin.mpg.de/ac).

65. I. Chorkendorff, J. W. Niemantsverdriet, *Concepts of Modern Catalysis and Kinetics* (2007).

66. A. Mittasch, W. Frankenburg, Early studies of multicomponet catalysts. *Adv. Catal.* **2**, 81–104 (1950).

67. Y. Ogura, K. Sato, S. I. Miyahara, Y. Kawano, T. Toriyama, T. Yamamoto, S. Matsumura, S. Hosokawa, K. Nagaoka, Efficient ammonia synthesis over a Ru/La0.5Ce0.5O1.75 catalyst pre-reduced at high temperature. *Chem. Sci.* **9**, 2230–2237 (2018).

68. G. Ertl, Reactions at Surfaces: From Atoms to Complexity (Nobel Lecture). *Angew. Chemie Int. Ed.* **47**, 3524–3535 (2008).

69. G. Somorjai, *Introduction to Surface Chemistry and Catalysis* (1993).

70. H. Liu, Ammonia synthesis catalyst 100 years: Practice, enlightenment and challenge. *Cuihua Xuebao/Chinese J. Catal.* **35** (2014), pp. 1619–1640.

71. G. A. Somorjai, N. Materer, Surface structures in ammonia synthesis. *Top. Catal.* **1**, 215–231 (1994).

72. A. Boisen, S. Dahl, J. K. Nørskov, C. H. Christensen, Why the optimal ammonia synthesis catalyst is not the optimal ammonia decomposition catalyst. *J. Catal.* **230**, 309–312 (2005).

73. M. Kitano, S. Kanbara, Y. Inoue, N. Kuganathan, P. V Sushko, T. Yokoyama, M. Hara, H. Hosono, Electride support boosts nitrogen dissociation over ruthenium catalyst and shifts the bottleneck in ammonia synthesis. *Nat. Commun.* **6**, 1–9 (2015).

74. M. Saito, M. Itoh, J. Iwamoto, C. Y. Li, K. I. Machida, Synergistic effect of MgO and CeO2 as a support for ruthenium catalysts in ammonia synthesis. *Catal. Letters*. **106**, 107–110 (2006).

75. X. Wang, J. Ni, B. Lin, R. Wang, J. Lin, K. Wei, Highly efficient Ru/MgO-CeO2 catalyst for ammonia synthesis. *Catal. Commun.* **12**, 251–254 (2010).

76. X. Ju, L. Liu, P. Yu, J. Guo, X. Zhang, T. He, G. Wu, P. Chen, Mesoporous Ru/MgO prepared by a deposition-precipitation method as highly active catalyst for producing COx-free hydrogen from ammonia decomposition. *Appl. Catal. B Environ.* **211**, 167–175 (2017).

77. A. S. Chellappa, C. M. Fischer, W. J. Thomson, W. J. Chellappa, A.S., Fischer, C.M.,Thomson, Ammonia decomposition kinetics over Ni-Pt/Al2O3 for PEM fuel cell applications. *Appl. Catal. A.* **227**, 231–240 (2002).

78. J. C. Ganley, F. S. Thomas, E. G. Seebauer, R. I. Masel, A priori catalytic activity correlations: the difficult case of hydrogen production from ammonia. *Catal. Letters*. **96**, 117–122 (2004).

79. A. J. Medford, A. Vojvodic, J. S. Hummelshøj, J. Voss, F. Abild-Pedersen, F. Studt, T. Bligaard, A. Nilsson, J. K. Nørskov, From the Sabatier principle to a predictive theory of transition-metal heterogeneous catalysis. *J. Catal.* **328**, 36–42 (2015).

80. C. J. H. Jacobsen, S. Dahl, B. G. S. Clausen, S. Bahn, A. Logadottir, J. K. Nørskov, Catalyst design by interpolation in the periodic table: Bimetallic ammonia synthesis catalysts. *J. Am. Chem. Soc.* **123**, 8404–8405 (2001).

81. W. Tsai, W. H. Weinberg, Steady-state decomposition of ammonia on the Ru(001) surface. *J. Phys. Chem.* **91**, 5302–5307 (1987).

82. M. C. J. Bradford, P. E. Fanning, M. A. Vannice, Kinetics of NH 3 Decomposition over Well Dispersed Ru. *History*. **484**, 479–484 (2000).

83. C. Egawa, T. Nishida, S. Naito, K. Tamaru, Ammonia decomposition on (1 1 10) and (0 0 1) surfaces of ruthenium. *J. Chem. Soc. Farady Trans. Phys. Chem. Condens. Phases*. **80**, 1595–1604 (1984).

84. V. Prasad, A. M. Karim, A. Arya, D. G. Vlachos, Assessment of overall rate expressions and multiscale, microkinetic model uniqueness via experimental data injection: Ammonia decomposition on Ru/γ-Al2O3 for hydrogen production. *Ind. Eng. Chem. Res.* **48**, 5255–5265 (2009).

85. F. Hayashi, Y. Toda, Y. Kanie, M. Kitano, Y. Inoue, T. Yokoyama, M. Hara, H. Hosono, Ammonia decomposition by ruthenium nanoparticles loaded on inorganic electride C12A7:e-. *Chem. Sci.* **4**, 3124–3130 (2013).

86. H. Shi, K. Jacobi, G. Ertl, Dissociative chemisorption of nitrogen on Ru(0001). *J. Chem. Phys.* **99**, 9248–9254 (1993).

87. O. Hinrichsen, F. Rosowski, A. Hornung, M. Muhler, G. Ertl, The kinetics of ammonia synthesis over Ru-based catalysts: 1. The dissociative chemisorption and associative desorption of N2. *J. Catal.* **165**, 33–44 (1997).

88. F. Schuth, R. Palkovits, R. Schlogl Ogl, D. S. Su, Ammonia as a possible element in an energy infrastructure: catalysts for ammonia decomposition. *Energy Environ. Sci.* **5**, 6278 (2012).

89. D. A. Hansgen, L. M. Thomanek, J. G. Chen, D. G. Vlachos, Experimental and theoretical studies of ammonia decomposition activity on Fe-Pt, Co-Pt, and Cu-Pt bimetallic surfaces. *J. Chem. Phys.* **134**, 184701 (2011).

90. D. A. Hansgen, D. G. Vlachos, J. G. Chen, Using first principles to predict bimetallic catalysts for the ammonia decomposition reaction. *Nat. Chem.* **2**, 484–489 (2010).

91. J. Ji, X. Duan, G. Qian, X. Zhou, G. Tong, W. Yuan, Towards an efficient CoMo/γ-Al2O3 catalyst using metal amine metallate as an active phase precursor: Enhanced hydrogen production by ammonia decomposition. *Int. J. Hydrogen Energy*. **39**, 12490–12498 (2014).

92. P. Xie, Y. Yao, Z. Huang, Z. Liu, J. Zhang, T. Li, G. Wang, R. Shahbazian-Yassar, L. Hu, C. Wang, Highly efficient decomposition of ammonia using high-entropy alloy catalysts. *Nat. Commun.* **10** (2019), doi:10.1038/s41467-019-11848-9.

93. D. M. Prices, Daily metal Price (2020).

94. L. H. Yao, Y. X. Li, J. Zhao, W. J. Ji, C. T. Au, Core–shell structured nanoparticles (M@SiO 2 , Al2O3 , MgO; M = Fe, Co, Ni, Ru) and their application in COx -free H2 production via NH3 decomposition. *Catal. Today*. **158**, 401–408 (2010).

95. M. Feyen, C. Weidenthaler, R. Güttel, K. Schlichte, U. Holle, A. H. Lu, F. Schüth, High-temperature stable, iron-based core-shell catalysts for ammonia decomposition. *Chem. - A Eur. J.* **17**, 598–605 (2011).

96. A. Jedynak, Z. Kowalczyk, D. Szmigiel, W. Raróg, J. Zieliski, Ammonia decomposition over the carbon-based iron catalyst promoted with potassium. *Appl. Catal. A Gen.* **237**, 223–226 (2002).

97. J. Ji, X. Duan, G. Qian, P. Li, X. Zhou, D. Chen, W. Yuan, Fe particles on the tops of carbon nanofibers immobilized on structured carbon microfibers for ammonia decomposition. *Catal. Today*. **216**, 254–260 (2013).

98. X. Duan, G. Qian, X. Zhou, Z. Sui, D. Chen, W. Yuan, Tuning the size and shape of Fe nanoparticles on carbon nanofibers for catalytic ammonia decomposition. *Appl. Catal. B Environ.* **101**, 189–196 (2011).

99. A.-H. H. Lu, J.-J. J. Nitz, M. Comotti, C. Weidenthaler, K. Schlichte, C. W. Lehmann, O. Terasaki, F. Schüth, Spatially and Size Selective Synthesis of Fe-Based Nanoparticles on Ordered Mesoporous Supports as Highly Active and Stable Catalysts for Ammonia Decomposition. *J. Am. Chem. Soc.* **132**, 14152–14162 (2010).

100. D. Varisli, N. G. Kaykac, CO x free hydrogen production over cobalt incorporated silicate structured mesoporous catalysts. *Appl. Catal. B Environ.* **127**, 389–398 (2012).

101. X.-K. K. Li, W.-J. J. Ji, J. Zhao, S.-J. J. Wang, C.-T. T. Au, Ammonia decomposition over Ru and Ni catalysts supported on fumed SiO 2 , MCM-41, and SBA-15. *J. Catal.* **236**, 181–189 (2005).

102. Z. P. Hu, C. C. Weng, C. Chen, Z. Y. Yuan, Catalytic decomposition of ammonia to COx-free hydrogen over Ni/ZSM-5 catalysts: A comparative study of the preparation methods. *Appl. Catal. A Gen.* **562**, 49–57 (2018).

103. I. Lucentini, A. Casanovas, J. Llorca, Catalytic ammonia decomposition for hydrogen production on Ni, Ru and Ni[sbnd]Ru supported on CeO2. *Int. J. Hydrogen Energy*. **44**, 12693–12707 (2019).

104. W. Zheng, J. Zhang, Q. Ge, H. Xu, W. Li, Effects of CeO2 addition on Ni/Al2O3 catalysts for the reaction of ammonia decomposition to hydrogen. *Appl. Catal. B Environ.* **80**, 98–105 (2008).

105. Z. Lendzion-Bieluń, R. Pelka, W. Arabczyk, Study of the kinetics of ammonia synthesis and decomposition on iron and cobalt catalysts. *Catal. Letters*. **129**, 119–123 (2009).

106. Ł. Czekajło, Z. Lendzion-Bieluń, Effect of preparation conditions and promoters on the structure and activity of the ammonia decomposition reaction catalyst based on nanocrystalline cobalt. *Chem. Eng. J.* **289**, 254–260 (2016).

107. L. Torrente-Murciano, A. K. Hill, T. E. Bell, Ammonia decomposition over cobalt/carbon catalysts—Effect of carbon support and electron donating promoter on activity. *Catal. Today*. **286**, 131–140 (2017).

108. D. R. Strongin, G. A. Somorjai, THE EFFECTS OF POTASSIUM ON THE AMMONIA SYNTHESIS OVER IRON SINGLE CRYSTAL SURFACES. *Catal. J.* **109**, 51–60 (1988).

109. S. Dahl, E. Törnqvist, I. Chorkendorff, Dissociative adsorption of N2 on Ru(0001): A surface reaction totally dominated by steps. *J. Catal.* **192**, 381–390 (2000).

110. G. A. Somorjai, (Springer, Berlin, Heidelberg, 1984; https://link.springer.com/chapter/10.1007/978-3-642-82253-7_1), pp. 1–22.

111. S. Dahl, A. Logadottir, R. C. Egeberg, J. H. Larsen, I. Chorkendorff, E. Törnqvist, J. K. NØrskov, Role of steps in N2 activation on Ru(0001). *Phys. Rev. Lett.* **83**, 1814–1817 (1999).

112. R. Van Hardeveld, F. Hartog, The statistics of surface atoms and surface sites on metal crystals. *Surf. Sci.* **15**, 189–230 (1969).

113. C. J. H. Jacobsen, S. Dahl, P. L. Hansen, E. Törnqvist, L. Jensen, H. Topsøe, D. V Prip, P. B. Møenshaug, I. Chorkendorff, Structure sensitivity of supported ruthenium catalysts for ammonia synthesis. *J. Mol. Catal. A Chem.* **163**, 19–26 (2000).

114. A. M. Karim, V. Prasad, G. Mpourmpakis, W. W. Lonergan, A. I. Frenkel, J. G. Chen, D. G. Vlachos, Correlating particle size and shape of supported Ru/γ-Al2O3 catalysts with NH3 decomposition activity. *J. Am. Chem. Soc.* **131**, 12230–12239 (2009).

115. K. Kishida, M. Kitano, Y. Inoue, M. Sasase, T. Nakao, T. Tada, H. Abe, Y. Niwa, T. Yokoyama, M. Hara, H. Hosono, Large Oblate Hemispheroidal Ruthenium Particles Supported on Calcium Amide as Efficient Catalysts for Ammonia Decomposition. *Chem. - A Eur. J.* **24**, 7976–7984 (2018).

116. D. Szmigiel, W. Raróg-Pilecka, E. Miśkiewicz, Z. Kaszkur, Z. Kowalczyk, Ammonia decomposition over the ruthenium catalysts deposited on magnesium-aluminum spinel. *Appl. Catal. A Gen.* **264**, 59–63 (2004).

117. W. Raróg, Z. Kowalczyk, J. Sentek, D. Składanowski, D. Szmigiel, J. Zieliñski, Decomposition of ammonia over potassium promoted ruthenium catalyst supported on carbon. *Appl. Catal. A Gen.* **208**, 213–216 (2001).

118. W. Pyrz, R. Vijay, J. Binz, J. Lauterbach, D. J. Buttrey, Characterization of K-promoted Ru catalysts for ammonia decomposition discovered using high-throughput experimentation. *Top. Catal.* **50**, 180–191 (2008).

119. H. Sheng Zeng, K. Inazu, K. I. Aika, The working state of the barium promoter in ammonia synthesis over an active-carbon-supported ruthenium catalyst using barium nitrate as the promoter precursor. *J. Catal.* **211**, 33–41 (2002).

120. Z. Hu, J. Mahin, S. Datta, T. E. Bell, L. Torrente-Murciano, Ru-Based Catalysts for H2 Production from Ammonia: Effect of 1D Support. *Top. Catal.* **1** (2018), pp. 1–3.

121. K. ichi Aika, T. Takano, S. Murata, Preparation and characterization of chlorine-free ruthenium catalysts and the promoter effect in ammonia synthesis. 3. A magnesia-supported ruthenium catalyst. *J. Catal.* **136**, 126–140 (1992).

122. P. Yu, J. Guo, L. Liu, P. Wang, F. Chang, H. Wang, X. Ju, P. Chen, Effects of Alkaline Earth Metal Amides on Ru in Catalytic Ammonia Decomposition. *J. Phys. Chem. C.* **120**, 2822–2828 (2016).

123. S. F. Yin, B. Q. Xu, X. P. Zhou, C. T. Au, A mini-review on ammonia decomposition catalysts for on-site generation of hydrogen for fuel cell applications. *Appl. Catal. A Gen.* **277**, 1–9 (2004).

124. J. Zhang, H. Xu, Q. Ge, W. Li, Highly efficient Ru/MgO catalysts for NH 3 decomposition: Synthesis, characterization and promoter effect. *Catal. Commun.* **7**, 148–152 (2006).

125. S. Murata, K. I. Aika, Removal of chlorine ions from Ru/MgO catalysts for ammonia synthesis. *Appl. Catal. A*, *Gen.* **82**, 1–12 (1992).

126. E. D'Addio, thesis, University of Delaware (2011).

127. J. J. Hanak, The "multiple-sample concept" in materials research: Synthesis, compositional analysis and testing of entire multicomponent systems. *J. Mater. Sci.* **5**, 964–971 (1970).

128. W. F. Maier, Early years of high-throughput experimentation and combinatorial approaches in catalysis and materials science. *ACS Comb. Sci.* **21**, 437–444 (2019).

129. J. G. Creer, P. Jackson, G. Pandy, G. G. Percival, D. Seddon, The design and construction of a multichannel microreactor for catalyst evaluation. *Appl. Catal.* **22**, 85–95 (1986).

130. R. J. Hendershot, C. M. Snively, J. Lauterbach, High-throughput heterogeneous catalytic science. *Chem. - A Eur. J.* **11** (2005), pp. 806–814.

131. NIST, *NIST/SEMATECH e-Handbook of Statistical Methods* (2012).

132. J. Urschey, A. Kühnle, W. F. Maier, Combinatorial and conventional development of novel dehydrogenation catalysts. *Appl. Catal. A Gen.* **252**, 91–106 (2003).

133. K. Takahashi, I. Miyazato, S. Nishimura, J. Ohyama, Unveiling Hidden Catalysts for the Oxidative Coupling of Methane based on Combining Machine Learning with Literature Data. *ChemCatChem*. **10**, 3223–3228 (2018).

134. T. N. Nguyen, T. T. P. Nhat, K. Takimoto, A. Thakur, S. Nishimura, J. Ohyama, I. Miyazato, L. Takahashi, J. Fujima, K. Takahashi, T. Taniike, High-Throughput Experimentation and Catalyst Informatics for Oxidative Coupling of Methane. *ACS Catal.* **10**, 921–932 (2020).

135. R. J. Hendershot, S. S. Lasko, M. F. Fellmann, G. Oskarsdottir, W. Nicholas Delgass, C. M. Snively, J. Lauterbach, A novel reactor system for high throughput catalyst testing under realistic conditions. *Appl. Catal. A Gen.* **254**, 107–120 (2003).

136. J. C. Dellamorte, M. A. Barteau, J. Lauterbach, Opportunities for catalyst discovery and development: Integrating surface science and theory with high throughput methods. *Surf. Sci.* **603**, 1770–1775 (2009).

137. J. Emmanuel, B. E. Hayden, J. Saleh-Subaie, The particle size dependence of CO oxidation on model planar titania supported gold catalysts measured by parallel thermographic imaging. *J. Catal.* **369**, 175–180 (2019).

138. K. Mingle, thesis, University of South Carolina (2018).

139. K. McCullough, T. Williams, K. Mingle, P. Jamshidi, J. Lauterbach, High-throughput experimentation meets artificial intelligence: A new pathway to catalyst discovery. *Phys. Chem. Chem. Phys.* **22** (2020), pp. 11174–11196.

140. L. Ward, A. Agrawal, A. Choudhary, C. Wolverton, A general-purpose machine learning framework for predicting properties of inorganic materials. *Npj Comput. Mater.* **2**, 16028 (2016).

141. B. R. Goldsmith, J. Esterhuizen, J.-X. Liu, C. J. Bartel, C. Sutton, Machine learning for heterogeneous catalyst design and discovery. *AIChE J.* **64**, 2311–2323 (2018).

142. Z. Li, S. Wang, W. S. S. Chin, L. E. E. Achenie, H. Xin, High-throughput screening of bimetallic catalysts enabled by machine learning. *J. Mater. Chem. A.* **5**, 24131–24138 (2017).

143. E. J. Kluender, J. L. Hedrick, K. A. Brown, R. Rao, B. Meckes, J. S. Du, L. M. Moreau, B. Maruyama, C. A. Mirkin, Catalyst discovery through megalibraries of nanomaterials. *Proc. Natl. Acad. Sci. U. S. A.* **116**, 40–45 (2019).

144. B. Sun, H. Barron, G. Opletal, A. S. Barnard, From Process to Properties: Correlating Synthesis Conditions and Structural Disorder of Platinum Nanocatalysts. *J. Phys. Chem. C.* **122**, 28085–28093 (2018).

145. A. Corma, J. M. Serra, E. Argente, V. Botti, S. Valero, Application of artificial neural networks to combinatorial catalysis: Modeling and predicting ODHE catalysts. *ChemPhysChem.* **3**, 939–945 (2002).

146. A. Corma, J. M. Serra, P. Serna, M. Moliner, Integrating high-throughput characterization into combinatorial heterogeneous catalysis: Unsupervised construction of quantitative structure/property relationship models. *J. Catal.* **232**, 335–341 (2005).

147. T. Williams, K. McCullough, J. A. Lauterbach, Enabling Catalyst Discovery through Machine Learning and High-Throughput Experimentation. *Chem. Mater.* **32**, 157–165 (2020).

148. J. Hattrick-Simpers, C. Wen, J. Lauterbach, The materials super highway: integrating high-throughput experimentation into mapping the catalysis materials genome. *Catal. Letters*. **145**, 290–298 (2015).

149. E. Sasmaz, K. Mingle, J. Lauterbach, High-throughput screening using Fourier-transform infrared imaging. *Engineering*. **1**, 234–242 (2015).

150. J. Hu, L. Zhang, H. Song, J. Hu, Y. Lv, Ratiometric Cataluminescence for Rapid Recognition of Volatile Organic Compounds Based on Energy Transfer Process. *Anal. Chem.* (2019), doi:10.1021/acs.analchem.9b00592.

151. S. Wang, W. Shi, C. Lu, Chemisorbed Oxygen on the Surface of Catalyst-Improved Cataluminescence Selectivity. *Anal. Chem.* **88**, 4987–4994 (2016).

152. H. Su, E. S. Yeung, High-throughput screening of heterogeneous catalysts by laser-induced fluorescence imaging. *J. Am. Chem. Soc.* **122**, 7422–7423 (2000).

153. M. Krämer, M. Duisberg, K. Stöwe, W. F. Maier, Highly selective CO methanation catalysts for the purification of hydrogen-rich gas mixtures. *J. Catal.* **251**, 410–422 (2007).

154. P. Kondratyuk, G. Gumuslu, S. Shukla, J. B. Miller, B. D. Morreale, A. J. Gellman, A microreactor array for spatially resolved measurement of catalytic activity for high-throughput catalysis science. *J. Catal.* **300**, 55–62 (2013).

155. W. F. Maier, K. Stowe, S. Sieg, Combinatorial and high-throughput materials science. *Angew. Chemie - Int. Ed.* **46**, 6016–6067 (2007).

156. S. Senkan, K. Krantz, S. Ozturk, V. Zengin, I. Onal, High-throughput testing of heterogeneous catalyst libraries using array microreactors and mass spectrometry. *Angew. Chemie - Int. Ed.* **38**, 2794–2799 (1999).

157. S. Thomson, C. Hoffmann, S. Ruthe, H. W. Schmidt, F. Schüth, The development of a high throughput reactor for the catalytic screening of three phase reactions. *Appl. Catal. A Gen.* **220**, 253–264 (2001).

158. C. M. Snively, J. Lauterbach, Experimental aspects of asynchronous rapid-scan Fourier transform infrared imaging. *Appl. Spectrosc.* **59**, 1075–1081 (2005).

159. R. Vijay, thesis, University of Dealware (2007).

160. R. Bhargava, I. W. Levin, in *Spectrochemical Analysis Using Infrared Multichannel Detector*.

161. E. N. Lewis, P. J. Treado, R. C. Reeder, G. M. Story, A. E. Dowrey, C. Marcott, I. W. Levin, Fourier Transform Spectroscopic Imaging Using an Infrared Focal-Plane Array Detector. *Anal. Chem. Appl. Spectrosc. Anal. Chem.* **67**, 3377–33 (1995).

162. R. De Maesschalck, D. Jouan-Rimbaud, D. L. Massart, The Mahalanobis distance. *Chemom. Intell. Lab. Syst.* **50**, 1–18 (2000).

163. PID Theory Explained - NI, (available at https://www.ni.com/en-us/innovations/white-papers/06/pid-theory-explained.html).

164. S. Sandler, in *Chemical, Biochemical, and Engineering Thermodynamics* (2006), pp. 703–777.

165. N. M. Deraz, The comparative jurisprudence of catalysts preparation methods: I. precipitation and impregnation methods. *J. Ind. Environ. Chem.* **2**, 19–21 (2018).

166. P. Munnik, P. E. De Jongh, K. P. De Jong, Recent Developments in the Synthesis of Supported Catalysts. *Chem. Rev.* **115**, 6687–6718 (2015).

167. J. Park, J. Regalbuto, A simple, accurate determination of oxide PZC and the strong buffering effect of oxide surfaces at incipient wetness. *J. Colloid Interface Sci.* **175**, 239–252 (1995).

168. L. Jiao, J. R. Regalbuto, The synthesis of highly dispersed noble and base metals on silica via strong electrostatic adsorption: II. Mesoporous silica SBA-15. *J. Catal.* **260**, 342–350 (2008).

169. S. Cao, J. R. Monnier, J. R. Regalbuto, Alkali promotion of alumina-supported ruthenium catalysts for hydrogenation of levulinic acid to Γ-valerolactone. *J. Catal.* **347**, 72–78.

170. S. Cao, J. R. Monnier, C. T. Williams, W. Diao, J. R. Regalbuto, Rational nanoparticle synthesis to determine the effects of size, support, and K dopant on Ru activity for levulinic acid hydrogenation to γ-valerolactone. *J. Catal.* **326**, 69–81 (2015).

171. B. E. Warren, *X-Ray Diffraction* (1990).

172. M. M. Blum, H. John, Historical perspective and modern applications of Attenuated Total Reflectance - Fourier Transform Infrared Spectroscopy (ATR-FTIR). *Drug Test. Anal.* **4**, 298–302 (2012).

173. P. Griffiths, J. de Haseth, *Fourier Transform Infrared Spectroscopy* (2007).

174. F. Solymosi, J. Raskó, An infrared study of the influence of CO adsorption on the topology of supported ruthenium. *J. Catal.* **115**, 107–119 (1989).

175. C. M. Gunathunge, J. Li, X. Li, M. M. Waegele, Surface-Adsorbed CO as an Infrared Probe of Electrocatalytic Interfaces. **40**, 36 (2020).

176. C. A. Rice, S. D. Worley, C. W. Curtis, J. A. Guin, A. R. Tarrer, The oxidation state of dispersed Rh on Al2O3. *J. Chem. Phys.* **74**, 6487–6497 (1981).

177. A. M. Sica, J. H. Z. Dos Santos, I. M. Baibich, C. E. Gigola, Preparation and characterization of W/γ-Al2O3 and Pd-W/γ-Al2O3 catalysts from organometallic precursors. The catalytic activity for NO decomposition. *J. Mol. Catal. A Chem.* **137**, 287–295 (1999).

178. M. Haneda, T. Fujitani, H. Hamada, Effect of iridium dispersion on the catalytic activity of Ir/SiO2 for the selective reduction of NO with CO in the presence of O2 and SO2. *J. Mol. Catal. A Chem.* **256**, 143–148 (2006).

179. 4.8: UV/Vis and IR Spectroscopy - Chemistry LibreTexts, (available at https://chem.libretexts.org/Bookshelves/Analytical_Chemistry/Book%3A_Physical_Methods_in_Chemistry_and_Nano_Science_(Barron)/04%3A_Chemical_Speciation/4.02%3A_IR_Spectroscopy).

180. P. J. Dyson, J. S. McIndoe, *Transition Metal Carbonyl Cluster Chemistry* (CRC Press, 2018; https://www.taylorfrancis.com/books/transition-metal-carbonyl-cluster-chemistry-paul-dyson-scott-mcindoe/10.1201/9781315273815).

181. F. M. Hoffmann, R. A. De Paola, Anomalous C-O bond weakening of side-on-bonded carbon monoxide on a potassium-promoted Ru(001) surface. *Phys. Rev. Lett.* **52**, 1697–1700 (1984).

182. S. F. A. Kettle, in *Inorganic Chemistry Metal Carbonyl Chemistry* (Springer-Verlag, 2006; https://link.springer.com/chapter/10.1007/BFb0047780), pp. 111–148.

183. C. M. Gunathunge, J. Li, X. Li, M. M. Waegele, Surface-Adsorbed CO as an Infrared Probe of Electrocatalytic Interfaces. **40**, 36 (2020).

184. E. Smith, G. Dent, *Modern Raman Spectroscopy - A Practical Approach* (2019).

185. J. W. Niemantsverdriet, *Spectroscopy in Catalysis* (Wiley-VCH, ed. 3, 2007).

186. C. Wang, L. Sun, Q. Cao, B. Hu, Z. Huang, X. Tang, Surface structure sensitivity of manganese oxides for low-temperature selective catalytic reduction of NO with NH3. *Appl. Catal. B Environ.* **101**, 598–605 (2011).

187. Z. Huang, X. Gu, W. Wen, P. Hu, M. Makkee, H. Lin, F. Kapteijn, X. Tang, A “Smart” Hollandite DeNO x Catalyst: Self-Protection against Alkali Poisoning . *Angew. Chemie*. **125**, 688–692 (2013).

188. J. Luo, Q. Zhang, A. Huang, S. L. Suib, Total oxidation of volatile organic compounds with hydrophobic cryptomelane-type octahedral molecular sieves. *Microporous Mesoporous Mater.* **35**–**36**, 209–217 (2000).

189. C. Wang, J. Ma, F. Liu, H. He, R. Zhang, The Effects of Mn2+ Precursors on the Structure and Ozone Decomposition Activity of Cryptomelane-Type Manganese Oxide (OMS-2) Catalysts. *J. Phys. Chem. C.* **119**, 23119–23126 (2015).

190. M. Sun, L. Yu, F. Ye, G. Diao, Q. Yu, Z. Hao, Y. Zheng, L. Yuan, Transition metal doped cryptomelane-type manganese oxide for low-temperature catalytic combustion of dimethyl ether. *Chem. Eng. J.* **220**, 320–327 (2013).

191. S. Ming, P. Wang, P. Liu, J. Duan, F. Mei, L. Pang, Z. Chen, T. Li, Promotional effect of metal cations doping on OMS-2 catalysts for NH3-SCR reaction. *Chem. Eng. J.* **379** (2020), doi:10.1016/j.cej.2019.122287.

192. D. RN, S. YF, N. EJ, S. SL, O. CL, S. Levine, N. JM, SYNTHESIS AND CHARACTERIZATION OF OCTAHEDRAL MOLECULAR SIEVES (OMS-2) HAVING THE HOLLANDITE STRUCTURE. *Chem. Mater.* **6**, 815–821 (1994).

193. L. W. Chu, G. H. Hsiue, I. N. Lin, Synthesis of Ba2Ti9O20 materials via a dissolution-precipitation mechanism in a hydrothermal process. *Acta Mater.* **54**, 1671–1677 (2006).

194. H. S. Potdar, S. Vijayanand, K. K. Mohaideen, K. R. Patil, P. A. Joy, R. R. Madhavan, K. V. G. Kutty, R. D. Ambashta, P. K. Wattal, A simple chemical co-precipitation/calcination route for the synthesis of simulated synroc-B and synroc-C powders. *Mater. Chem. Phys.* **123**, 695–699 (2010).

195. Q. Feng, K. Yanagisawa, N. Yamasaki, Hydrothermal Soft Chemical Process for Synthesis of Manganese Oxides with Tunnel Structures. *J. Porous Mater.* **5**, 153–162 (1998).

196. A. Byström, A. M. Byström, IUCr, The crystal structure of hollandite, the related manganese oxide minerals, and α-MnO2. *Acta Crystallogr.* **3**, 146–154 (1950).

197. M. J. Geselbracht, L. D. Noailles, L. T. Ngo, J. H. Pikul, R. I. Walton, E. S. Cowell, F. Millange, D. O'Hare, Probing Molten Salt Flux Reactions Using Time-Resolved in Situ High-Temperature Powder X-ray Diffraction: A New Synthesis Route to the Mixed-Valence NaTi2O4. *Chem. Mater.* **16**, 1153–1159 (2004).

198. T. Gao, M. Glerup, F. Krumeich, R. Nesper, H. Fjellvâg, P. Norby, Microstructures and spectroscopic properties of cryptomelane-type manganese dioxide nanofibers. *J. Phys. Chem. C.* **112**, 13134–13140 (2008).

199. L. Sun, Q. Cao, B. Hu, J. Li, J. Hao, G. Jing, X. Tang, Synthesis, characterization and catalytic activities of vanadium-cryptomelane manganese oxides in low-temperature NO reduction with NH3. *Appl. Catal. A Gen.* **393**, 323–330 (2011).

200. C. Chlique, D. Lambertin, F. Frizon, P. Deniard, S. Jobic, Effect of temperature on the γ-MnO2/"Ag2O" hydrogen getter structure. *Fusion Eng. Des.* **112**, 475–479 (2016).

201. O. A. Drozhzhin, V. V. Grigoriev, A. M. Alekseeva, S. V. Ryazantsev, O. A. Tyablikov, D. Chernyshov, A. M. Abakumov, E. V. Antipov, Phase Transformations and Charge Ordering during Li+ Intercalation into Hollandite-Type TiO2 Studied by Operando Synchrotron X-ray Powder Diffraction. *Eur. J. Inorg. Chem.* **2020**, 743–748 (2020).

202. S. Roy, A. Ito, M. Nagao, F. Hayashi, K. Furui, H. Shiiba, K. Yubuta, T. Sudare, C. Terashima, K. Teshima, Flux Growth of Single-Crystalline Hollandite-Type Potassium Ferrotitanate Microrods From KCl Flux. *Front. Chem. | www.frontiersin.org.* **1**, 714 (2020).

203. K. J. Takeuchi, S. Z. Yau, A. Subramanian, A. C. Marschilok, E. S. Takeuchi, The Electrochemistry of Silver Hollandite Nanorods, Ag x Mn 8 O 16 : Enhancement of Electrochemical Battery Performance via Dimensional and Compositional Control. *J. Electrochem. Soc.* **160**, A3090–A3094 (2013).

204. J. H. Jo, J. U. Choi, M. K. Cho, Y. Aniskevich, H. Kim, G. Ragoisha, E. Streltsov, J. Kim, S. Myung, Hollandite-Type $VO_{1.75}(OH)_{0.5}$: Effective Sodium Storage for High-Performance Sodium-Ion Batteries. *Adv. Energy Mater.* **9**, 1900603 (2019).

205. R. Hu, Y. Cheng, L. Xie, D. Wang, Effect of doped Ag on performance of manganese oxide octahedral molecular sieve for CO oxidation. *Chinese J. Catal.* **28**, 463–468 (2007).

206. J. Chen, J. Li, H. Li, X. Huang, W. Shen, Facile synthesis of Ag-OMS-2 nanorods and their catalytic applications in CO oxidation. *Microporous Mesoporous Mater.* **116**, 586–592 (2008).

207. W. Y. Hernández, M. A. Centeno, S. Ivanova, P. Eloy, E. M. Gaigneaux, J. A. Odriozola, Cu-modified cryptomelane oxide as active catalyst for CO oxidation reactions. *Appl. Catal. B Environ.* **123–124**, 27–35 (2012).

208. V. P. Santos, O. S. G. P. Soares, J. J. W. Bakker, M. F. R. Pereira, J. J. M. Órfão, J. Gascon, F. Kapteijn, J. L. Figueiredo, Structural and chemical disorder of cryptomelane promoted by alkali doping: Influence on catalytic properties. *J. Catal.* **293**, 165–174 (2012).

209. V. P. Santos, M. F. R. Pereira, J. J. M. Órfão, J. L. Figueiredo, Catalytic oxidation of ethyl acetate over a cesium modified cryptomelane catalyst. *Appl. Catal. B Environ.* **88**, 550–556 (2009).

210. V. D. Makwana, Y. C. Son, A. R. Howell, S. L. Suib, The role of lattice oxygen in selective benzyl alcohol oxidation using OMS-2 catalyst: A kinetic and isotope-labeling study. *J. Catal.* **210**, 46–52 (2002).

211. G. D. Yadav, R. K. Mewada, Selectivity engineering in the synthesis of value added chemicals: Oxidation of 1-octanol to 1-octanal over nano-fibrous Ag-OMS-2 catalysts. *Chem. Eng. Res. Des.* **90**, 86–97 (2012).

212. R. Kumar, S. Sithambaram, S. L. Suib, Cyclohexane oxidation catalyzed by manganese oxide octahedral molecular sieves-Effect of acidity of the catalyst. *J. Catal.* **262**, 304–313 (2009).

213. S. Adjimi, J. M. García-Vargas, J. A. Díaz, L. Retailleau, S. Gil, M. Pera-Titus, Y. Guo, A. Giroir-Fendler, Highly efficient and stable Ru/K-OMS-2 catalyst for NO oxidation. *Appl. Catal. B Environ.* **219**, 459–466 (2017).

214. M. L. Foo, W.-L. Lee, T. Siegrist, G. Lawes, A. P. Ramirez, N. P. Ong, R. J. Cava, Electronic characterization of alkali ruthenium hollandites: KRu 4 O 8 , RbRu 4 O 8 and Cs 0.8 Li 0.2 Ru 4 O 8. *Mater. Res. Bull.* **39**, 1663–1670 (2004).

215. J. Liu, V. Makwana, J. Cai, S. L. Suib, M. Aindow, Effects of alkali metal and ammonium cation templates on nanofibrous cryptomelane-type manganese oxide octahedral molecular sieves (OMS-2). *J. Phys. Chem. B*. **107**, 9185–9194 (2003).

216. X. Fu, J. Feng, H. Wang, K. M. Ng, Morphological and structural evolution of α-MnO2 nanorods synthesized via an aqueous route through MnO4-/Mn2+ reaction. *J. Solid State Chem.* **183**, 883–889 (2010).

217. D. Portehault, S. Cassaignon, E. Baudrin, J. P. Jolivet, Morphology control of cryptomelane type MnO2 nanowires by soft chemistry growth mechanisms in aqueous medium. *Chem. Mater.* **19**, 5410–5417 (2007).

218. T. Gao, H. Fjellvg, P. Norby, Structural and morphological evolution of β-MnO2 nanorods during hydrothermal synthesis. *Nanotechnology*. **20** (2009), doi:10.1088/0957-4484/20/5/055610.

219. X. F. Shen, Y. S. Ding, J. C. Hanson, M. Aindow, S. L. Suib, In situ synthesis of mixed-valent manganese oxide nanocrystals: An in situ synchrotron X-ray diffraction study. *J. Am. Chem. Soc.* **128**, 4570–4571 (2006).

220. B. R. Chen, W. Sun, D. A. Kitchaev, J. S. Mangum, V. Thampy, L. M. Garten, D. S. Ginley, B. P. Gorman, K. H. Stone, G. Ceder, M. F. Toney, L. T. Schelhas, Understanding crystallization pathways leading to manganese oxide polymorph formation. *Nat. Commun.* **9** (2018), doi:10.1038/s41467-018-04917-y.

221. D. M. Alonso, R. Mariscal, R. Moreno-Tost, M. D. Z. Poves, M. L. Granados, Potassium leaching during triglyceride transesterification using K/γ-Al2O3 catalysts. *Catal. Commun.* **8**, 2074–2080 (2007).

222. S. Benjapornkulaphong, C. Ngamcharussrivichai, K. Bunyakiat, Al2O3-supported alkali and alkali earth metal oxides for transesterification of palm kernel oil and coconut oil. *Chem. Eng. J.* **145**, 468–474 (2009).

223. H. Ma, S. Li, B. Wang, R. Wang, S. Tian, Transesterification of Rapeseed Oil for Synthesizing Biodiesel by K/KOH/γ-Al2O3 as Heterogeneous Base Catalyst. *J. Am. Oil Chem. Soc.* **85**, 263–270 (2008).

224. M. Verziu, M. Florea, S. Simon, V. Simon, P. Filip, V. I. Parvulescu, C. Hardacre, Transesterification of vegetable oils on basic large mesoporous alumina supported alkaline fluorides-Evidences of the nature of the active site and catalytic performances. *J. Catal.* **263**, 56–66 (2009).

225. J. P. Da Costa Evangelista, A. D. Gondim, L. Di Souza, A. S. Araujo, Alumina-supported potassium compounds as heterogeneous catalysts for biodiesel production: A review. *Renew. Sustain. Energy Rev.* **59** (2016), pp. 887–894.

226. B. W. Krupay, Y. Amenomiya, Alkali-promoted alumina catalysts. I. Chemisorption and oxygen exchange of carbon monoxide and carbon dioxide on potassium-promoted alumina catalysts. *J. Catal.* **67**, 362–370 (1981).

227. W. H. J. Stork, G. T. Pott, Studies of compound formation on alkali/γ-aluminum oxide catalyst systems using chromium, iron, and manganese luminescence. *J. Phys. Chem.* **78**, 2496–2506 (1974).

228. A. Iordan, M. I. Zaki, C. Kappenstein, Interfacial chemistry in the preparation of catalytic potassium-modified aluminas. *J. Chem. Soc. Faraday Trans.* **89**, 2527–2536 (1993).

229. Y. Wang, Jian Hua Zhu, Wen Yu Huang, Synthesis and characterization of potassium-modified alumina superbases. *Phys. Chem. Chem. Phys.* **3**, 2537–2543 (2001).

230. S. Soled, γ-Al2O3 viewed as a defect oxyhydroxide. *J. Catal.* **81**, 252–257 (1983).

231. L. B. Sun, F. N. Gu, Y. Chun, J. Yang, Y. Wang, J. H. Zhu, Attempt to generate strong basicity on silica and titania. *J. Phys. Chem. C*. **112**, 4978–4985 (2008).

232. M. I. Zaki, T. H. Ballinger, J. T. Yates, Protection of Rh/Al2O3 catalysts by potassium functionalization of the Al2O3 support. *J. Phys. Chem.* **95**, 4028–4033 (1991).

233. Y. Wang, Jian Hua Zhu, Wen Yu Huang, Synthesis and characterization of potassium-modified alumina superbases. *Phys. Chem. Chem. Phys.* **3**, 2537–2543 (2001).

234. T. Baba, H. Handa, Y. Ono, Superbase character of alumina loaded with potassium by impregnation from ammoniacal solution. *J. Chem. Soc. Faraday Trans.* **90**, 187–191 (1994).

235. K. Nagaoka, T. Eboshi, N. Abe, S. Miyahara, K. Honda, K. Sato, Influence of basic dopants on the activity of Ru/Pr6O11 for hydrogen production by ammonia decomposition. *Int. J. Hydrogen Energy*. **39**, 20731–20735 (2014).

236. M. E. Gálvez, S. Ascaso, P. Stelmachowski, P. Legutko, A. Kotarba, R. Moliner, M. J. Lázaro, Influence of the surface potassium species in Fe-K/Al2O3 catalysts on the soot oxidation activity in the presence of NOx. *Appl. Catal. B Environ.* **152–153**, 88–98 (2014).

237. A. K. Hill, L. Torrente-Murciano, In-situ H2 production via low temperature decomposition of ammonia: Insights into the role of cesium as a promoter. *Int. J. Hydrogen Energy*. **39**, 7646–7654 (2014).

238. T. V Choudhary, C. Sivadinarayana, D. W. Goodman, Catalytic ammonia decomposition: COx-free hydrogen production for fuel cell applications. *Catal. Letters*. **72**, 197–201 (2001).

239. A. Di Carlo, L. Vecchione, Z. Del Prete, Ammonia decomposition over commercial Ru/Al2O3 catalyst: An experimental evaluation at different operative pressures and temperatures. *Int. J. Hydrogen Energy*. **39**, 808–814 (2014).

240. Q. Tang, X. Huang, C. Wu, P. Zhao, Y. Chen, Y. Yang, Structure and catalytic properties of K-doped manganese oxide supported on alumina. *J. Mol. Catal. A Chem.* **306**, 48–53 (2009).

241. A. Devadas, S. Baranton, T. W. Napporn, C. Coutanceau, Tailoring of RuO2 nanoparticles by microwave assisted “instant method” for energy storage applications. *J. Power Sources*. **196**, 4044–4053 (2011).

242. Ž. Petrović, M. Ristić, M. Marciuš, B. Sepiol, H. Peterlik, M. Ivanda, S. Musić, Formation of RuO2 nanoparticles by thermal decomposition of Ru(NO)(NO3)3. *Ceram. Int.* **41**, 7811–7815 (2015).

243. C. Chlique, D. Lambertin, F. Frizon, P. Deniard, S. Jobic, Effect of temperature on the γ-MnO2/“Ag2O” hydrogen getter structure. *Fusion Eng. Des.* **112**, 475–479 (2016).

244. T. Liu, Q. Li, Y. Xin, Z. Zhang, X. Tang, L. Zheng, P. X. Gao, Quasi free K cations confined in hollandite-type tunnels for catalytic solid (catalyst)-solid (reactant) oxidation reactions. *Appl. Catal. B Environ.* **232**, 108–116 (2018).

245. J. Luo, A. Huang, S. H. Park, S. L. Suib, C. L. O’Young, Crystallization of Sodium-Birnessite and Accompanied Phase Transformation. *Chem. Mater.* **10**, 1561–1568 (1998).

246. L. Zhou, J. Zhang, J. He, Y. Hu, H. Tian, Control over the morphology and structure of manganese oxide by tuning reaction conditions and catalytic performance for formaldehyde oxidation. *Mater. Res. Bull.* **46**, 1714–1722 (2011).

247. X. Zhang, W. Yang, J. Yang, D. G. Evans, Synthesis and characterization of α-MnO2 nanowires: Self-assembly and phase transformation to β-MnO2 microcrystals. *J. Cryst. Growth*. **310**, 716–722 (2008).

248. G. Green, W. Griffith, D. Hollinshead, L. S, M. Schroder, Oxo Complexes of Ruthenium (VI) and (VII) as Organic Oxidants. *J. Chem. Soc. Perkin Trans.* **1** (1984).

249. A. J. Bailey, W. P. Griffith, S. I. Mostafa, P. A. Sherwood, Studies on Transition-Metal Oxo and Nitrido Complexes. 13. Perruthenate and Ruthenate Anions as Catalytic Organic Oxidants. *Inorg. Chem.* **32**, 268–271 (1993).

250. A. Lebedeva, B. L. Albuquerque, J. B. Domingos, J. F. Lamonier, J. M. Giraudon, P. Lecante, A. Denicourt-Nowicki, A. Roucoux, Ruthenium Trichloride Catalyst in Water: Ru Colloids versus Ru Dimer Characterization Investigations. *Inorg. Chem.* **58**, 4141–4151 (2019).

251. V. Mazzieri, F. Coloma-Pascual, A. Arcoya, P. C. L’Argentière, N. S. Fígoli, XPS, FTIR and TPR characterization of Ru/Al 2 O 3 catalysts. *Appl. Surf. Sci.* **210**, 222–230 (2003).

252. P. Betancourt, A. Rives, R. Hubaut, C. E. Scott, J. Goldwasser, A study of the ruthenium-alumina system. *Appl. Catal. A Gen.* **170**, 307–314 (1998).

253. J. C. Dellamorte, J. Lauterbach, M. A. Barteau, Rhenium promotion of Ag and Cu-Ag bimetallic catalysts for ethylene epoxidation. *Catal. Today*. **120**, 182–185 (2007).

254. T. C. R. Rocha, M. Hävecker, A. Knop-Gericke, R. Schlögl, Promoters in heterogeneous catalysis: The role of Cl on ethylene epoxidation over Ag. *J. Catal.* **312**, 12–16 (2014).

255. H. Tan, K. Li, S. Sioud, D. Cha, M. H. Amad, M. N. Hedhili, Z. A. Al-Talla, Synthesis of Ru nanoparticles confined in magnesium oxide-modified mesoporous alumina and their enhanced catalytic performance during ammonia decomposition. *Catal. Commun.* **26**, 248–252 (2012).

256. E. A. Blekkan, A. Holmen, S. Vada, Alkali promotion of alumina-supported colbalt Fischer-Tropsch catalysts studied by TPR, TPD and pulse chemisorption. *Acta Chem. Scand.* **47**, 275–280 (1993).

257. C. F. J. Barnard, S. C. Bennett, Oxidation States of Ruthenium and Osmium. *Platin. Met. Rev.* **48**, 157–158 (2004).

258. V. Prasad, A. M. Karim, A. Arya, D. G. Vlachos, Assessment of overall rate expressions and multiscale, microkinetic model uniqueness via experimental data injection: Ammonia decomposition on Ru/γ-Al2O3 for hydrogen production. *Ind. Eng. Chem. Res.* **48**, 5255–5265 (2009).

259. X. K. Li, W. J. Ji, J. Zhao, S. J. Wang, C. T. Au, Ammonia decomposition over Ru and Ni catalysts supported on fumed SiO 2, MCM-41, and SBA-15. *J. Catal.* **236**, 181–189 (2005).

260. C. Chen, Y. Chen, A. M. Ali, W. Luo, J. Wen, L. Zhang, H. Zhang, Bimetallic Ru-Fe Nanoparticles Supported on Carbon Nanotubes for Ammonia Decomposition and Synthesis. *Chem. Eng. Technol.* **43**, 719–730 (2020).

261. J. Zhang, J. O. Müller, W. Zheng, D. Wang, D. Su, R. Schlögl, Individual Fe-Co alloy nanoparticles on carbon nanotubes: Structural and catalytic properties. *Nano Lett.* **8**, 2738–2743 (2008).

262. B. Lorenzut, T. Montini, M. Bevilacqua, P. Fornasiero, FeMo-based catalysts for H 2 production by NH 3 decomposition. *Appl. Catal. B Environ.* **125**, 409–417 (2012).

263. J. Ji, X. Duan, G. Qian, X. Zhou, G. Tong, W. Yuan, Towards an efficient CoMo/γ-Al2O3 catalyst using metal amine metallate as an active phase precursor: Enhanced hydrogen production by ammonia decomposition. *Int. J. Hydrogen Energy*. **39**, 12490–12498 (2014).

264. X. Duan, G. Qian, X. Zhou, D. Chen, W. Yuan, MCM-41 supported CoMo bimetallic catalysts for enhanced hydrogen production by ammonia decomposition. *Chem. Eng. J.* **207**–**208**, 103–108 (2012).

265. W. Zheng, T. P. Cotter, P. Kaghazchi, T. Jacob, B. Frank, K. Schlichte, W. Zhang, D. S. Su, F. Schüth, R. Schlögl, Experimental and theoretical investigation of molybdenum carbide and nitride as catalysts for ammonia decomposition. *J. Am. Chem. Soc.* **135**, 3458–3464 (2013).

266. S. Podila, S. F. Zaman, H. Driss, Y. A. Alhamed, A. A. Al-Zahrani, L. A. Petrov, Hydrogen production by ammonia decomposition using high surface area Mo2N and Co3Mo3N catalysts. *Catal. Sci. Technol.* **6**, 1496–1506 (2016).

267. W. Guo, D. G. Vlachos, Patched bimetallic surfaces are active catalysts for ammonia decomposition. *Nat. Commun.* **6**, 1–7 (2015).

268. D. A. Hansgen, D. G. Vlachos, J. G. Chen, Ammonia decomposition activity on monolayer Ni supported on Ru, Pt and WC substrates. *Surf. Sci.* **605**, 2055–2060 (2011).

269. K. Lamb, S. S. Hla, M. Dolan, Ammonia decomposition kinetics over LiOH-promoted, A-Al 2 O 3 -supported Ru catalyst. *Int. J. Hydrogen Energy*. **44**, 3726–3736 (2019).

270. S. Bajus, F. Agel, K. M, N. Bhrian, P. Wasserscheid, Alkali hydroxide-modified Ru/g-Al2O3 catalysts for ammonia decomposition. *Appl. Catal. A Gen.* **510**, 189–195 (2016).

271. A. Daisley, J. S. J. Hargreaves, R. Hermann, Y. Poya, Y. Wang, A comparison of the activities of various supported catalysts for ammonia synthesis. *Catal. Today*. **357**, 534–540 (2020).

272. B. Lin, L. Heng, B. Fang, H. Yin, J. Ni, X. Wang, J. Lin, L. Jiang, Ammonia Synthesis Activity of Alumina-Supported Ruthenium Catalyst Enhanced by Alumina Phase Transformation. *ACS Catal.* **9**, 1635–1644 (2019).

273. C. Fernández, C. Sassoye, D. P. Debecker, C. Sanchez, P. Ruiz, Effect of the size and distribution of supported Ru nanoparticles on their activity in ammonia synthesis under mild reaction conditions. *Appl. Catal. A Gen.* **474**, 194–202 (2014).

274. C. Fernández, C. Pezzotta, E. M. Gaigneaux, N. Bion, D. Duprez, P. Ruiz, Disclosing the synergistic mechanism in the catalytic activity of different-sized Ru nanoparticles for ammonia synthesis at mild reaction conditions. *Catal. Today*. **251**, 88–95 (2015).

275. H. Liu, H. Wang, J. Shen, Y. Sun, Z. Liu, Promotion effect of cerium and lanthanum oxides on Ni/SBA-15 catalyst for ammonia decomposition (2007), doi:10.1016/j.cattod.2007.10.048.

276. I. Lucentini, A. Casanovas, J. Llorca, Catalytic ammonia decomposition for hydrogen production on Ni, Ru and Ni[sbnd]Ru supported on CeO2. *Int. J. Hydrogen Energy*. **44**, 12693–12707 (2019).

277. S. F. Yin, B. Q. Xu, W. X. Zhu, C. F. Ng, X. P. Zhou, C. T. Au, Carbon nanotubes-supported Ru catalyst for the generation of CO x-free hydrogen from ammonia. *Catal. Today*. **93–95**, 27–38 (2004).

278. T. V. Choudhary, C. Sivadinarayana, D. W. Goodman, Catalytic ammonia decomposition: COx-free hydrogen production for fuel cell applications. *Catal. Letters*. **72**, 197–201 (2001).

279. M. B. Alves, F. C. M. Medeiros, P. A. Z. Suarez, Cadmium compounds as catalysts for biodiesel production. *Ind. Eng. Chem. Res.* **49**, 7176–7182 (2010).

280. T. Ogawa, Y. Kobayashi, H. Mizoguchi, M. Kitano, H. Abe, T. Tada, Y. Toda, Y. Niwa, H. Hosono, High electron density on ru in intermetallic YRu2 : The application to catalyst for ammonia synthesis (2018), doi:10.1021/acs.jpcc.8b02128.

281. J. Huang, M. Yuan, X. Li, Y. Wang, M. Li, J. Li, Z. You, Inhibited hydrogen poisoning for enhanced activity of promoters-Ru/Sr2Ta2O7 nanowires for ammonia synthesis. *J. Catal.* **389**, 556–565 (2020).

282. K. Okura, T. Okanishi, H. Muroyama, T. Matsui, K. Eguchi, Promotion effect of rare-earth elements on the catalytic decomposition of ammonia over Ni/Al 2 O 3 catalyst. *"Applied Catal. A, Gen.* **505**, 77–85 (2015).

283. M. A. Al-Saleh, M. M. Hossain, M. A. Shalabi, T. Kimura, T. Inui, Hydrogen spillover effects on Pt-Rh modified Co-clay catalysts for heavy oil upgrading. *Appl. Catal. A Gen.* **253**, 453–459 (2003).

284. P. Y. Lin, M. Meng, J. J. Yuan, S. M. Yu, Y. L. Fu, Spillover effect and CO oxidation activity on the supported noble metals-metal oxides catalysts. *Stud. Surf. Sci. Catal.* **112**, 201–210 (1997).

285. L. Wang, C. Yin, R. T. Yang, Selective catalytic reduction of nitric oxide with hydrogen on supported Pd: Enhancement by hydrogen spillover. *Appl. Catal. A Gen.* **514**, 35–42 (2016).

286. D. Nabaho, J. W. Niemantsverdriet, M. Claeys, E. Van Steen, Hydrogen spillover in the Fischer-Tropsch synthesis: An analysis of platinum as a promoter for cobalt-alumina catalysts. *Catal. Today*. **261**, 17–27 (2016).

287. T. W. Hansen, J. B. Wagner, P. L. Hansen, S. Dahl, H. Topsøe, C. J. H. Jacobsen, Atomic-resolution in situ transmission electron microscopy of a promoter of a heterogeneous catalyst. *Science (80-.).* **294**, 1508–1510 (2001).

288. M. Chen, M. Yuan, J. Li, Z. You, Ammonia synthesis over Cs- or Ba-promoted ruthenium catalyst supported on strontium niobate. *Appl. Catal. A Gen.* **554**, 1–9 (2018).

289. M. Yu, A novel hollow fiber membrane reactor for high purity H2 generation from thermal catalytic NH3 decomposition (2018), pp. 1–56.

290. F. R. García-García, A. Guerrero-Ruiz, I. Rodríguez-Ramos, in *Topics in Catalysis* (2009; https://link.springer.com/content/pdf/10.1007%2Fs11244-009-9203-7.pdf), vol. 52, pp. 758–764.

291. W. Raróg-Pilecka, E. Miśkiewicz, D. Szmigiel, Z. Kowalczyk, Structure sensitivity of ammonia synthesis over promoted ruthenium catalysts supported on graphitised carbon. *J. Catal.* **231**, 11–19 (2005).

292. S. Speakman, Introduction to X-ray Powder Diffraction Data Analysis. *Cent. Mater. Sci. Eng. MIT*.

293. F. Girgsdies, E. M. Group, Peak Profile Analysis in X-ray Powder Diffraction. *Fritz-Haber-Institut der MPG* (1200) (available at http://www.fhi-berlin.mpg.de/acnew/department/pages/teaching/pages/teaching__wintersemester__2015_2016/frank_girgsdies__peak_profile_fitting_in_xrd__151106.pdf).

294. T. H. de Keijser, J. I. Langford, E. J. Mittemeijer, A. B. P. Vogels, Use of the Voigt function in a single-line method for the analysis of X-ray diffraction line broadening. *J. Appl. Crystallogr.* **15**, 308–314 (1982).

295. J. M. Serra, A. Chica, A. Corma, Development of a low temperature light paraffin isomerization catalysts with improved resistance to water and sulphur by combinatorial methods. *Appl. Catal. A Gen.* **239**, 35–42 (2003).

296. A. Corma, J. M. Serra, P. Serna, S. Valero, E. Argente, V. Botti, Optimisation of olefin epoxidation catalysts with the application of high-throughput and genetic algorithms assisted by artificial neural networks (softcomputing techniques). *J. Catal.* **229**, 513–524 (2005).

297. K. Huang, F.-Q. Chen, D.-W. Lü, Artificial neural network-aided design of a multi-component catalyst for methane oxidative coupling. *Appl. Catal. A Gen.* **219**, 61–68 (2001).

298. Z. Y. Hou, Q. Dai, X. Q. Wu, G. T. Chen, Artificial neural network aided design of catalyst for propane ammoxidation. *Appl. Catal. A Gen.* **161**, 183–190 (1997).

299. T. Williams, thesis (2019).

300. L. M. Falicov, T. And, G. A. Somorjai, Correlation between catalytic activity and bonding and coordination number of atoms and molecules on transition metal surfaces: Theory and experimental evidence. *Chemistry (Easton).* **82**, 2207–2211 (1985).

301. B. Hammer, J. K. Nørskov, in *Impact of Surface Science on Catalysis* (2000), vol. 45, pp. 71–129.

302. A. J. Chowdhury, W. Yang, E. Walker, O. Mamun, A. Heyden, G. A. Terejanu, Prediction of Adsorption Energies for Chemical Species on Metal Catalyst Surfaces Using Machine Learning. *J. Phys. Chem. C.* **122**, 28142–28150 (2018).

303. D. A. Hansgen, D. G. Vlachos, J. G. Chen, Using first principles to predict bimetallic catalysts for the ammonia decomposition reaction. *Nat. Chem.* **2**, 484–489 (2010).

304. A. Vojvodic, J. K. Nørskov, F. Abild-Pedersen, Electronic structure effects in transition metal surface chemistry. *Top. Catal.* **57**, 25–32 (2014).

305. S. Bhattacharjee, U. V Waghmare, S.-C. Lee, An improved d-band model of the catalytic activity of magnetic transition metal surfaces. *Sci. Rep.* **6**, 35916 (2016).

306. H. Xin, S. Linic, Communications: Exceptions to the d-band model of chemisorption on metal surfaces: The dominant role of repulsion between adsorbate states and metal d-states. *J. Chem. Phys.* **132**, 221101 (2010).

307. S. J. Carey, W. Zhao, C. T. Campbell, Bond Energies of Adsorbed Intermediates to Metal Surfaces: Correlation with Hydrogen–Ligand and Hydrogen–Surface Bond Energies and Electronegativities. *Angew. Chemie - Int. Ed.* **57**, 16877–16881 (2018).

308. Y. Kudriavtsev, A. Villegas, A. Godines, R. Asomoza, Calculation of the surface binding energy for ion sputtered particles. *Appl. Surf. Sci.* **239**, 273–278 (2005).

309. X. Shen, Y. Pan, B. Liu, J. Yang, J. Zeng, Z. Peng, More accurate depiction of adsorption energy on transition metals using work function as one additional descriptor. *Phys. Chem. Chem. Phys.* **19**, 12628–12632 (2017).

310. Y. Li, L. Yao, S. Liu, J. Zhao, W. Ji, C. T. Au, Cs-modified iron nanoparticles encapsulated in microporous and mesoporous SiO2 for COx-free H2 production via ammonia decomposition. *Catal. Today*. **160**, 79–86 (2011).

311. H. Silva, M. G. Nielsen, E. M. Fiordaliso, C. D. Damsgaard, C. Gundlach, T. Kasama, I. B. Chorkendorff, D. Chakraborty, Synthesis and characterization of Fe–Ni/γ-Al2O3 egg-shell catalyst for H2 generation by ammonia decomposition. *Appl. Catal. A Gen.* **505**, 548–556 (2015).

312. P. B. Weisz, C. D. Prater, Interpretation of Measurements in Experimental Catalysis. *Adv. Catal.* **6**, 143–196 (1954).

313. R. Reid, in *The properties of gases and liquids* (New York: McGraw-Hill, 1987).

314. P. Panagiotopoulou, Methanation of CO2 over alkali-promoted Ru/TiO2 catalysts: II. Effect of alkali additives on the reaction pathway. *Appl. Catal. B Environ.* **236**, 162–170 (2018).

315. A. M. Abdel-Mageed, ‖ D Widmann, S. E. Olesen, I. Chorkendorff, J. Biskupek, R. J. Behm, Selective CO Methanation on Ru/TiO 2 Catalysts: Role and Influence of Metal−Support Interactions (2015), doi:10.1021/acscatal.5b01520.

316. S. Y. Chin, C. T. Williams, M. D. Amiridis, FTIR studies of CO adsorption on Al2O3- and SiO 2-supported Ru catalysts. *J. Phys. Chem. B.* **110**, 871–882 (2006).

317. A. Waghray, J. Wang, R. Oukaci, D. G. Blackmond, Influence of alkali promoters in the selective hydrogenation of 3-methyl-2-butenal over Ru/SiO2 catalysts. *J. Phys. Chem.* **96**, 5954–5959 (1992).

318. F. Solymosi, J. Raskó, An infrared study of CO and NO adsorption on alumina-supported iridium catalyst. *J. Catal.* **62**, 253–263 (1980).

319. Bradshaw A.M., Pritchard J., in *Proceedings of the Royal Society of London. Series A, Mathematical and Physical Sciences* (1970; https://about.jstor.org/terms), vol. 316, pp. 169–183.

320. X. Mo, J. Gao, N. Umnajkaseam, J. G. Goodwin, La, V, and Fe promotion of Rh/SiO2 for CO hydrogenation: Effect on adsorption and reaction. *J. Catal.* **267**, 167–176 (2009).

321. H. W. K. Tom, C. M. Mate, X. D. Zhu, J. E. Crowell, T. F. Heinz, G. A. Somorjai, Y. R. Shen, Surface studies by optical second-harmonic generation: The adsorption of O2, CO, and sodium on the Rh(111) surface. *Phys. Rev. Lett.* **52**, 348–351 (1984).

322. E. L. Garfunkel, J. E. Crowell, G. A. Somorjai, The strong influence of potassium on the adsorption of CO on platinum surfaces. A thermal desorption spectroscopy and high-resolution electron energy loss spectroscopy study. *J. Phys. Chem.* **86**, 310–313 (1982).

APPENDIX A

PERMISSION TO REPRRINT

1. T Williams, K McCullough and J Lauterbach, “Enabling catalyst discovery through machine learning and high-throughput experimentation.” Chemistry of Materials 32 (1) 2020, 157-165.

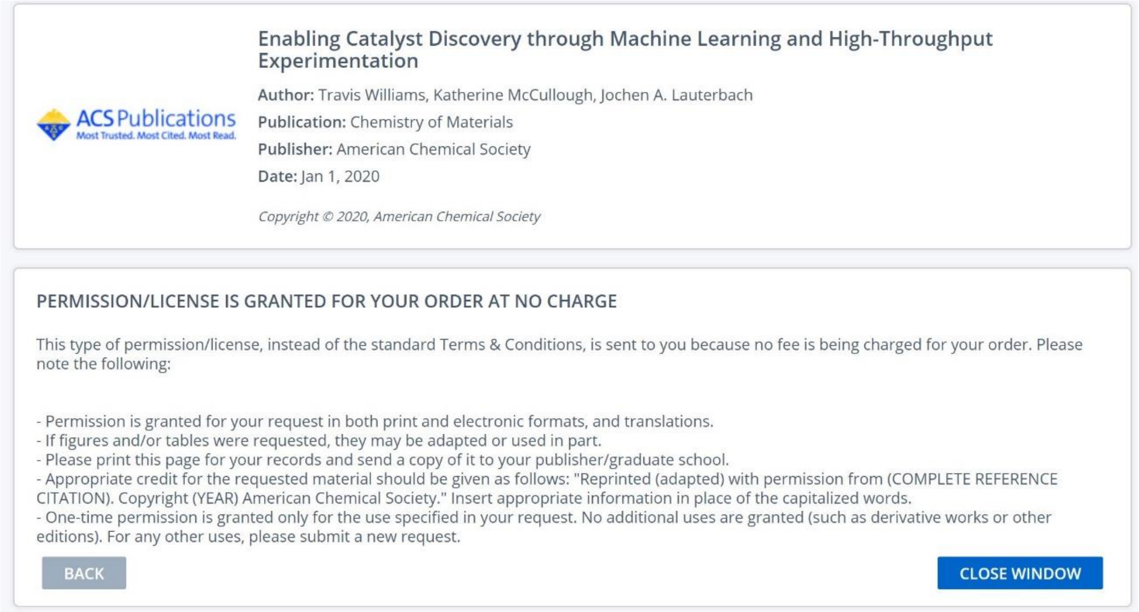

Enabling Catalyst Discovery through Machine Learning and High-Throughput Experimentation

Author: Travis Williams, Katherine McCullough, Jochen A. Lauterbach
Publication: Chemistry of Materials
Publisher: American Chemical Society
Date: Jan 1, 2020

Copyright © 2020, American Chemical Society

PERMISSION/LICENSE IS GRANTED FOR YOUR ORDER AT NO CHARGE

This type of permission/license, instead of the standard Terms & Conditions, is sent to you because no fee is being charged for your order. Please note the following:

- Permission is granted for your request in both print and electronic formats, and translations.
- If figures and/or tables were requested, they may be adapted or used in part.
- Please print this page for your records and send a copy of it to your publisher/graduate school.
- Appropriate credit for the requested material should be given as follows: "Reprinted (adapted) with permission from (COMPLETE REFERENCE CITATION). Copyright (YEAR) American Chemical Society." Insert appropriate information in place of the capitalized words.
- One-time permission is granted only for the use specified in your request. No additional uses are granted (such as derivative works or other editions). For any other uses, please submit a new request.

2. K McCullough, T Williams, K Mingle, P Jamshidi, J Lauterbach, “High throughput experimentation meets artificial intelligence: a new pathway to catalyst discovery.” Physical Chemistry Chemical Physics 22 (20) 2020, 11174-11196.

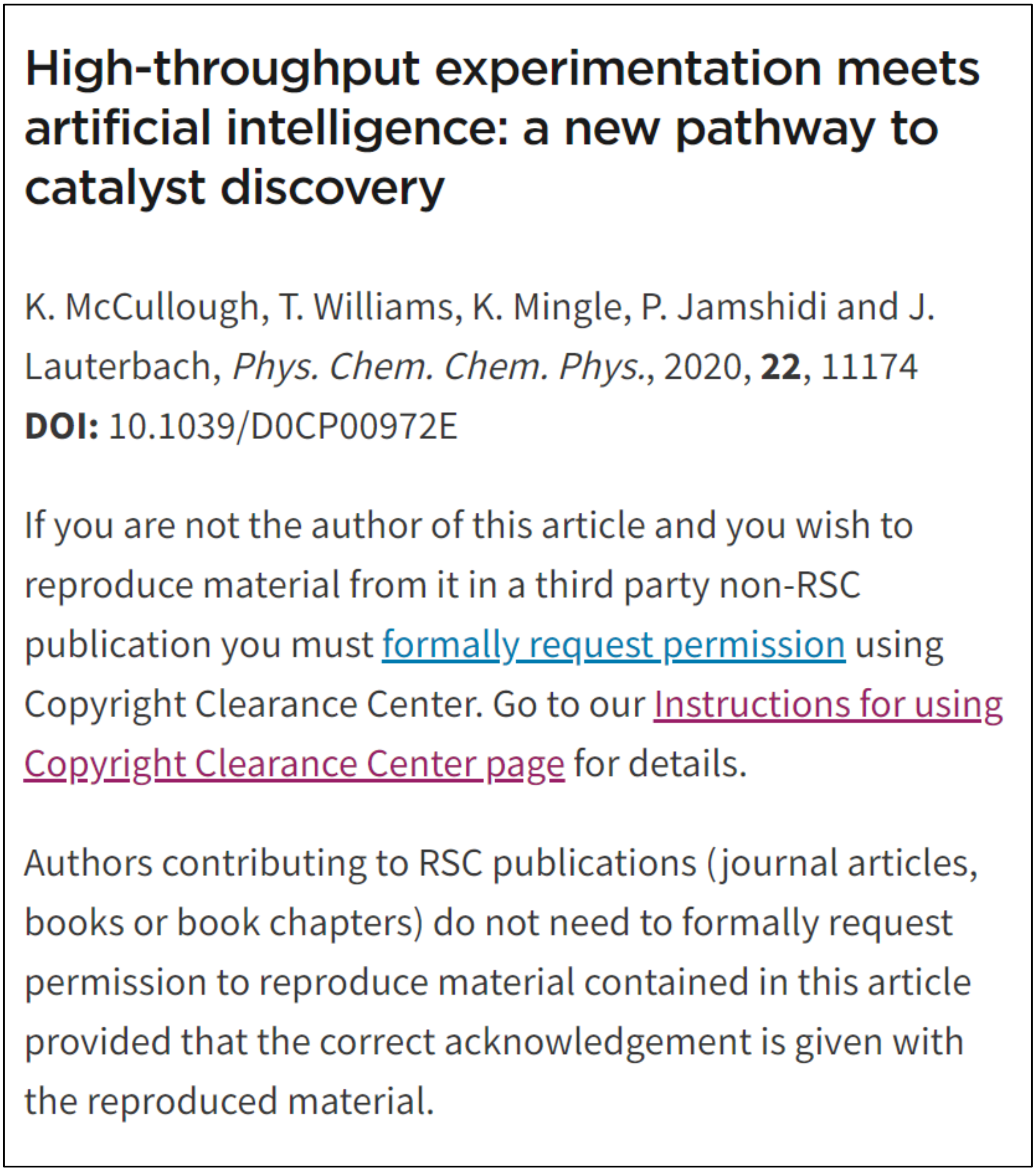

High-throughput experimentation meets artificial intelligence: a new pathway to catalyst discovery

K. McCullough, T. Williams, K. Mingle, P. Jamshidi and J. Lauterbach, *Phys. Chem. Chem. Phys.*, 2020, **22**, 11174
DOI: 10.1039/D0CP00972E

If you are not the author of this article and you wish to reproduce material from it in a third party non-RSC publication you must formally request permission using Copyright Clearance Center. Go to our Instructions for using Copyright Clearance Center page for details.

Authors contributing to RSC publications (journal articles, books or book chapters) do not need to formally request permission to reproduce material contained in this article provided that the correct acknowledgement is given with the reproduced material.

3. K McCullough, PH Chiang, JD Jimenez, J Lauterbach, “Material discovery and high throughput exploration of Ru based catalysts for low temperature ammonia decomposition.” Materials 13 (8) 2020, 1869.

MDPI Open Access Information and Policy

All articles published by MDPI are made immediately available worldwide under an open access license. This means:

- everyone has free and unlimited access to the full-text of *all* articles published in MDPI journals;
- everyone is free to re-use the published material if proper accreditation/citation of the original publication is given;
- open access publication is supported by the authors' institutes or research funding agencies by payment of a comparatively low **Article Processing Charge (APC)** for accepted articles.

Permissions

No special permission is required to reuse all or part of article published by MDPI, including figures and tables. For articles published under an open access Creative Common CC BY license, any part of the article may be reused without permission provided that the original article is clearly cited. Reuse of an article does not imply endorsement by the authors or MDPI.